Spacecraft Charging and Attitude Control Characterization of Electrospray Thrusters on a Magnetically Levitated Testbed

By

Fernando Mier-Hicks

M.S, Aerospace Engineering, Massachusetts Institute of Technology (2014)

B.S, Mechatronics Engineering, Monterrey Institute of Technology (2011)

Submitted to the Department of Aeronautics and Astronautics in partial fulfilment of the requirements for the degree of

DOCTOR OF PHILOSOPHY

at the

MASSACHUSETTS INSTITUTE OF TECHNOLOGY

January 2017 [February 2017]

Signature redacted

Author.....
Department of Aeronautics and Astronautics
January 2017

Signature redacted

Certified by.....
Dr. Paulo C. Lozano
Associate Professor of Aeronautics and Astronautics
Thesis Supervisor

Signature redacted

Certified by.....
Dr. Manuel Martinez-Sanchez
Professor Emeritus of Aeronautics and Astronautics

Signature redacted

Certified by.....
Dr. Kerri Cahoy
Associate Professor of Aeronautics and Astronautics

Signature redacted

Certified by.....
Dr. Shu T. Lai
Visiting scientist

Signature redacted

Accepted by.....
Prof. Youssef Marzouk
Associate Professor of Aeronautics and Astronautics
Chair, Graduate Program Committee

Spacecraft Charging and Attitude Control Characterization of Electrospray Thrusters on a Magnetically Levitated Testbed

By

Fernando Mier-Hicks

Submitted to the Department of Aeronautics and Astronautics in partial fulfilment of the requirements for the degree of Doctor of Philosophy in Aeronautics and Astronautics at the Massachusetts Institute Technology

January 2017

Abstract

Electrospray thrusters are an attractive technology for small satellite propulsion. A thorough study of the spacecraft charging and attitude control performance of electrospray thrusters acting on a small satellite is presented. The experimental portion of the study employs a new type of magnetically levitated testbed to measure thrust, characterize spacecraft charging phenomena, and demonstrate precision attitude control maneuvers. The testbed magnetically levitates a mockup-satellite in vacuum conditions. The satellite carries thrusters, batteries, radio, and high voltage thruster electronics. The magnetic levitation and high vacuum provide a zero-friction environment for the thrusters to actuate. The thrusters are placed on the satellite in such a way to produce a net torque when fired. The thrusters are fired and the corresponding rotational movement of the satellite is analyzed to calculate thrust. The uncertainty of the thrust measurement is estimated to be ± 0.35 μN (3σ).

Theoretical and experimental methods were developed to investigate the spacecraft charging characteristics anticipated to be observed on spacecraft during the operation of electrospray thrusters. These devices can produce positively and negatively charged ion-beams. An electrical model of this configuration was created to predict the charging properties of electrically isolated systems. This model simulates a bipolar electrospray thruster system. Experiments were conducted on the magnetic levitation testbed. The results from the experimental tests demonstrate that neutralization with heavy ionic species is indeed possible. The thrusters are able to fire in a bipolar configuration for long periods of time inducing

bounded spacecraft charging in the range from -400V to +600V when emitting currents of about 20 μA. It was found that the presence of low-energy ions produced by the fragmentation of large clusters and the external space plasma play a significant role in the neutralization characteristics. This electrical model was verified by reproducing the experimental results, thus validating its use to estimate bulk spacecraft charging properties.

Electrospray thrusters are capable of producing impulse bits in the 10^{-6} N·s or lower, depending on the configuration. These characteristics have the potential to allow for long term pointing in the arcsecond range or better with practically no jitter. Experimental work is performed on the magnetic levitation testbed to demonstrate the actuation characteristics under non-optimal control. It is found that subject to a noisy attitude sensor and external perturbations, electrospray thrusters are capable of producing pointing accuracies of 22 arcseconds 3σ error during 10 hours on a platform similar in size and mass to a 1U CubeSat. The implementation of such capabilities could complement or eliminate the need of reaction wheels and magnetorquers, especially in missions beyond low earth orbit, while including propulsive capabilities for additional maneuverability in technology development or scientific missions.

Thesis Supervisor: Dr. Paulo C. Lozano
Title: Associate Professor of Aeronautics and Astronautics

Committee Member: Dr. Manuel Martinez-Sanchez
Title: Professor Emeritus of Aeronautics and Astronautics

Committee Member: Dr. Kerri Cahoy
Title: Associate Professor of Aeronautics and Astronautics

Committee Member: Dr. Shu T. Lai
Title: Visiting Scientist

ACKNOWLEDGMENTS

Undertaking this PhD has been a life-changing experience. It would not have been possible to do without the support and guidance that I received from many people.

First and foremost, I wish to thank my advisor and friend, Professor Paulo Lozano, he has been a tremendous mentor for me. I thank him for giving me the opportunity to work along with him and learn from such a bright mind. The enthusiasm and joy he has for research was contagious and motivational for me. I thank him for encouraging my research and for allowing me to grow as a research scientist. Without his guidance and constant feedback this PhD would not have been achievable.

I want to thank all the AeroAstro and SPL members for countless hours of company, teaching and friendship, inside and outside of the laboratory. They helped make my stay at MIT a very happy and fun experience. In particular, the experimental work would not have been possible without the insight and guidance of Todd Billings. I would also like to thank my committee members, Professor Manuel Martinez-Sanchez, Professor Kerri Cahoy and Professor Shu Lai for the time invested in reviewing my work. I want to thank them for letting my defense be an enjoyable moment, and for their brilliant comments and suggestions. Thanks to Dr. Francois Martell for the insight, recommendations and advice given throughout my graduate career. I would also like to thank my sponsors, Conacyt, DoD and AFOSR for generously supporting me during my studies.

I have been blessed with a tremendously supportive and encouraging family. My father Angel, and grandfather Enrique, exposed me to engineering and science at an early age. I will always be grateful to them for guiding me and showing me what technology can do for us. I specially thank my father, for giving me the opportunity to use his home-made lab as my classroom when I was young, as well as guiding me and helping with my projects. I am confident that without their influence I would not be where I am. My mother, Mariela, has been a source of incredible support and encouraging words. The path I have taken has been possible, in large part, to her support and advice. I will be eternally in debt for all the sacrifices my parents have made in order for me to be where I am. The rest of my family deserves just as much recognition and gratitude, my brothers and sister, my grandmother, uncles and aunts, all of them giving unconditional support and offering insightful advice.

Lastly I want thank Annie, my lovely wife. I thank you helping me proof read my work. Thank you for all the encouragement and wise advice you have provided me. Thank you for always being there for me. Thank you for always surrounding me with so much love and joy. I would not have made it without you.

TABLE OF CONTENTS

1 Introduction 17

1.1 Satellite technology 17

1.1.1 Small satellites 17

1.1.2 Space propulsion 19

1.1.3 Current small satellite propulsion technologies 22

1.1.4 Electrosprays 24

1.1.5 Applications 26

1.2 Spacecraft charging and electrosprays 28

1.2.1 Space environment 29

1.2.2 Introduction to spacecraft charging 29

1.2.3 Space plasma and charging dynamics 33

1.2.4 Spacecraft charging in ion engines and Hall thrusters 36

1.2.5 Neutralizing cathodes 37

1.2.6 Spacecraft charging in electrosprays thrusters 38

1.3 Introduction to attitude control 39

1.3.1 State of the Art ACDS for small satellites 41

1.3.2 Thrusters as attitude control actuators 44

1.4 Conventional instruments 44

1.4.1 Thrust measurement 44

1.4.2 Spacecraft charging 46

1.4.3 Attitude control 46

1.4.4 Magnetically levitated CubeSat testbed 47

1.5 Thesis Contributions 48

2 Experimental methods 49

2.1 Magnetic Levitation CubeSat Testbed 49

2.1.1 Concept and design 51

2.1.2 Magnetic torque perturbation 55

2.2 Sensors and actuators 58
2.2.1 Levitation electromagnet 58
2.2.2 Vertical position sensor 60
2.2.3 Electromagnetic brake 62
2.2.4 Lifting mechanism 64
2.2.5 Helmholtz coils 65
2.2.6 Charge sensor 66
2.2.7 Angular encoder 68
2.2.8 CubeSat balancing 71
2.2.9 Inertia measurement 72
2.3 Plasma generator 74
2.3.1 Plasma characterization 80
2.4 Software and levitation controller 83
2.4.1 Magnetic levitation controller algorithm 84
2.5 Power processing unit 86
2.5.1 Thruster requirements 87
2.5.2 High voltage generation 88
2.5.3 High voltage switching 88
2.5.4 Housekeeping circuitry 91
2.5.5 High voltage ground selectivity 92
2.5.6 Performance and construction 92
3 Thrust characterization 94
3.1 Counteracting horizontal magnetic fields 94
3.1.1 Impact of restoring torque on thrust measurements 96
3.2 Thrust measurement methodology 97
3.3 Continuous thrust 100
3.4 Error propagation 100
3.5 Electrospray thrust measurements 105

4 Spacecraft charging and electrosprays 105

4.1.1 Bipolar operation 105

4.1.2 Floating power supply 107

4.1.3 Effects of ion fragmentation 109

4.1.4 Plasma environment as neutralization source 111

4.2 Charging model 113

4.2.1 Emitted and intercepted currents 114

4.2.2 Return current 116

4.2.3 Plasma current 117

4.3 Model results 119

4.3.1 Ideal bipolar operation 120

4.3.2 Differential interception 121

4.3.3 Differential startup voltage 123

4.3.4 Return current, mono-energetic beam 124

4.3.5 Return current, thruster ion beam 126

4.3.6 Return current, single emitter 127

4.3.7 Plasma effects, LEO 129

4.3.8 Plasma effects, GEO 131

4.4 Spacecraft charging effects on thrust 132

4.5 Experimental spacecraft charging results 133

4.5.1 Static, non-levitated experiments 133

4.5.2 Charge sensor shield 138

4.5.3 Single thruster experiments 142

4.5.4 Experimental evidence of return current 147

4.5.5 Bipolar operation experiments 148

4.5.6 Experiments with plasma 153

5 Attitude control and electrosprays 165

5.1 Chemical thrusters as reaction thrusters 165

5.2 On-Off thrusters 167
5.2.1 Electrosprays as attitude control thrusters 170
5.3 Attitude controller and power processing unit 171
5.4 Experimental results 173
5.4.1 Counteracting perturbations 173
5.4.2 Small step response 175
5.4.3 Large step response 176
5.4.4 Long duration 177
6 Conclusions and recommendations 179
6.1 MagCube 179
6.2 Spacecraft charging 180
6.3 Attitude control 183
7 References 185

TABLE OF FIGURES

Fig. 1.1 Two 30-cm long satellites, Planet Labs Doves, being launched by the ISS. Credit: NASA 18
Fig. 1.2 Change in velocity with respect of propellant mass fraction for different I_{sp}. 21
Fig. 1.3 Electrospray single emitter. 24
Fig. 1.4 Electrospray thruster concept. 25
Fig. 1.5 iEPS device next to a US quarter for scale. Credit: Vickmark 26
Fig. 1.6 Direct lunar impact trajectory. Credit: Whitlock 27
Fig. 1.7 Damage on a solar panel caused by sustained arcing on EOS-AM1. Credit: NASA 31
Fig. 1.8 Paschen curves for different gases as a function of pressure times gap length. 32
Fig. 1.9 Tether damage of TSS-1R. Credit NASA. 33
Fig. 1.10 Gridded Ion engine schematic. Credit: NASA 36
Fig. 1.11 General schematic of a Hall thruster. Credit: McWalter 37
Fig. 1.12 Cross Section of a hollow cathode with a keeper electrode. Credit: Goebel 38
Fig. 1.13 Precise, 3-axis, stellar based CubeSat attitude determination and control system in a Micro-package (0.5U). Credit BCT 43
Fig. 1.14 Simplified schematic of high precision torsional balance. Credit Ziemer. 45
Fig. 1.15 CubeSat mounted in traditional 3-axis air bearing. Credit: Hindawei 47
Fig. 2.1 Concept of magnetically levitated CubeSat testbed. 49
Fig. 2.2 Levitated structure. 50
Fig. 2.3 Main components of magnetic levitation CubeSat testbed. 51
Fig. 2.4 MagCube mounted inside the vacuum chamber. 52
Fig. 2.5 Wire vibration dampers 53
Fig. 2.6 MagCube inside the vacuum chamber. 54
Fig. 2.7 FTS-100, a micro force probe sensor. 55
Fig. 2.8 Horizontal magnetic field of a non-ideal magnet. Credit: MagCam 56
Fig. 2.9 Placement of the Helmholtz coils near the levitation region. 57
Fig. 2.10 Orthogonal Helmholtz coils used to counteract horizontal magnetic fields around the levitation region. 58
Fig. 2.11 Levitation electromagnet and gimballing structure. 59
Fig. 2.12 Vertical position sensor concept. 60
Fig. 2.13 Circuit schematic of the vertical position sensor. 61

Fig. 2.14 Calibration fit of the vertical position sensor 61
Fig. 2.15 Construction of vertical position sensor 62
Fig. 2.16 Electromagnetic brake construction 64
Fig. 2.17 MIGAone-10 65
Fig. 2.18 Lifter mechanism construction 65
Fig. 2.19 Helmholtz coil construction. 66
Fig. 2.20 Charge sensor concept and construction. 67
Fig. 2.21 Transfer function of charge sensor with linear fit. 67
Fig. 2.22 Measured satellite potential while satellite is rotating at 1.7 RPM with no thruster emission. 68
Fig. 2.23 MicroE Mercury 3500V angular encoder system. 69
Fig. 2.24 Noise of angular encoder measurement. Blue trace is the smoothed angle signal. 70
Fig. 2.25 Balancer CAD and construction. 72
Fig. 2.26 Trifilar pendulum construction. 74
Fig. 2.27 Barium oxide coated filament of a fluorescent lightbulb. 75
Fig. 2.28 Main parts of the MagCube cathode. 76
Fig. 2.29 Assembled cathode. 77
Fig. 2.30 Ignited MagCube cathode with visible plasma plume (blue glow) and filament glow (orange glow). 78
Fig. 2.31 Hot cathode concept 79
Fig. 2.32 Tungsten foil hot-cathode in operation. Argon outlet is the small structure directly below the filament. 79
Fig. 2.33 Representative IV curve for Langmuir probe immersed in a plasma. 80
Fig. 2.34 Characterization of an IV curve from the Langmuir probe. The probe was immersed in a plasma environment similar to a 400 km orbit. 82
Fig. 2.35 Screenshot of MagCube software. 84
Fig. 2.36 MagCube driving electronics box. 84
Fig. 2.37 PPU block diagram 86
Fig. 2.38 Floating power supply concept. In an ideal case both thrusters emit the same amount of current, but of opposite polarities 88
Fig. 2.39 Comparison of high voltage relays. Reed relay on the left. Two telecom relays on the middle. The blue arrow points to the orifice purposely introduced to the relay to evacuate gases. 89

Fig. 2.40 Architecture of the PPU. 90
Fig. 2.41 Iterations of PPU design. 93
Fig. 3.1 Impact of Helmholtz angle and magnitude on oscillation profile. 95
Fig. 3.2 Levitated structure angular position and speed over 10 hours, under high vacuum conditions 97
Fig. 3.3 Representative thrust measurement sequence 98
Fig. 3.4 Quadratic fit on angular position to find thrust. 99
Fig. 3.5 Resolving thrust steps 100
Fig. 3.6 Angular acceleration measurements for trials at different current levels. Horizontal line is the mean. Star markers correspond to the mean value. Error bars are the final characteristic angular uncertainty (3σ). 102
Fig. 3.7 Thrust measurement of electrospray thrusters by different entities. 105
Fig. 4.1 Electrospray thrusters in the bipolar configuration. 106
Fig. 4.2 Schematic of a satellite firing electrospray thrusters in the bipolar configuration. 108
Fig. 4.3 Relevant potentials in the bipolar configuration for two dissimilar thrusters. 109
Fig. 4.4 Paths of ions born from a fragmentation event assuming a positively charged spacecraft. 110
Fig. 4.5 Current sources used to model an electrospray thruster 114
Fig. 4.6 Experimental I-V curve compared to the electrical model. (a) shows the complete emission profile. (b) displays the detailed region bounded by the box in (a). 115
Fig. 4.7 RPA curve of an iEPS fueled with EMI-BF4 and firing in positive mode. 117
Fig. 4.8 Simulated plasma current for a 1-U CubeSat with respect to satellite potential. 119
Fig. 4.9 Ideal bipolar emission with no plasma. No charging present. 121
Fig. 4.10 Simulation of differential interception case. 122
Fig. 4.11 Simulation of differential startup voltage. 124
Fig. 4.12 Monoenergetic beam energy distribution. 125
Fig. 4.13 Simulation of the return current effects for a monoenergetic beam. 125
Fig. 4.14 Ion beam energy distribution of an iEPS filled with EMI-Bf4. 126
Fig. 4.15 Simulation of the return current effects for bipolar iEPS ion beams. 127
Fig. 4.16 Representative ion beam energy distribution of a single emitter wetted with EMI-Bf4 and fired at 1600V. 128
Fig. 4.17 Simulation of the return current effects for an ion beam with low fragmentation. 128

Fig. 4.18 Simulation of the plasma current effects in LEO environment..... 130
Fig. 4.19 Simulation of the plasma current effects in GEO environment. 131
Fig. 4.20 Effects of satellite potential on thrust. The two coordinates represent the satellite potential boundary measured for the test described in Fig. 4.33. 133
Fig. 4.21 Static test configuration. 135
Fig. 4.22 Single electrospray thruster firing in static test..... 136
Fig. 4.23 Single thruster firing in static test while the satellite is manually discharged. . 138
Fig. 4.24 MagCube tests with thrusters in the bipolar configuration. 139
Fig. 4.25 Satellite potential drift. Top is negative emission, bottom is positive emission. 140
Fig. 4.26 Charge sensor equipped with shield..... 141
Fig. 4.27 Guard visible on the bottom side of the CubeSat..... 141
Fig. 4.28 Sliced view of charge sensor shield and CubeSat guard..... 142
Fig. 4.29 Results of single electrospray thruster test in maglev testbed. (a) displays the complete test. (b) shows a detailed view of the turn-off transient shown in the leftmost box region of (a). (c) displays a detailed view of the turn-on transient shown in the rightmost box region of (a). 144
Fig. 4.30 Recreation of results of single thruster test in maglev testbed by simulation. (a) displays the entire simulation. (b) and (c) show the transient details of the leftmost and rightmost boxes of (a) respectively. 146
Fig. 4.31 Evidence of return current while firing an electrospray thruster in the maglev tested..... 148
Fig. 4.32 Effects of the return current on the extractor. 149
Fig. 4.33 Experiment and simulation results of firing electrospray thrusters in the bipolar configuration. (a) and (b) show measured thruster variables and measured satellite potential, respectively. (c) and (d) display the simulated thruster variables and simulated satellite potential, respectively..... 150
Fig. 4.34 Satellite potential for different emitted current levels..... 152
Fig. 4.35 Satellite potential evolution while emitting low currents. 153
Fig. 4.36 Exposed electronics and thrusters in the levitated CubeSat..... 154
Fig. 4.37 Side openings in thrusters. 154
Fig. 4.38 Effects of plasma leaking into thruster substrate. 155
Fig. 4.39 Electrospray thrusters on the top face of a CubeSat. 156
Fig. 4.40 Shielded thruster mount and shielded connector. 157

Fig. 4.41 Electrospray firing at constant current while the plasma parameters are varied. 158
Fig. 4.42 Effects of a MEO-like plasma on a spacecraft firing a single electrospray thruster. 160
Fig. 4.43 Pair of thrusters in the bipolar configuration firing in a dense plasma environment. 162
Fig. 4.44 Thrusters firing in the bipolar configuration while plasma parameters were varied. 163
Fig. 5.1 Representative action of an attitude controller employing ON-OFF thrusters. .. 166
Fig. 5.2 ACDS test case arrangement and behavior. 167
Fig. 5.3 Propellant lifetime with respect to I_{bit} for different deadbands. 168
Fig. 5.4 I_{bit} required for a certain deadband for different t_{coast}. 169
Fig. 5.5 MagCube schematic for attitude control experiments. 172
Fig. 5.6 Attitude control PID Diagram. 173
Fig. 5.7 Activating the attitude controller. 174
Fig. 5.8 One degree step changes. 176
Fig. 5.9 Twenty three degree setpoint change 176
Fig. 5.10 Satellite holding attitude for ten hours. Dashed lines indicate 3σ boundary..... 177
Fig. 5.11 Manipulation for a constant setpoint during a 10 hour period. Dashed line indicates average manipulation over the entire test. 178

NOMENCLATURE

Δv	=	Orbital change in velocity
$\dot{m}$	=	Propellant mass flow rate
λ_D	=	Debye length
$\Delta\omega$	=	Change in satellite's angular velocity
2θ	=	Attitude deadband or precision
ADCS	=	Attitude Determination and Control System
c	=	Exhaust exit velocity
C_{sc}	=	Spacecraft self-capacitance
F	=	Thrust
F_{bit}	=	Minimum thrust bit
I	=	Inertia of levitated structure
I_{bit}	=	Minimum impulse bit
I_e	=	Electron plasma current
iEPS	=	ion Electrospray Propulsion System
I_i	=	Ion ram current
I_{sp}	=	Specific impulse
J	=	Current flux
J_e	=	Electron current flux
J_i	=	Ion current flux
L	=	Lever arm
MagCube	=	Magnetically levitated CubeSat testbed
m_p	=	Propellant mass
m_{sc}	=	Dry spacecraft mass
n_e	=	Plasma density
PPU	=	Power Processing Unit
t	=	Firing time
T_{bit}	=	Minimum firing time bit
T_{coast}	=	Time between firings, coasting time.
T_e	=	Electron plasma temperature
T_{life}	=	Propellant lifetime
V_{sat}	=	Satellite potential with respect to external environment
V_{th}	=	Thruster voltage
q/m	=	Charge to mass ratio of emitted species
α	=	Angular acceleration
η	=	Efficiency

1 Introduction

1.1 Satellite technology

The space industry is on the verge of a disruptive revolution. In the last couple of years, commercial companies have taken over tasks once only doable by large governmental corporations such as NASA. The International Space Station (ISS) is currently being serviced by commercial companies on a regular basis. These significant changes complement the past, and outdated, space philosophy to change. The idea that the only way to get to space is by building large, complex and costly spacecraft is no longer the dominant idea. New opportunities emerge for audacious missions that are willing to change the paradigms of traditional satellite engineering.

Space has always been a risky endeavor. Sending a satellite into Earth's orbit requires extensive knowledge and engineering in all systems involved, from the main rocket's actively cooled nozzle to the screws and nuts in the payload structure. Space systems are inherently high-cost due to their advanced technology and their need of reliability; they must be proven to work under all circumstances on most cases. A failed attempt in space is embarrassing, time consuming and extremely unprofitable. Since the system is costly to begin with, increasing its reliability and ability to tolerate more risk escalates the cost even more. These characteristics also increase the complexity of the project because extra systems that increase reliability and redundancy have to be incorporated into the design. As complexity grows, the time to design and execute the mission also grows. Following this philosophy we end up with what, until recent years, has been the only way to get into space; very few, complex, large and extremely high cost missions.

1.1.1 Small satellites

Small satellites were conceived to invert the space spiral and make space more accessible. California Polytechnic State University created the CubeSat standard [1], a small satellite architecture that tips the space spiral upside down. The rapid pace in the miniaturization of high performance space technologies has allowed small satellites, such as popular CubeSats, to expand their mission capabilities in engineering and scientific applications. CubeSats are standardized small satellites where each unit, or "U", measures 10x10x10 cm and has a mass of about 1 kg [1]. Several of these units can be stacked to provide larger volumes for different

spacecraft designs. Being much smaller than the traditional satellite, CubeSats weigh orders of magnitude less than a traditional spacecraft. With current launch costs averaging around $10,000 per kilogram launched [2], CubeSats reduce cost by reducing volume and mass. These small satellites usually ride along bigger satellites and get individually deployed at some point in orbit. Other options for deployment include launching them from the International Space Station. The whole premise relies on less costly, less risk averse, and more frequent missions.

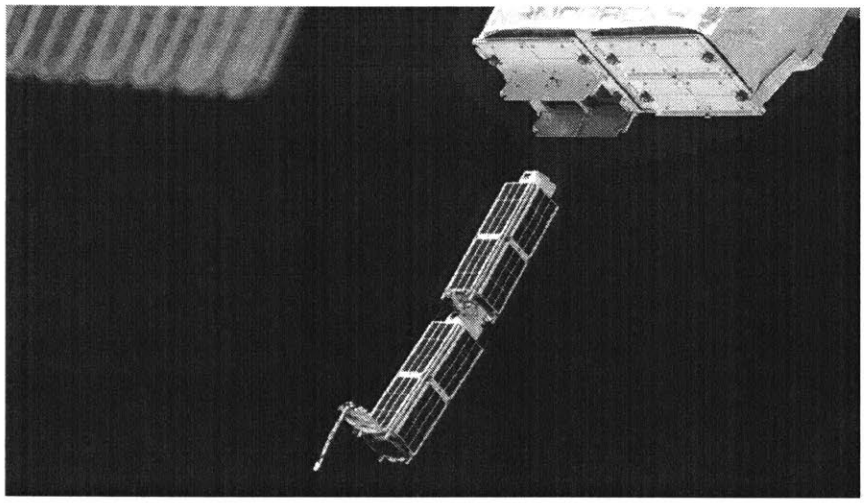

Fig. 1.1 Two 30-cm long satellites, Planet Labs Doves, being launched by the ISS. Credit: NASA

The CubeSat philosophy relies on accepting a larger risk in every mission but, ideally, with no compromise on quality. A higher risk tolerance translates into faster development cycles which reduces cost tremendously. CubeSat are usually not tested as thoroughly as traditional satellites. CubeSat are tested by flying. To reduce costs even further CubeSats often rely on Commercial Off-The-Shelf components (COTS) in their construction. Standard electronic components that are used every day in smartphones and other miniaturized devices have characteristics that make them very attractive to space designs. Low power consumption and high computing capabilities along with a small footprint make these COTS very desirable in small satellite designs. Even though COTS are not designed to be radiation tolerant, CubeSats are usually in low enough orbits to avoid significant radiation doses that could damage their components. Satellites that benefit from processors that follow Moore's law (computing power increases two fold every 2 years) are able to engage more demanding missions while at the same time consume moderate amounts of power and occupy a fraction of the available satellite volume.

Besides computing power, COTS components are also desirable in communications circuits. Radio transceivers and amplifiers capable of handling several watts of power open up high data rate communications channels to these small satellites. To generate enough power in such a small area, high efficiency solar cells are employed in almost all CubeSats. With efficiencies ranging in the upper 20% range, 1-U CubeSats are able to generate around 5 watts of power. To control the attitude of the satellite, miniature reaction wheels and magnetorquers exist in several configurations [3]. The full extent of CubeSats has only begun to be explored. Current missions range from atmosphere analysis to multi-satellite constellations for frequent Earth imaging.

COTS devices including communication modules, battery systems, solar panels and micro-computers have all been proven in space on different CubeSat missions. Nevertheless, capabilities of these spacecraft remain constrained by the orbit in which the launcher injects them; these satellites usually ride as secondary payloads. Once deposited in their predetermined orbit, they drift and are victim of orbital perturbations that usually end in atmospheric re-entry. Propulsion would open up the range of missions CubeSats could execute. Besides extending the orbital lifetime of small satellite missions, propulsion would open up the possibility of small satellites escaping Earth's gravitational field, becoming interplanetary probes [4]. Several asteroid mining companies plan to employ a fleet of interplanetary small satellites to prospect and inspect potential asteroids.

Propulsion is one of the most technically-challenging subsystems for a small satellite, the miniaturization of propulsion devices that are used on larger spacecraft is limited not only by the lack of technologies but in some cases by the physics governing the specific thruster.

1.1.2 Space propulsion

In the vacuum of space, Newtonian physics primarily limits the propulsion devices used to those that work by expelling some mass, commonly referred as propellant, to some velocity. Newton's third law, *"For every action there is an equal and opposite reaction"*, states that by accelerating propellant, the spacecraft will suffer an opposite but equal force. This force is called thrust. Since the spacecraft has to carry the propellant mass it will be ejecting, it is easy to see the reduction in acceleration this causes due to the increase of total mass. After ejecting the propellant, the spacecraft will be traveling faster than before, this change in velocity is

usually referred as delta-v or Δv. Delta-v is a common way to gauge orbital maneuvers, the more delta-v required to perform an orbital change the more propellant the spacecraft will have to consume to achieve the change in velocity. Common orbital maneuvers include changing the orbital plane, increasing the semi major axis, or circularizing the orbit, all of these can be classified by how much delta-v is needed to perform them. It is important to notice that some maneuvers do not change the velocity of the spacecraft but still require the use of propellant. Attitude control and atmospheric drag compensation are examples of maneuvers that do not modify the spacecraft velocity but they do consume propellant, therefore a delta-v cost can be associated to them. Other types of propulsion devices that do not work on the ejection of mass principle, such as solar sails and tethers, are usually bulky and not practical for use in small satellites.

The basic equation governing propulsion in space is the well-known rocket equation.

$$\frac{m_{sc}}{m_p + m_{sc}} = e^{\frac{-\Delta V}{c}} \qquad \textbf{Eq. 1.1}$$

This equation is derived from a closed system with no external forces acting on it while using momentum conservation as a method to relate the exhaust properties with thrust. The rocket equation, Eq. 1.1, relates the spacecraft mass, m_{sc}, and propellant mass, m_p, with the change in velocity, ΔV, that can be achieved after the thrusting device expels all the propellant mass at velocity c. Further analysis of the closed system provides the following relationship.

$$F = \dot{m}\, c \qquad \textbf{Eq. 1.2}$$

The previous equation relates the thrust, F, generated by the propulsion device and states that is directly proportional to the velocity at which the propellant mass is ejected, c, times the mass flow rate of the propellant, $\dot{m}$. It is useful to redefine the exhaust velocity of the engine, c, with the total impulse given to the spacecraft. The specific impulse, I_{sp}, is defined in Eq. 1.3 as the total impulse imparted to the spacecraft divided by the weight of the propellant used to produce this impulse, if the exhaust velocity is constant. The total impulse imparted is equal to the mass flow rate, $\dot{m}$, multiplied by the exhaust velocity, c, and the burn time, t. The weight of the propellant is simply its mass, m, times the gravity constant, g. The specific impulse equation simplifies to the exhaust velocity divided by the gravitational acceleration at Earth's surface, 9.81 m/s^2. The units of specific impulse are seconds.

$$I_{sp} = \frac{\dot{m}\, c\, t}{m\, g} = \frac{c}{g} \qquad \textbf{Eq. 1.3}$$

The rocket equation shows the exponential relationship between the propellant that is needed to be ejected from the spacecraft to provide thrust and the amount of change in velocity

achieved by this action. Analyzing the equations stated earlier we can infer the general trades that have to be made in terms of propellant mass, the final change in velocity that can be achieved, and the specific impulse of the propulsion device.

Fig. 1.2 shows the propellant mass fraction needed to accelerate a spacecraft in order to achieve a certain delta-v. The propellant mass fraction is simply ratio between the propellant mass and the initial mass of the spacecraft. An 80% mass fraction indicates 80% of the total mass of the spacecraft is propellant. It is assumed that the spacecraft mass includes the propulsion system mass but excludes the propellant mass. Several specific impulses are graphed to give a comparison of different thruster technologies. A low propellant mass fraction and high delta-v is desirable, but not always possible. It is clear to see how a high I_{sp} allows the spacecraft to carry less propellant for any given change in velocity, but not without consequence.

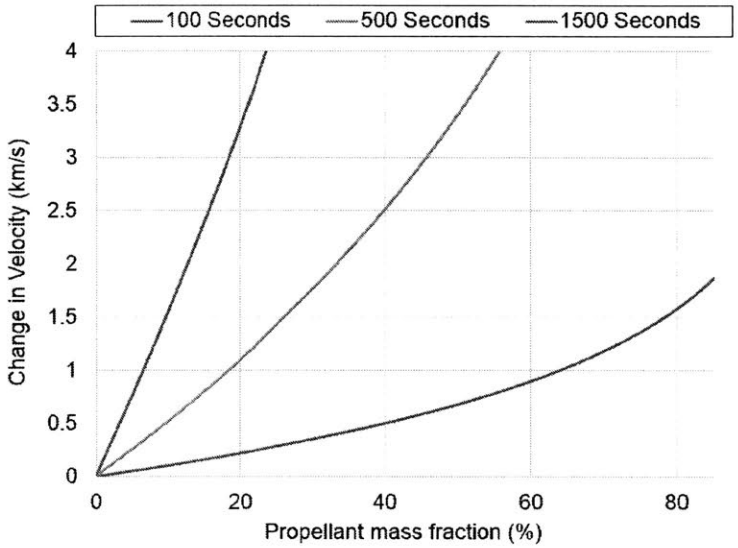

Fig. 1.2 Change in velocity with respect of propellant mass fraction for different I_{sp}.

Currently, there are mainly two main propulsion systems, chemical or electrical energy. Chemical propulsion is based on the use of energetic chemical reactions to accelerate the propellant through a nozzle. Electric propulsion usually employs electric fields to accelerate ions and provide thrust. Both methods have very different applications and characteristics. In order to describe the differences between the two classes of propulsion technologies it is useful to analyze the power and energy input to the device. Energy must be transformed from its initial state, either electric or chemical, to kinetic energy in the exhaust particles and of the spacecraft. This means that a high exhaust velocity requires a larger amount of energy.

The energy imparted to the exhaust particles cannot be provided instantaneously, meaning we can assume that the acceleration of the exhaust particles takes place at a fixed rate, therefore at a specific power level. An efficiency factor, η, describes the efficiency of the engine to impart energy to the exhaust particles. If the efficiency factor is also taken into account, we arrive at the following equation relating power, P, spacecraft mass, m_{sc}, and acceleration, a, of the spacecraft.

$$P = \frac{Energy}{Time} = \frac{m_{sc}\, a\, c}{2\,\eta} \qquad \textbf{Eq. 1.4}$$

For a fixed power, a higher exhaust velocity, c, entails a lower acceleration of the spacecraft and vice versa. This is the common relation in space propulsion, higher specific impulse generally entails lower thrust due to the limit on how much energy the rocket can carry or produce at a given time.

Chemical thrusters generally provide more thrust at lower specific impulses than their electric counterparts. They accelerate a large mass of propellant to relatively low velocities. The majority of electric thrusters on the other hand accelerate heavy ions to very high velocities, providing higher specific impulses but lower thrust levels. Small satellites cannot afford to carry large amounts of propellant so they are generally in need of high specific impulse thrusters that produce thrust while consuming small amounts of propellant. The lower thrust level from the high specific impulse device is compensated by activating the thruster for a longer period of time. It is not unusual to fire electric thrusters for thousands of hours [2]. The mass and volume of the electronics needed to drive electric thrusters are also important factors of the overall system. Since the thruster power is proportional to the square of the specific impulse, there is a practical limit on how high the specific impulse can be. Usually there is an optimal value of specific impulse depending on the goals of each mission. Popular electric thruster technologies for large satellites rely on bulky tanks and heavy thrusters. Scaling these devices down to the CubeSat volume is challenging to say the least.

1.1.3 Current small satellite propulsion technologies

Chemical and electrical propulsion systems both offer different characteristics useful in certain situations with certain disadvantages as well. The chemical thruster category is mainly composed of solid and liquid rocket engines. These devices produce exothermal reactions by burning or chemically decomposing the propellant to provide an energetic reaction that expels

the products of the combustion through a nozzle. Electric thrusters such as ion engines and Hall thrusters, generally ionize a noble gas that then is accelerated using an electric field. The ions escape the device with great velocity, producing thrust.

Both electrical and chemical thrusters have been proven in space by a multitude of missions [2]. The new trend that pushes the miniaturization of larger satellites into CubeSats has pushed propulsion technologies to their physical limits. Chemical propulsion simply does not have a high enough specific impulse to provide any useful orbital maneuvers exempting those that require very low amounts of delta-v, and therefore low amounts of propellant for the CubeSat to carry. Further miniaturization of a chemical thruster to the CubeSat level is extremely challenging and will reduce its performance compared with a larger system. Nevertheless, there are COTS chemical propulsion systems for available for CubeSats [5, 6].

Electric propulsion thruster components used in large satellites are difficult to miniaturize to the CubeSat volume. Plumbing, valves, tanks and ionization chamber are few of the components that are required for the most basic device. All of these components pose a challenge when trying to scale to a small satellite size. Ion engines and Hall thrusters are devices that were initially designed to operate at powers in the 100-1000 Watts. Considering that CubeSats generally only have a few watts of power capacity, it can be clearly seen that the power processing unit (PPU) for a traditional electric thruster would also require considerable engineering. Aside from these constraints, when shrinking down ion engines or Hall thrusters the plasma density in their ionization chambers also has to be increased to deliver the same performance. The smaller surface area combined with higher fluxes, due to denser plasma, increase heat losses. Working at elevated temperatures due to heat losses in a low power device translates into poor efficiency.

Electrospray thrusters, a new type of electric propulsion technology that attempts to fill the gap in propulsion technologies for small satellites will be the main topic of this work. Electrosprays differ significantly from their more mature electric counterparts mainly in the lack of the need to ionize the propellant. Also, passive feeding of propellant to the emission sites simplifies the device and allows for the total lack of complicated plumbing systems. Finally, electrospray thrusters do not produce any significant thermal processes, in principle making the engines last longer and have higher efficiencies.

1.1.4 Electrosprays

Electrospray thrusters are a type of electric propulsion device for spacecraft that work by emitting positively or negatively charged particles from an electrically conductive liquid by means of a high electrical field. The specific nature of emitted charges depends on the thruster's operational characteristics and the type of liquid used. When room temperature ionic liquids are used, the emission typically consists of molecular ions and/or small ion clusters [7]. Room temperature ionic liquids are molten salts that remain in the liquid phase at ambient temperature. These substances are comprised of positive and negative ions, with no intervening solvent and exhibit zero vapor pressure, thus allowing their use in space without concerns of evaporation. Ions are expelled from the device at high velocities generating thrust with a high specific impulse. The emission of charged particles from this, and other types of electric thrusters, play a fundamental role in how the potential of the spacecraft varies with respect to the local environment or within different parts of the vehicle. It is important to predict and control the charging characteristics to prevent a decrease of performance, or even damage to payloads and subsystems.

To achieve ionic emission, large electric fields on the order of 1V/nm are required on the surface of the liquid [8]. To reach such field magnitudes, sharp emitter structures capable of transporting the liquid are used. A voltage difference is applied between the conductive liquid and a downstream extractor electrode aperture, as shown in Fig. 1.3. The potential difference produces an instability on the liquid surface which shapes it into a sharp meniscus. At the apex of this meniscus the field is intensified to the values required for ion emission. These ions are then accelerated by the same electric field that extracted them from the ionic liquid. Ions that successfully pass through the extractor generate net thrust for the spacecraft. Due to their inherently small scale, electrospray thrusters are attractive as a propulsion technology for small satellites. In addition, since they are modular, they are also scalable to larger spacecraft classes.

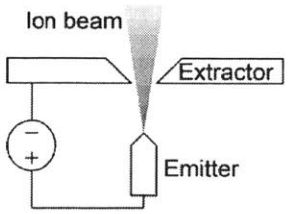

Fig. 1.3 Electrospray single emitter.

Each electrospray emission site generates tens to hundreds of nA in ionic current with velocities in the km/s range and produce tens of nN of thrust [9]. The typical droplet mass is between 3000 and 10,000 atomic masses. Larger thrust is obtained when operating a large number of emitters in a parallel array configuration.

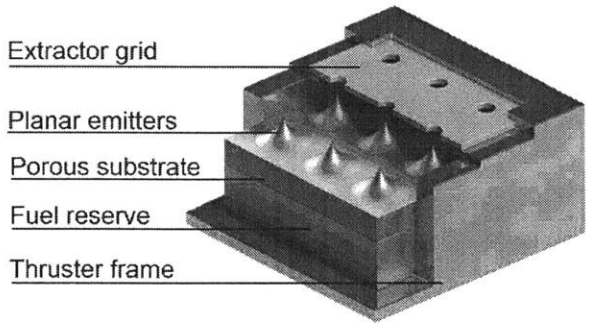

Fig. 1.4 Electrospray thruster concept.

Several array configurations utilizing micro-fabrication techniques have been proposed [10-13]. In this study, ion Electrospray Propulsion Systems (iEPS) are used. These thrusters are developed at the Space Propulsion Laboratory at MIT [11] and schematically depicted in Fig. 1.4. They are typically fueled with the ionic liquid EMI-BF4.

The thruster arrays are housed in a silicon frame that has dimensions of 13 x 12 x 2.4 millimeters. The frame contains a porous glass emitter substrate holding 480 laser-ablated tips. Above these tips sits a gold-coated, silicon extractor grid. Emitted ions move through the apertures in the grid to the outside environment. The array produces about 0.1 μN of thrust per μA of emitted current [11]. The arrays used in this study operate nominally around 150 μA of current which translates into ~12 μN of thrust per thruster. The propellant used travels from a fuel reserve by capillary action. Therefore, no valves or plumbing are needed to manage the propellant. Including this reserve, each iEPS module has dimensions of 14mm x 14mm x 14mm. The small scales of these thrusters, along with their high specific impulse, makes them ideal candidates for small satellite propulsion [14].

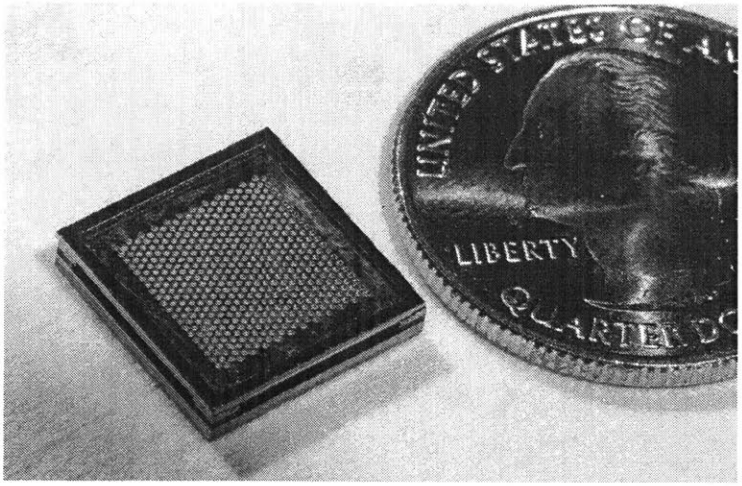

Fig. 1.5 iEPS device next to a US quarter for scale. Credit: Vickmark

1.1.5 Applications

A clear application of electrospray thrusters is drag cancellation. For example, at a 400km orbit, the drag force experienced by a 1-U CubeSat during solar mean is in the order of ~0.8 μN [2]. With this level of drag, the CubeSat could reenter the atmosphere in a year or less. Thrusters could be used to counteract atmospheric drag, extending mission lifetime. As an example, a 1-U CubeSat equipped with electrospray thrusters operating at a specific impulse of 1000 seconds would only need ~3 grams of propellant to counteract drag for a year. This would double the mission lifetime compared to current orbit lifetimes.

Several detailed studies have shown the attractiveness of electrospray propulsion systems when applied to small satellites. Whitlock describes the effectiveness of the thrusters in a proposed Lunar impactor mission [4]. A 3U CubeSat equipped with electrospray thrusters climbs from a geostationary orbit to a lunar impacting orbit, Fig. 1.6. His results show that this could be accomplished in as little as 72 days using 387 grams of propellant with a specific impulse of 2500 seconds. The total delta-v required for this missions would be close to 2 km/s. According to Whitlock, a near-Earth object could also be explored with a small satellite equipped with a large array of electrospray thrusters. In this mission the spacecraft could escape Earth's gravity from a GEO orbit in 360 days using a propulsion system capable of delivering 2.2 mN. In these two missions an electrospray thruster system would operate in orbits higher than LEO which has important impacts on the satellite design.

When the CubeSat travels through the cislunar space, it will be surrounded by the dilute space plasma characteristic of these altitudes. Since electrospray thrusters accelerate charged species, in certain scenarios there could be an imbalance of currents flowing in and out of the spacecraft, leading to spacecraft charging. This undesirable effect can be addressed by studying the interaction of the propulsion system with the space plasma and with the satellite. Currently, one of the biggest uncertainties in electrospray operation are the effects of charging and neutralization dynamics. Since it is expected that these effects will be different from conventional electric propulsions devices, it becomes relevant to study their operational effects.

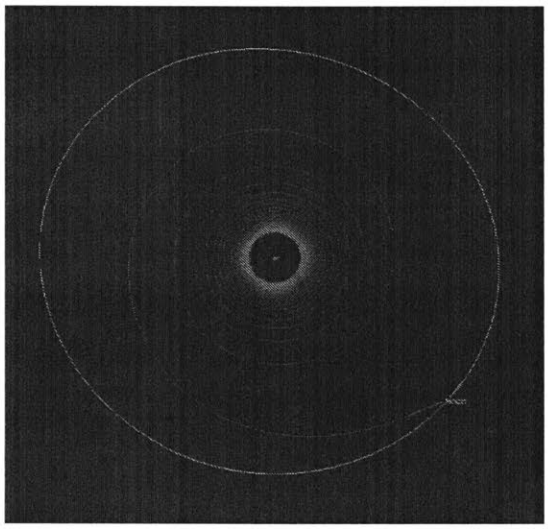

Fig. 1.6 Direct lunar impact trajectory. Credit: Whitlock

Attitude control for small satellites is usually achieved with reaction wheels. Reaction wheels are usually desaturated using magnetorquers which are ineffective at higher orbits since Earth's magnetic field weakens with altitude [2]. Therefore, to desaturate the wheels at high orbits the satellite would require reaction thrusters. If the satellite is carrying a propulsion system capable of attitude maneuvers, such as electrospray thrusters, then reaction wheels could be omitted altogether. This will simplify the design considerably and increase the total volume available for the payload. This would be the case of the lunar impactor mission described previously. Furthermore, if the thrusters have a low minimum impulse bit they could be used to perform precise attitude control maneuvers. The precision on these maneuvers could open up the possibility to use laser communication or perform a specific type of scientific mission not available otherwise.

In this work, a comprehensive study of charging dynamics of a spacecraft employing electrospray thrusters is presented. Plasma interactions are included in this analysis. Precise attitude control maneuvers are demonstrated in a realistic spacecraft charging environment, providing evidence that electrospray thrusters can successfully operate under the influence of spacecraft charging operational effects.

1.2 Spacecraft charging and electrosprays

Specific impulse and thrust are the most important performance parameters of a thruster but not the only ones. For example, chemical propulsion systems produce vibrations and extreme temperature swings near the nozzle, making the placement of the nozzle on the spacecraft a very important engineering task. Similarly, electric propulsion systems can produce unattractive effects on its host spacecraft if not engineered correctly. One of the most important unwanted effects while operating an electric thruster is spacecraft charging.

Spacecraft charging occurs when there is a current imbalance of electric currents from the spacecraft to the environment. In LEO the space environment is usually a relatively high density, low temperature, plasma which interacts electrically with the satellite. In GEO the environment is dominated by a relatively low density high temperature plasma. Electrons and positive ions present in the plasma can collide with the spacecraft and deposit their charge, at the same time, backscattered and secondary electrons are leaving the spacecraft and carrying their negative charge with them. Finally, radiation (photon or from primary electron impact on surfaces) produce secondary emission of particles when intercepted by the spacecraft [15]. In a non-charging scenario all these currents balance out and the satellite stabilizes at a safe potential and does not charge. Spacecraft charging can disturb scientific measurements onboard, in severe cases it can cause the mission to fail [16].

Current imbalances cause the net charge on the satellite to increase positively or negatively. If an electric propulsion device were to continuously emit a positively charged ion beam, the satellite may charge sufficiently negative to prevent emitted ions from escaping the spacecraft. The ions that return generate no net thrust. For this reason, plasma based electric propulsion devices, such as ion engines and Hall thrusters, neutralize their positively charged ion beams with an external cathode.

1.2.1 Space environment

Space is not entirely vacuum. The dominant environment between 120 and 1000 km altitude is the remaining neutral atmosphere along with plasma, also referred as the thermosphere [15]. A plasma is an ionized gas consisting of positive ions and free electrons. Satellites interact with this plasma in different ways. If the spacecraft becomes charged by other means, like charge emission, then the plasma will also react to the charged spacecraft in some way. Below 100 km the atmosphere is homogenous and it is mainly composed of molecular nitrogen and oxygen. Above 100 km there is an essentially collision free environment mainly composed of atomic oxygen product of solar photo-dissociation. At 800 km and above, atomic hydrogen is the main component. Around 500 km of altitude, the kinetic temperature of the gas is usually between 500 and 2000K. The neutral density is in the order of 2×10^{6} to $3\times10^{8}/cm^{3}$ [17]. Ambient pressure at these altitudes ranges from 1×10^{-10} to 5×10^{-8} Torr [17]. The neutral environment between 100 and 800 km, the thermosphere, is well understood and quantified.

The main parameters that are used to describe space plasma are density and temperature. If the plasma is assumed quasi-neutral (equal number of ions and electrons per unit volume), then density refers to how many electrons or ions are present per unit volume in the plasma. Temperature is a statistical measure of how fast electrons or ions are moving in the plasma. These two quantities along with the spacecraft potential govern the current fluxes that the spacecraft receives from the external plasma. Most spacecraft orbit around the Earth in the atmospheric region called the ionosphere. In this region the plasma density is high (1×10^{6} - $1\times10^{4}/cm^{3}$) but with low temperature, well below 1eV [17].

1.2.2 Introduction to spacecraft charging

A spacecraft immersed in a plasma environment will charge to a fixed potential when the input and output currents balance out to zero. The charging behavior of a spacecraft in space resembles a capacitor, electrically speaking. A capacitor changes its potential depending on the amount of charge it holds and its capacitance. The capacitance of the spacecraft in this scenario is the self-capacitance, C_{sc}, and the potential is the satellite potential, V_{sat}, with respect to the external environment.

$$V_{sat} = \frac{Q}{C_{sc}} \qquad \textbf{Eq. 1.5}$$

For back of the envelope calculations it is common to assume a spherical spacecraft and calculate its self-capacitance in this manner. For a sphere of radius R the self-capacitance is given by:

$$C_{sphere} = \varepsilon_0 4\pi R \qquad \textbf{Eq. 1.6}$$

For a spherical spacecraft with a one meter radius the self-capacitance would be around 10^{-10} F or 100 pF, a very small value. More detailed analysis require a better estimate of the self-capacitance of the spacecraft using numerical methods, although the initial estimate would not be too far off. In spacecraft charging analysis the external plasma potential is usually defined as zero volts, in some other plasma sciences this might not be the case. In this case then, when the spacecraft collects positive charge it would charge up positively with respect to the external plasma.

In the thermosphere, where most satellites orbit, plasma currents are the main drivers for spacecraft charging [15]. Electrons being much more mobile than ions have a higher flux towards a neutral spacecraft so satellites in this region of the atmosphere tend to charge up negatively. To get an idea of the timescales of this process we can present the following example. Assuming that the plasma properties in a LEO orbit cause an electron current flux density of J=0.5 nA/cm^2, a 1 meter radius spherical spacecraft would charge up to 1000 V in 7 milliseconds [15]. It is clear that even small currents fluxes can charge up a large satellite to high potentials in a short amount of time. The main reason is that the self-capacitance of spacecraft is very low, even if the satellite is physically large.

The plasma density, n_e, and the plasma temperature, T_e, are responsible for a relevant parameter of spacecraft charging, the Debye length, λ_D:

$$\lambda_D = \sqrt{\frac{\varepsilon_0 k_b T_e}{n_e q_e^2}} \qquad \textbf{Eq. 1.7}$$

The Debye length dictates how far into the plasma the effect of an electrostatic charge permeates through. A charged object placed in a plasma that has a Debye length of 1 meter will only perturb the plasma within 1 meter. Instruments and charges placed farther away from the original charged object will not detect or "feel" its presence, the plasma will have shielded itself up to the Debye length. The Debye length is important because it governs the length-scales involved in spacecraft charging. Imagine a completely enclosed electronics box on the outside part of a satellite. This box contains high voltage electronics and we want to maintain it out of contact with the external plasma. Let us assume that a small orifice is present in one of the sides

of this otherwise completely enclosed box. Plasma will only be able to permeate inside the box if this orifice is larger than the plasma Debye length [16]. The importance of the Debye length is accentuated by looking at the different values it has at different orbits. In Low Earth Orbit (LEO) using the typical plasma parameters mentioned before, one could expect Debye's lengths in the order of 1.2 -1.7 millimeters [16]. In contrast the dilute plasma in GEO has a Debye length of several meters. The Debye length also defines which type of equations can be used to analyze the plasma interaction phenomena.

There are two main types of spacecraft charging that satellites experience, surface charging and deep dielectric charging. Surface charging is usually referred to the accumulation of charges in the surface of the spacecraft, it is then assumed that the whole satellite is at a single potential. The deposition of charges can come from various sources, external plasma, photoelectric currents, energetic particles etc. In certain scenarios different surfaces of the spacecraft can charge to different potentials causing differential charging.

Deep dielectric charging occurs when energetic particles (MeV or higher) are able to penetrate deep into dielectric materials and deposit their charge in them. This causes only the dielectric to charge and may eventually lead to an electric breakdown, causing a discharge within the dielectric [15]. Spacecraft charging effects mainly interferes with scientific instruments and onboard electronics, the latter in some scenarios can cause catastrophic failures.

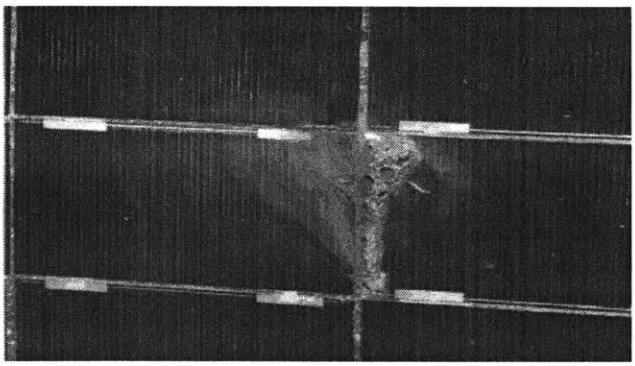

Fig. 1.7 Damage on a solar panel caused by sustained arcing on EOS-AM1. Credit: NASA

If differential charging happens in nearby parts and the potential difference is high enough, an ElectroStatic Discharge (ESD) can occur. The resulting ESD could permanently damage

sensitive electronics on board the spacecraft, FPGA or microcontrollers. These scenarios are rare but have happened. Sometimes the potential difference is not caused by the external environment but by the spacecraft itself. Some instruments require biasing grids or detector to high voltages to perform their measurements. The risk of an ESD is increased as the environment pressure rises.

In 1889 Paschen found an empirical law relating the breakdown voltage, which is the voltage necessary to start a discharge or electric arc, between two electrodes in a gas as a function of pressure and gap length.

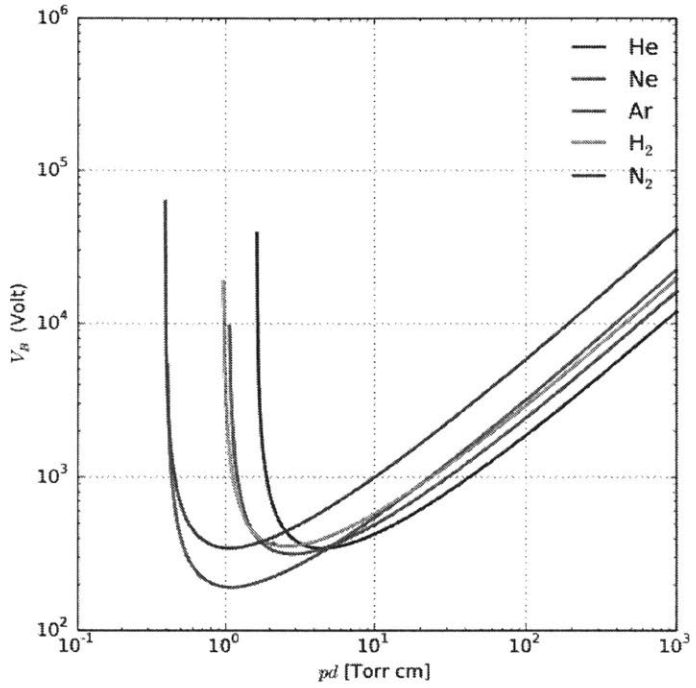

Fig. 1.8 Paschen curves for different gases as a function of pressure times gap length.

There is no such thing as a perfect vacuum, not even in space. In LEO, the neutral gas pressure can reach 10^{-8} Torr, at this pressure and assuming oxygen as the main gas, the breakdown voltage needed for a ESD to develop across a one centime gap is extremely large, millions of volts. An ESD in space usually develops due to outgassing or some other kind of gas leak. Outgassing or gas leaks can increase the local environmental pressure to values in which the breakdown voltage is reduced significantly. This was the case of the Tethered Flight System mission (TSS-1R). The satellite was biased to -3500V with respect to the shuttle orbiter. The tether system developed a leak that introduced gas into the deployer reel and elevated the

pressure enough for a discharge to happen. The mission was lost due to this large discharge [16].

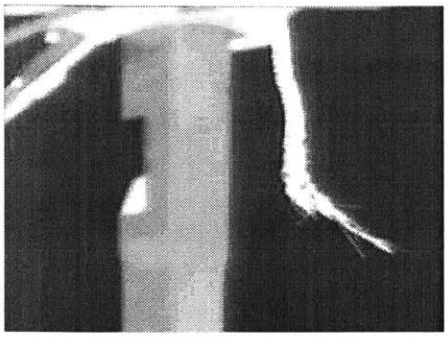

Fig. 1.9 Tether damage of TSS-1R. Credit NASA.

Catastrophic ESD events are far less common compared to spacecraft charging events that can cause instrument malfunction. Nevertheless the dangers of an ESD are a lot more severe. The potential that the satellite charges to may interfere with the measurements of external energetic particles or plasma properties.

1.2.3 Space plasma and charging dynamics

A spacecraft immersed in a plasma will collect currents that reduce its potential with respect to the plasma. The influx plasma current will cause the potential of the satellite to change and this will in turn modify the influx currents from the plasma. If the plasma conditions are static, the satellite will acquire an equilibrium potential and the input and output currents will balance out. If the satellite charges positively with respect to the plasma then mobile electrons will be attracted to the satellite and provide a negative current to it, lowering its potential. The same reasoning, to some extent, applies if the satellite charges to a negative polarity, the main difference being that ions have considerably less mobility due to their higher mass. Therefore electrons are more effective at neutralizing. If an engineering choice could be made usually one would prefer that the spacecraft charges positively so electrons help bring the potential down.

The amount of current flux density received by the satellite from the plasma is dependent on several plasma parameters. In high altitude space plasmas, such as GEO orbits, densities are so low that space-charge limits are never reached, in this situation the particles impacting the spacecraft will be limited by their angular momenta. This regime is referred as the Orbit Motion Limited (OML) regime or thick-sheath regime. For this regime to occur, the Debye length of

the plasma must be significantly larger than the spacecraft itself. If the Debye length is smaller than the spacecraft, the particles will not orbit the satellite but rather impact it if they go towards it. When the Debye length is much smaller than the object immersed in the plasma it is said to be in the thin-sheath regime. In either regime, the final equilibrium potential that a surface immersed in a plasma achieves is difficult to calculate and usually requires laboratory testing.

Thin sheath regime

In LEO, with Debye Lengths of fractions of a centimeter the thick-sheath does not apply for objects larger than a centimeter, therefore for simple analysis thin sheath probe theory can be used [15]. The spacecraft is assumed to be at zero potential and not moving through the plasma. The electronic flux arriving at the spacecraft will then be equal to the unrestricted electronic thermal flux which is defined by:

$$J_e = \frac{n_e}{4}\sqrt{\frac{8\,k\,T_e}{\pi\,m_e}} = n_e\sqrt{\frac{k\,T_e}{2\pi\,m_e}} \qquad \textbf{Eq. 1.8}$$

Where n_e is the number of electrons per m^3, and T_e is electron temperature, m_e is the electron mass and k is Boltzmann's constant. The total electronic current collected by the spacecraft would be:

$$I_{esat} = q_e J_e A_s = q_e A_s n_e \sqrt{\frac{k\,T_e}{2\pi\,m_e}} \qquad \textbf{Eq. 1.9}$$

Where A_s is the satellite collecting area and q_e the electronic charge. In a typical LEO plasma of 10^6 electrons/cm^3 and temperatures of 0.1 eV one could expect electron thermal fluxes of 1.5 $\mu A/cm^2$ or 15mA/m^2, for a neutral spacecraft.

An important effect arises if we take into account the spacecraft motion through the plasma. Spacecraft in LEO travel supersonically with respect to the plasma ions and subsonically with respect to the electrons, therefore a wake lacking ions is generated on the back of the spacecraft. This region fills up with fast electrons but, since there are no fast ions that can fill the gap, space-charge builds up and limits the number of electrons in the wake. It can be said that only the ram side of spacecraft can collect ions if the satellite travels supersonically with respect to the ions [16]. Since in LEO the Debye length is in the order of fractions of a centimeter then the effective flux of ions to the satellite surfaces is basically the equivalent to the ion ram flux. The ion ram flux is given by the velocity of the spacecraft, v_{sc}, ram surface area, A_{ram}, and ion density, n_i, (in a quasineutral plasma the same as electron density). Therefore the ionic ram current collected by the spacecraft can be defined as:

$$I_i = q_i n_i v_{sc} A_{ram} \qquad \textbf{Eq. 1.10}$$

Following the approach for the electron current density, for ion current density in a standard LEO plasma of 10^6 electrons/cm^3 and temperature of 0.1 eV one could expect ion ram fluxes of 0.1 μA/cm^2 or 1mA/m^2. It is important to notice that the ionic current only depends on the plasma density, on the other hand the electron current depends on density and temperature.

Thick sheath regime

In GEO orbits the thick sheath regime applies. For a satellite charged up to positive potentials, with respect to the plasma, the electronic current collected by the spacecraft will be the unrestricted electronic thermal flux amplified by a factor Q. The factor Q can be thought of as the attracting force the particles feel towards the spacecraft. Since the Debye length is larger than the spacecraft, more particles are attracted from farther away than in the thin-sheath case resulting in a larger plasma current.

The geometry of the object immersed in the plasma has a significant effect on the factor Q. The values of Q for different geometries are shown below [18]:

$$M = \frac{-q\Phi}{kT}$$
$$Q_{sphere} = 1 + M$$
$$Q_{cylinder} = 2\sqrt{\frac{M}{\pi}} + e^M erfc(\sqrt{M}) \qquad \textbf{Eq. 1.11}$$

The electronic current for the thick-sheath regime at zero volts would then be:

$$I_{esat} = q_e J_e A_s Q = q_e A_s n_e Q \sqrt{\frac{k\,T_e}{2\pi\, m_e}} \qquad \textbf{Eq. 1.12}$$

As an order of magnitude reference, collected electron currents for neutral GEO satellites have been measured to be 1-5μA/m^2, significantly lower than LEO plasma fluxes [17].

Table 1.1 Summary of plasma properties and currents for different orbits [19]

Orbit	n_e (cm^{-3})	T_e (eV)	J_e (μA/cm^2)	J_{i_ram} (μA/cm^2)
LEO	~10^6 to 10^5	0.1 to 1	~1.5	~ 0.1 to 0.01
GEO	~1	10^3	2.5x10^{-4}	~5x10^{-8}

1.2.4 Spacecraft charging in ion engines and Hall thrusters

Electrical propulsion devices that rely on electrostatic acceleration of ions produce a plume of positively charged ions. This positively charged plume needs to be neutralized with electrons in order to avoid spacecraft charging. This is usually done via an external cathode. The operation and characteristics of two main types of ion thrusters systems will be described next, the gridded ion engine and the Hall thruster.

A gridded electrostatic ion engine is composed of an ionization chamber, a pair of grids and an external cathode. Gas is injected in the ionization chamber which is then ionized by energetic electrons which are produced by different means (radiofrequency excitation, hot cathode filament, etc.). The positively charged ions are then extracted by a grid arrangement in the back of the device. After entering the grid system ions are accelerated due to the potential difference between the grids, generating the thrust. Electrons from an external cathode are injected into the ion beam to neutralize it.

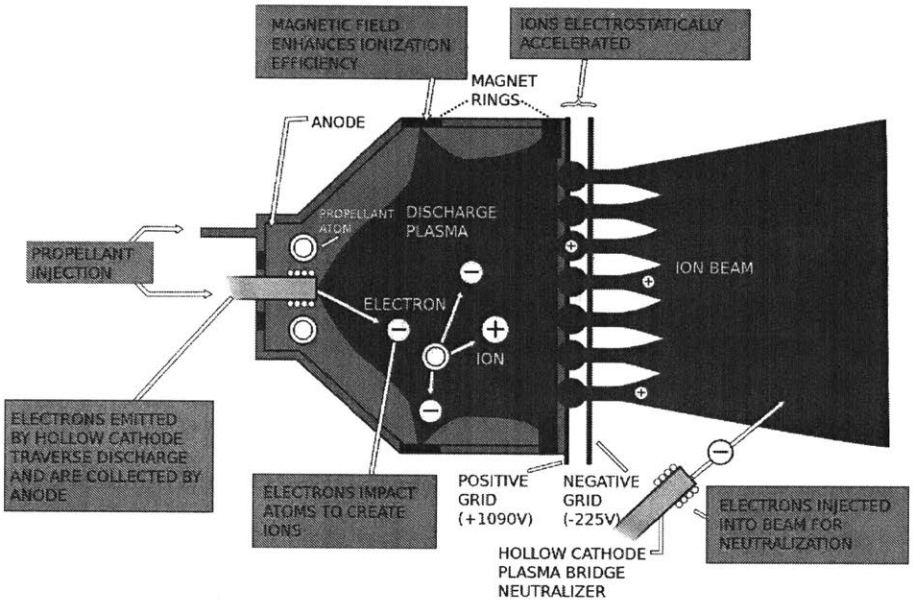

Fig. 1.10 Gridded Ion engine schematic. Credit: NASA

Hall thrusters are usually built around an annular section of material, with a strong radial magnetic field in the exhaust section. An electric field is established between the inlet of the thruster and an external cathode. Gas is injected in the inlet of the device and becomes ionized due to collisions from electrons trapped in the radial magnetic field. The ions are accelerated

through the electric field and are expelled. Electrons from an external cathode are injected into the beam and follow the ions to provide a quasi-neutral beam. Some portion of the electron current from the external cathode go into the thruster were they get trapped and ionize the neutral gas being injected.

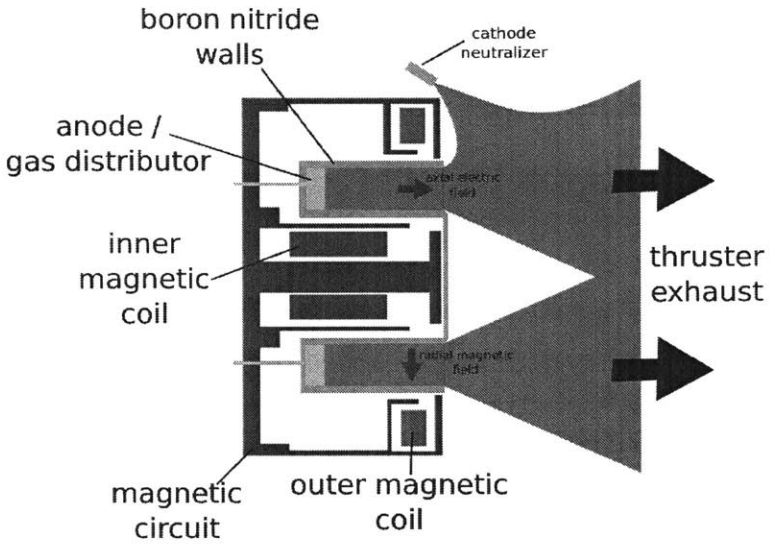

Fig. 1.11 General schematic of a Hall thruster. Credit: McWalter

The neutralization of the beam is typically done via an external cathode. Cathodes are an integral part of these types of thrusters, they have a large influence on the lifetime and performance of the device. Since electrons are much more mobile than ions, the neutralization dynamics of plasma thrusters occur as fast as the characteristic charging time. Although early anxiety surrounded the possibility of effectively neutralizing these devices, now it is well known that electron emitting cathodes work for this purpose [20, 21].

1.2.5 Neutralizing cathodes

When electric propulsion devices were first introduced, in the 1960s, hot filament cathodes that relied on thermionic emission of electrons were used. Tungsten filaments were heated up to 2600K and the thermionically extracted electrons were used to neutralize the beam, they only had 100 hours of life and were very inefficient [22].

The hollow cathode remedied the setbacks of hot cathodes. Hollow cathodes are made of a tube that is impregnated with an active electron emitter substance with low work function. A heater is placed around the outside of the tube which heats the low work function material. A

small orifice at the end of the tube permits the extracted electrons to leave the device. A gas is injected into the tube and carries an electron rich plasma through the orifice. The gas is needed to remove space-charge limits that will otherwise limit the electron production from the low work function material. High currents at low voltages are possible with this device when compared to other vacuum cathode devices and hot filaments.

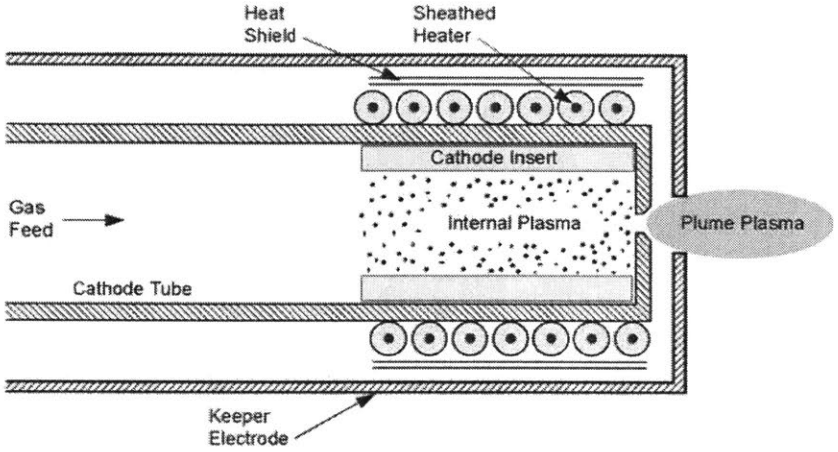

Fig. 1.12 Cross Section of a hollow cathode with a keeper electrode. Credit: Goebel

The high density of neutrals in the active area reduce the energy of sputtering ions to about 20 eV [22]. Emission current densities of 1 to 10 A/cm^2 are typical for hollow cathodes. The geometry of the cathode makes it easy to thermally insulate the active material, reducing thermal losses. A keeper electrode that encloses the entire cathode is often employed to reduce ion bombardment on the cathode. The keeper is biased positively to repel high energy ions from the main beam, which would sputter the cathode orifice, this electrode increases the life of the device.

1.2.6 Spacecraft charging in electrosprays thrusters

Electrospray thrusters are electrostatic devices that use electric fields to accelerate charged species. This is where the similarities end between electrosprays and Ion or Hall thrusters. Electrosprays thrusters do not actively ionize their propellant using energetic electrons, they use ionic evaporation to produce ionized species which are then accelerated by electric fields. **Electrospray thrusters can accelerate positive or negative ions, generating either a positive or negative ion beam, depending on the polarity of the voltage applied to their terminals.** Ion or Hall thrusters only accelerate a positive ion beam. This difference has an important charge neutralization implication, electrosprays, in theory, could operate without an

external cathode. If two separate thrusters are fired in such a way so that one provides a positive ion beam and the other a similar negative ion beam, then in theory, the spacecraft would not charge, and the thrusters could operate indefinitely.

External cathodes can, and are, used in electrospray propulsion systems to provide the neutralization for a positive ion beam similar to how ion or hall thrusters operate. Busek Company produced an electrospray propulsion system for the LISA mission, in which a field emission cathode was used to provide neutralization to a positive ion beam [23].

The more attractive neutralization scheme for an electrospray propulsion system is to operate the devices in bipolar mode. While one thruster is emitting positive ions an identical thruster will emit the same number of negatively charged ions. If the two thrusters are placed close to each other and firing in the same direction a quasi-neutral ion beam will leave the spacecraft. Besides not needing an external cathode, this scheme is very attractive because then, both ion beams can produce thrust and no propellant is wasted. The bipolar mode of operation raises important questions, mainly the neutralizing implications of the different properties between highly mobile electrons and negative ions.

The study of the spacecraft charging characteristics induced by electrospray thrusters operating on a spacecraft constitute a significant portion of this work and are described in detail in Section 4.

1.3 Introduction to attitude control

Attitude refers to the three-dimensional orientation of a vehicle with respect to a specified reference frame [2]. In satellite engineering, the system that is responsible for maintaining the attitude of the satellite throughout the mission is named the Attitude Determination and Control System (ADCS). The attitude determination system deals with the estimation of the orientation of the spacecraft relying on sensor information often relying in sensor fusion algorithms. The control portion of the system activates attitude actuators to modify the orientation of the satellite as commanded by the controller. The final goal of the ADCS is to point the spacecraft to a certain orientation with some precision. The final orientation precision that the ADCS can maintain depends on the type of attitude sensors used, the attitude actuators, the magnitude of external disturbances on the spacecraft and the control algorithms implemented.

Precise motion and attitude control would be a major enabler of many small satellite missions, but still has yet to be demonstrated in space [24].Such motion control could be translational or rotational (or both). Missions involving much larger satellites have demonstrated outstanding performance in this type of maneuvering, such as the Hubble Space Telescope pointing accuracy of 0.001 arcseconds [2] or the LISA Pathfinder relative translational control to within a few microns [23] . The overly constraining dimensions and mass of small satellites make it particularly challenging to get anywhere close to achieving such high performance. Nevertheless, this is a capability that needs to be developed for small satellites if their use is to be extended to fulfill more ambitious requirements and perform new and valuable missions.

For instance, the current state-of-the-art in attitude determination and control systems (ADCS) for CubeSats is represented by an accuracy of not much less than about 1° to 5° RMS, sometimes limited by the performance of the attitude sensors [24]. These levels of ADCS accuracy are suitable for coarse camera or solar panel alignment, but are still far from what is required in high precision optical sensing, such as astronomical observations or optical communications (< 0.01° or less than about 40 arcseconds).

Most reaction thrusters have been based on chemical propulsion, which is characterized by its low specific impulse. Using chemical thrusters as long-term attitude actuators in small satellites would likely require a relatively large amount of propellant compared to the satellite size. In addition, ancillary components such as valves, regulators, pressurization system and complex thermal management are difficult to include in the limited volume of a small vehicle. Cold gas thrusters do not suffer from thermal issues, but also require several of these components and are characterized by much lower specific impulse. In this work, the use of electrospray thrusters as attitude actuators is analyzed in detail in Section 5. Electrospray thrusters should be able to provide very minute forces consistent with their application to fine mobility of small vehicles without taking excessive volume, mass and power from the main satellite bus.

Two small satellite mission examples that would benefit substantially from precise attitude control are free-space optical communications and scientific observation missions. Precise pointing of narrow optical beams could enable high link efficiency leading to high data rates. A number of such concepts are currently under development [25], including the work reported

in [26, 27], where fast steering mirrors (FSM) would be used to compensate for the coarse attitude control provided by the satellite bus while a 10 watt 1550 nm amplified laser beam is aimed at a 30 cm aperture ground station. Such implementation would enable data rates >50 Mbps, which can be compared with the average ~9600bps data rates representative of LEO CubeSats today [28]. The authors in those studies estimate a FSM pointing accuracy requirement of 6.9 arcseconds using a 2.1 milliradians (full-width, half-max) downlink beam capable of 10 Mbps downlink rates. In this particular case, the ACDS system on the host satellite would require a ±1 degree pointing accuracy. In particular, if the propulsion-based satellite bus attitude precision in [27] could get down to the sub 10 arcsecond range, then the FSM and ACDS actuators could be omitted altogether, significantly simplifying the optical communication assembly. Further improvements in pointing accuracy would have a dramatic impact: the data rate (DR) depends on the laser beamwidth, ϕ, such that $DR \propto \phi^{-2}$ and the beamwidth is proportional to the ultimate pointing error of the system. For constant power, any decrease in pointing error will substantially increase the communications data rate.

Scientific observation missions would also benefit from fine attitude control by enabling small satellites to precisely point instruments, mainly telescopes, over long periods of time to a variety of targets and for a number of purposes [29]. For example, CubeSat missions are being designed to detect Earth-sized exoplanets located in the habitable zone of their host stars via the transit method. This application would require at least 5 arcseconds accuracy from the attitude control system [30]. While reaction wheels and piezo stages have been proposed to reach this upper limit, missions like this would certainly benefit from an inherently precise satellite bus such that ancillary components could be eliminated, thus increasing the satellite capabilities. This could be especially valuable when a constellation of satellites is implemented and propulsion is required to deploy and maintain the relative position of vehicles in the constellation.

1.3.1 State of the Art ACDS for small satellites

Even though large spacecraft, like Hubble, are able to maintain an orientation within hundreds of arcsecond the same cannot be said about small satellites. The tight volume and mass constraints in a small satellite make the miniaturization of a complex control system very challenging. Attitude sensors for small satellites are usually limited to sun and earth sensors, magnetometers and miniaturized start trackers.

Sun and Earth sensors are composed of an array of light sensitive devices that estimate the direction of the incoming light rays either from the Sun or Earth. Since the position of the Earth and Sun are known, the satellite can extrapolate its orientation with the sensors information. Sun sensors can have accuracies near 0.01 degrees while Earth sensors have accuracies of around 0.1 degrees [2]. Magnetometers are orthogonally placed coils that detect the orientation of Earth's magnetic field with respect to the satellite, much like a compass. Magnetometers have lower accuracies than Earth sensors due to the dynamic nature of Earth's magnetic field. Almanacs of Earth's magnetic field that depicting the strength and direction of the magnetic field in a specific location are usually used to map the magnetometer data to an actual orientation.

A star tracker sensor uses a camera to take pictures of the night sky which are then compared to a star almanac stored on board. Star trackers provide the most accurate orientation estimation of all attitude sensors but are usually the slowest due to the time the camera has to be exposed in order to detect sufficient number of starts. These relatively long exposures mean that star tracker can't be used when the satellite is rotating at a relatively high velocity as this will blur the image significantly. For small satellites like CubeSats, Sun and Earth sensors along with magnetometers are usually embedded in the solar panels or other areas of the spacecraft and occupy a relatively small volume. Past CubeSat missions have been able to maintain orientation to within 3-2 degrees [24].

Attitude actuators have proved to be harder to miniaturize compared to sensors. There are three main types of attitude control actuators suitable for small satellites, magnetorquers, reaction wheels and reaction thrusters. Magnetorquers are composed of orthogonally placed coils that generate a magnetic field that interacts with Earth's magnetic field to produce torques on the spacecraft. They have no moving parts which makes them a very reliable actuator. A significant disadvantage of magnetorquers is that they cannot be used to produce torques parallel to magnetic field lines. The torque produced by magnetorquers is usually much lower than one achieved with reaction wheels or thrusters. Because magnetorquers rely on Earth's magnetic field, and the field magnitude is reduced as the cube to the center of the Earth, magnetorquers are less effective at higher orbits [2].

Reaction wheels are orthogonally placed flywheels attached to motors. The rotation of the flywheel produces a counteracting torque on the motor which is attached to the spacecraft.

Reaction wheels are able to provide smooth changes in torque allowing for precise attitude control. These devices are usually the actuator of choice for 3-axis stabilized small satellites. Reactions wheels have a maximum speed and need to be desaturated once this speed is reached. In order to desaturate a reaction wheel, an external torque must be applied to the spacecraft, this is usually achieved with magnetorquers or thrusters. This implies that a reaction wheel actuator is always accompanied by a magnetorquer or thruster system. The high performance of a reaction wheel system is somewhat obscured by operating life and introduction of jitter and vibrations to the spacecraft. Since the wheels are mechanical devices prone to wear and spinning at high speeds, they are usually the component with lowest reliability of the spacecraft. The mechanical nature of the device also makes it bulky, occupying a third or more of the small satellite volume.

A number of ACDS for small satellites are currently under development to achieve pointing accuracy as low as 10 arcseconds in a small envelope of about 0.5U. Most rely on star trackers for fine attitude determination and high precision reaction wheels as attitude actuators [3, 31]. Reaction wheels usually introduce unwanted jitter in the satellite due to imperfect rotor balance and might be disproportionally large and heavy in small satellites. In low earth orbits (LEO), magnetorquers can be used to dump angular momentum to de-saturate the reaction wheels. For orbits higher than LEO, including interplanetary trajectories, reaction thrusters need to be used for this purpose [2]. If these thrusters had the performance required to achieve precise attitude control, then reaction wheels could be omitted altogether. Such implementations would be particularly beneficial for missions that require both attitude control and main propulsion, as long as thrusters could be used for both tasks.

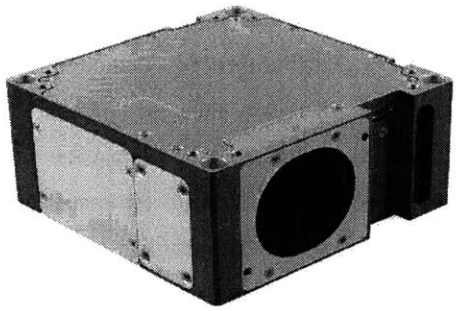

Fig. 1.13 Precise, 3-axis, stellar based CubeSat attitude determination and control system in a Micro-package (0.5U). Credit BCT

Thruster technology has proven to be one of the most challenging technologies to miniaturize to small satellites scales. For ACDS, thrusters need to be positioned on different locations on the spacecraft to provide a moment arm and produce torque on different axes.

1.3.2 Thrusters as attitude control actuators

Usually, reaction thrusters are low thrust devices meant to produce torques on the spacecraft axes. They are mounted in pairs to produce pure torques, as opposed to a force and a torque. Since the propellant of a thruster is limited, the lifetime of an ACDS that employs only thrusters as actuators is limited by the amount of propellant carried. Several thrusters are usually located in different parts of the spacecraft to provide positive and negative torques in the different axes. Reaction thrusters are commonly used to desaturate reaction wheels.

Since the ACDS lifetime, when employing reaction thrusters, is limited by propellant, an efficient high specific impulse thruster is desired. Furthermore, attitude maneuvers are usually slow which means a low thrust device could be used. This is especially true while performing precise attitude control maneuvers. These two aspects make electrospray thrusters ideal candidates as attitude control actuators for small satellites. A study of the performance of electrospray thrusters as fine attitude control actuators is described in section 5.

1.4 Conventional instruments

1.4.1 Thrust measurement

Thrust and specific impulse are probably the most relevant parameters of any propulsion system. Therefore, their study and characterization is an important task. iEPS emission profile has been extensively characterized using techniques such as time of flight spectroscopy and retarding potential analyzer energy distributions [11]. Although thrust calculations and models can be created based on the data gathered by these techniques it is clear that a direct thrust measurement would be preferred. A thrust balance is a clear necessity for accurate thrust characterization. For example, the laser interferometer space antenna (LISA) mission will require a propulsion system capable of producing thrust levels as low as 1 μN with 0.1 μN resolution [23]. Characterizing the performance of candidate propulsion systems would then require a thrust stand that is capable of performing thrust measurements with a resolution of tens of nN. There are several hurdles that tackle the design and operation of thrust stands in the μN range. Calibrating such thrust stands requires the application of a known force in the

μN range which is not trivial. The environment surrounding vacuum chambers is usually mechanically noisy, introducing unwanted vibrations to the sensitive instrument that can affect the readings.

Traditionally, thrust measurements on the μN range employ a torsional balance. In a torsional balance a lever arm is supported by a low friction bearing, usually a specially designed, high-precision torsional bearing. The thruster is mounted on one side of the lever and a counterweight on the other. The rotational position of the lever is carefully monitored. When the thruster fires, it imparts a torque to the torsional balance which is proportional to thrust. The torque causes a small displacement of the arm which is then recorded. To obtain higher precision, a counteracting and known force is usually applied to the arm in such a way as to counteract any movement produced by the thruster. The thrust measurement is then proportional to the counteracting force applied to the arm. By not allowing the arm to move, the thrust measurement is then independent of the stiffness of the joint in question, still constrained by a very low friction and stiction in the joint. These two approaches work well and have been studied extensively [32-35] .

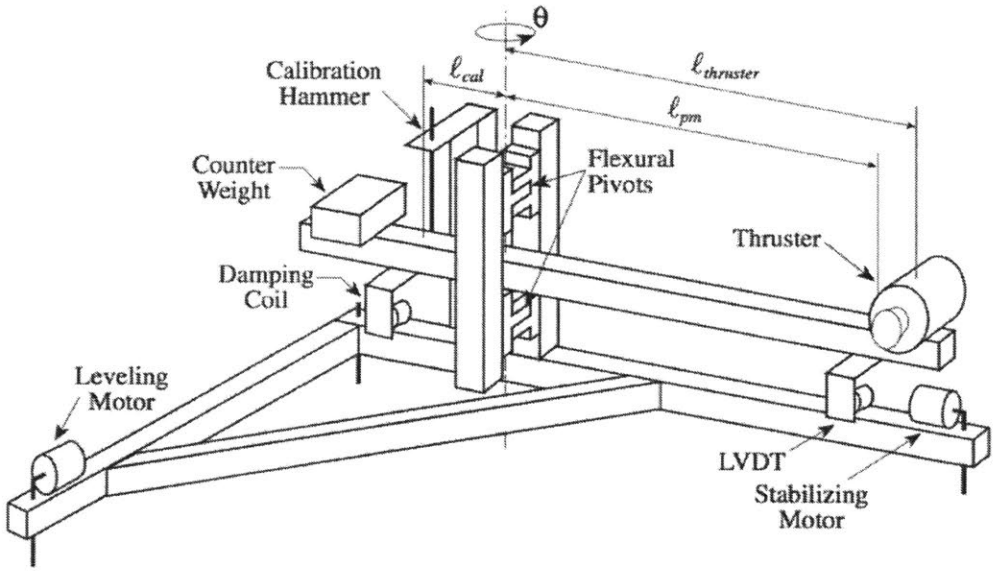

Fig. 1.14 Simplified schematic of high precision torsional balance. Credit Ziemer.

For the measurement to be accurate several variables have to be controlled or known with high accuracy: mechanical properties of the joints, static friction coefficient, stiffness and any nonlinearities they might have. Secondly the balance has to be calibrated using a known force

that either calibrates the device or acts as a control force to maintain the lever arm fixed. This force will have to be equal to the thrust being produced by the thruster, in case of electrosprays around 12 μN. Producing such small forces accurately is done in practice but not without challenges [33]. The traditional approach is to use a capacitive comb that induces electrostatic forces on the opposite side of the arm.

This work characterizes thrust of electrospray devices using a new type of thrust measurement instrument that provides some benefits and drawbacks compared to traditional torsional thrust balances.

1.4.2 Spacecraft charging

In order to characterize spacecraft charging behaviors of a satellite employing electric thrusters a high electrical isolation testbed must be used. As mentioned in Section 1.2.2, the minute self-capacitance of satellites makes any small current have a large effect on satellite potential. This is especially true for any leakage current to ground that might be present on the system. Long and thin high-dielectric materials can be employed to increase the testbed electrical isolation. For high current experiments in which the leakage current might be negligible a simpler isolation scheme can be used. An example of a high current experiment, in which leakage current is not important is described in [36]. The approach uses a transformer to provide galvanic isolation between the thruster system and the chamber ground.

The spacecraft

charging characteristics of electrospray thrusters studied in this work used a novel type of testbed that provided excellent electrical isolation by employing magnetic levitation. The small currents involved in the operation of the iEPS thrusters requires a high electrical isolation environment to accurately monitor spacecraft charging phenomena.

1.4.3 Attitude control

It is common to study satellite attitude control performance using air bearings [37, 38]. Air bearings use a thin film of pressurized air to provide a very low friction load-bearing interface between two surfaces. They can allow limited rotation about three rotational axes, or translation on a single plane. The minimal friction allows the satellite attitude actuators to apply torques in a similar way as if they were in space. The air currents produced by the air bearing, although small, can introduce undesirable vibrations and other perturbations to the satellite being tested

[37]. Because the iEPS thrusters only operate under vacuum and produce μN levels of thrust, a different testbed must be used to determine their performance as attitude thrusters.

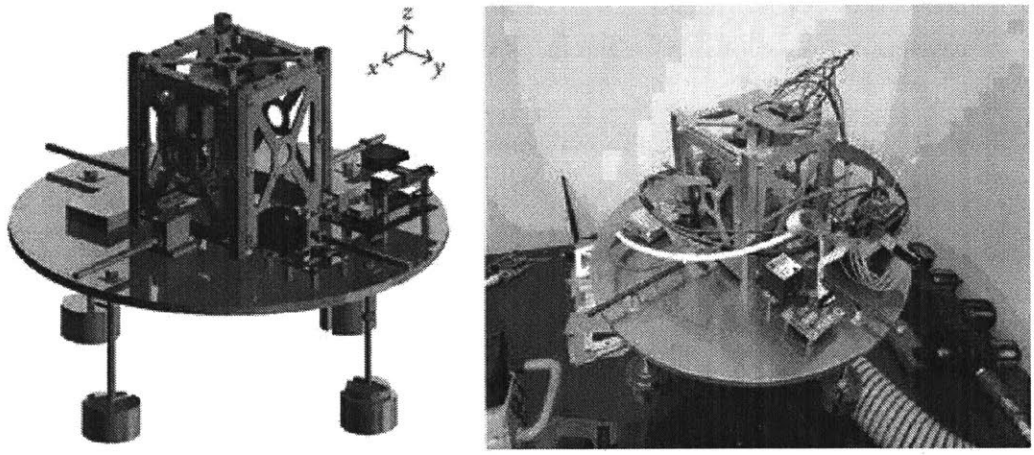

Fig. 1.15 CubeSat mounted in traditional 3-axis air bearing. Credit: Hindawei

1.4.4 Magnetically levitated CubeSat testbed

The development of a testbed capable of measuring additional performance properties of the thrusters, besides thrust, including spacecraft charging and attitude control attributes posed several challenges. The thrust produced by the thrusters is in the order of tens of μN, such low forces require a very sensitive instrument that can isolate external force sources such as vibrations. To study the charging phenomena that occurs while firing, one must electrically isolate the satellite system so it is allowed to charge. Finally a zero friction environment is required to study the performance of the electrospray devices as reaction thrusters. Attitude sensors that accurately measure the angular position of the system must be present in the instrument both to provide a feedback loop and as a final performance metric. With all these features and requirements in mind a Magnetically levitated CubeSat testbed (MagCube) was conceived.

The majority of the experimental data presented in this work is gathered from experiments performed in the MagCube.

1.5 Thesis Contributions

This work concentrates on the analysis and measurement of properties and phenomena of electrospray propulsion systems: Thrust, spacecraft charging characteristics and attitude control performance. In order to study these areas substantial instrumentation and models had to be developed. The contributions of this thesis are listed below:

- **Detailed study of neutralization dynamics of an electrospray propulsion system, using heavy ions as the neutralizing species.** Previous electric propulsion devices use some form of external cathode to provide electrons for the neutralization to the of ion beam. The model envisioned in this thesis is a completely different approach, two ion beams of opposite charge are emitted from the spacecraft, balancing the charge of the spacecraft.
- **Electrical model of charging characteristic of an electrospray propulsion system.** Via equivalent circuits this work attempts to model all the relevant processes affecting charging of a spacecraft operating electrospray thrusters.
- **Effects of spacecraft charging on thruster performance and overall satellite operations.** Different modes of thruster operation are described and recommended for specific missions.
- **A new type of magnetically levitated testbed was designed and constructed to aid in experimentation and measurement efforts of the propulsion system.** The instrument described in this work exploits the properties of magnetic levitation to develop a zero friction environment that is completely isolated from external bodies. Thorough efforts on the characterization and counteracting of external magnetic disturbances on the testbed were conducted.
- **Attitude control performance of electrospray thrusters operating on a CubeSat.** Control algorithms are developed to maximize the accuracy of the control system. The first demonstration of arcsecond-level attitude control precision of a CubeSat using electrospray thrusters is presented.
- **Electronics that drive the thrusters were also designed and tested, recommendations are made on the best architectures.**

2 Experimental methods

2.1 Magnetic Levitation CubeSat Testbed

The MagCube levitates a mockup satellite using magnetic fields inside a vacuum chamber, which electrically and mechanically isolates the satellite from the chamber. The levitated satellite is equipped with batteries, computer, radio, high voltage circuitry and electrospray thrusters. While magnetically levitated and under vacuum, the satellite can rotate freely and completely around a single zero-friction Degree of Freedom (DoF), Fig. 2.1. The thrusters are commanded to fire via radio causing the satellite to rotate. The rotational movement of the satellite can then be analyzed and thrust calculated. A charge sensor is placed in close proximity to, but not contacting, the levitated satellite to measure its floating potential in real time. The charge sensor is used to study the spacecraft charging phenomena induced by the thrusters and other external sources. Finally, a high accuracy angular sensor provides angular information of the levitated satellite in real time, allowing the analysis of precise attitude control maneuvers. All of these measurements take place simultaneously.

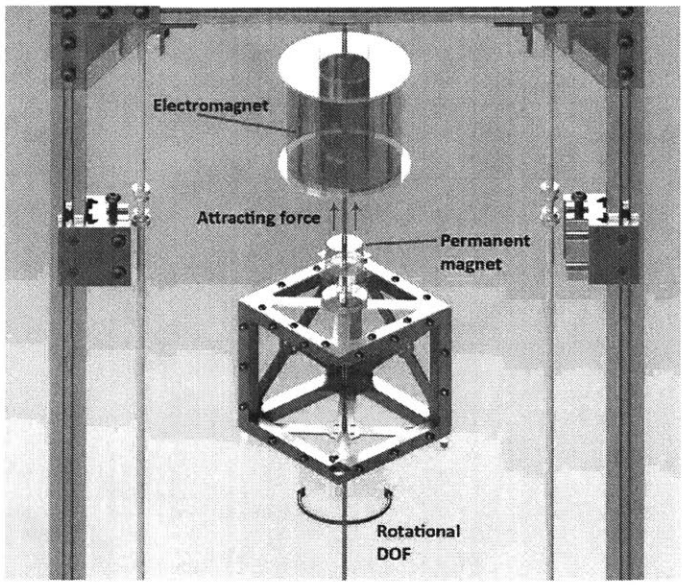

Fig. 2.1 Concept of magnetically levitated CubeSat testbed.

Magnetically levitated systems have been used in the past to study CubeSat components such as magnetorquers [39] and reaction wheels [40]. A magnetically suspended chemical rocket thrust stand has also been attempted [41]. These testbeds operated under atmospheric

conditions and measured relatively large forces, compared to electrospray thrusters capabilities. The MagCube adopts features from some of these systems and incorporates new ones. The design of the MagCube was heavily influenced by a previous version built by the same author [42-44].

The main component of the testbed is the levitation system. In 1847, Ernshaw established that stable magnetic levitation is impossible while utilizing only permanent magnets. For this reason, the MagCube requires an active actuator, a levitation electromagnet that is controlled by a levitation algorithm. A permanent magnet attached to the mock-up CubeSat, via a long shaft, is attracted or repelled by the levitation electromagnet which is placed directly above it. The CubeSat, shaft, and other attachments make up the bulk structure that is levitated, referred to as the levitated structure, Fig. 2.2.

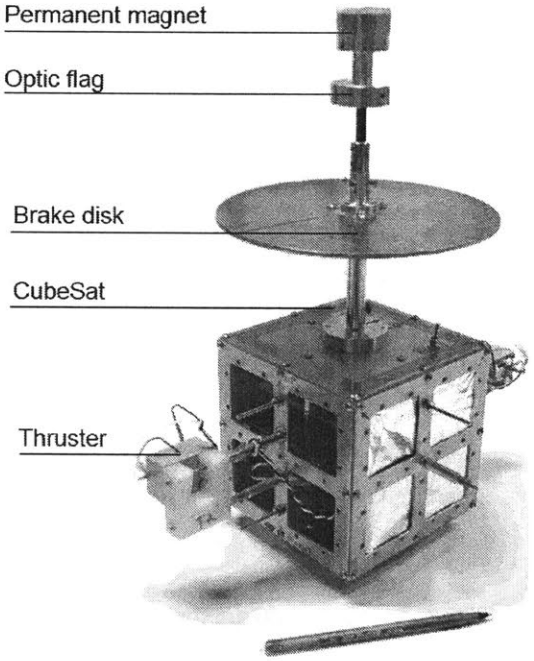

Fig. 2.2 Levitated structure.

The magnetic levitation constrains the 5 remaining DOFs with the magnetic force trying to align the two magnetic dipoles together. The levitation allows the levitated satellite to rotate 360 degrees about the zero-friction DoF. This simple attribute constitutes an important advantage over classical torsional balances. A 360 degree rotation allows a more thorough study of the propulsion device specially when acting as an attitude control actuator. The complete

electrical isolation of the levitated structure with respect to the chamber is also useful while trying to measure spacecraft charging effects using non-contact charge sensors.

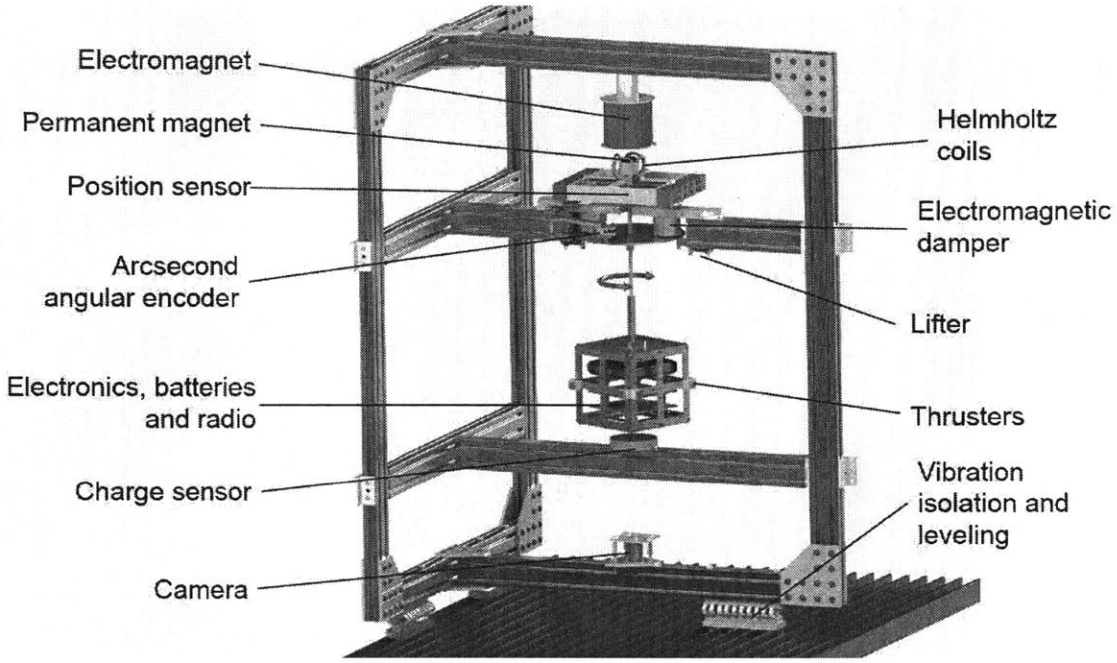

Fig. 2.3 Main components of magnetic levitation CubeSat testbed.

2.1.1 Concept and design

The main challenge faced during the development of the testbed was the non-contact constraint imposed by the zero-friction DoF and the vacuum safe requirement for the majority of the components. The final testbed design consists of an extruded aluminum frame that houses all the actuators and sensors necessary for operation, Fig. 2.3. The main levitation electromagnet sits at the top of the structure. A movable structure supported at three points by linear bearings is used to house the vertical position sensor, Helmholtz coils, electromagnetic damper and angular encoder. This upper structure allows to adjust the vertical position of the sensors and actuators with respect to the electromagnet. This feature allows the testing of different designs of levitated structures. A detailed view of the area that houses the majority of sensors and actuators on the upper movable structure can be seen in Fig. 2.9. The vertical position sensor is mounted on its own linear stage which allows fine adjustment of the distance between the sensor and the levitation electromagnet sitting above. The position of the vertical position sensor dictates the stability of the levitated object and more importantly the amount of current necessary for the electromagnet to achieve levitation.

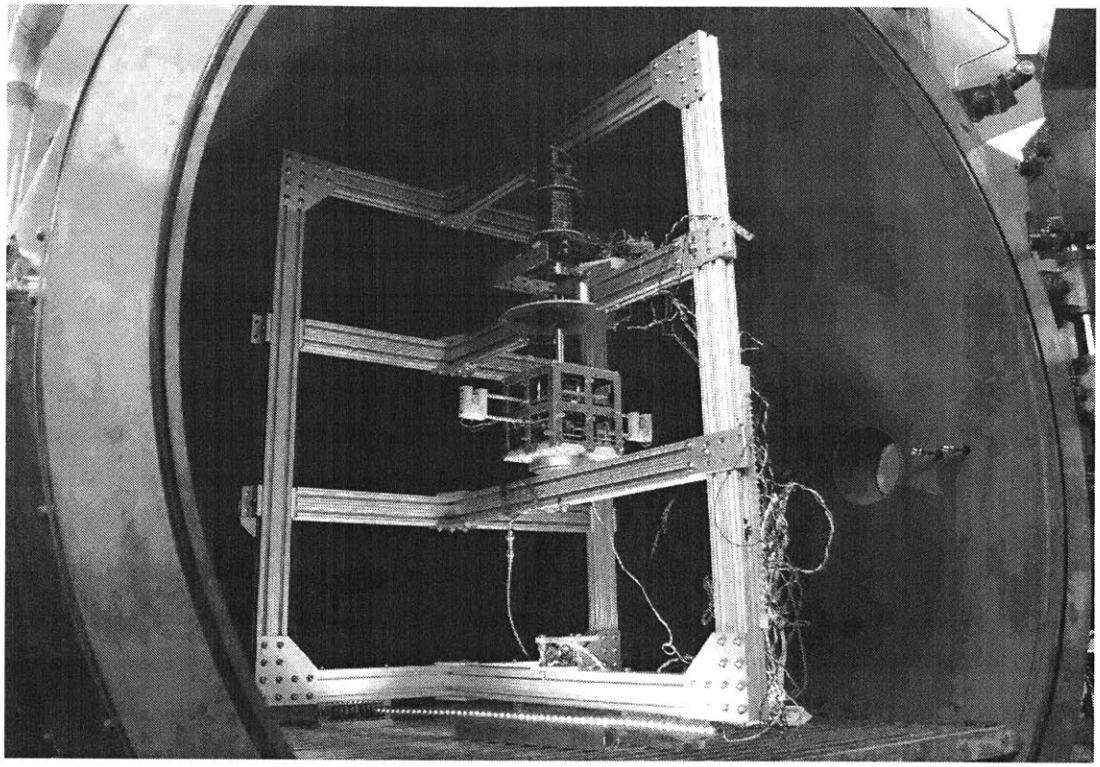

Fig. 2.4 MagCube mounted inside the vacuum chamber.

The mockup CubeSat used in the experiments is an enlarged version of a standard CubeSat. The enlarged 13 centimeter sided CubeSat allows for easier integration of custom made electronics and other hardware into the satellite. The permanent magnet used for levitation is attached to the CubeSat via a long 0.25 inch diameter aluminum shaft. The separation provided by the shaft provides several benefits to the testbed, mainly an unobstructed environment where the thrusters can fire without objects (mainly sensors) in the vicinity, which can obstruct the ion beam path emanating from the thrusters. The shaft separates the CubeSat from the crowded sensor/actuator area of the top movable section of the testbed. Lastly, shaft couplings allow the CubeSat to be removed from the testbed without having to remove the whole levitated structure, see Fig. 2.2.

The permanent magnet that supports the structure, levitates around 1 to 3 millimeters away from the levitation electromagnet, depending on the weight of the CubeSat. Below the levitated CubeSat a lower structure is supported on three sides by linear bearings and houses the spacecraft charge sensor. On the bottom side of the testbed a camera acts as an angular encoder. The camera tracks fiducial markers located on the bottom of the CubeSat. This encoder provides

rough angular information, ±1°, and is not used for fine measurements. The whole testbed sits on top of wire spring dampers that are mounted to the vacuum chamber floor. The dampers reduce the propagation of external vibrations to the levitated structure, Fig. 2.5.

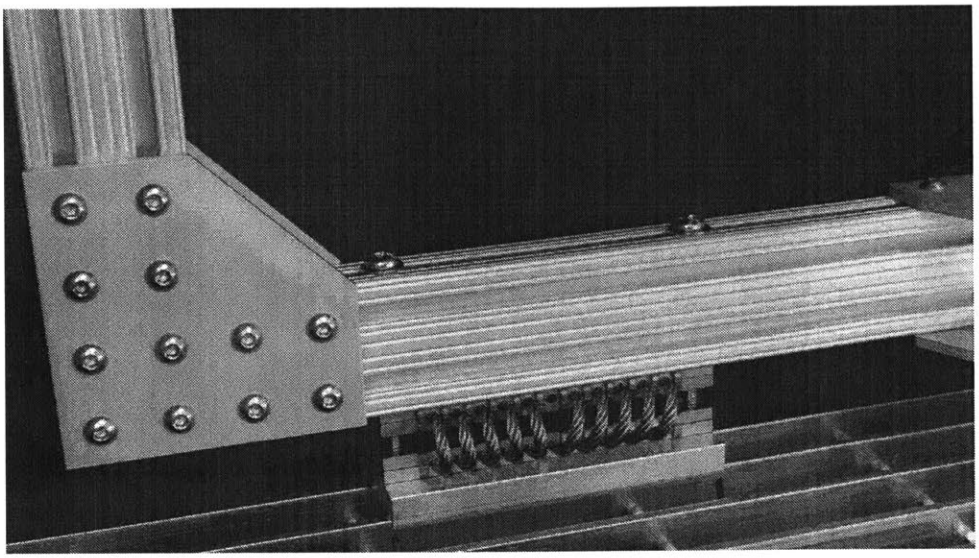

Fig. 2.5 Wire vibration dampers.

The zero friction environment experienced by the CubeSat implies that any rotational movement will last for a long period of time. For this reason, an electromagnetic, non-contact brake is installed on the testbed. The brake is used to slow down the satellite rotations in a short amount of time.

An orthogonal pair of Helmholtz coils are positioned around the levitation region to reduce the perturbation torques produced by the levitation scheme further described in section 2.1.2. During spacecraft charging experiments it is useful to electrically ground the satellite at a given instant, this is done with help of a mechanism that mechanically contacts the satellite with a grounded electrode, this mechanism is referred as the "lifter". The position of all these sensors and actuators can be seen in Fig. 2.3 and Fig. 2.4. Their purpose, design and performance are described in more detail in the following sections.

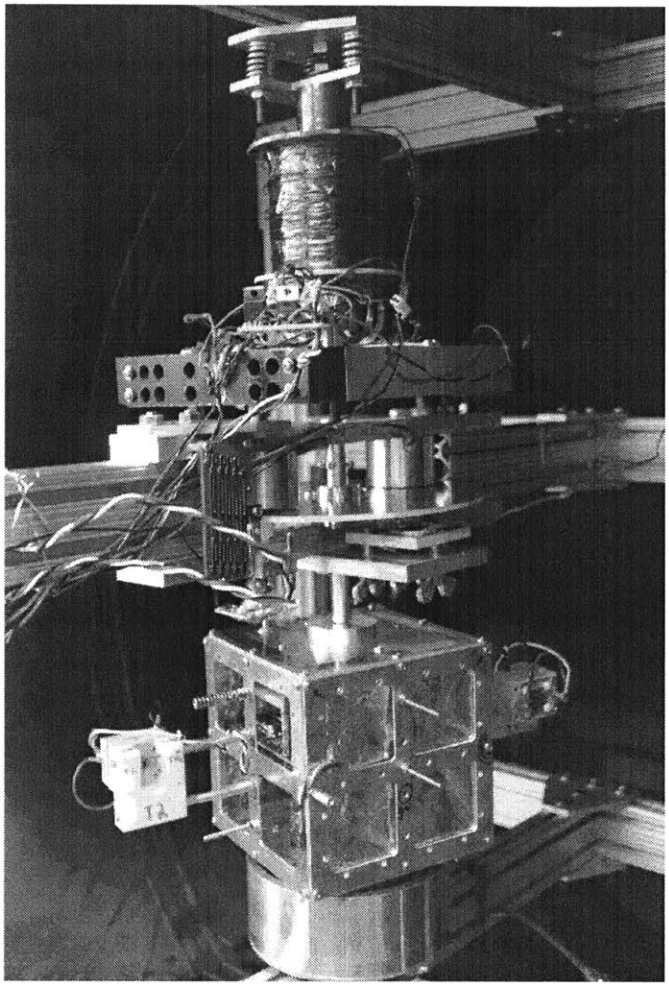

Fig. 2.6 MagCube inside the vacuum chamber.

Thrust measurements

There are several methods that can be employed to measure thrust in the MagCube. The first method is to fire the thrusters for a specific amount of time and measure the change in angular velocity of the levitated structure. Due to its simplicity, this method is used throughout this work and is further discussed in section 3.

The second method to estimate thrust is based on COTS force probes. Companies such as Femto Tools, produce micro force sensor probes with force ranges going from 0 to 100 μNewtons [45]. The company states a resolution of 5 nanoNewtons at 10Hz. The precision declared for this probes is very attractive. A pair of probes could be used to measure thrust directly in the zero friction environment of the MagCube. The probes are very fragile so the

designed setup would have to carefully position them in such a way so the probes counteract the torque produced by the thrusters by contacting the CubeSat in opposite corners. If such a setup could be constructed with no loss in probe performance, final thrust measurements could have accuracies in the order of nanoNewtons. This method was not investigated in this work but it is attractive as a future improvement of the testbed.

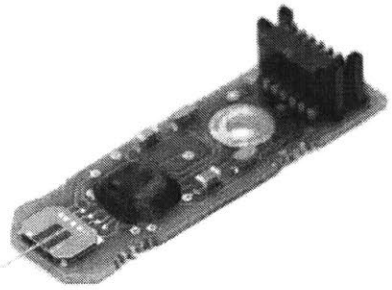

Fig. 2.7 FTS-100, a micro force probe sensor.

The third method to measure thrust, is the one followed by standard torsional balances designers. An actuator that provides calibrated forces in the order of the thrust produced by the thrusters is used to counteract the torque induced in the balance arm [33]. In this case the levitated structure acts as the balance arm. Commanding the thrusters to fire, and modulating the calibration force until the satellite remains stationary (thrust force is equal to calibration force) yields the thrust measurement. The difficulty of this method relies on the calibration force analysis and construction of the actuator. It is not trivial to design an actuator that can reliably impart μN forces to the levitated structure. Unfortunately, employing this method will remove some of the desirable attributes of the MagCube, such as the 360 degree rotation capability. This method was not investigated in this work.

2.1.2 Magnetic torque perturbation

Several tests of the MagCube were performed both in air and vacuum before actual thrust measurements took place. During these tests, it was observed that the levitated structure experienced rotational oscillations about the friction-free axis, similar to a torsion pendulum [43, 46]. The oscillations had a period of around 3-10 minutes. The oscillations occurred both in vacuum and atmospheric conditions. The oscillatory behavior hinted to an unwanted restoring torque being present in the system. The external torque would corrupt the thrust measurement and therefore was undesirable. A set of tests were conducted to understand the source of the unwanted restoring torque.

To model any oscillatory behavior, we can approximate it to a harmonic oscillator. Then the restoring torque constant, k, is given by the period of the oscillations, T, and the moment of inertia of the levitated structure, I:

$$T = 2\,\pi\,\sqrt{\frac{I}{K}} \qquad \textbf{Eq. 2.1}$$

A longer oscillation period is then seen as a positive attribute, meaning the restoring torque constant has been reduced. The tests performed allowed the levitated structure to oscillate freely under controlled conditions, the oscillation period was the main parameter studied. The tests were performed under atmospheric conditions to allow for rapid changes in the experimental parameters. A small enclosure that prevented external air currents from affecting the levitated structure was used during all tests. Several parameters were explored to pinpoint the nature of the restoring torque including:

- Modifying the center of gravity of the levitated CubeSat.
- The level of the testbed frame with respect to gravity.
- Placement of external ferrous objects in close proximity to the permanent magnet.
- External magnetic fields of varying magnitudes and directions.

The tests indicated that external horizontal magnetic fields (perpendicular to the gravity vector) had the most impact in the oscillation profile. The rationale for external magnetic fields disturbing the levitated structure is as follows. In an ideal scenario, the magnetic vector of the permanent magnet being levitated would be perfectly aligned with its geometrical axis. In reality, misalignments of the magnetic vector with respect to the geometric axis are present due to manufacturing tolerances. Similarly, the electromagnet magnetization vector is not perfectly parallel with the local gravity vector due to leveling tolerances on the supports of the testbed frame and the effects of Earth's magnetic field. These two misalignments produce small horizontal components of magnetic field. The two horizontal magnetic components, from the permanent magnet and the electromagnet, will try to align themselves producing a restoring torque. The same effect is exploited in satellite

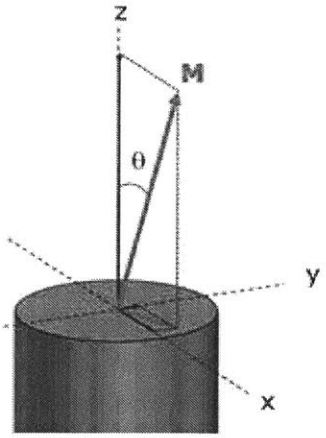

Fig. 2.8 Horizontal magnetic field of a non-ideal magnet. Credit: MagCam

magnetorquers. A similar magnetic perturbation is used to modify the rotation of a levitated top in [47].

The magnetic restoring torque interferes with the friction-free environment which is desirable to measure thrust in the MagCube, therefore it is important to reduce its effect as much as possible. Only one horizontal magnetic field component must be compensated for, either the one in the permanent magnet or the one in the electromagnet. Since the electromagnet is fixed in the balance frame and not levitated, it is then easier to mitigate its horizontal magnetic field. In order to counteract the small horizontal magnetic field, two pairs of orthogonal Helmholtz coils are placed close to the levitation region, between the permanent magnet and the electromagnet.

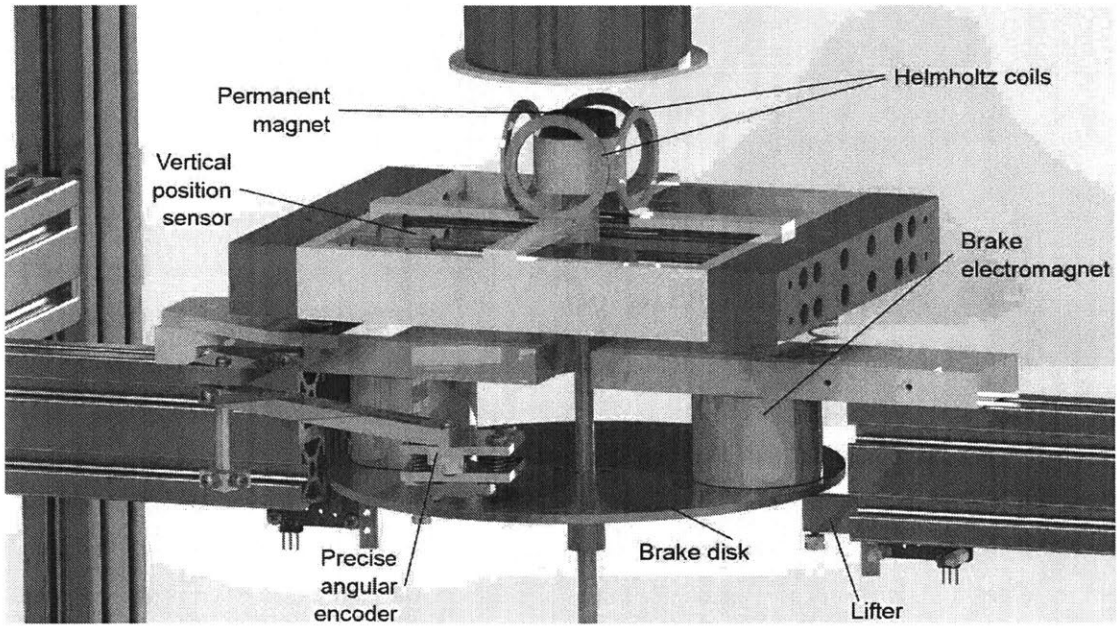

Fig. 2.9 Placement of the Helmholtz coils near the levitation region.

Orthogonal Helmholtz coils can generate a magnetic field with an arbitrary angle and magnitude. The goal is to create a magnetic field that has such an angle and magnitude to cancel out the horizontal component of the magnetic field in the levitation region. It is important to notice that magnetic fields in the levitation region are not uniform, therefore even with Helmholtz coils, some non-uniformity of the horizontal magnetic fields will remain. Therefore, completely removing the restoring torque constant proves to be a challenging feat. More details on the magnetic perturbation and its compensation can be found in Section 3.1.

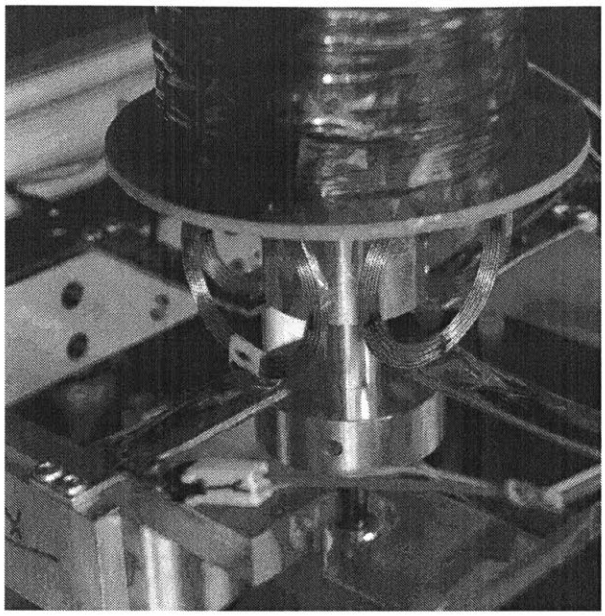

Fig. 2.10 Orthogonal Helmholtz coils used to counteract horizontal magnetic fields around the levitation region.

2.2 Sensors and actuators

The MagCube is designed to operate inside a vacuum chamber. The materials used in the design must have low outgassing properties. Disregard of this constraint could lead to vacuum chamber contamination and deposition of volatile materials that could, in some instances, deteriorate the vacuum level reached by the chamber or induce unwanted electric effects when the system is energized. This sole requirement proved important when choosing the material for different parts as well as electronics employed in the MagCube. The majority of plastics tend to outgas in vacuum. Special care had to be taken in order to choose only low outgassing plastics, such as Teflon or PEEK. Lastly, the non-contact characteristics of the testbed disqualified most of the COTS sensors available on the market. For these reasons, custom made sensors and actuators had to be fabricated in certain cases.

2.2.1 Levitation electromagnet

In order to sustain stable magnetic levitation an active controller system must be used [48]. To achieve this, an electromagnet is used as an actuator and a vertical position sensor is used as a feedback signal to control the position of the levitated structure. A custom made, vacuum-safe, electromagnet was fabricated due to lack of commercially available products. The

electromagnet was sized to levitate a one kilogram mass attached to a permanent magnet 1-5 millimeters away. The electromagnet windings were wound around a solid steel core to increase magnetic permeability. The permanent magnet used has a surface field of 5903 Gauss and is attached to the top of the levitated structure. The permanent magnet is attracted to the steel core of the electromagnet even when no current is flowing through the electromagnet coils. This bias attractive force was taken into account to size both the electromagnet and the permanent magnet on the levitated structure. Magnetostatic simulations were run in Maxwell V14 to verify the design against requirements. The final design produces around 10 Newtons of steady bias lifting force between the steel core of the electromagnet and the permanent magnet on the satellite [42]. Additionally the system must also be able to repel the CubeSat in the case that it gets too close to the steel core and the weight of the satellite is no longer sufficient to keep it separated. Running one Ampere of current in reverse provides a net repulsion force of around one Newton [42].

The electromagnet is mounted on a gimballing system that allows orientation adjustments in 2 axis. This allows to orient the electromagnet with respect to the testbed frame reducing misalignments. More details on the electromagnet construction and its performance can be found in [42].

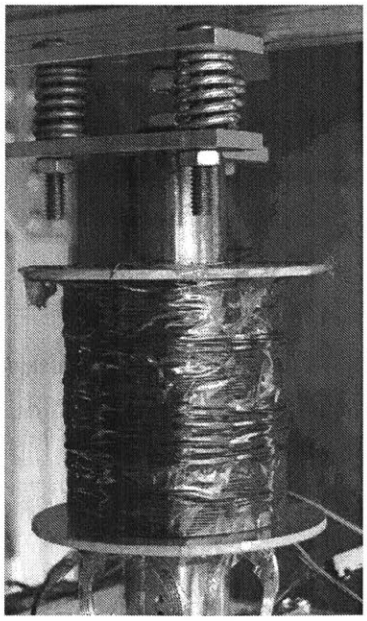

Fig. 2.11 Levitation electromagnet and gimballing structure.

2.2.2 Vertical position sensor

For the magnetic levitation controller to work, it requires an accurate feedback signal containing information about the vertical position of the permanent magnet with respect to the electromagnet resting on top. The levitation algorithm will increase the current through the electromagnet if the levitated structure is lower than the commanded set point. It will decrease the current if the levitated structure is higher than expected. By doing this thousands of times a second, stable levitation can be achieved and the permanent magnet of the levitated structure will stay close to the desired height.

The non-contact constraint on sensor posed several challenges which eliminated most of the COTS options available. The final sensor design relies on an optical shadow sensor based on the sensor developed at Stanford University used to control the test mass of the LISA mission [49]. The sensor uses two laser beams, (5 milliWatt and 650 nanometers wavelength) that are semi obstructed by an optical flag attached to the levitated structure, Fig. 2.12.

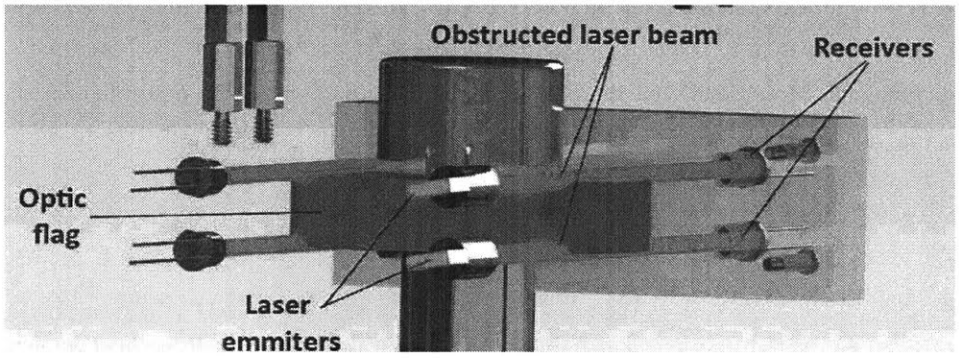

Fig. 2.12 Vertical position sensor concept.

As the satellite moves up and down, it obstructs more light on one of the laser beams and allows more light to pass on its counterpart. The light intensity is read by photodiodes connected in a differential configuration followed by a transimpedance amplifier, Fig. 2.13. This arrangement allows for a very high resolution position readout.

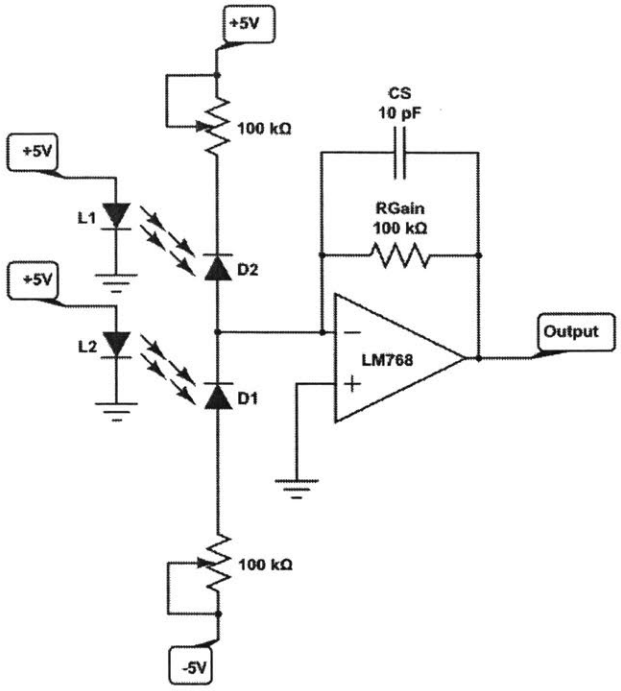

Fig. 2.13 Circuit schematic of the vertical position sensor.

The microcontroller that directly reads the sensors output uses a 16-bit analogue to digital converter over a ± 5 Volts range. The arrangement results in a theoretical resolution of 12 nanometers per bit. The useful linear range of the sensors is about 500 µm as can be seen in Fig. 2.14.

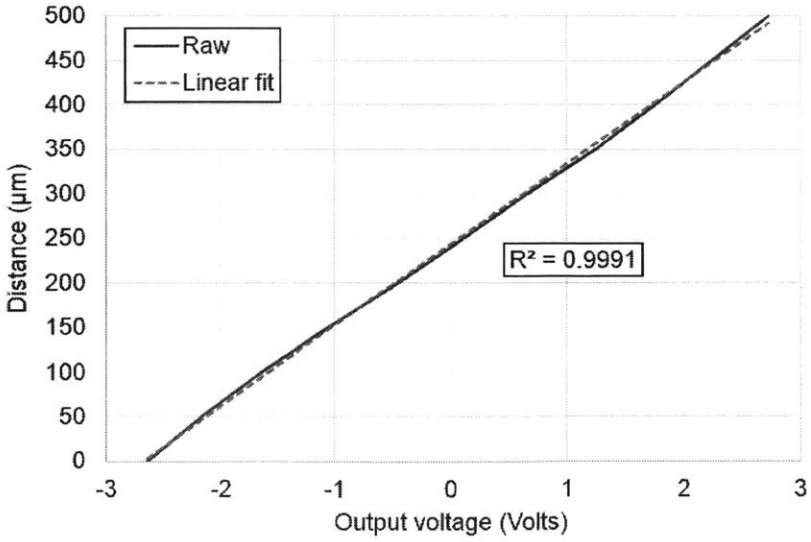

Fig. 2.14 Calibration fit of the vertical position sensor

The actual resolution of the sensor is mainly limited by imperfections in the optical flag construction. The vertical position envelope during levitation was around 20-30 μm from the setpoint, [43]. Since the vertical position of the levitated structure is not a crucial parameter for the instrumentation present in the MagCube, it is only present to enable levitation, no further improvements or performance analysis of the sensor were pursued.

The optical shadow sensor is mounted on a vertical stage that sits on the upper movable platform of the testbed. The vertical position of the sensor with respect to the electromagnet is adjustable. Therefore, the height at which the satellite nominally levitates with respect to the electromagnet can be adjusted. If the sensor is positioned in such a way that the steady bias force of the permanent magnet is close to the levitated structure weight, then the electromagnet only has to disturb this state to ensure stable levitation. This feature allows the current of the electromagnet to be small. In some cases, as low as 100 milliamps when the sensor is correctly positioned. The sensor is built around a square aluminum frame that allows all the components to stand far away from the levitated structure, to minimize any potential perturbations on the zero-friction axis.

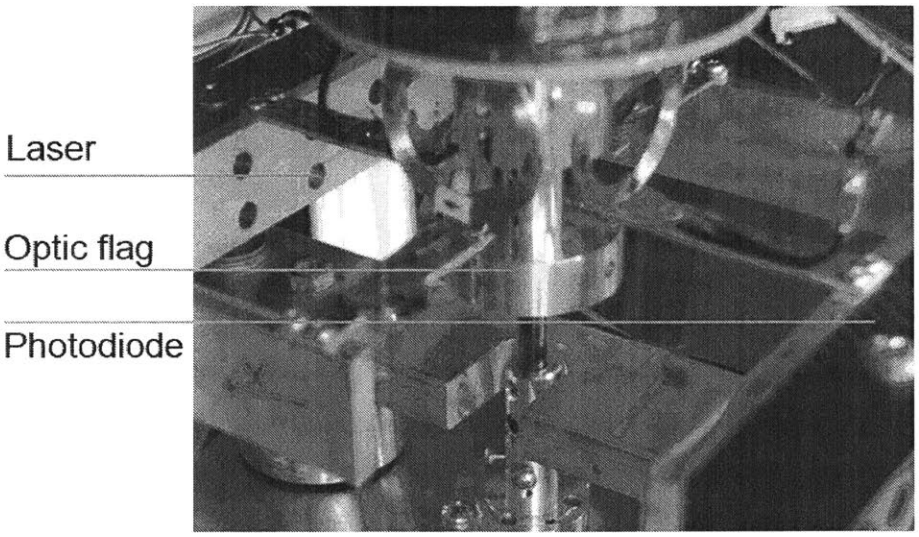

Fig. 2.15 Construction of vertical position sensor.

2.2.3 Electromagnetic brake

The zero-friction rotational axis of the MagCube makes any rotational movement gained by the levitated structure last for a long period of time. An electromagnetic brake is used to reduce the rotational speed of the levitated structure in a relatively short amount of time when

necessary, enabling fast cycles in experimentation without breaking vacuum. An electromagnetic brake operates by inducing Eddy currents in moving conducting materials, dissipating kinetic energy into heat. In its simplest form it consists of a magnetic field source in close proximity to a moving conductor material which is to be slowed down. Magnetic damping is only possible when the magnetic field through a material is changing, either in magnitude, or relative position. Magnetic dampening can be estimated using the following equation:

$$F = k\frac{v\,A\,B\,h}{r^2\,\Omega} \qquad \textbf{Eq. 2.2}$$

Where F is the braking force, k is a constant, v is the relative velocity between the magnetic field and the conducting material and A is the area of the conducting material. Electromagnetic properties of the equation include B which is the magnetic flux, h is the thickness of the material, r is the distance between the magnetic field and conductor, and finally Ω represents the resistivity of the material. The final design of the magnetic damper used in the MagCube maximizes the braking force by increasing the relative velocity between the magnet and the conductor and reducing the distance between them. The damper consists of a 30 centimeter diameter aluminum disk attached to the levitated structure. Two electromagnets are placed on the upper movable platform of the testbed in such a way as to minimize the distance between the electromagnets and the aluminum disk. The electromagnets are in close proximity, but not contacting, the periphery of the aluminum disk of the brake.

When the levitated structure is to be braked, current is passed through the electromagnets generating a magnetic field. As the levitated structure rotates, the aluminum disk moves with it and through the magnetic field created by the electromagnets. As stated earlier, this induces Eddy currents which translate into magnetic dampening. The effect of magnetic damping reduces the rotational speed of the levitated structure in a short amount of time, minutes, to a point were experiments can proceed. The electromagnets are connected in a series configuration to ensure the same current travels through both of them. Having equal currents helps reduce any potential perturbations on the levitation system.

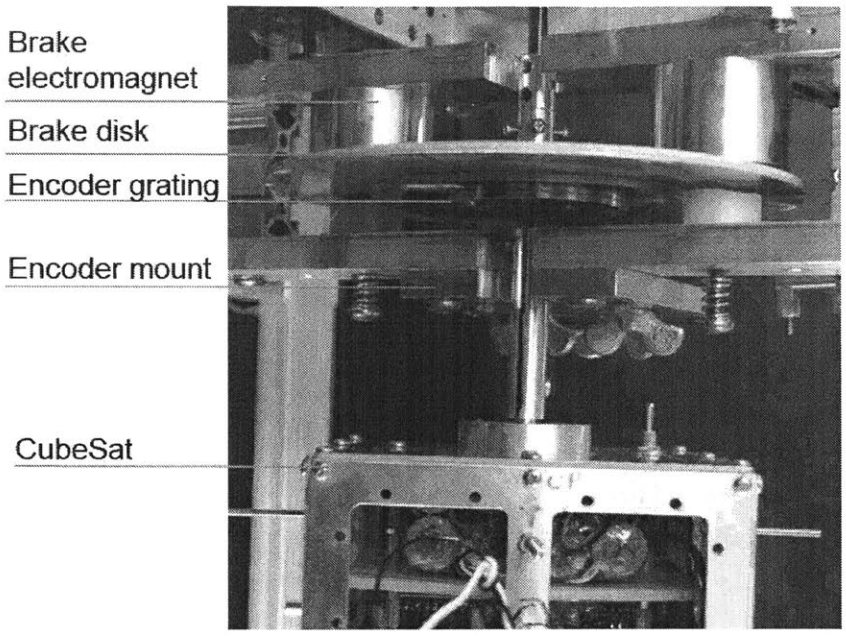

Fig. 2.16 Electromagnetic brake construction.

2.2.4 Lifting mechanism

In some instances the levitation controller is not able to counteract all external perturbations and the levitated structure falls a short distance, ~8mm, onto the testbed frame. The perturbations usually come from people or large masses abruptly moving, such as people jumping around the vacuum chamber. Since the magnetic force falls off with distance squared, the electromagnet and driving circuitry are not able to provide enough force to lift the satellite once it has fallen. The large vacuum chamber used to house the MagCube takes around 10 hours for a complete pump down cycle. If the levitated structure were to fall once it is under vacuum conditions, the chamber would have to be vented to manually lift the levitated structure into the levitation region followed by a lengthy pump down cycle. To avoid this time-consuming endeavor, the MagCube is equipped with a lifting mechanism which is able to raise the CubeSat and reestablish magnetic levitation, all without breaking vacuum. The mechanism is also used to contact the levitated structure with a grounded electrode to dissipate any accumulated charge product of thruster operation which is useful during spacecraft charging experiments.

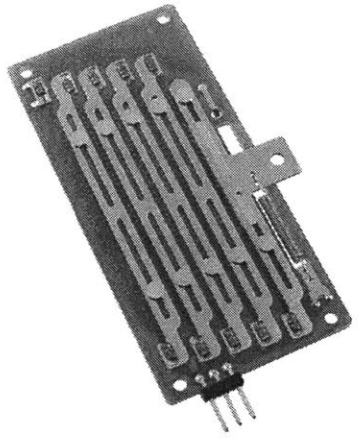

Fig. 2.17 MIGAone-10

The lifting mechanism employs a modular shape memory alloy wire actuator, the MIGAone-10. These actuators are vacuum-safe, small, and strong. They are also exceedingly simple to operate and control. Furthermore, during thrust measuring tests, a fast spinning CubeSat can be brought to a halt in a matter of seconds by deploying the lifting mechanism and mechanically braking the satellite.

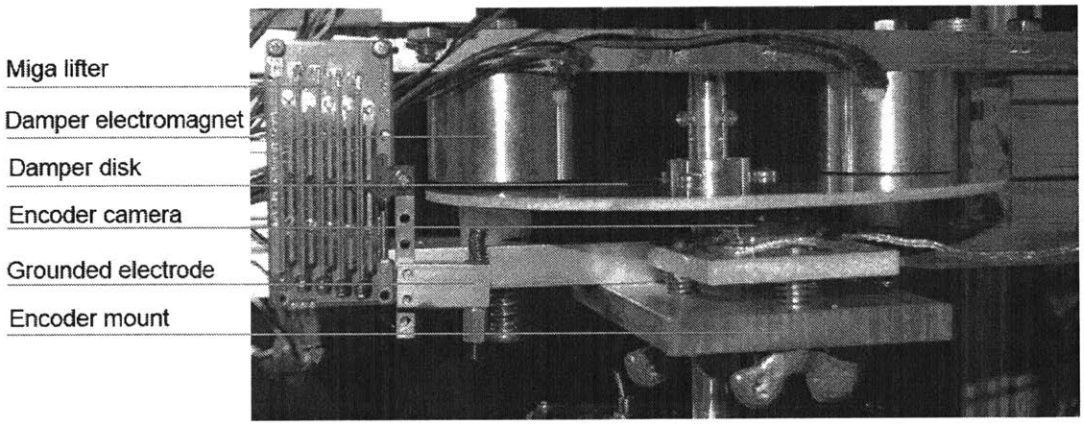

Fig. 2.18 Lifter mechanism construction.

2.2.5 Helmholtz coils

As described in Section 2.1.2 a pair of orthogonal Helmholtz coils are used to counteract any external horizontal magnetic fields in the levitation region. Each Helmholtz coil is composed of a 5 cm diameter winding. Four of them are placed in an orthogonal fashion around the levitation region. The current flowing through the coils is controlled in such a way as to provide an arbitrary direction and magnitude of the final horizontal magnetic field. The coils

are a fundamental part of the MagCube, without them the unwanted restoring torque will mask the small μN forces the thrusters produce. They are also useful to purposely introduce torque perturbations on the satellite, basically acting as a synchronous motor. This would be useful in attitude control experiments, as it could simulate external disturbances present in orbit. This possibility was not pursued in this work.

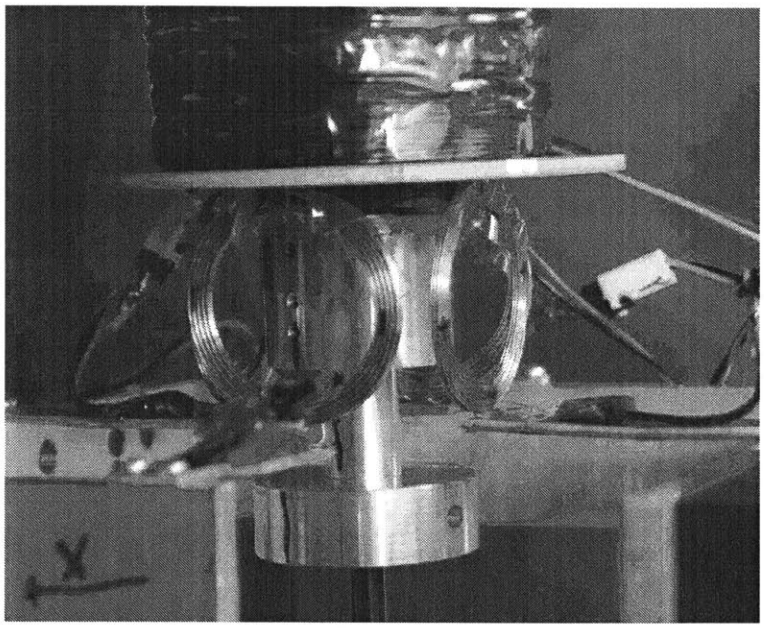

Fig. 2.19 Helmholtz coil construction.

2.2.6 Charge sensor

In order to characterize the spacecraft charging processes that can occur when the thrusters are activated, a non-contact charge sensor was designed and integrated into the MagCube. The concept behind the charge sensor is, in its simplest form, a capacitor. The levitating satellite acts as one plate while a shielded metal disk acts as the other. The shielded metal disk is placed in close proximity to the bottom metallic face of the levitated satellite. When the levitated structure charges, it induces a mirror charge on the shielded metal disk which is then measured by a high impedance electrometer. A Keithley 6514 digital electrometer was used to perform this measurement.

The disk is shielded to avoid unwanted sources of charge that could be collected by the sensor plate. The shield is composed of a metallic housing that is grounded and covers the inner disk from all sides except the top one, used for measuring. The wire used to carry the sensor

plate signal is a shielded coaxial cable grounded to the chamber. The charge sensor plate has a diameter of 68.6mm and sits ~3mm below the levitated satellite.

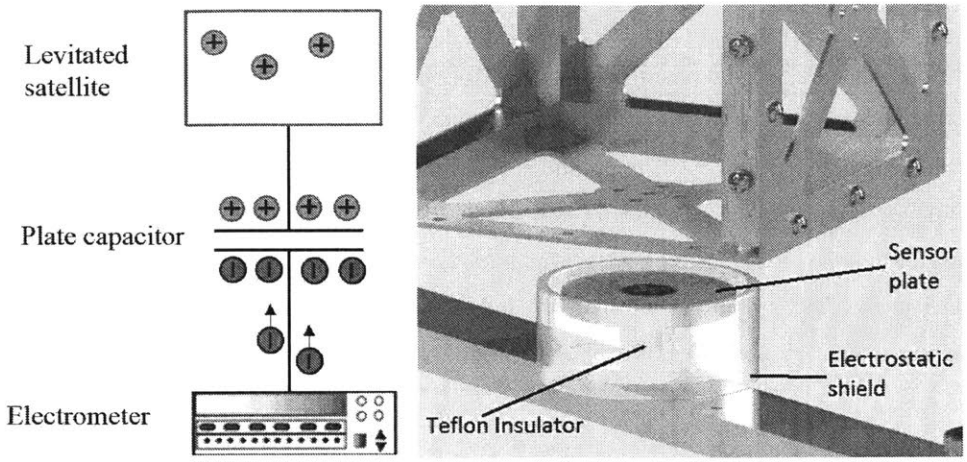

Fig. 2.20 Charge sensor concept and construction.

The charge sensor is calibrated by biasing the levitating structure to several known potentials with an external high voltage power supply. The calibration approach exploits the fact that knowing the satellite potential is more relevant than measuring the amount of Coulombic charge the satellite has. The procedure generates a linear transfer function of the satellite potential versus the measured mirror charge on the sensor plate, Fig. 2.21. The linear fit has a correlation coefficient of R=0.99.

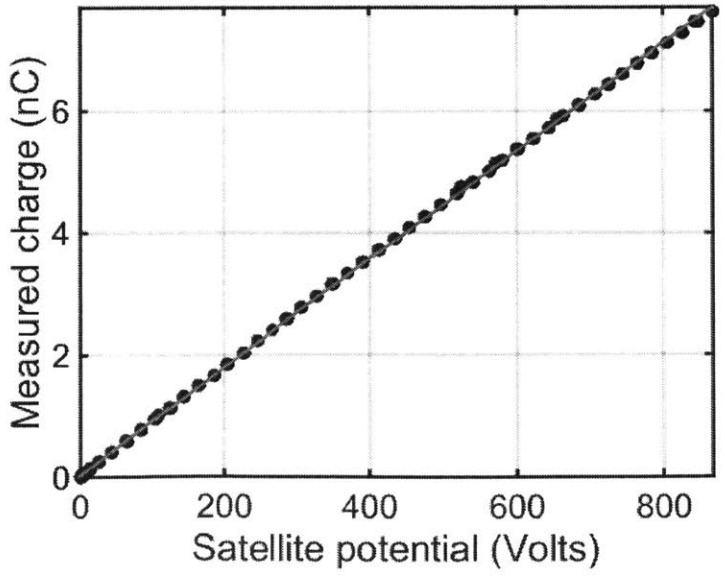

Fig. 2.21 Transfer function of charge sensor with linear fit.

The orientation and distance of the levitated structure with respect to the sensor plate affects the capacitive coupling of the device. Any movement of the levitated satellite therefore reduces charge sensor performance. The effect of movements on the measured satellite potential can be observed when the satellite is rotating with a constant speed and no thrusters are active, Fig. 2.22. Taking into account the error introduced by satellite movement, the uncertainty of the charge sensor is estimated to be ±10V. Tests described in section 4.5 have charging levels of around ±800V. The uncertainty of the charge measurement in these cases is then 1.25%. The sensor effectively measures the potential between the levitated structure and the grounded metallic chamber used for the experiments.

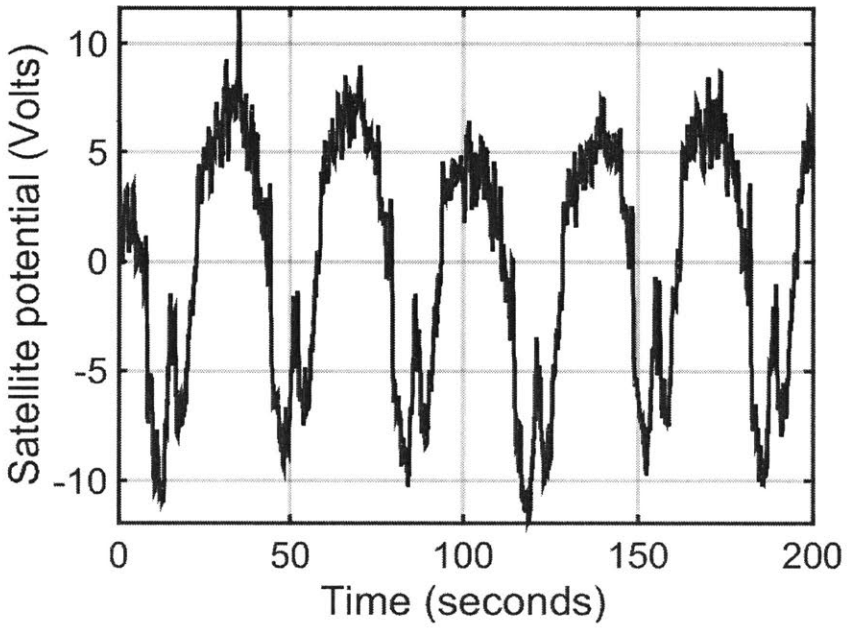

Fig. 2.22 Measured satellite potential while satellite is rotating at 1.7 RPM with no thruster emission.

2.2.7 Angular encoder

In order to characterize the performance of electrospray thrusters as attitude control actuators the precise angular position, arcsecond level, of the levitated structure must be known. In traditional satellites a suite of sensors is used to determine the attitude position of the spacecraft. Sun sensors, star trackers, magnetometers and gyros are the most commonly used attitude determination sensors in small satellites. Since the goal of this work is only to characterize the performance of the thrusters as attitude control actuators, an external angular

encoder is used to relay angular data. This scheme simplifies the design of the tests and allows to isolate the performance of the thrusters rather than analyzing the complete ACDS system. The MagCube tracks the angular position of the levitated structure using a non-contact MicroE Mercury 3500V angular encoder with a 4.25 inch diameter rotary grating. The encoder is composed of a camera that reads a circular grating which is mounted on the object of which angular data is desired. The camera sits around 2mm below the grating and it is mechanically and electrically isolated from the grating. This is essential as a non-contact sensor is required to maintain the zero-friction environment of the testbed.

These type of encoders are usually employed to read the angular position of precision shafts rolling in high quality ball bearings, therefore with little vibration, eccentricity and misalignments. The levitation environment of the CubeSat is very different from these ideal conditions. Vertical vibrations and eccentricities on the mechanical setup reduce the precision of the encoder significantly. A sturdy mechanical mount for the encoder camera must be used in order to reduce the external disturbances and improve the accuracy of the encoder.

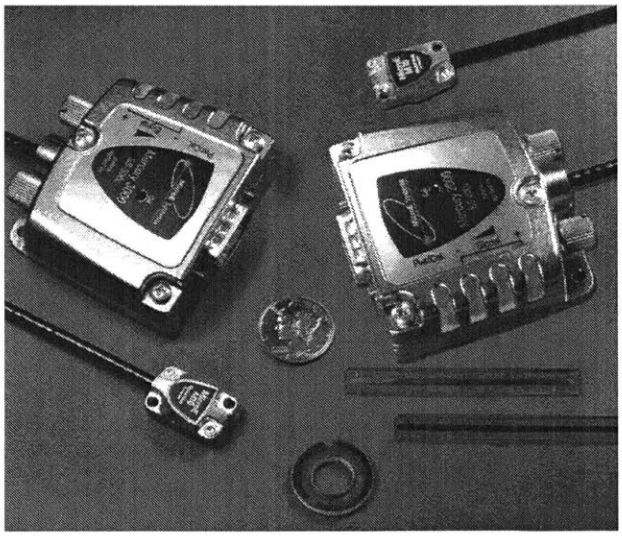

Fig. 2.23 MicroE Mercury 3500V angular encoder system.

The encoder datasheet indicates a ±2.1 arcseconds accuracy with ideal scale mounting concentricity [50]. During static tests, in which the satellite was not levitating but resting on a surface, therefore assumed immobile, the sensor provided an angle measurement with an error of ±3.71 arcseconds 3σ. When the satellite is levitated, the accuracy of the angular reading is lower than the static case. Dynamic effects such as vibrations are introduced by the non-perfect levitation scheme, the laboratory environment in which the testbed is mounted and external

vibrations from people and vehicles nearby. Attempts were made to characterize the angular error while the satellite was levitating but proved challenging. The main difficulty relied on restricting the rotation of the satellite about the zero-friction axis while simultaneously leaving the 3 positional degrees of freedom unrestricted.

A representative angular evolution of the levitated satellite under vacuum conditions and with no thrust acting on it is shown in Fig. 2.24. In this case, the satellite is only perturbed by the restoring torque mentioned in section 2.1.2, which leads to an oscillatory behavior. The noise on the raw angle signal is clearly visible.

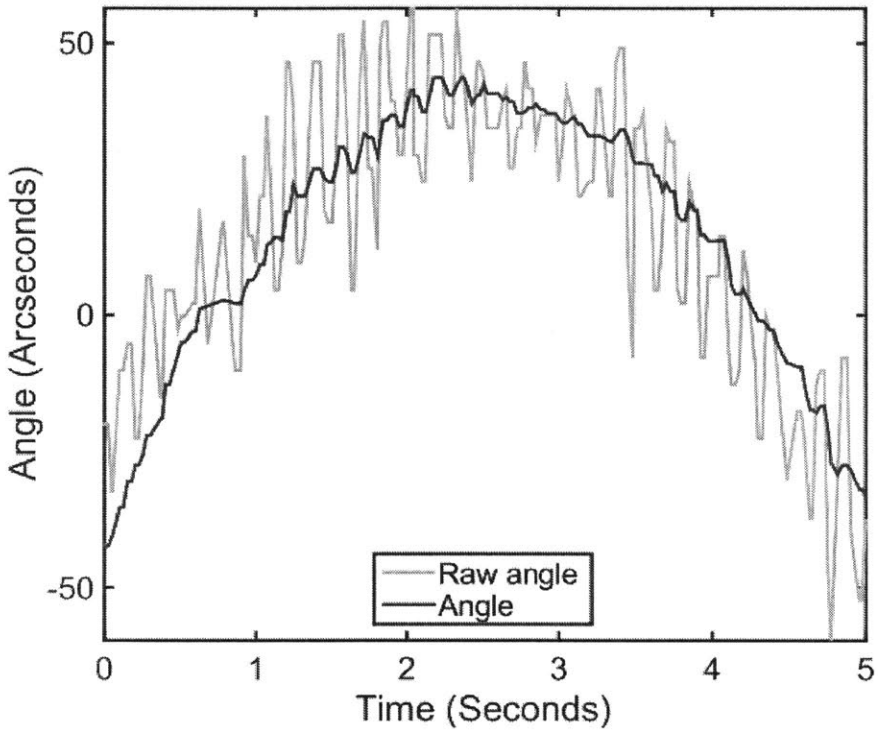

Fig. 2.24 Noise of angular encoder measurement. Blue trace is the smoothed angle signal.

The sampling rate of the raw angular signal is significantly higher than the timescales in which the levitated satellite rotates, even when actuated by thrusters. Therefore a real time 10-sample averaging filter was used to smooth the raw angle before feeding it into the attitude control algorithm, represented as the blue line in Fig. 2.24. Ten samples seemed to be enough to smooth out the high frequency noise without producing too much lag on the filtered signal

with respect to the raw data. The standard deviation of the difference between the raw angle and filtered angle is 9.9 arcseconds.

2.2.8 CubeSat balancing

In order to obtain accurate data from the MagCube the levitated structure needs to be balanced, this is, the center of gravity (CG) of the structure needs to be as close as possible to the zero friction axis of the structure. The vertical position of the CG is not as crucial. There are multiple ways of balancing a structure, from using "string-hanging" methods, to precisely calculating the CG positioned using detailed CAD. In the MagCube case there is a precise CAD model of the levitated shaft structure but not of the CubeSat electronics and hardware inside of it. Therefore, CAD models can be used to balance the shaft structure but not the CubeSat that is attached to it. The shaft structure and its attachments are designed in such a way as to make it symmetric around the zero-friction axis. The CubeSat requires manual balancing. Since the CubeSat can be easily detached from the shaft structure, this is easily done before each test.

An active balancing technique for the CubeSat was conceived from common propeller balancing machines. The procedure goes as follows: First, two short shafts are attached to the CubeSat faces along the axis that needs to be balanced. The CubeSat shafts are then placed on two low friction bearings that rest on the leveled balancer frame. The bearings allow the CubeSat to rotate with very low friction along the axis that needs to be balanced. Any CG offset forces the satellite to rotate in such a way as to place the CG down. Once the CubeSat settles, weight is added in the side facing up. This is repeated until the CubeSat can rest in any orientation without moving. A CAD rendering and the final apparatus are shown in Fig. 2.25.

In order to characterize the CG offset uncertainty a series of objects with different masses were attached a certain distance of the central axis of an otherwise balanced CubeSat. Once a heavy enough object was placed with a sufficient lever arm, the CubeSat would rotate, overcoming the friction of the bearings. It was calculated that the balancer apparatus was able to place the CG of the CubeSat within $\pm$ 0.3 mm of the CubeSat's central axis.

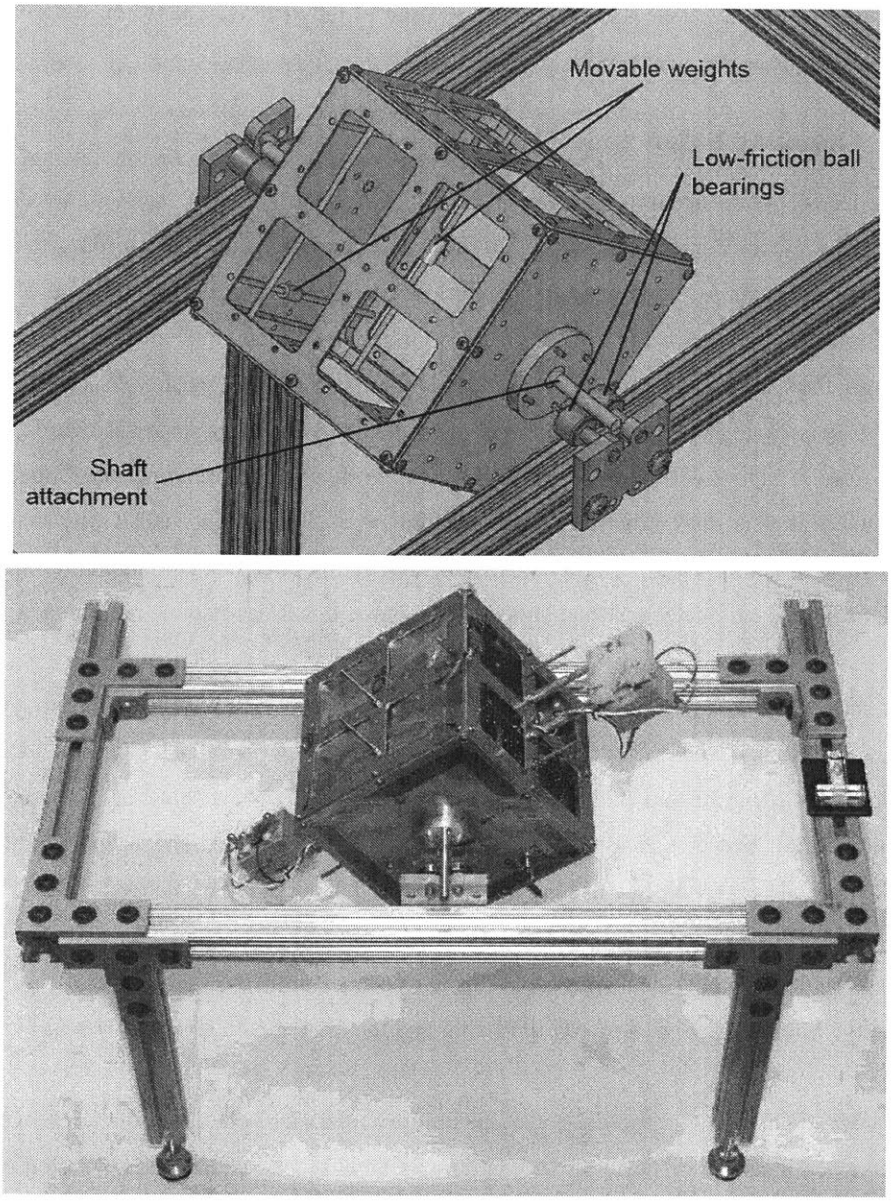

Fig. 2.25 Balancer CAD and construction.

2.2.9 Inertia measurement

Section 2.1.1, described the different methods available to the MagCube to measure thrust. The approached followed in this work requires the knowledge of the levitated structure's moment of inertia. Similarly to finding the center of gravity, there are multiple methods for determining the moment of inertia of an object. As mentioned earlier, a detailed CAD model of

the levitated shaft and all attachments is available, its inertia can then be calculated very accurately by the CAD software. The CubeSat, with cable harnesses and custom electronics, does not possess a sufficiently detailed CAD, therefore its inertia needs to be measured experimentally.

For this, a trifilar pendulum was used. In a trifilar pendulum the object of which the moment of inertia is to be measured rests on a platform supported by three long filaments. The platform is free to rotate along the vertical axis but since the filaments cannot stretch, the platform slightly raises for every degree it is rotated. If disturbed, the platform will rotate back and forth in an oscillatory fashion. The frequency of the oscillations is directly proportional to the moment of inertia of the platform and the object placed on top of it by the trifilar pendulum equation:

$$I = \frac{R^2 g\, T^2}{4\,\pi^2\, L}(m_p + m_o) - I_p \qquad \textbf{Eq. 2.3}$$

Where R is the distance from the center of the platform to the filaments, g is the standard gravity constant, T is the period of oscillation, L is the filament length, m_p is the platform mass, m_o is the object mass and I_p is the platform moment of inertia. This simple approach allows us to determine the moment of inertia of the CubeSat with ease. There are a couple of constraints that limit the accuracy of the apparatus. First, the equation assumes that the object to be measured is balanced along the inertia axis, and it is centered in the platform. It also assumes that all the filaments are the same length and that the platform is leveled with respect to gravity. All these factors reduce the accuracy of the inertia measurement.

The apparatus implemented for the MagCube consisted of a thin aluminum disk with a diameter of 9.50 inches suspended by 0.5mm diameter stainless steel wires of approximately 113 cm in length. The apparatus measured the oscillation period by means of a phototransistor coupled to a light source that passed through a small slit on the disk.

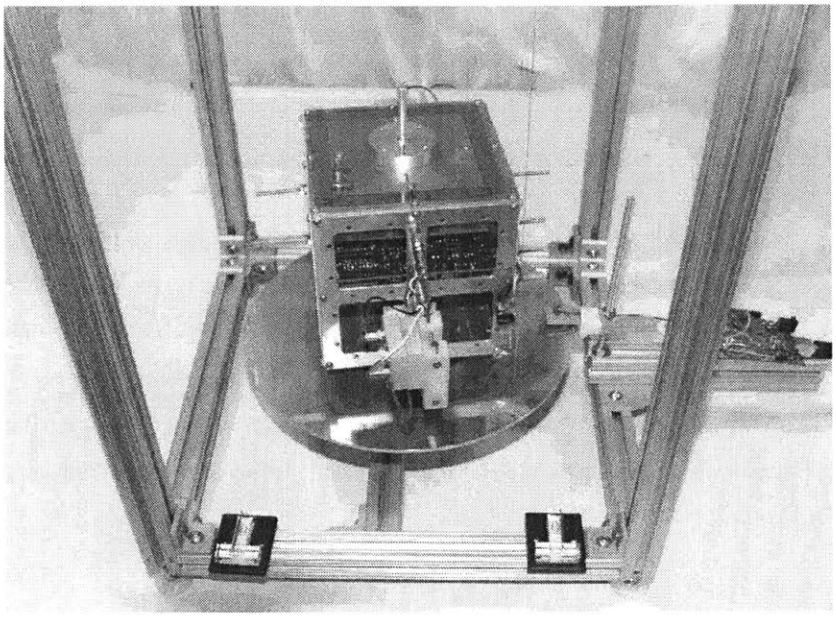

Fig. 2.26 Trifilar pendulum construction.

The accuracy of the pendulum was determined using a steel disk of accurate dimensions as a test object. The inertia of the disk was known by means of an accurate CAD model. The disk was designed in such a way as to have a similar moment of inertia to the CubeSat as well as similar mass. Using this test object in several trials, The L and R parameters of the trifilar pendulum equation were fitted using least squares. Several other test objects with known masses and moment of inertias were also tested to ensure the accuracy of the pendulum. The uncertainty of the measured moment of inertia for the test object with similar mass and moment of inertia as the CubeSat was 3.01×10^{-5} kg m^2 or 0.5%. This value is used as the estimated uncertainty of the apparatus.

2.3 Plasma generator

As discussed in section 1.2.3, the plasma environment of space has a significant effect on spacecraft charging processes that are experienced by a satellite. In order to recreate a plasma environment similar to space inside the vacuum chamber holding the MagCube a plasma generator was designed, built and characterized. The characteristics of the space plasma environment is a strong function of altitude. Generally a lower orbit entails a higher plasma density. According to the Low Earth Orbit Charging NASA handbook [16], in order to accurately recreate a LEO space environment the plasma electron density should be more than

10^5 electrons /cm^3. Electron temperature should be no more than 3 eV. The plasma should be isotropic.

Low temperature, high density plasmas like the one described by the NASA manual are usually generated with cathodes. An effort to design and construct a low-cost cathode to use as a plasma generator for the MagCube was conducted. First generation cathodes employed in conventional electric propulsion thrusters, used a heated tungsten wire to produce a stream of thermionically produced electrons. These early cathodes were very inefficient as Tungsten has a relatively high work-function. Currently, high-performance state of the art cathodes use exotic, low-work function materials such as barium oxide or LaB6 compounds [22]. These specialized chemicals are expensive and difficult to source and machine in their pure form.

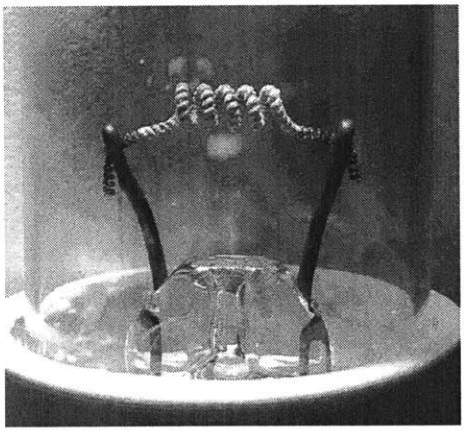

Fig. 2.27 Barium oxide coated filament of a fluorescent lightbulb.

The first attempt of a cathode used in the MagCube employed tungsten filaments extracted from fluorescent lightbulbs. These filaments are coated with BaO compounds to lower their work function and are conveniently housed in the glass tube of the lamp. By carefully cutting the glass tube, the filaments can be retrieved and used as thermionic emitters for a cathode. The low-cost of fluorescent lamps and the relatively easy retrieval of filaments makes it simple to gather a large number of them. Filaments had a propensity of burning out during operation. This frequent filament burn-out forces the user to replace filaments constantly, therefore, the easiness in which the filaments are replaced is paramount. In this cathode design, Argon gas is flowed through a metal block that houses several filaments. A voltage is applied between the cathode orifice and an upstream electrode that acts as a keeper, Fig. 2.28.

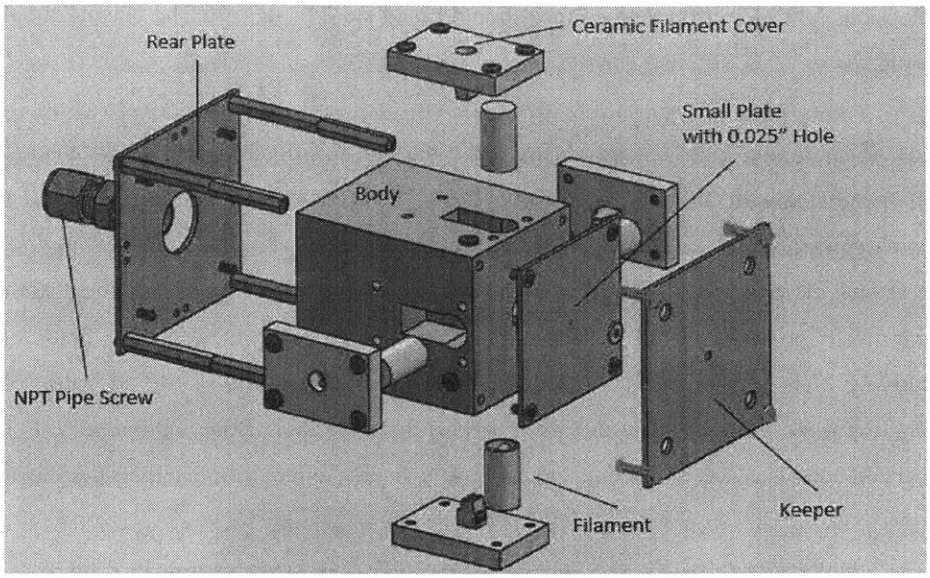

Fig. 2.28 Main parts of the MagCube cathode.

The aluminum block acting as the filament holder is a 2" x 2" x 2.5" block. The cathode and keeper orifices are constructed from stainless steel plates with dimensions of 2" x 2" and 2.5" x 2.5" respectively. Several plates with different hole sizes where constructed to explore the effect of the orifice diameter on cathode operation. The relatively large size of the aluminum block provided enough space to implement a satisfactory method to mount the filaments and still prevent them from touching each other. This was accomplished by slots machined into the front of the body on each side.

The filaments are mounted on 4 ceramic plates with help of a screw connector terminal that is epoxied in place. These ceramic plates are then attached to the cathode body via screws. Each plate is able to house two filaments for a total of 8 filaments. The design makes filament replacement straightforward.

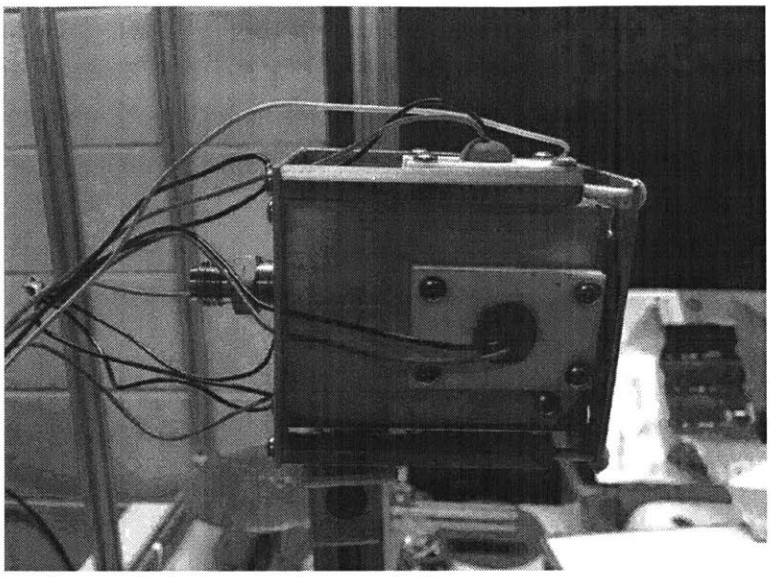

Fig. 2.29 Assembled cathode.

To operate the cathode a gradual warmup phase of the filaments lasting for 30 minutes was conducted while flowing 2 sccm of Argon through the cathode. The warmup phase ensured that no water or other contaminants where present in the filaments when heated to their final temperature, which avoided BaO coating degradation. Once the filaments had been conditioned the flow of Argon was increased to 10sccm, to facilitate cathode ignition. The keeper was then biased to 500V with a current limit of 0.5A. In some instances the cathode was able to ignite under these conditions, but more frequently a purging of the gas line was needed to kick start ignition. When the gas line is purged, a momentarily high flow rate is passed through the cathode which aids in ignition. Once the discharge occurs the cathode is able to operate while the flowrate is reduced down to 5sccm.

The cathode was able to ignite successfully in several experiments, firing continuously for up to 45 minutes. The failure mechanism usually consisted of a discharge between the keeper and the filaments, which destroyed them instantaneously. As single filaments were lost, the cathode operation became more erratic. Once only two or one filament remained, the cathode was very difficult to ignite. The position, size and performance of each filament had a significant effect on the cathode operation. Since all the filaments were retrieved and mounted by hand, there existed significant variability between each test. Although the design and flexibility of the design was a success, the operation and lifetime of the cathode for the purposes

of recreating the space environment were not optimal. Therefore, a more robust and simpler approach was attempted, a hot cathode.

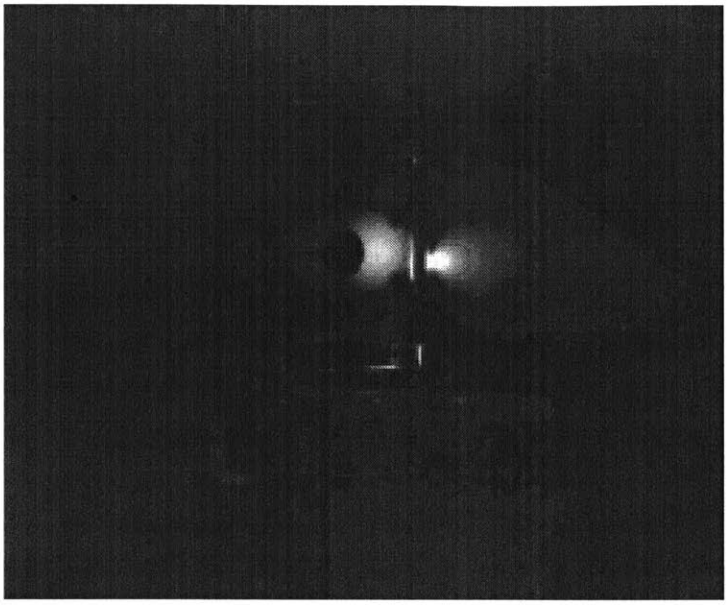

Fig. 2.30 Ignited MagCube cathode with visible plasma plume (blue glow) and filament glow (orange glow).

Hot Cathode

A biased heated tungsten foil, proved to be a more robust solution to recreating a space plasma environment. In this cathode design, a 0.01 x 1 x 200 mm tungsten foil is placed in close proximity to an Argon gas outlet, Fig. 2.31. In vacuum conditions the tungsten foil is heated up until it glows white-hot by passing a current thorough it. A small Argon flowrate of around 2-10 sccm is forced through the gas outlet which is placed close to the tungsten foil. By biasing the foil with a small negative voltage, around -20 to -5 volts, electrons generated by thermionic emission on the foil are repelled with sufficient velocities to cause Argon ionization (ionization potential of ~15.7eV), producing a low temperature plasma. This solution avoided any potential discharges that might otherwise have destroyed the foil.

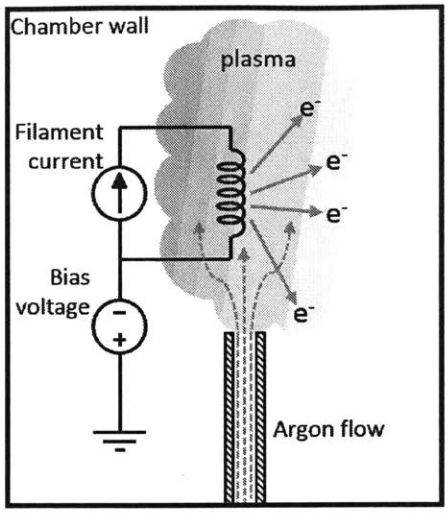

Fig. 2.31 Hot cathode concept.

The properties of the plasma generated by the hot cathode are easy to control by varying the Argon flowrate, heating power, and/or bias voltage. The tungsten foil never failed even after hours of continuous and stable operation.

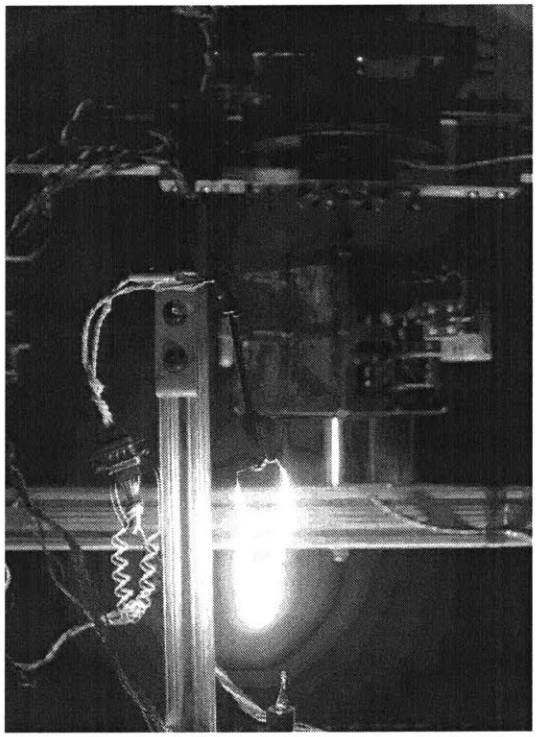

Fig. 2.32 Tungsten foil hot-cathode in operation. Argon outlet is the small structure directly below the filament.

2.3.1 Plasma characterization

The plasma generated by the hot tungsten filament cathode was characterized using a Langmuir probe. A Langmuir probe works by inserting one electrode into a plasma with a time-varying electric potential. The currents collected by the probe at different potentials is then used to estimate plasma parameters. Plasma potential, plasma density and electron temperature, are quantities that can be measured using a Langmuir probe. There are two main types of analysis used in plasma characterization, thin and thick-sheath theory. The methods differ by the ratio of the probe size to the Debye length of the plasma under study, as discussed in section 1.2.3. For thin-sheath to apply, the probe must be larger than the plasma Debye length. Thick-Sheath theory, or orbital limited motion (OML) is applied when the size of the probe is smaller than the Debye length. Plasma probes are biased to different voltages, collecting different currents for each potential which produces a current versus voltage curve (IV curve). A representative IV curve for a Langmuir probe immersed in a plasma is shown below:

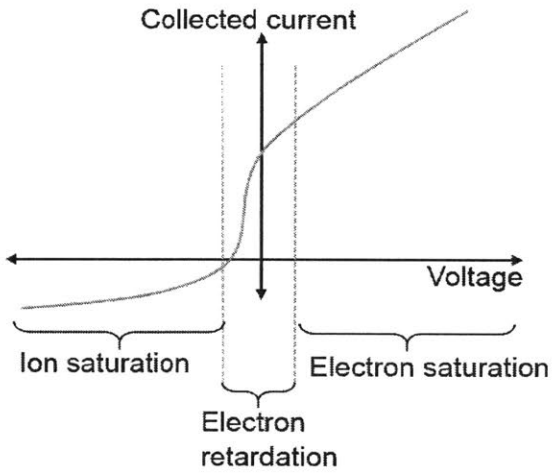

Fig. 2.33 Representative IV curve for Langmuir probe immersed in a plasma.

A plasma IV curve obtained with a Langmuir probe has three distinct regions. In the ion saturation region, the probe is so negative that most of the electrons in the plasma are repelled and are not able to reach the probe. The current in this region is therefore mostly ionic. Similarly, in the electron saturation region the probe is so positive that most of the ions do not reach it, leaving only electron current. In the electron retardation region the probe retards electrons that would otherwise reach the probe.

To characterize the plasma of the hot cathode employed in the MagCube, a rectangular Langmuir probe with dimensions of 90 x 90mm was used. The probe had its edges shielded with grounded metallic foil to avoid any edge effects which might introduce unwanted artifacts on the IV curve. The probe was biased from -50 to +50V and the collected current was measured with a high impedance electrometer (Keithley 6517).

The probe was placed in a similar location as where the CubeSat would be during experiments. To extract the relevant plasma properties, mainly electron density and electron temperature, an approach based on Sawyers work was followed [18]. This process assumes thin-sheath theory. The steps for the process go as follows:

1. The ion saturation current is calculated by creating a line fit for the ion saturation region of the IV curve.
2. Subtract the ion saturation current from the total measured current, to obtain the electron current.
3. Plot the natural log of the electron current.
4. Place log-linear fits on the electron retardation and saturation regions.
5. Find the intersection of the two log-linear fits from the previous step.

The voltage of this intersection is the plasma potential. The electron saturation current is the current of this intersection point. The electron temperature is the inverse of the slope of the log-linear fit in the electron retardation region, in eVs. The plasma density can then be found using the 1-D approximation equation for planar probes in Thin-Sheath theory [18]:

$$n_e = \frac{I_{esat}}{A\, q \sqrt{\frac{k\, T_e}{2\, \pi\, m_e}}} \qquad \textbf{Eq. 2.4}$$

Where A is the surface of the collecting probe, q is the electronic charge, T_e is the plasma temperature, m_e is the electron mass, and k is Boltzman's constant. I_{esat} refers to the electronic saturation current and n_e is the electron density. Finally the Debye length, Eq. 1.7, is calculated using the electron temperature, plasma density obtained from Eq. 2.4. The Debye length is then compared to the size of the probe used to acquire the data. As described earlier, in order for Thin-Sheath theory to apply, the size of the probe must be larger than the calculated Debye length.

It should be noted that thin and thick sheath theory are simple approximations to characterize plasmas. Extracting plasma properties from an IV curve is a challenging endeavor. There are

multiple external variables that affect the state of the plasma and therefore the collected current on the probe. Furthermore, some plasma environments do not precisely fall into one category or the other. Therefore, the estimated plasma properties presented in this work should be taken as approximations only.

The goal of the plasma generator in the MagCube is to simulate a LEO plasma environment. According to the NASA LEO spacecraft charging handbook, the average plasma density in a 400km altitude orbit is in the order of $10^6 cm^{-3}$ [16]. Plasma temperatures vary between 0.1 and 1 eV. In order to generate a similar kind of plasma with the hot filament cathode, a trial and error approach was followed. The variables in the cathode operation were: filament current, biased voltage and Argon flowrate. An IV curve was acquired with the Langmuir probe for each of the several different combinations of operating parameters. The combinations of parameters were varied until a 400km altitude environment match was found. Below is the raw IV curve that matches a LEO environment alongside the processed data according to the process described previously:

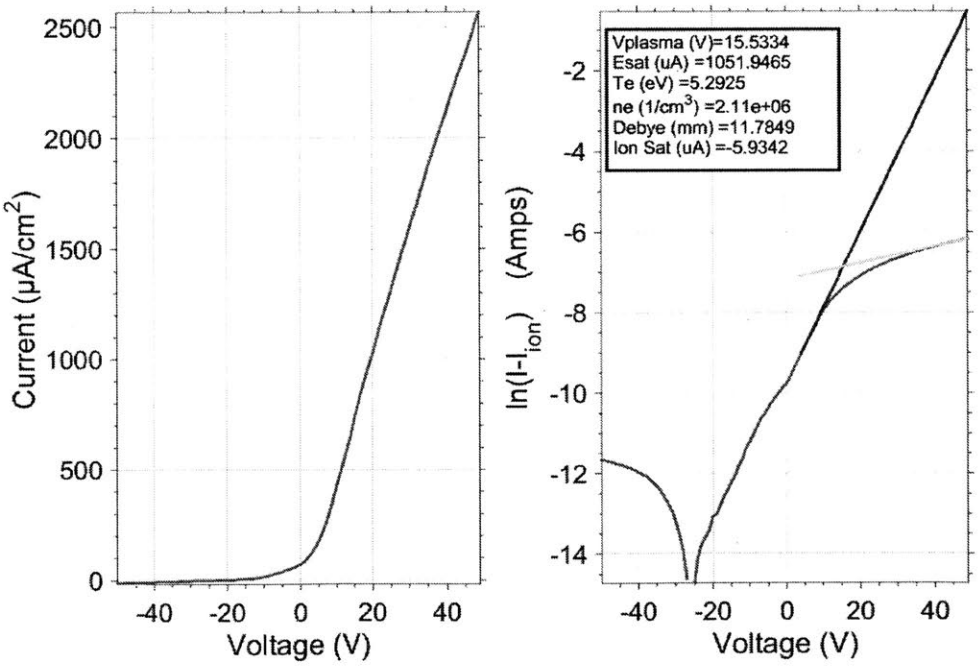

Fig. 2.34 Characterization of an IV curve from the Langmuir probe. The probe was immersed in a plasma environment similar to a 400 km orbit.

The LEO plasma environment was recreated with a filament current of 6A, Argon flowrate set to 10sccm and cathode bias of -5V. The resulting plasma environment had an estimated

density of 2 x 10^6 cm^{-3} and a temperature of around 5.3 eV. Note that the temperature of the plasma is higher than the plasma temperature in a 400km orbit. The implication being that the flux is overestimated by a factor of $\sim\sqrt{5}$ or 2. This is the downside of employing such a simple hot cathode, low plasma temperatures are challenging to achieve. A more sophisticated cathode, such as the hollow cathode attempted but ultimately not used, could have provided a cooler plasma.

To lower the density of the plasma, and therefore, simulate higher orbits, the current flowing through the filament was reduced. Lower density plasmas have a correspondingly larger Debye length which if they exceed the Langmuir probe size nullify the use of the simple thin-sheath theory used to analyze the data. The characterization of these lower density plasmas was outside the scope of this work and only rough order of magnitudes were produced using other data available during experiments. Although full characterization of the low density plasmas was not pursued, the temperature of these low density plasmas, to a first order, should still be retrievable from the Langmuir probe curves. The procedure and data used to estimate the plasma parameters for low density plasmas is discussed in section 4.5.6.

2.4 Software and levitation controller

An important portion of the MagCube project was spent coding a practical graphical user interface (GUI) in which the user could control all aspects of the MagCube and the PPU inside the satellite. All the computer software was coded in C# and was used in a Windows operating system. The software logs and displays the different signals of the instrument in real time, it also controls all relevant actuators on the MagCube. A USB-6229 DAQ from National Instruments is used for the majority of data acquisition tasks.

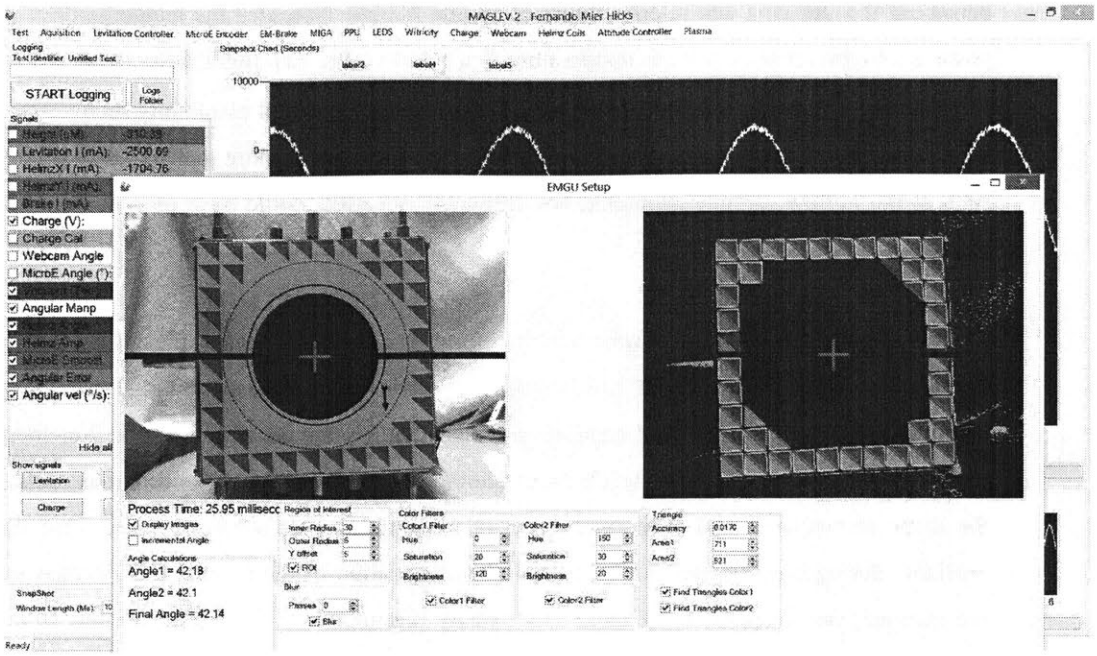

Fig. 2.35 Screenshot of MagCube software.

The electronics of the MagCube are housed on a metallic box near the chamber. The electronics consist of electromagnet drivers, the levitation microcontroller and several power supplies.

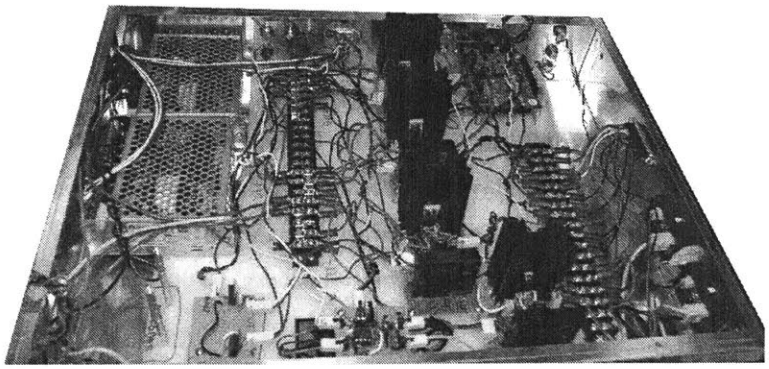

Fig. 2.36 MagCube driving electronics box.

2.4.1 Magnetic levitation controller algorithm

Achieving stable magnetic levitation necessitates an active control system. The levitation controller algorithm is based on a PID controller. It first measures the vertical position of the CubeSat using the vertical position sensor described in section 2.2.2. This value is compared to the desired position of the object, which is defined by the user. An error signal, $E(t)$, is generated by subtracting the current position and the desired position. The error signal is then multiplied

by a user defined constant *P*. Next, the integral of the error signal is multiplied by a user defined constant *I*. Finally the error signal is differentiated and multiplied by a constant D. The user defined constants used in these operations stand for Proportional, Integral and Derivative (PID) respectively. The three different operations are combined into a manipulation signal, M(t), that controls a linear amplifier which directly controls the amount of current flowing through the electromagnet. The purpose of these operations and constants is to provide different controlling regimes.

$$M(t) = \boldsymbol{P} \cdot E(t) + \boldsymbol{I} \cdot \int E(t) + \boldsymbol{D} \cdot \frac{d(E(t))}{dt} \qquad \textbf{Eq. 2.5}$$

The *P* constant deals with the instantaneous error in position. If the satellite is lower than expected this part of the controller will boost the current of the electromagnet to some value that is proportional to the error in position. Similarly, if the satellite is higher than expected the current will decrease proportional to the error. The *I* constant, along with the integral of the error, attempt to reduce steady error over time. If the satellite has been lower than expected for a period of time, the integral of the error will start increasing in value, therefore the current of the electromagnet will be increased slightly until the steady error disappears altogether. Finally the *D* constant and the derivative of the error attempts to reduce oscillations in the system. If the satellite is changing position very rapidly with respect to time, such as in an oscillation movement, the derivative term will dominate over the other terms and will modify the current on the electromagnet accordingly.

Magnetic levitation is intrinsically a nonlinear control problem. The force that the electromagnet induces on the levitated object is inversely proportional to the square of the separation distance. The farther the object, the harder it is for the electromagnet to influence it. The particular application of the MagCube allows for a linearization of the problem around the set point. Since the CubeSat will levitate at a constant set point the non-linear problem becomes linear in a very short range of distances away from the set point. Linearizing the problem allows the simplification of the control algorithm to a standard PID. The main PID algorithm and rest of housekeeping code of the levitation controller is handled by an Atmel AT328P microcontroller connected to a 16-bit ADC and DAC. The controller loop runs at 20 kilohertz.

2.5 Power processing unit

In order to fire the thrusters in the MagCube, a completely self-contained electronic system is necessary. The electronic system must provide electrical power, computing capabilities, radio communications and a power processing unit to generate the high voltage necessary to drive the thrusters. The following sections describe the design and performance of a custom designed PPU, specific for iEPS thrusters. A block diagram of the complete electronic system is shown below:

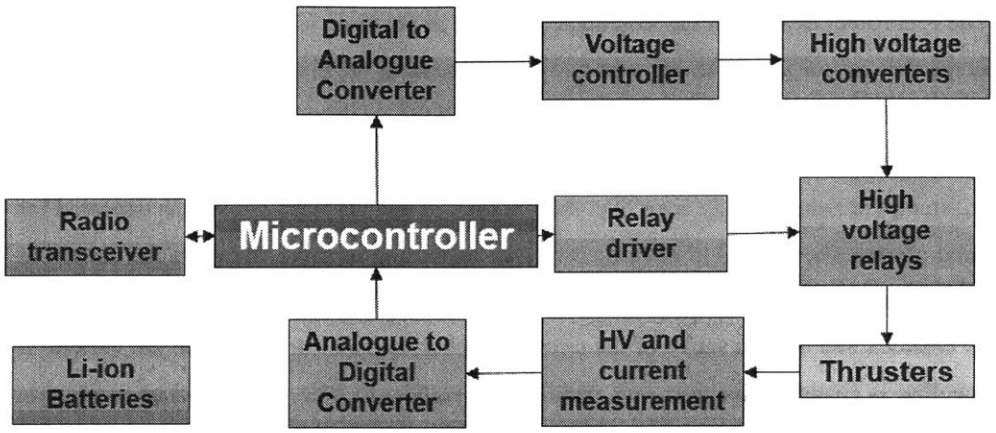

Fig. 2.37 PPU block diagram

The microcontroller is the brains of the whole system, in this case an AT328P. Housekeeping circuits provide it with high voltage monitor and current monitor signals. Resistive voltage dividers are used to measure the high voltage output of the high voltage converters. Optocouplers are used to measure the high side current that the thrusters consume. This information is used by the microcontroller to set the voltage of the high voltage converters, based on an internal, user-defined, voltage or current controller setpoint. An Xbee radio is used to communicate the housekeeping data the microcontroller gathers to an external PC. In the architecture depicted in Fig. 2.37, only a single magnitude of high voltage is available to the thrusters. This implies that if multiple thrusters need to be fired, all of them will have an identical voltage across their terminals. This is acceptable for thrust characterization experiments. For attitude control experiments a different voltage/current setpoints are required for separate thruster pairs. For this reason, two completely independent PPUs are mounted on the levitated CubeSat. Each PPU controls a specific set of thrusters, mounted in such a way that the pair of thrusters driven by PPU1 can produce a positive torque and the ones driven by PPU2

produce a negative torque. In this way, fast response times can be achieved on both directions with different thrust profiles (see section 5 for more details).

2.5.1 Thruster requirements

The electrospray thrusters for which the PPU was designed fire at voltage levels of around 700 to 1000V. Each thruster nominally consumes 150 μA [11]. The thrusters operate on a bipolar voltage source that must alternate the polarity at a low frequency. The purpose of the voltage alternation is to avoid electrochemistry effects on the thruster substrate which might degrade their performance [51]. If a thruster was fired continuously in a single polarity, excess charge accumulated on the propellant tank would surpass the electrochemical potential of the liquid and start corroding the metallic contacts in the tank. The alternation frequency depends on the capacitance of the thrusters inner electrode and the current being emitted. In theory, the thrusters could be switched with a firing period of 100's of milliseconds. For all practical purposes the alternation frequency employed in the SIEPS ranges from a few seconds to a few minutes if highly porous electrodes are used.

As explained section 1.2.6, in order to avoid spacecraft charging a thruster pair must emit the same amount of negative and positive current, to balance charging. The use of an isolated series connection, emitter-extractors-emitter, ensures the same amount of current travels through both thrusters. An important requirement following this connection setup is the galvanic isolation (preventing current flow) between the high voltage (HV) ground and the low voltage (LV) ground, Fig. 2.38. The galvanic isolation is achieved by means of a capacitor. The high voltage supply ground must be able to float with respect to low voltage ground in order to ensure the series connection between thrusters. This small detail has important consequences for the electric design of the PPU. More details about the floating PPU concept can be found in section 4.

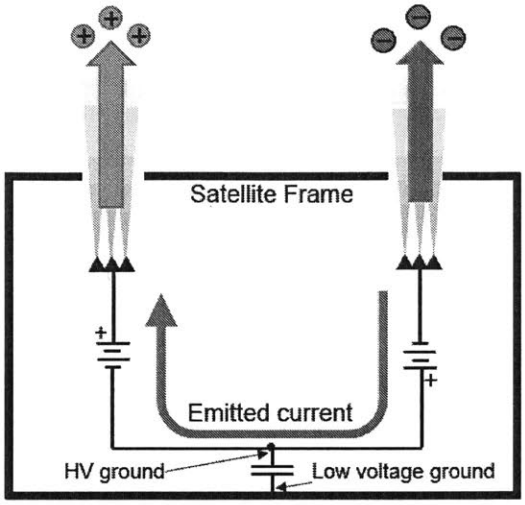

Fig. 2.38 Floating power supply concept. In an ideal case both thrusters emit the same amount of current, but of opposite polarities.

2.5.2 High voltage generation

In order to boost the relatively low voltage, < 12V, provided by the satellite to values high enough for emission, ~1kV, the PPU employs a set of high voltage converters. Several circuits can accomplish this goal. A simple transformer followed by a rectifier circuit could fulfill this requirement. More advanced options include the use of a Cockcroft–Walton multiplier, which use a series of diodes and capacitors to generate high voltages. Efficiency of these converters is important since satellites rely on solar panels for power generation and their power generation is limited.

For the final PPU design used in the MagCube a pair of PICO1500AV COTS high voltage converters are used. Designing a custom high voltage converter was outside the scope of this project. These models are able to generate up to ±1.5 kV at 600μA with ~80% efficiencies. The modules provide galvanic isolation between the low and high voltage grounds, which meets the requirement mentioned in the previous section. Using a positive and a negative module allows to generate a total differential voltage of around 3000 volts, sufficient to drive a pair thrusters.

2.5.3 High voltage switching

Traditional components used to switch high voltage are either solid-state semiconductor devices or high voltage relays. High voltage transistors have leakage currents of tens of μA reaching hundreds of μA at higher temperatures. The leakage current is comparable to the

current consumed by the thrusters therefore their use will decrease the efficiency of the PPU significantly. The other alternative is the use of high voltage relays. A compact form factor is desired and therefore reed relays dominate the available options such as the SLR405SD from Cynergy. These relays are single pole single throw (SPST) and have dimensions of 29 x 14 x 10mm. They are capable of switching up to 3kV. These relays have been tested on previous PPU designs successfully. Depending of the number of thruster channels a significant number of these relays might be needed on the PPU. Their relatively large footprint makes for a bulky design.

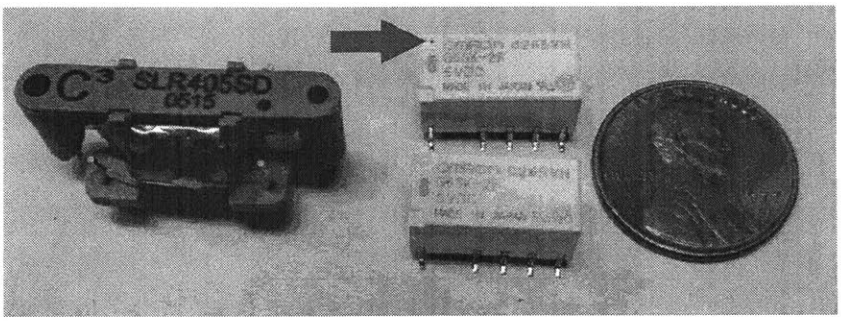

Fig. 2.39 Comparison of high voltage relays. Reed relay on the left. Two telecom relays on the middle. The blue arrow points to the orifice purposely introduced to the relay to evacuate gases.

A smaller footprint solution for high voltage switching can be achieved by exploiting the vacuum environment. One can benefit from the excellent insulating properties of vacuum to switch high voltage between closely placed contacts which might otherwise arc in air. A sealed OMROM G6SK relay is used for this purpose. The relay originally comes in a sealed environment which protects its contacts from the environment. The seal is purposely broken by making a small hole in the relay body, blue arrow in Fig. 2.39. The air inside the relay vents through this hole under vacuum conditions, allowing a much higher voltage to be switched. These relays are 1/3 the size of a traditional high voltage rated relay, such as the Cynergy relay, allowing a significant reduction of PPU size. They are also Double-Pole-Double-Throw (DPDT) instead of the regular Single-Pole-Single-Throw (SPST), which allows to use less relays to provide the same functionality. Finally these modified relays have a much stronger actuation force and therefore are less prone to contact soldering, a problem which traditional high voltage reed relays suffer from.

An H-bridge configuration is used to provide polarity alternation, the relays used for this purpose are shown around a dashed box in Fig. 2.40. Individual relays are used to provide

thruster channel selectivity represented by simple switches in Fig. 2.40. Thrusters are represented by solid boxes with an emitter connection, *Em,* and an extractor connection, *Ext.*

In the specific relay state of Fig. 2.40, the positive high voltage flows through the upper left relay to then reach the emitter connection of thruster A1. The negative high voltage flows through the lower-right relays to reach thruster B1. This scheme allows any number of *A* thrusters to be paired with any number of *B* thrusters, which maximizes the thruster configurations available.

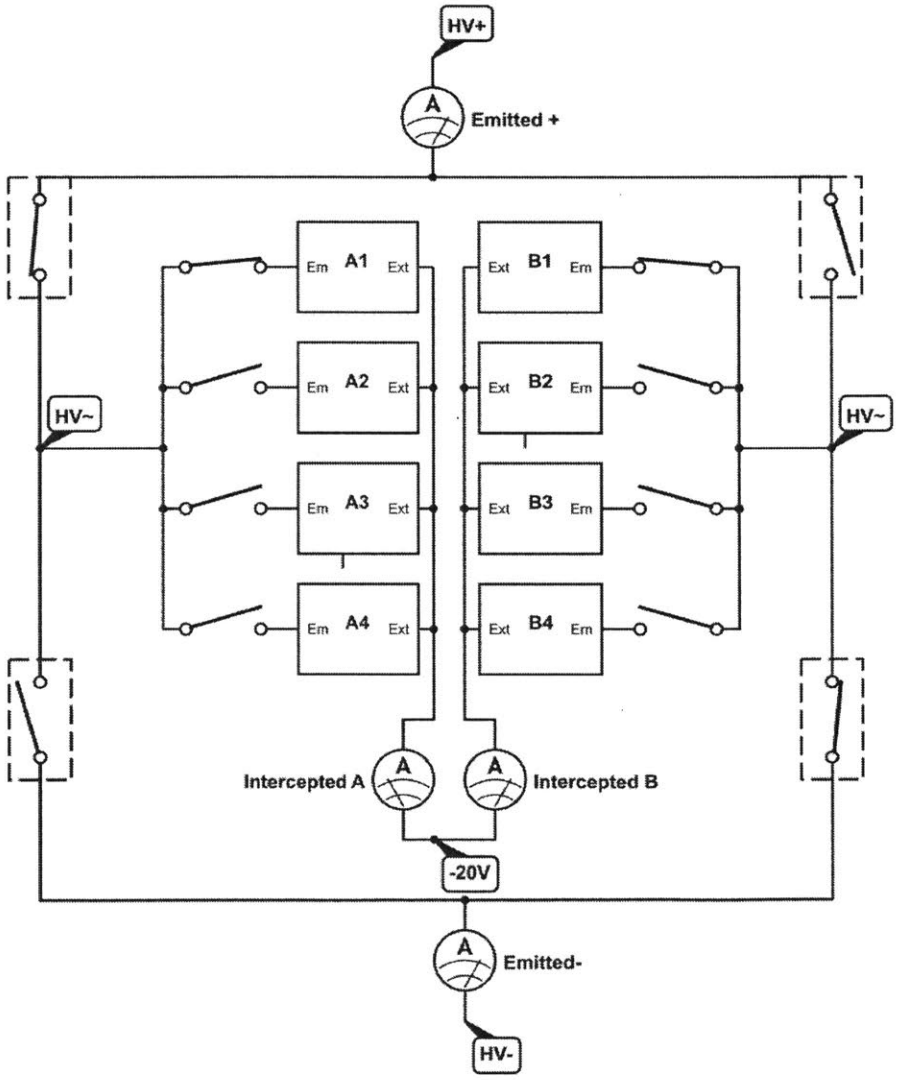

Fig. 2.40 Architecture of the PPU.

2.5.4 Housekeeping circuitry

Thrust generated by electrospray thrusters is proportional to the emitted current. Measuring the current being delivered to the thrusters is then key to control thrust, if we can adjust the voltage to sustain a fixed emitted current then the thrust of the devices will be constant. An ideal PPU design will include a current controller which measures the current being consumed by the thrusters and then varies the high voltage in order to maintain a constant current.

There are two schemes that allow measurement of the current delivered to the thrusters, measuring in the low voltage side or in the high voltage side of the high voltage converters. By measuring in the low voltage side, current being consumed by the high voltage converter can be translated into the current being sourced at the high voltage side. Usually the current input to the high voltage converter will be measured using a low value shunt resistor. There is a non-linear relationship that equates the input current with the output current of the converter, which depends on the high side load and efficiency of the converter. This approach is difficult to implement since the high voltage load is unknown to begin with. Furthermore, only a single total emitted current can be estimated. Firing multiple thrusters is then problematic as there would be no way to distinguish the current being consumed by each thruster. The benefit of this approach is that since all the measurements are made on the low voltage side, no high voltage isolation components are needed, which reduces the complexity of the design considerably.

Another approach is to measure the current on the high voltage side of the high voltage converter using optocouplers, which is the method followed in this design. The PPU employs the SFH628A bipolar optocoupler. The multiple optocouplers in the PPU design allow to measure positive and negative high side currents as well as the currents collected in the two extractor connections. The optocouplers are represented by Ammeter in the schematic in Fig. 2.40. The four optocouplers provide a wealth of information on the thruster operation and allows for a more intelligent PPU. Additional optocouplers could be added to each thruster channel in order to monitor each thruster current independently. This would be very useful when a large number of thruster channels are fired simultaneously.

The optocouplers are not perfect sensors, each individual component has a different gain which is affected considerably by temperature. The PPU uses a calibration channel, a thruster channel that has a known precision resistor instead of a thruster, to calibrate the optocouplers.

To calibrate the optocouplers, the relays of the calibration channel are engaged and a known voltage is applied. Since the resistance of the calibration channel is known, the current can then be calculated using Ohm's law. This approach can then be used to calibrate all the optocouplers in the PPU. Temperature effects could also be incorporated by a more thorough analysis. This was not pursued in this work.

2.5.5 High voltage ground selectivity

As mentioned in section 2.5.1, a galvanic isolation between the high voltage supply ground and the low voltage satellite ground is needed in order to ensure identical emitted currents from a thruster pair operating in bipolar mode. In some cases it is beneficial to have the option of removing, or shorting, this galvanic isolation. For example, when a thruster is first fired it requires a significantly higher voltage than normal in order for it to start emitting [11]. Several short-circuit-like transients can occur while the thruster is being conditioned [11]. As it will be later discussed in section 4.1.2, these sporadic transients could result in the high voltage portion of the PPU floating to very high potentials with respect to the satellite ground. If the high voltage portion of the PPU floats higher than a certain potential it could cause permanent malfunctions in the HV converters or failure in other components.

By shorting the galvanic isolation of the HV ground and LV ground the thrusters are no longer in a series connection and the HV ground cannot float anymore, eliminating possible failures of the PPU. Breaking the galvanic isolation also simplifies thruster firing since only a single voltage converter needs to be activated to condition a specific thruster. It is clear that if only one thruster is operated the satellite would charge. Since the conditioning sequence lasts only a couple of minutes this is an acceptable situation. The detrimental effects of spacecraft charging explained in later sections can be tolerated for short spans of time. Once all thrusters are conditioned one could reestablish the galvanic isolation to ensure identical emitted currents in the bipolar configuration. The galvanic isolation selection is accomplished with the same type of relay used for thruster selectivity and polarity alternation. The relay is able to short the capacitor used for the galvanic isolation when needed. Opening the relay reestablishes the galvanic isolation.

2.5.6 Performance and construction

The PPU design went through several iterations to land on a final design with the characteristics described above. The boards were designed using mainly through-hole

components and sockets. Although larger than surface mount components, through-hole components facilitate replacement of failed component which is common while initially debugging the HV system. They also reduce the cost of development since no automatized assembly is required, manual soldering can be used to assemble the boards.

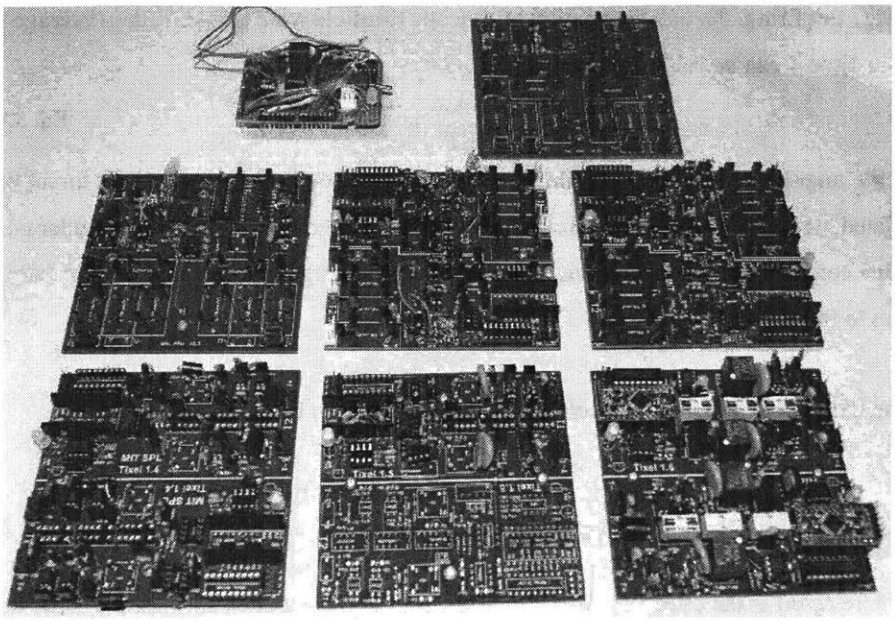

Fig. 2.41 Iterations of PPU design.

The final PPU design is composed of two stand-alone PPUs in a single board. The PPUs are able to drive 2 thruster pairs independently, useful for attitude control experiments. The PPUs maximum voltage is ±1500V and each can supply up to 600μA of current. The housekeeping information supplied by circuitry in the PPU proved invaluable on MagCube experiments. Operation characteristics and experiments made with the PPU can be found in sections 4.5 and 5.3.

3 Thrust characterization

Simple physics are needed to directly measure thrust in the MagCube. By knowing the moment of inertia of the levitated structure, I, the thruster lever arm, L, change in angular velocity after firing, $\Delta\omega$ and the amount of time the thrusters were active, T, then average thrust over the time T can be calculated as follows:

$$F = \frac{I\,\Delta\omega}{L\,T} = \frac{I\alpha}{L} \qquad \textbf{Eq. 3.1}$$

If the angular acceleration profile over time, α, is known, then continuous thrust can be calculated. It is challenging to obtain a clean angular acceleration profile from angular position data that contains a non-zero amount of noise. Differentiating twice greatly amplifies any noise present in the signal.

The theoretical thrust of an electrospray thruster is given by [52]:

$$\bar{F} = I_{thr}\sqrt{\frac{2\,V_{Th}}{(q/m)}} \qquad \textbf{Eq. 3.2}$$

Where (q/m) is the effective charge to mass ratio of the expelled species, V_{th} is the thruster voltage, and I_{thr} is the thrust current. The thrust of electrospray devices is proportional to the thruster current and varies with the square root of the applied voltage. Various factors can be applied to this equation to account for inefficiencies and other processes [53], but it serves as a good first order thrust estimation.

3.1 Counteracting horizontal magnetic fields

As explained in section 2.1.2, a pair of orthogonal Helmholtz coils are used to counteract the unwanted external horizontal magnetic field in the levitation region. This reduces the perturbation torque induced by the levitation scheme. The angle and magnitude of this unwanted horizontal magnetic field are quantities difficult to estimate. In order to find the specific values for the magnitude and angle that the Helmholtz coils need to generate to cancel it, angle and magnitude sweeps are performed. A plot of a typical angular sweep and its effects on the levitated structure oscillations can be seen in Fig. 3.1. Once the CubeSat is levitating, a magnitude is "guessed" and applied to the Helmholtz coils. The magnetic field angle is then slowly varied, sweeping from 0 to 360 degrees. At some specific angle, minute 450 in Fig. 3.1, the period of the oscillations increases significantly and an abrupt change in the equilibrium

point in the oscillations is seen. These abrupt changes indicate a change in the potential wells caused by the restoring torque. The angle is then fixed at this specific value and the magnitude of the magnetic field is swept from zero to some arbitrary value. Whatever value of amplitude produces the longest period is chosen as the specific magnitude. After these sweeps a combination of angle and magnitude is found such that the magnetic restoring torque on the CubeSat is minimum.

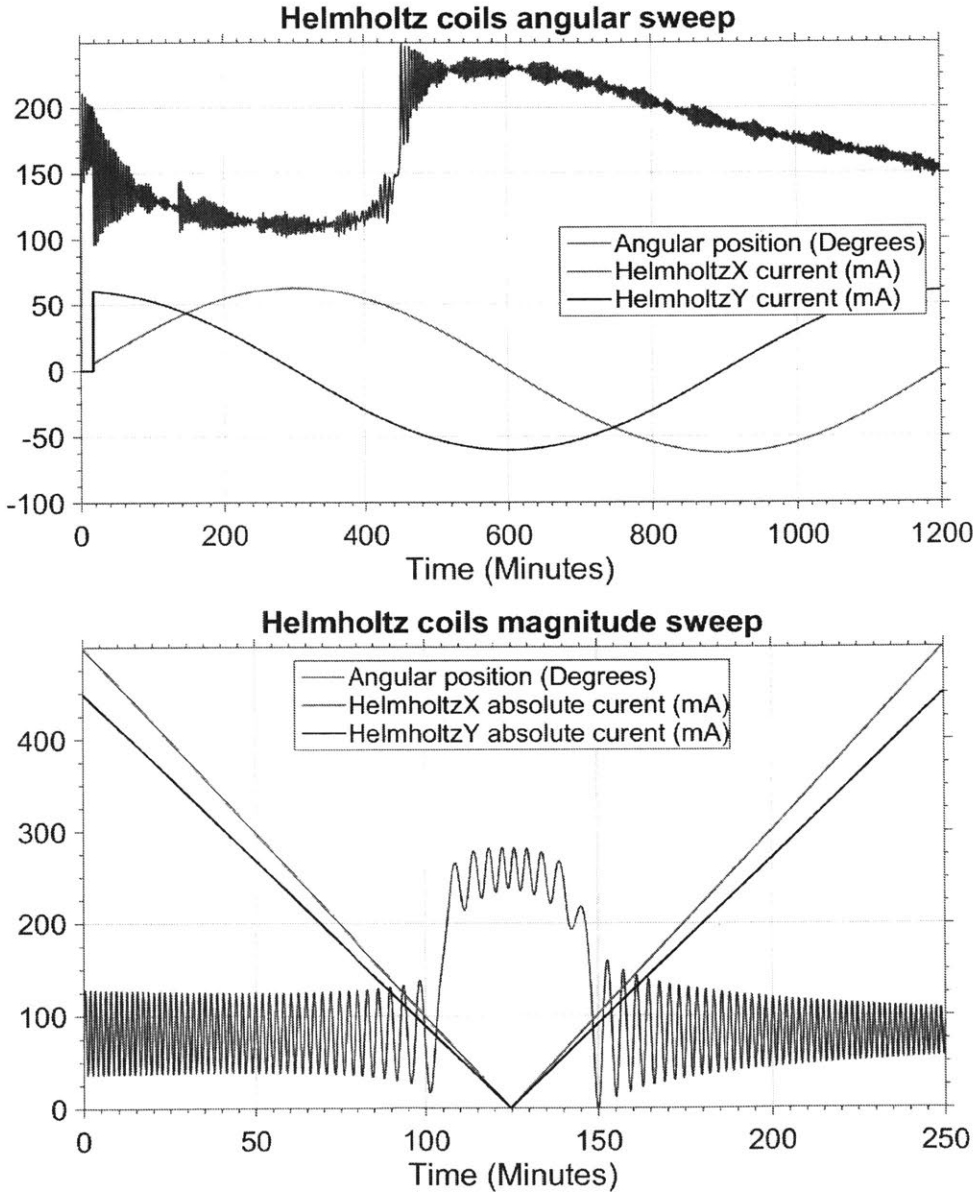

Fig. 3.1 Impact of Helmholtz angle and magnitude on oscillation profile.

Clearly, the Helmholtz coils have a dramatic effect on the oscillation profile. The point where the CubeSat oscillates about follows the Helmholtz magnetic field angle until it reaches a specific point at minute 450. The period is also seen to increase around this specific angle, meaning the restoring torque is at is minimum. In ideal tests, the Helmholtz coils were able to increase the oscillation period 5 fold, implying a 25 reduction on the restoring torque. This is an important result, since it enables low-thrust measurements.

3.1.1 Impact of restoring torque on thrust measurements

In order to calculate the impact of the restoring torque on thrust measurements, a transformation of torque to thrust must be made. Assuming the thruster lever arm is known, the restoring torque constant can be transformed into an equivalent thrust constant, with units of Newtons per degree. In typical tests the moment of inertia of the levitated structure was measured to be 0.005 $kg \cdot m^2$. The oscillation period, once the Helmholtz are calibrated to the specific angle and magnitude, reached values close to 15 minutes. Using Eq. 2.1 and a thruster lever arm of 5 centimeters, the equivalent restoring thrust constant estimate is 0.044 μN per degree. This constant should only be used to gauge the magnitude of the perturbing torque, in reality it's not constant over the angular position of the levitated structure.

The oscillation profile of the levitated structure differs from an ideal harmonic oscillator for large oscillation amplitudes, similar to the deviation of an ideal pendulum for large angles. The addition of non-uniformities in the horizontal magnetic field complicates the calculation of a continuous thrust restoring function even further. The cumulative effects imply that the equivalent thrust constant is not really constant for all angular positions. A similar non-harmonic oscillatory effect in levitated magnets is described in [54].

The magnetic levitation environment along with high vacuum conditions produce negligible rotational friction to the levitated structure. Once spinning, the levitated structure will keep doing so for hours without losing significant angular velocity. Fig. 3.2 is a plot depicting the undisturbed angular position of the levitated structure along with its angular speed over 10 hours under high vacuum conditions (5 x 10^{-7} Torr). Note the different scale for the angular position units. The levitated structure's angular velocity was reduced by the negligible, but ever present friction, from 4 to 1.25 degrees per second after 10 hours. During this timeframe, the levitated structure performed close to 250 full rotations.

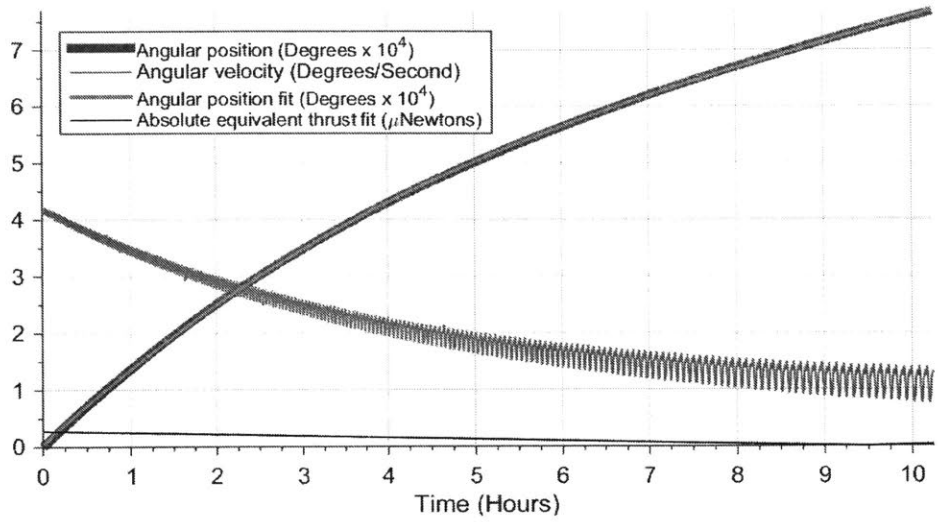

Fig. 3.2 Levitated structure angular position and speed over 10 hours, under high vacuum conditions

It is important to notice the superimposed oscillating behavior of the decaying angular velocity. The oscillations on the angular velocity are caused by the small restoring torque still present in the system, even with the Helmholtz coils activated. The levitated structure speeds up and slows down every full rotation making a repetitive effect. Further adjustments to the Helmholtz coils could help reduce this restoring torque. As the levitated structure slows down, the effects of the restoring torque constant become more apparent. The calculated damping coefficient for this particular test is 4×10^{-5} s^{-1}.

By fitting a cubic polynomial to the angular position profile and differentiating twice, we obtain a linear angular acceleration representative for the test. By assuming a moment of inertia and thruster lever arm, we can transform the angular acceleration into a torque, and then into an equivalent thrust. The equivalent thrust would represent the effect of the damping in thrust measurements. Any thrust levels below the equivalent thrust will be obscured by the damping effect of friction. For a levitated structure moment of inertia of 0.005273 $kg \cdot m^2$ and a thruster lever arm of 5 centimeters the equivalent thrust caused by damping is not higher than 0.3 μN.

3.2 Thrust measurement methodology

To perform a thrust measurement in the MagCube, the following procedure was followed. The testbed is placed under vacuum conditions and the CubeSat is levitated, the Helmholtz

coils are activated at the specific angle and amplitude. Any rotational movement is eliminated using the electromagnetic damper. Once the levitated structure is immobile, the electromagnetic damper is disabled and the thrusters are fired. After some arbitrary time, the CubeSat gains some angular speed and the thrusters are turned off. Thrust is then simply calculated by using Eq. 3.1.

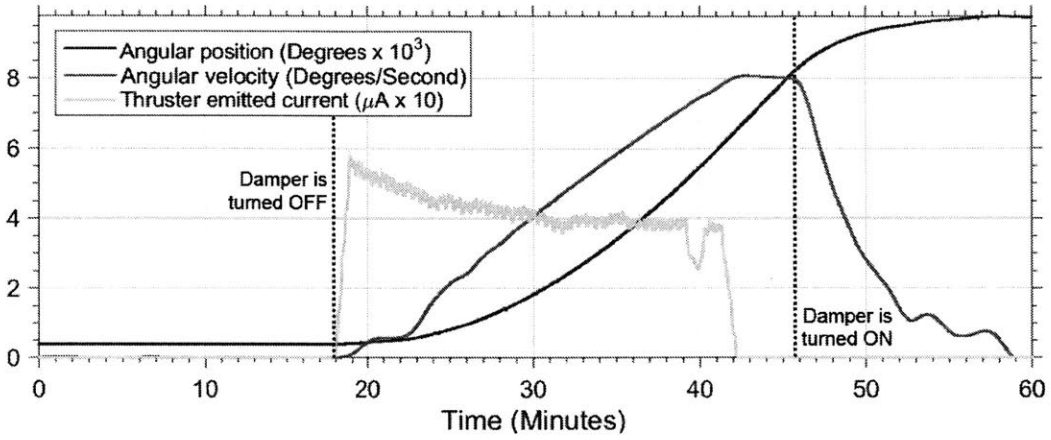

Fig. 3.3 Representative thrust measurement sequence

The plot above depicts a representative thrust measurement test. Notice the different scales for the angular position and emitted current. The angular speed profile was obtained by numerically differentiating the angular position data. A moving average filter was used to smooth the resulting derivative. Further derivation to extract angular acceleration without artifacts from the data proved very challenging.

At the beginning of the test, the electromagnetic brake is activated to reduce any rotational speed the levitated CubeSat may have. Once the levitated structure is rotationally immobile, the electromagnetic damper is disabled and the thrusters are fired, minute 18. As the thrusters exert a torque on the levitated structure, the angular velocity starts to increase. The thrusters are then turned off, minute 42, at this time the levitated structure stops accelerating and the angular speed remains constant. After some time coasting with a constant angular velocity, the electromagnetic brake is activated to slow the CubeSat down, minute 46. The CubeSat performed about 25 full rotations while the thrusters were active. The data required to perform a thrust estimate for this test is the firing time, 21.1 minutes, and the change in angular velocity, 8.2 °/s. The change in angular velocity was calculated manually, measuring the speed before and after the thrusters were fired. The inertia of the levitated structure was 0.005273 kg·m^2 and

the lever arm was 8.55 cm. Two thrusters were fired simultaneously in the bipolar configuration. The final average thrust estimate for this specific test is 6.9 μN of total thrust.

If we assume constant thrust through the firing time (a lousy assumption since the emitted current was not constant), we can then adjust a quadratic fit into the angular position profile. The polynomial fit starts at the point in time when the thrusters start firing and ends when the thrusters are commanded to stop. Differentiating the polynomial fit is straightforward and will result in a linear angular velocity profile. Differentiating once more will result in a constant angular acceleration value. The angular acceleration can then be transformed into torque by knowing the moment of inertia of the levitated structure. Torque is then transformed into thrust by knowing the lever arm of the thrusters. The quadratic fit procedure is shown below:

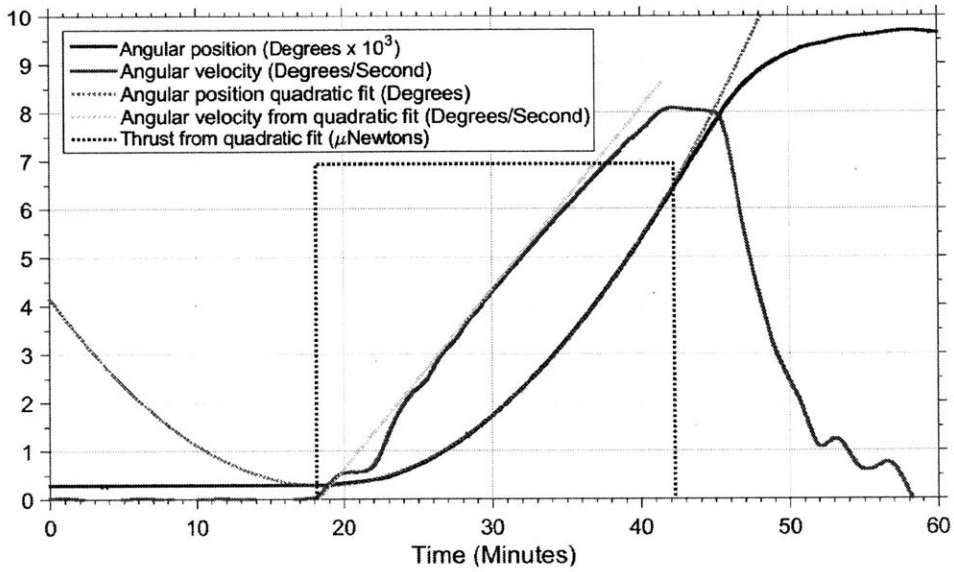

Fig. 3.4 Quadratic fit on angular position to find thrust.

Since the quadratic fit assumes a constant thrust, any real thrust transients disappear from the estimates. The angular velocity depicted by the red line on the plot above, is the numerical derivative of the raw angular position data which agrees with the fitted angular velocity profile in green. The final average thrust estimate using this approach is very similar than the one before, 6.87 μN of total thrust.

3.3 Continuous thrust

Besides average thrust, one can attempt to retrieve the continuous thrust profile from a firing sequence. Below is a long duration test in which the continuous thrust profile was estimated by differentiating twice the angular position signal in post-process. Significant smoothing of the angular data was done to reduce the double differentiation error. The thrusters are initially fired when the CubeSat is immobile.

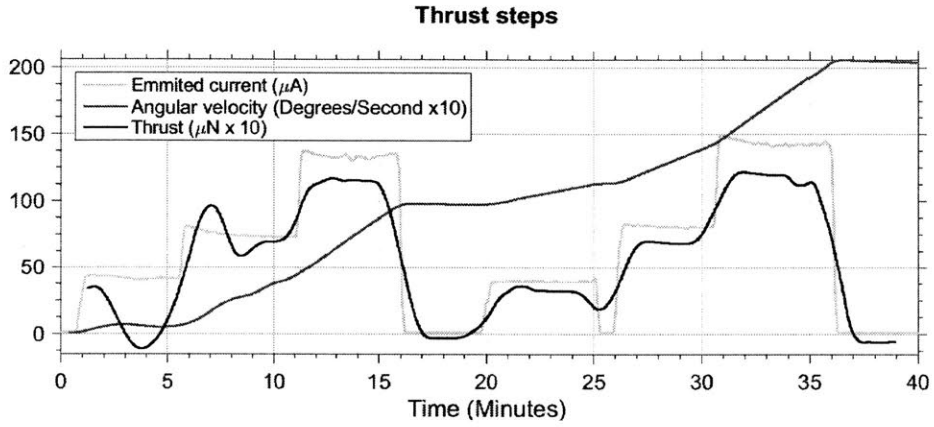

Fig. 3.5 Resolving thrust steps

Notice the different scales of thrust and angular velocity, used to aid in the visualization of the data. The thrust estimates at the beginning of the test present more artifacts due to the satellite being almost immobile, when the restoring torque is most powerful. After minute 10, once the satellite has gained around 5 °/s of rotational speed, thrust estimates become cleaner since the restoring torque has less effects at higher angular speeds. The effects of the restoring torque on thrust measurements are visibly diminished at higher rotational speeds. The lag, or slow response of the thrust estimate can be attributed to the smoothing filter applied to the angular data. It reduces noise but introduces lag.

3.4 Error propagation

The basis of thrust measurements in the MagCube that were followed in this work rely on Eq. 3.1. To calculate the uncertainty in the thrust measurement, δF,we proceed with the standard error propagating formula:

$$\delta F = F\sqrt{\left(\frac{\delta I}{I}\right)^2 + \left(\frac{\delta L}{L}\right)^2 + \left(\frac{\delta \alpha}{\alpha}\right)^2} \qquad \textbf{Eq. 3.3}$$

The fractional uncertainty of the moment of inertia is estimated in section 2.2.9. The estimated uncertainty of the lever arm, L, is dependent on the precision of the parts used in the CubeSat construction and the exact position of the thrusters. An estimate for the uncertainty of this variable is 1 mm. The uncertainty in the angular acceleration measurement is more complicated to obtain. In traditional torsional balances, a calibration force acting at some distance from the fulcrum, a torque, is used to calibrate the instrument [32]. In the MagCube a calibration torque could be used in the same way, the difficulty relies on delivering this precise and known torque to the levitating satellite. Although the Helmholtz coils could impart a torque to the CubeSat its characterization is challenging to say the least.

The angular acceleration estimate is produced by the angular encoder measurement. As explained in section 2.2.7, the sensor has noise which is difficult to characterize while the CubeSat is levitating. The angular reading is further affected by the magnetic perturbations. A shown in Fig. 3.2, the magnetic perturbations impose a repetitive pattern on top of an otherwise linear position profile (ignoring friction dampening). The imposed pattern and the sensor noise prove challenging to separate from each other, further complicating uncertainty estimations. For these reasons, a separate approach was taken to characterize the angular acceleration uncertainty.

The approach followed relies on the thrusters mounted on the CubeSat to impart a constant torque on the satellite. In other words, the thrusters are used as constant torque actuators, a calibration technique used in traditional torsional balances [32]. This procedure assumes that at constant current, the thrusters produce a constant thrust, a valid assumption according to Eq. 3.2. The thruster is fired with a constant current using a current controller algorithm in the PPU. The uncertainty analysis consists of firing a pair of thrusters for a 5 minute period, multiple times, and at different current levels. The angular acceleration of each firing is measured. Each current level had 5-7 different trials, Fig. 3.6

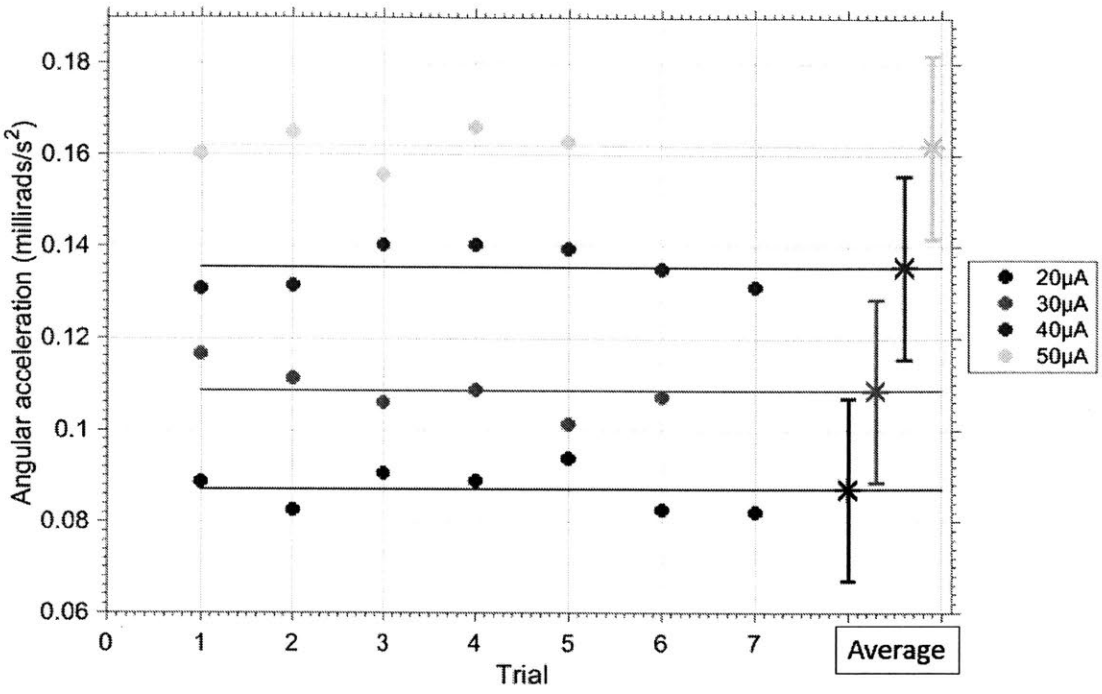

Fig. 3.6 Angular acceleration measurements for trials at different current levels. Horizontal line is the mean. Star markers correspond to the mean value. Error bars are the final characteristic angular uncertainty (3σ).

According to Eq. 3.2 thrust goes as the square root of the applied voltage. Therefore, it is beneficial to maintain a similar voltage through all trials while ensuring current is constant for each trial at a specific current level. The current and voltage relation of an electrospray thruster is dependent, among other factors, on the available propellant in the emitter substrate. Once propellant starts to be depleted on the tips, a higher voltage is required to extract the same amount of current. Currently, thrusters equipped with large propellant reservoirs or tanks experience propellant depletion only after hundreds of hours firing at nominal currents [11]. The thrusters used for this analysis did not possess a propellant reservoir. Therefore, the firing time before propellant depletion occurred was limited to tens of minutes. For this reason, the number of trials is relatively low, 5 to 7. This number of trials enables the thrusters to fire with a relatively constant voltage through each current level.

To estimate the uncertainty on the angular acceleration, the data is assumed to be normally distributed. Due to the low number of trials a confidence interval must be used to obtain statistical parameters from the data. A 90% confidence interval is used to calculate the

population standard deviation under the normality assumption. The confidence intervals are given by:

$$\frac{(n-1)\sigma^2}{\chi_{\alpha-0.1}}, \frac{(n-1)\sigma^2}{\chi_{\alpha-0.9}} \quad \textbf{Eq. 3.4}$$

Where n is the number of samples and σ is the standard deviation. $\chi_{\alpha-0.1}$ and $\chi_{\alpha-0.9}$ are the parameters of the Chi-distribution. The confidence intervals state with 90% confidence that the variance of the population, σ^2, is within the calculated intervals. Intervals must be used due to the low number of samples and the normality assumption. The upper bound of this variance, is then used as the population variance for that emitted current level. With the population variance estimated, the population standard deviation is calculated. A 3-σ range is used to provide the final fractional uncertainty for each current level. The 3-σ range ensures that 99.7% of the samples fall under the predicted distribution. Using the 3-σ range, we then calculate the maximum fractional uncertainty, which is obtained by dividing the 3-σ range by the mean. The maximum fraction uncertainty can be described as the maximum error expected in the angular measurement for each trial, assuming a 90% confidence interval and that 99.7% of the samples fall in the distribution. The relevant data, for each current level, used in this analysis is shown below:

Table 3.1 Uncertainty analysis variables.

Parameter	20μA	30μA	40μA	50μA
Sample mean (millirads/s^2)	0.086	0.108	0.135	0.162
Population variance (millirads/s^2)^2	4.55x10^{-5}	5.05x10^{-5}	4.18x10^{-5}	4.05 x10^{-5}
Upper 3-σ range (millirads/s^2)	0.0202	0.0213	0.0194	0.0190
Maximum fractional uncertainty	23.3%	20.1%	14.3%	11.8%

For higher emitted currents, the fractional uncertainty is reduced. This can be attributed to the satellite gaining more speed in the 5 minute interval as a larger thrust is being produced. The dependence of the angular acceleration measurement uncertainty on rotational speed implies that MagCube benefits from long firing times and higher levels of thrust. To simplify the error analysis, the different 3-σ error ranges for each emitted current level are averaged to obtain a characteristic uncertainty of the angular acceleration, **±0.02 millirads/s^2**. This is the uncertainty used to plot the error bars in Fig. 3.6. The 3-σ range ensures 99.7 of the data is within the uncertainty stated.

The overall angular acceleration uncertainty, along with the uncertainties in inertia and lever arm measurements, can now be used to estimate the final uncertainty in thrust measurements. The table below summarizes all uncertainties pertinent to thrust estimation along with the final uncertainty in the thrust measurement as calculated by Eq. 3.3:

Table 3.2. Thrust measurement uncertainty calculation

Parameter	3σ-error, δx	Nominal value, x	Units	Fractional uncertainty, $\frac{\delta x}{x}$
I	3.01×10^{-5}	0.005273	kg m^2	0.57 %
L	0.001	0.15	m	0.66 %
α_{avg}	0.2×10^{-3}	-	rads/sec^2	-
F	**0.35**	**-**	**μN**	**-**

The final uncertainty in the thrust measurement is then calculated to be **±0.35 μN** (3σ). This uncertainty is typical of torsional balances[35] although uncertainties as low as 0.03 μN have been reported [32]. Improvements could be made on the angular acceleration measurement or in the reduction of magnetic perturbations (as they affect the angular acceleration measurement) to reduce thrust uncertainty even further.

There is a specific type of thrust measurement that has been traditionally more complicated for torsional balances to implement, thrust impulses [35]. Usually, in torsional balances designed to measure thrust impulses, an impulse is applied and the corresponding oscillatory response is analyzed to extract the impulse measurement. As with any other type of force testbed, calibration is achieved by applying known impulses to the instrument which is not trivial [33]. Thrusters that produce force in pulses, such as Pulsed Plasma Thrusters (PPT) have to be characterized by measuring their thrust impulse.

Pulsed thruster characterization could benefit from the thrust integrating nature of the MagCube. The levitated CubeSat could be equipped with a pulsed thruster which when fired would produce torque impulses. A fixed and possibly large number of thrust pulses could be commanded over a relatively long period of time, each pulse slightly increasing the angular velocity of the levitated structure. The impulse can then be calculated with the change in angular velocity and the number of firings. Thousands of consecutive firings could be made, as long as they can be counted, in order to ensure a large change in velocity and therefore reduce the uncertainty in the impulse measurement. This approach would yield an average impulse for the test.

3.5 Electrospray thrust measurements

Several thrust measurement trials similar to the ones in Fig. 3.3 and Fig. 3.6 were performed, at different emitted current levels. The thrust estimates from the iEPS are shown in Fig. 3.7. The error bars in the estimates are calculated using the thrust uncertainty calculated previously. Thrust shows a linear dependence with emitted current as stated by Eq. 3.2. Separate thrust measurements of iEPS were conducted at NASA Glen Research Center (GRC) [11]. These thrust measurements were performed on a high precision torsional balance. The final error on the GRC thrust estimates is less than 0.26 μN.

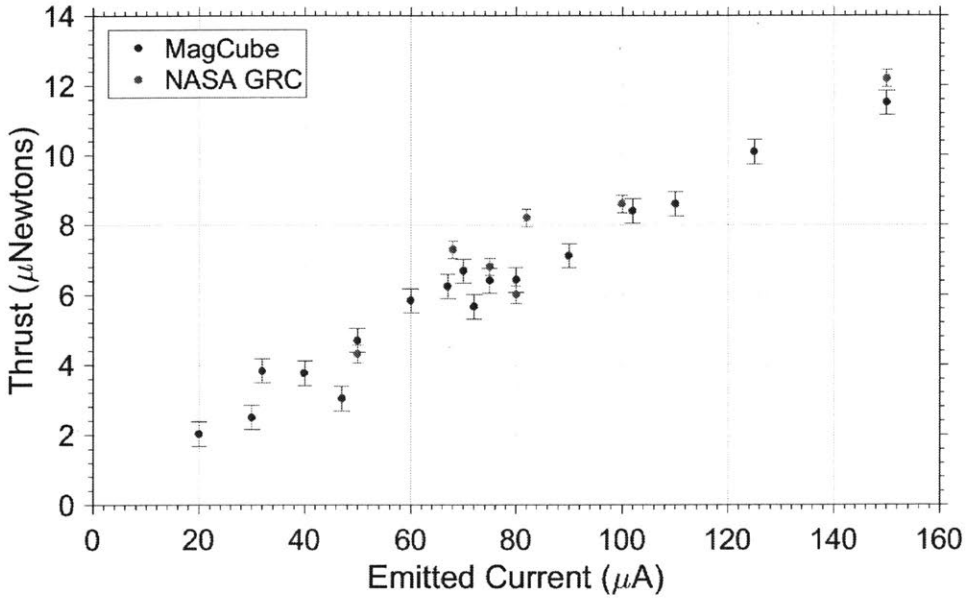

Fig. 3.7 Thrust measurement of electrospray thrusters by different entities.

4 Spacecraft charging and electrosprays

4.1.1 Bipolar operation

The capability of electrospray thrusters to emit either a positive or negative ion beam has an important charge neutralization implication. Electrosprays, in theory, could operate without an external cathode. If two separate thrusters are fired in such a way so that one provides a positive ion beam and the other a identical negative ion beam, then in theory, the spacecraft would not charge, and the thrusters could operate indefinitely. This scheme is referred to as bipolar

operation. The bipolar neutralization scheme is an unexplored area of research. The bipolar mode of operation also raises important questions when compared to traditional cathode-based neutralization, mainly the implications of the difference in the properties between electrons and negatively charged ions. Electrons have high mobility compared to heavy negatively charged ions.

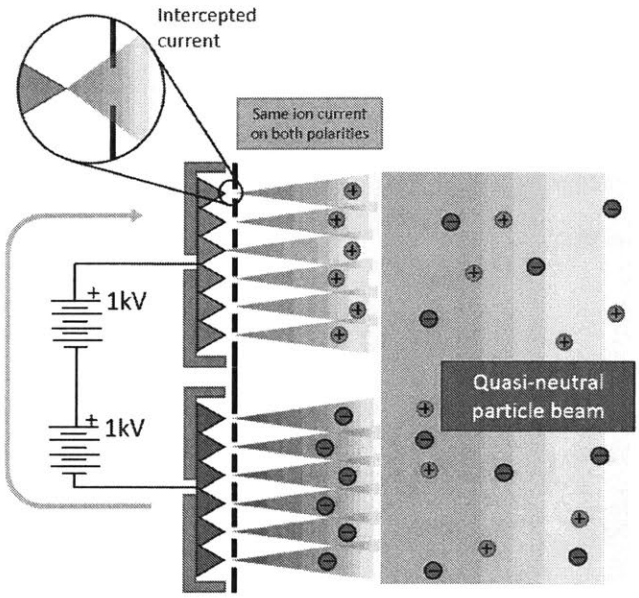

Fig. 4.1 Electrospray thrusters in the bipolar configuration.

A possible arrangement on how to achieve bipolar emission is show in Fig. 4.1. The design relies on a series connection to establish equal currents on both thrusters. Since they are connected in series, the same current must travel through both of them, ensuring a quasi-neutral particle beam composed of the same amount of positive and negative charge. Notice that the extractor grid is not connected to the high voltage power supplies. In an ideal scenario the extractor grid would be electrically connected to the satellite frame, usually electrical ground, and the high voltage power supplies would be galvanically isolated form the satellite ground. In this configuration, the high voltage power supplies would be able to electrically float with respect to the satellite ground. The isolation of the high voltage power supplies will become important in the neutralization scheme as explained in the next sections.

Bipolar operation also utilizes the polarity alternation scheme. Polarity alternation is required to avoid electrochemistry effects in the thruster tips and the propellant management electrode[51]. The alternation frequency is usually slow, ~30 seconds, and implies that a

thruster will emit positive ions for ~30 seconds and then emit negative ions once the power supply switches polarity. The polarity alternation scheme also ensures that all the propellant is available to the thruster.

There are certain processes that should limit the potential that a spacecraft can reach while operating electrospray thrusters in a bipolar configuration. These processes act as self-regulating mechanisms that ensure emission can proceed even with differences in emission profiles between thrusters. These mechanisms are discussed next.

4.1.2 Floating power supply

A key aspect on the PPU design that ensures the emitted currents on both thrusters are identical, is the galvanic isolation between the high voltage return, HV_{Ground}, and the spacecraft ground provided by the C_{HV} capacitor, see Fig. 4.2. This isolation allows the high voltage ground, HV_{ground}, of the PPU to float with respect to the satellite ground.

The current emitted by an electrospray thruster has approximately a quadratic dependence on the applied voltage once a threshold voltage is surpassed. The threshold value is usually referred as the startup voltage. Due to the non-zero divergence of the ion beam, a portion of the emitted current is intercepted by the extractor. This *intercepted current*, is usually <5% of the emitted current [11]. The current vs. voltage (I-V curve) characteristic of a typical iEPS device is shown in Fig. 4.6. Due to manufacturing tolerances no two thrusters are identical, which means that each thruster will emit a slightly different current at a given voltage. In the case that two non-identical thrusters are fired in the bipolar configuration at the same voltage, one of them will emit more current that its counterpart. Additionally, due to manufacturing variability, some tips are sharper and closer to the extractor which reduces the startup voltage for that specific device.

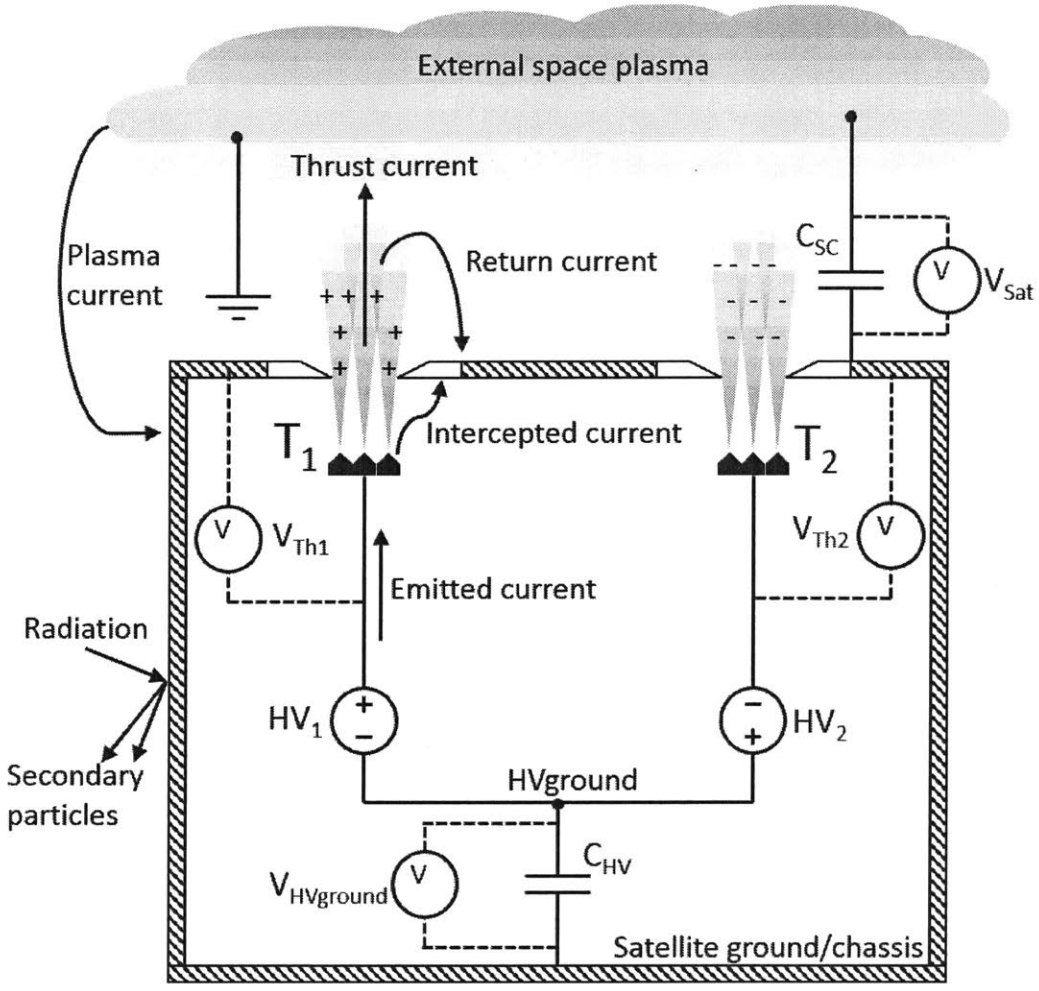

Fig. 4.2 Schematic of a satellite firing electrospray thrusters in the bipolar configuration.

To explain the first self-regulating mechanism, suppose that thruster T_1 in Fig. 4.2 emits slightly more current at a given voltage than thruster T_2. Once emitting, the difference in currents will charge C_{HV} negatively, shifting HV_{Ground} to a negative potential with respect to the satellite ground and therefore the extractors. Assuming the thruster voltage sources, HV_1 and HV_2, are constant, the potential differences between the thruster tips and the extractor, V_{Th1} and V_{Th2}, become more negative. The reduction in potential causes thruster T_1 to emit less positive ions and T_2 to emit more negative ions. This effect tends to balance the emitted currents reaching equilibrium when both positive and negative emitted currents are identical. When the equilibrium is reached, C_{Hv} stops charging and $V_{HVGround}$ is non-zero. Without the galvanic isolation provided by C_{HV}, the emitted currents would not equalize and charging would occur.

Ideally C_{HV} could have a capacitance close to zero, but in reality, a finite capacitance is needed to reduce the amount of noise produced by rapid changes in $V_{HVGround}$, increasing PPU performance. For this reason, a capacitance of 0.1μF to 10nF was used in simulations and experiments.

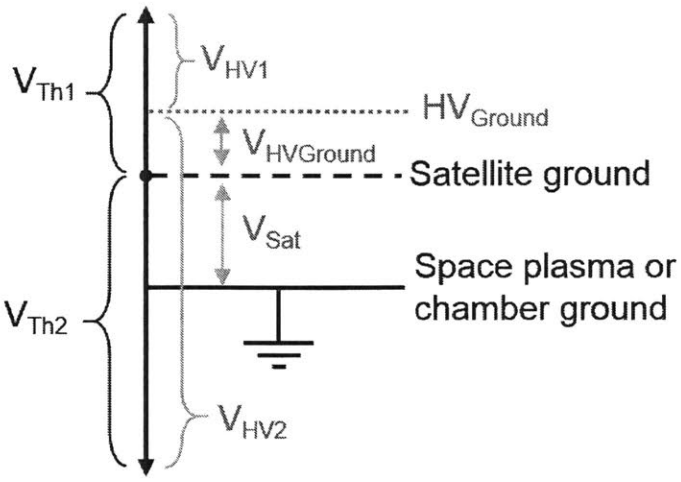

Fig. 4.3 Relevant potentials in the bipolar configuration for two dissimilar thrusters.

In Fig. 4.3, a summary of the different potentials in the bipolar configuration is shown. It is important to notice the distinction between the power supply voltages, V_{HV1} and V_{HV2} and the thruster voltages V_{Th1} and V_{Th2}. If $V_{HVGround}$ is zero, then the thruster voltages would become identical to the power supply voltages.

4.1.3 Effects of ion fragmentation

Besides the floating power supply scheme, there are other methods that limit the charging potential of the satellite when operating dissimilar thrusters. Electrospray thrusters are known to emit not only single ions, but also ions attached to a certain number of neutral pairs [7, 55]. The fraction of solvated ions with respect to single ions, can reach 30% or more in some cases [56, 57]. Some of these solvated ions are known to fragment during and after acceleration.

A dimer (defined as n=1) can separate into a pure ion and a neutral in a fragmentation event. If the fragmentation occurs outside of the thruster, the ion and neutral will travel at the same velocity as before, but they will be no longer attached, Fig. 4.4. The fragmented ion would then

have less energy compared to a single ion that was accelerated to the full thruster potential. When the spacecraft charges up, some ions will be electrostatically attracted to the satellite while ions of opposite polarity will be repelled. If the potential of the spacecraft is larger than the energy of an attracted ion, it will slow down, stop, and return to the spacecraft.

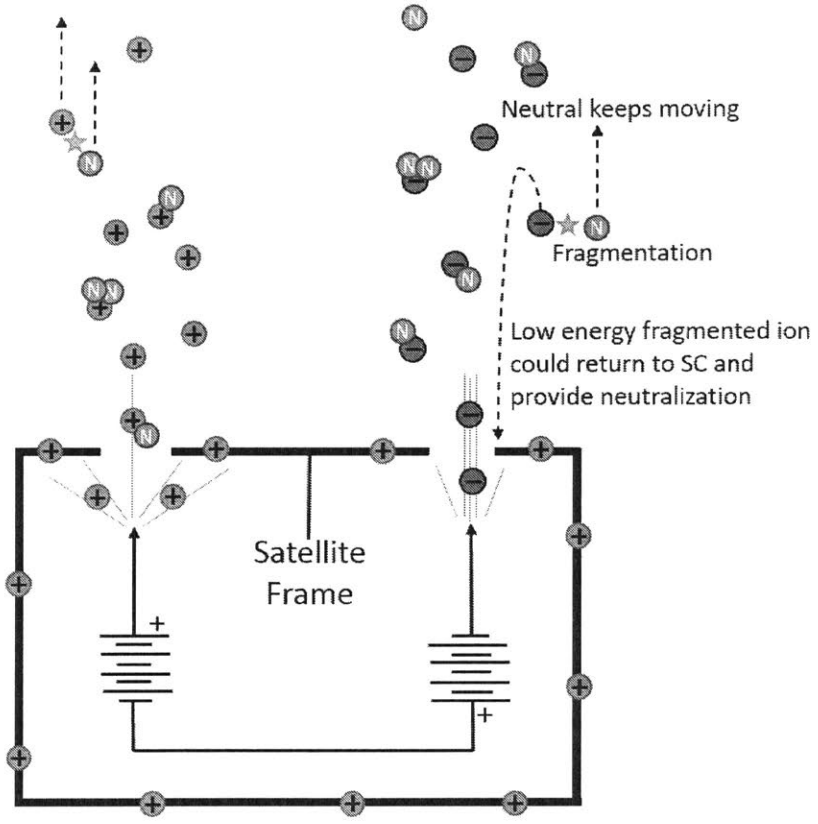

Fig. 4.4 Paths of ions born from a fragmentation event assuming a positively charged spacecraft.

When the ion collides with the spacecraft it will deposit its charge thus reducing the satellite potential. The ion collision could also create secondary particles that are repelled by the spacecraft and aid in neutralization. Interestingly, for electrospray thrusters, low-energy ions born from fragmentation events would return more readily. In the bipolar configuration, the returning ions enable the spacecraft potential to remain significantly lower than the full ion acceleration voltage applied to the thruster. The low energy ions that make it back to the spacecraft, *the return current*, will not produce thrust but will aid in the neutralization.

Even though the return current aids in neutralization, it might have unwanted effects on the spacecraft. The return current could contaminate the spacecraft with products of ion decomposition. This could be particularly problematic for any optics and solar panels onboard the satellite. Therefore, to reduce the chance of contamination, is important to reduce the magnitude of return current to a minimum.

4.1.4 Plasma environment as neutralization source

As discussed in section 1.2.3, the space plasma environment will tend to neutralize any satellite that charges to high potentials, this is especially true for the dense plasma in LEO. Since electrons in a plasma are more mobile than ions, the plasma will be more effective neutralizing a positively charged spacecraft than a negatively charged one. A dense plasma environment opens up an interesting neutralization possibility for electrosprays emitting relatively low amounts of ionic current.

The ~1.5 $\mu A/cm^2$ plasma electronic flux in LEO translates into 900μA of collected current for a 1U CubeSat that has 600cm^2 of surface area at zero potential bias [16]. 900μA is the equivalent current of six iEPS thrusters firing with nominal parameters (150μA per thruster). Since the thrusters are able to emit a negative ion beam, then in theory, six iEPS modules could fire in the negative mode, charging the satellite positively and relying solely on the plasma electronic flux to neutralize the spacecraft. This is referred as the *complete plasma neutralization mode,* as the plasma is used to completely neutralize the spacecraft. This mode of operation would not require to fire a thruster pair like in the bipolar configuration. This mode of operation is unheard of in the electric propulsion community. An external cathode is usually employed to neutralize the mA or higher positively charged ion beams traditional engines produce. As with the bipolar configuration, the capability of electrospray thrusters to emit negative ions is the main enabler of the complete plasma neutralization mode. It is important to notice that using the space plasma as a neutralization source is only feasible in LEO orbits, the plasma fluxes at MEO and GEO altitudes are simply too low compared to the emitted currents of the thrusters.

A spacecraft equipped with electrospray thrusters that used the complete plasma neutralization scheme would only fire the thrusters in negative mode. The ionic liquid reservoir, which acts as a propellant tank, will then accumulate positive charge to the point where electrochemistry reactions will start corroding the electrical connection to the propellant. If the

satellite fired its thrusters to the point of propellant exhaustion, then half of the propellant would most likely have electrochemically reacted with the propellant tank components. In this situation, half of the propellant would not have been available for thrust with a corresponding decrease in specific impulse.

A more benign operation mode would consist of firing a pair of thrusters in opposite polarities while ensuring the thruster in negative mode emits slightly more current than the one in positive mode. This is similar to the bipolar configuration but no series connection is established. Two independent high voltage supplies of opposite polarities are used to fire the thrusters. By firing two thrusters with opposing polarities, the amount of plasma current necessary to neutralize the satellite would be reduced to the difference in emitted currents. Depending on the PPU design, this difference in emitted currents could be made very small. With sufficiently small differences in the currents, operation could be opened to higher orbits where the plasma is more dilute. If the difference in currents is sufficiently small, one could even rely on the ionic plasma current for neutralization. This mode of operation is referred to as the *partial plasma neutralization mode* as the plasma is only used as a partial neutralization mechanism. The main charge balancing is produced by the bipolar ion beams. Since both polarities are fired over time, and the polarity of each thruster switched every so often, only a small amount of propellant would be lost to corrosion, bubbling or other mechanisms, on the reservoirs.

The complete or partial plasma neutralization modes simplify the design of PPU. The main purpose of the floating power supply discussed previously is to ensure identical emitted currents. Since the plasma neutralization modes do not impose an identical emitted current requirement, the galvanic isolation can be omitted altogether. This simplifies PPU design tremendously as it facilitates the HV converter design and makes housekeeping circuitry simpler. The simpler PPU could then be made smaller or capable of driving a larger number of thrusters. It is important to note that the plasma neutralization schemes only function with a sufficiently dense plasma. Interplanetary missions or satellites in high orbits must rely on the floating power supply and return current mechanisms for neutralization.

Photoelectric currents would also play a neutralizing role, especially when the spacecraft charges negatively. Photons from the sun will create low-energy secondary electrons, which will in turn be repelled by a negatively charged spacecraft, providing neutralization. In LEO,

the photoelectric current is roughly 2 x 10^{-9} A/cm^2. A 1-U CubeSat could have ~300 cm^2 area exposed to the sun, producing up to 0.3 μA of photoelectric current.

4.2 Charging model

The charging behavior of a spacecraft equipped with electrospray thrusters can be modelled with real and virtual capacitors connected to different parts of the satellite and the outside environment. A schematic of such a model is shown in Fig. 4.2. The circuit is simulated in an SPICE electronics package (MultiSim). Passive elements are used to model the complete system except for the thrusters, which are represented by a set of current sources controlled by non-linear expressions. The current sources are connected as shown in Fig. 4.5.

The difference between emitted and intercepted currents which makes it out of the thruster is referred to as the *out current*. A portion of the out current could be forced to return to the extractor if the spacecraft potential is non-zero. Low-energy ions that are produced by a spontaneous, meta-stable fragmentation event, would be the first contributors of this *return current*. The current that is able to exit the thruster and does not return to the spacecraft is referred to as the *thrust current*. The thrust current is simply the emitted current minus the intercepted and return currents.

The space plasma flux is represented by an equation driven current source which deposits its current to the satellite ground. Radiation-induced currents, and secondary particle generation could be represented by a series of non-linear, equation driven current sources but are not pursued in this work. More details on the modelling of these current sources is presented next.

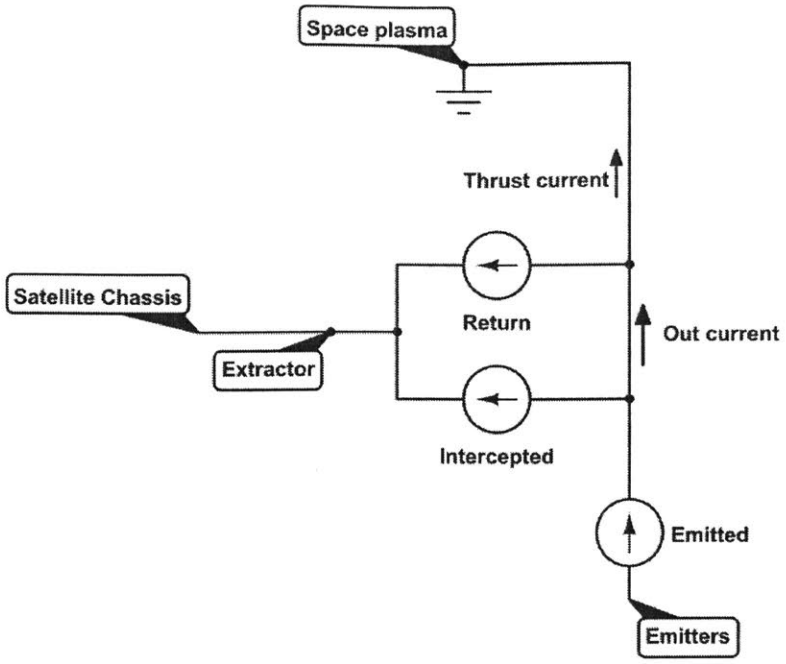

Fig. 4.5 Current sources used to model an electrospray thruster.

4.2.1 Emitted and intercepted currents

With normal electric fields in the range of 1-2 V/nm, individual ions are extracted from an ionic liquid by field emission [7]. After this threshold is achieved, field emission increases exponentially with the electric field [58]. Field emission continues until the ion transport to the apex of the tip is limited by the ionic liquid conductivity [58]. After this regime, the emission current presents a linear dependence with applied voltage for a single emission site. Guerra-Garcia shows that not all the tips in the thruster emit ions at the same potential [59]. The number of activated tips with increasing voltage can be approximated, to first order, as a linear relationship. The emission behavior after the exponential field emission regime can be approximated as linear fit for each emission site, quadratic for the total current.

A patched model is used to model the emission behavior. For voltages lower than the startup voltage, the emission behavior is approximated with an exponential relationship. For voltages higher than the startup voltage, a quadratic approximation is used. The two approximations meet at the startup voltage and provide a smooth transition.

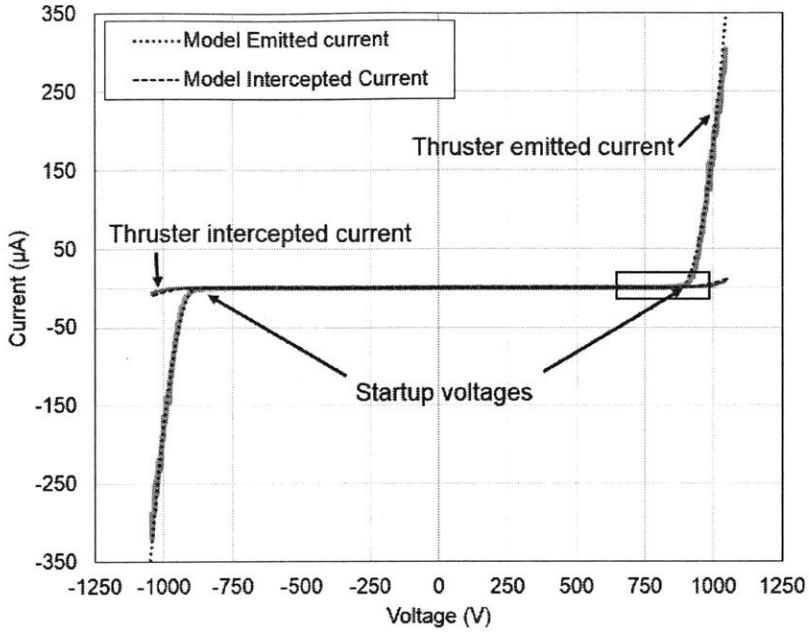

(a)

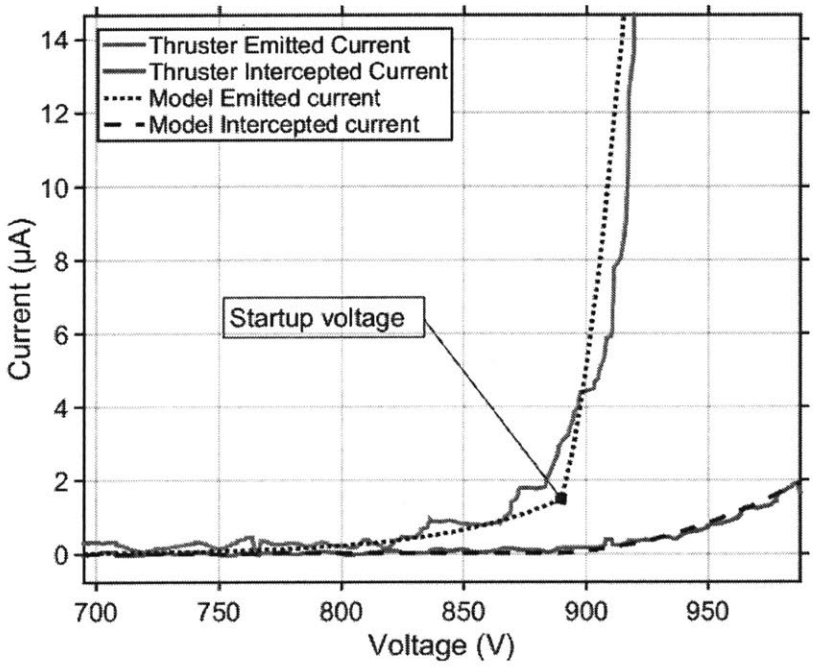

(b)

Fig. 4.6 Experimental I-V curve compared to the electrical model. (a) shows the complete emission profile. (b) displays the detailed region bounded by the box in (a).

The exponential model is controlled by two parameters, A and B, which relate to the activation energy of the process and other physical constants. Two parameters control the quadratic emission profile, the startup voltage, V_{str}, and a constant factor that controls the steepness, R. Eq. 4.1 shows the piecewise function that defines the thruster current versus voltage relation used in the electrical model. It only incorporates positive emission, the negative emission is obtained by simply inverting the emitted current sign.

$$I_{em}(V_{Th}) = \begin{cases} A\, V_{Th}(e^{B\sqrt{V_{Th}}}), & v \leq V_{str} \\ \dfrac{(V_{Th} - V_{str})^2}{R}, & v > V_{str} \end{cases} \qquad \textbf{Eq. 4.1}$$

The parameters in the model are fitted from experimental data. Positive and negative emission asymmetries could be modeled with slightly different parameters for each polarity. In this work, positive and negative emissions are taken to be symmetrical. The interception current is modelled as a fixed fraction, β, of the emitted current:

$$I_{intercepted} = \beta\, I_{emmited} \quad 0 < \beta < 1 \qquad \textbf{Eq. 4.2}$$

Fig. 4.6 shows the similarity between the emission profile of the model and a particular set of experimental data. With respect to the specific experimental data, the emitted and intercepted current models have an R^2 value of 0.97 and 0.99 respectively.

4.2.2 Return current

A Retarding Potential Analyzer (RPA) can be used to extract the energy distribution of an ion beam [11, 14]. This is useful to determine the amount of return current primarily produced by fragmentation events. A representative RPA curve of an electrospray thruster fueled with EMI-BF4 emitting positive ions is shown in Fig. 4.7 [11]. Due to the similarity of positive and negative emission energy distributions for a thruster fueled with EMI-BF4, the positive RPA curve in Fig. 4.7 is taken as a representative distribution for both polarities. A linear piecewise interpolation table referred as $f_{eng}(V_{Sat})$, is used to fit the return current model to the specific experimental data. The return current becomes non-zero when the spacecraft potential is non-zero and opposite in polarity with respect to the emitted current. When these conditions are met, the lookup table function is used to calculate the total return current fraction using Eq. 4.3 and Table 4.1.

$$I_{return}(V_{sat}) = \begin{cases} 0, & V_{sat} = 0 \\ 0, & V_{sat} > 0\,, I_{em} > 0 \\ 0, & V_{sat} < 0\,, I_{em} < 0 \\ I_{out}(\,f_{eng}(V_{sat})), & All\ other\ V_{sat} \end{cases} \qquad \textbf{Eq. 4.3}$$

In this model, the extractors are directly connected to the satellite chassis which is also satellite ground. The external environment is taken as the global ground.

Table 4.1 Lookup table used to fit RPA curve

Normalized ion energy	Normalized current
0	1
0.1	0.99
0.2	0.97
0.3	0.92
0.4	0.84
0.5	0.79
0.6	0.72
0.7	0.62
0.8	0.45
0.9	0.1
0.95	0
1	0

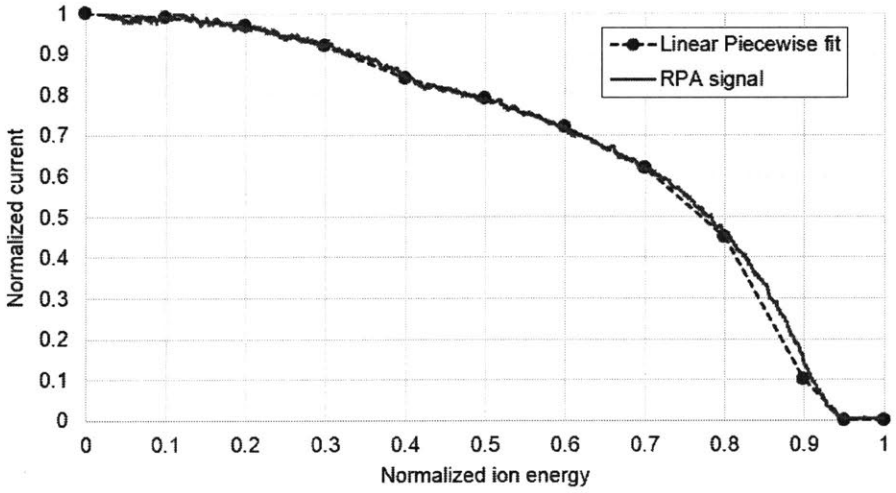

Fig. 4.7 RPA curve of an iEPS fueled with EMI-BF4 and firing in positive mode.

4.2.3 Plasma current

In the complete plasma neutralization mode, the plasma currents only becomes relevant in LEO. Thin-sheath theory is then used to model the plasma currents collected by the spacecraft at these altitudes. The first-order estimate of the collected plasma current is a function of plasma density, n_e, electron and ion temperature, T_e and T_i, the effective collecting area, A, and satellite potential, V_{sat}, as shown in Eq. 4.4.

$$I_{plasma}(V_{sat}) = \begin{cases} q_e n_e A\left(\frac{\bar{c_i}}{4} e^{\frac{-q_e V_{sat}}{k T_i}} - e^{-\left(\frac{T_e+T_i}{2T_e}\right)} \sqrt{\frac{k(T_e+T_i)}{m_e}}\right), & V_{sat} \geq 0 \\ q_e n_e A\left(e^{-\left(\frac{T_e+T_i}{2T_e}\right)} \sqrt{\frac{k(T_e+T_i)}{m_i}} - \frac{\bar{c_e}}{4} e^{\frac{-q_e V_{sat}}{k T_e}}\right), & V_{sat} < 0 \end{cases} \quad \textbf{Eq. 4.4}$$

$$\bar{c_e} = \sqrt{\frac{8\,k\,T_e}{\pi\, m_e}} \qquad \bar{c_i} = \sqrt{\frac{8\,k\,T_e}{\pi\, m_i}}$$

m_e and m_i are the electron and ion mass respectively. q_e is the electron charge. For orbits higher than LEO, thick sheath theory is used. As explained in section 1.2.3, a factor, Eq. 1.11, can be applied to Eq. 4.4, to take into account thick-sheath effects. The difference between both regimes can be seen in Fig. 4.8. The theoretical plasma collected current for a 1-U CubeSat in LEO has clear saturation regions when the satellite charges to relatively large positive or negative potentials. For the GEO case, since the Debye length is larger than the spacecraft, the satellite is able to attract more particles from farther away as its potential is increased. This is particularly clear as the satellite charges positively attracting more electrons and never really saturating. Even though the collected currents in GEO do not saturate, the plasma density is so low compared to LEO that the overall collected current is much less. Note the different in scales of the units for the collected currents in LEO and GEO. A dense plasma is a more effective neutralizer than a dilute one. The parameters used to model the GEO and LEO plasma environments is shown in Table 4.2. The total surface area of the 1-U CubeSat was assumed to be 0.006 m^2. The similarity of electron and ion currents in GEO can be attributed to the high plasma temperature.

Table 4.2 Simulation parameters for LEO and GEO plasma environments

Orbit	n_e (cm^{-3})	T_e (eV)
LEO	10^6	0.4
GEO	10	10^3

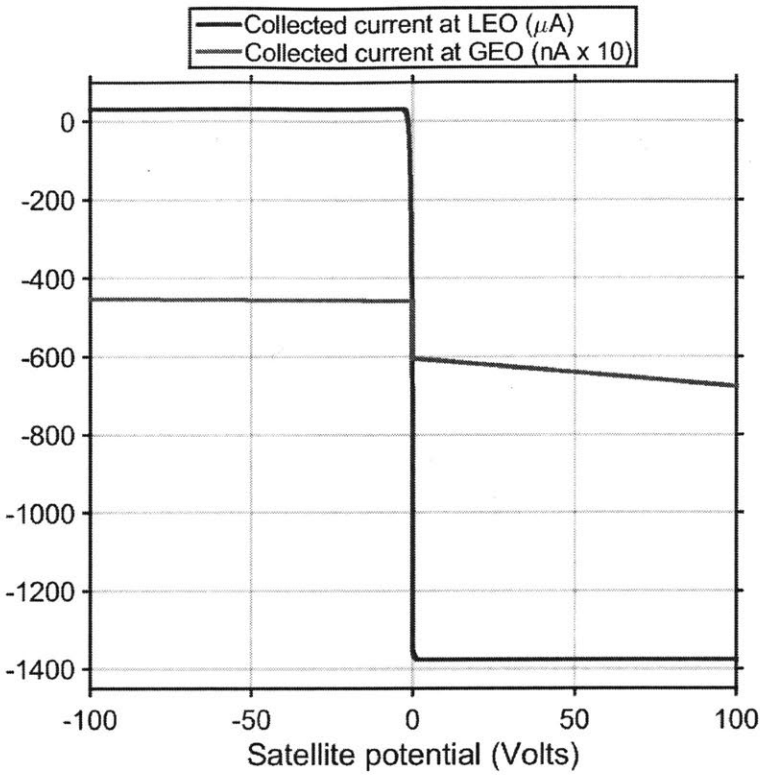

Fig. 4.8 Simulated plasma current for a 1-U CubeSat with respect to satellite potential.

4.3 Model results

The circuit simulated is identical to the one in Fig. 4.2, in which the thruster model is composed of the current sources network shown in Fig. 4.5.To describe the simulation results, we will start exploring the simplest emission cases and build on complexity. The potential of the high voltage power supply return, HV_{Ground}, with respect to the satellite will be referred to as $V_{HVGround}$. The potential at which the satellite floats with respect to the external plasma will be referred to as satellite potential or V_{Sat}. In this and other simulations the capacitances of C_{HV} and C_{SC} are chosen to make charging effects apparent in the timescales presented, slower than in reality. Similarly, the steepness factor R of the thruster model is chosen to aid in the visualization of the data. The standard voltage waveform applied to the thrusters is a square wave which alternates polarity. The rise time of the thruster voltages are representative of a non-instantaneous PPU, which reflects reality. Every simulation scenario is accompanied by a table describing all the simulation parameters used.

4.3.1 Ideal bipolar operation

The simplest case to analyze is the ideal bipolar operation. In this scenario, both thrusters have identical emission characteristics (in practice this will never be true). Identical magnitude voltages are applied to each thruster. No plasma is simulated in this test. Since both thrusters are emitting exactly the same amount of current, with opposite polarities, there is no charging of the satellite or of HV_{ground}.

Table 4.3 Parameters for ideal bipolar emission simulation.

	Parameter	Value	Units
T_1	V_{str}	900	V
	R	65×10^6	Ω^2
	β	25	%
T_2	V_{str}	900	V
	R	65×10^6	Ω^2
	β	25	%
	C_{SC}	10	pF
	C_{HV}	0.1	μF

The simulation shows the relevant variables over time. At time 500 ms, the polarity of the high voltage power supplies is reversed. Notice that emission only occurs when the magnitude of the thruster potentials is above the startup voltage of the thrusters, which in this example is 900V. The interception current is just a fraction, β, of the emitted current, in this case 25% (an unrealistically high value to aid in visualization). In reality iEPS thrusters have interception fractions of less than 1%. The thrust current is simply the emitted current minus the intercepted current. Only the thrust current contributes to thrust.

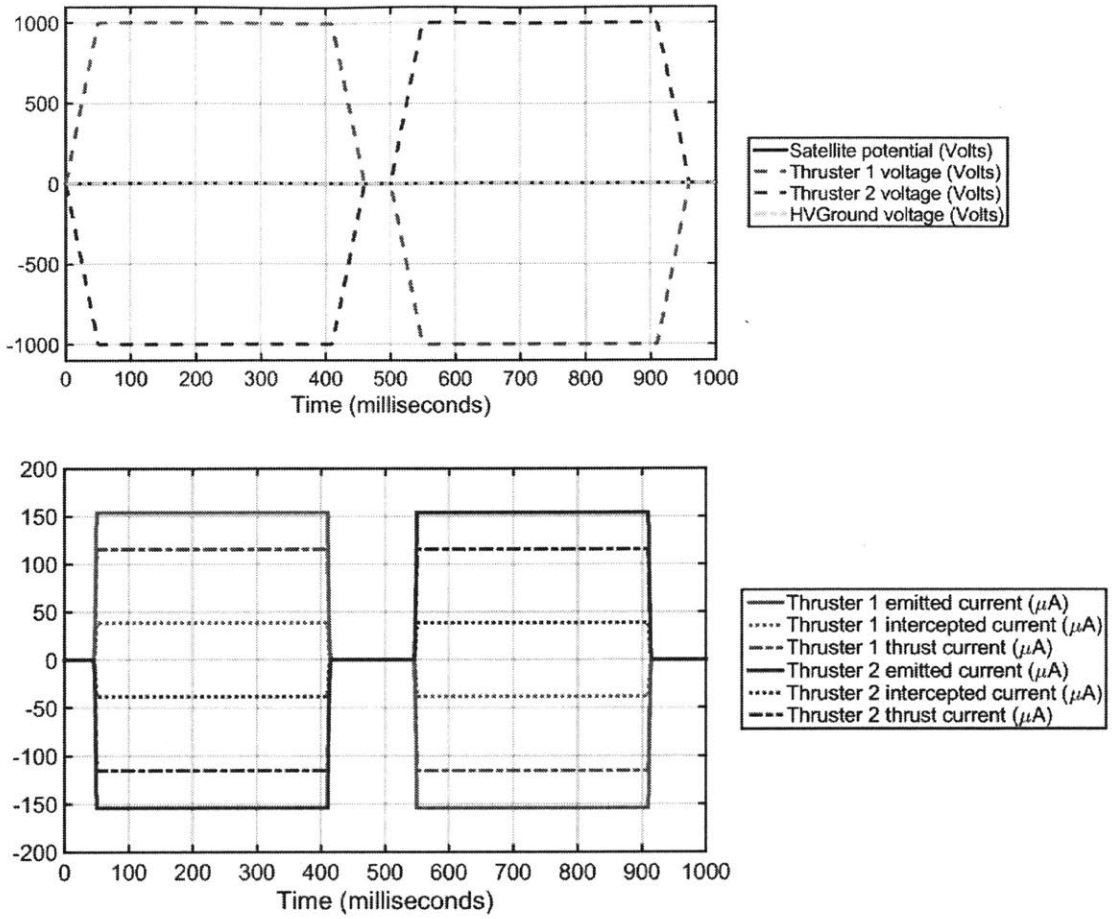

Fig. 4.9 Ideal bipolar emission with no plasma. No charging present.

4.3.2 Differential interception

If the emission profile of the thrusters is perturbed from the ideal case, spacecraft charging will be present. In the following simulation a different interception fraction was chosen for T2, highlighted in gray in Table 4.4. Plasma and return currents are disabled for this specific test.

Table 4.4 Simulation parameters for differential interception case

	Parameter	Value	Units
T_1	V_{str}	900	V
	R	65×10^6	Ω^2
	β	25	%
T_2	V_{str}	900	V
	R	65×10^6	Ω^2
	β	5	%
	C_{SC}	10	nF
	C_{HV}	0.1	μF

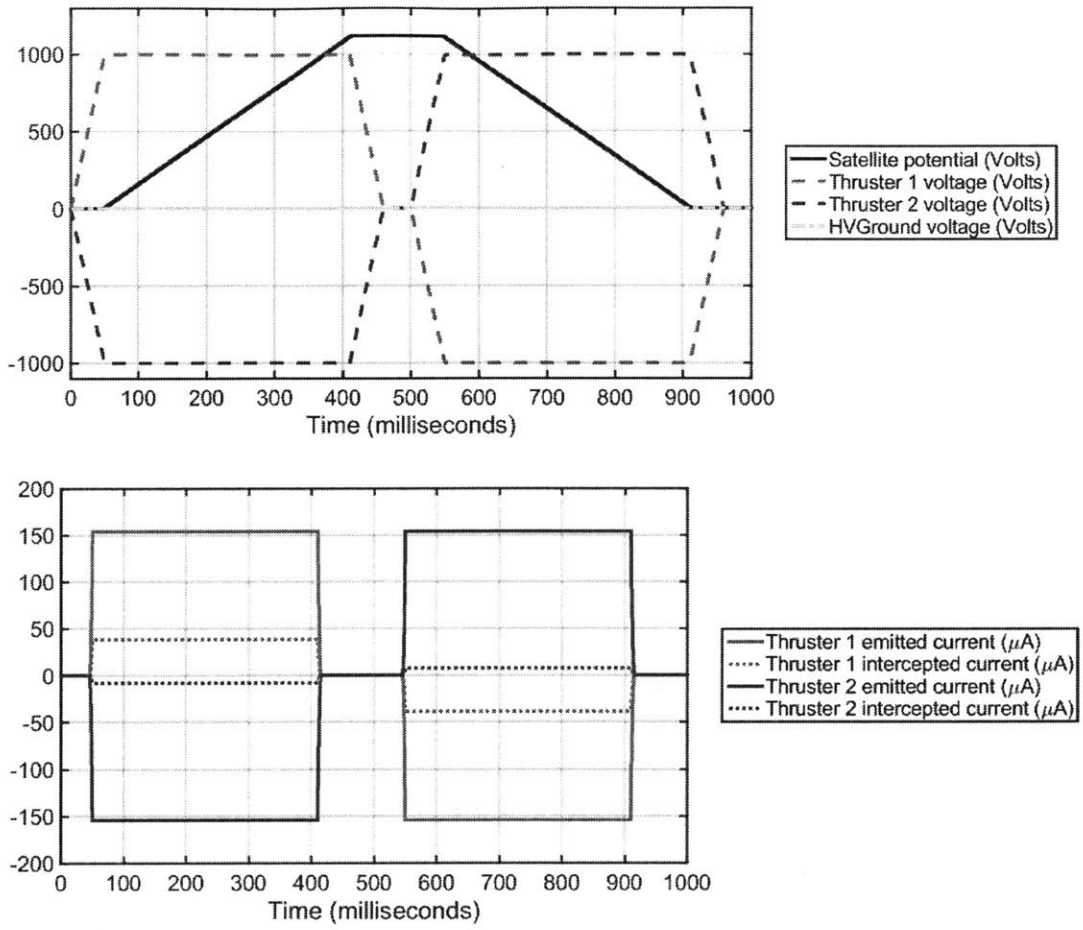

Fig. 4.10 Simulation of differential interception case.

The voltage waveforms applied to the thrusters are identical to the ones in the ideal case. As soon as the thrusters start emitting, the net current collected by the extractors is not zero due to the asymmetry in interception fractions. Since the extractors are connected to the satellite chassis, the whole spacecraft charges up following the polarity of the thruster with the larger interception fraction, T1. Since the emission parameters of the thruster are identical, they both emit the same amount of current at a given voltage, therefore HV_{ground} does not charge. The satellite continues to charge as emission continues. At time 390 ms, the satellite potential surpasses the thruster voltage. As discussed in section 4.2.2, if the satellite potential exceeds the thruster voltage, ions will be electrostatically attracted to the spacecraft and will eventually return to it providing neutralization. Therefore in reality, the satellite potential would never exceed the thruster potential. In this simulation the return current is disabled so no returning ions are simulated allowing this discrepancy to occur. The scenario in which there is no return

current would only be the case if there was a mechanism to remove the ions from the vicinity of the spacecraft as soon as they exit the extractor plane. This is not a realistic situation in space. Simulations described in the next sections do include the return current effects.

4.3.3 Differential startup voltage

The next scenario explores the effects of a differential startup voltage between the thrusters. The simulation parameters are shown in Table 4.5, the parameter modified with respect to the ideal case is highlighted in gray.

Table 4.5 Simulation parameters for the differential startup voltage case.

	Parameter	Value	Units
T_1	V_{str}	800	V
	R	65×10^6	Ω^2
	β	25	%
T_2	V_{str}	900	V
	R	65×10^6	Ω^2
	β	25	%
	C_{SC}	5	nF
	C_{HV}	0.1	μF

Due to the asymmetry in the emission profiles, T_1 emits more current at any given thruster voltage compared to T_2. At time 50 ms, in Fig. 4.11, the potential across T_1 surpasses its startup voltage and starts emitting. At this same instant, the potential across T_2 is not high enough and is still in the exponential part of its I-V curve emitting negligible amounts of current.

The positive charge expelled from T_1 forces the satellite to negatively charge with respect to global ground. The current imbalance also forces C_{HV} to negatively charge with respect to the satellite. The potential in C_{HV} shifts the thruster voltages negative. Once the potential across T_2 reaches its startup voltage, it starts emitting negative ions. There is now less of a difference in emitted currents, which slows down the rate at which the satellite charges, time 90 ms. As C_{HV} continues to charge negatively, the potential difference across T_2 becomes greater and the potential difference across T_1 becomes smaller. This shift in thruster potentials force T_2 to emit more current and T_1 to emit less current. The quadratic relationship between the emitted current and the thruster potential makes a difference of only a few volts very significant on the emission current. Therefore C_{HV} only has to charge a few tens of volts to balance the emission currents. Note the different scale on the units for HV_{ground}. The overshoots of the emitted currents visible at times 50 and 550 ms are caused by this non-instantaneous charging of C_{HV}. While C_{HV}

charges, the emitted currents are not identical. Eventually, C_{HV} charges to the potential that shifts the thruster power supply enough to make both emitted currents the same. Since in this particular simulation the interception fractions of both thrusters is the same, the satellite stops charging as soon as the emitted currents become identical.

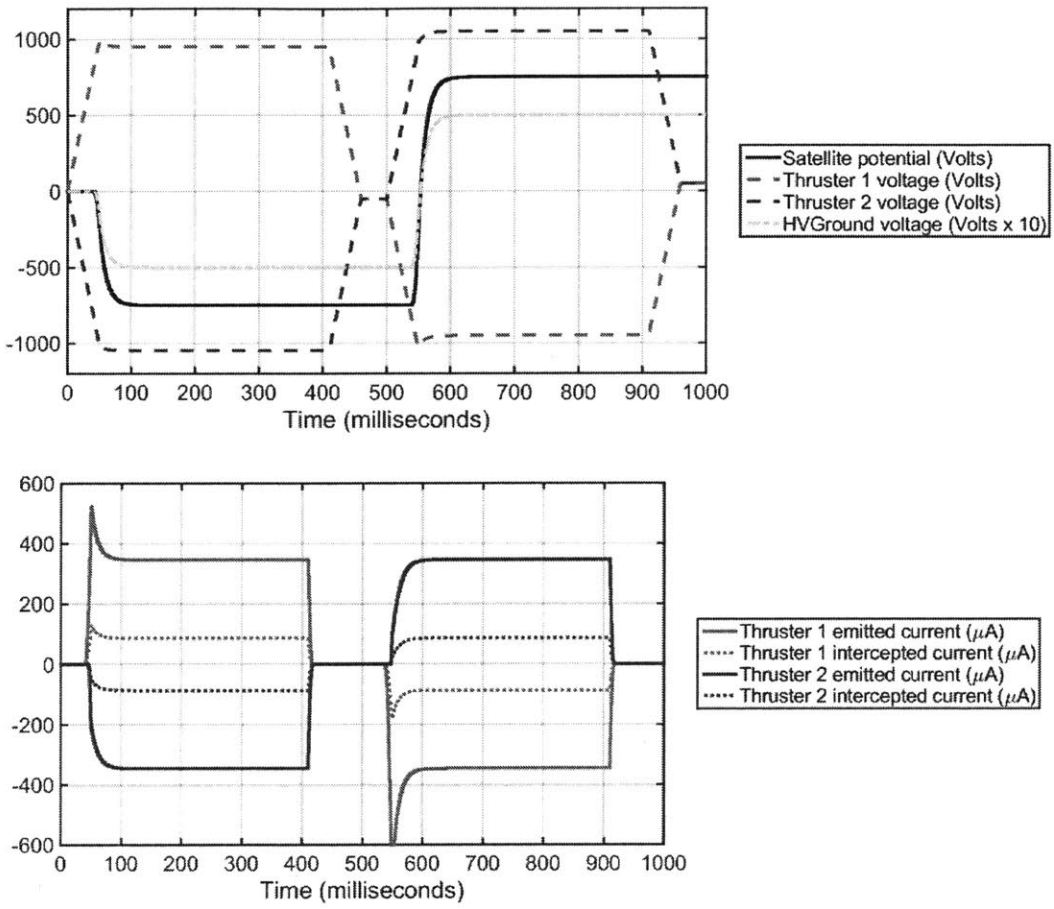

Fig. 4.11 Simulation of differential startup voltage.

4.3.4 Return current, mono-energetic beam

The neutralization effects of the return current are presented next. In this simulation the ion beam energy distribution is assumed to be monoenergetic at 97% of the thruster potential, Fig. 4.12. The normalization is performed with respect to the thruster potential. This energy distribution is not realistic for current iEPS thrusters, but it makes interpreting the data easier.

The simulation parameters are identical to the differential interception case, shown in Table 4.4 in which T_2 has a lower interception fraction than T_1.

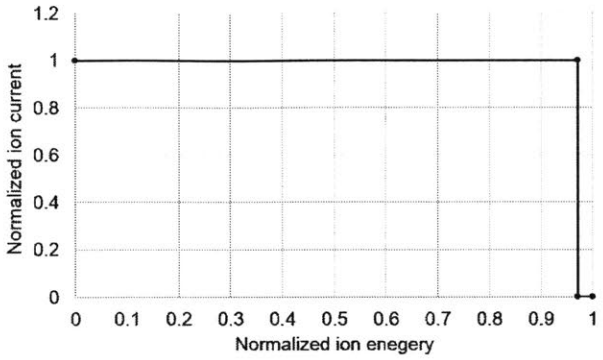

Fig. 4.12 Monoenergetic beam energy distribution.

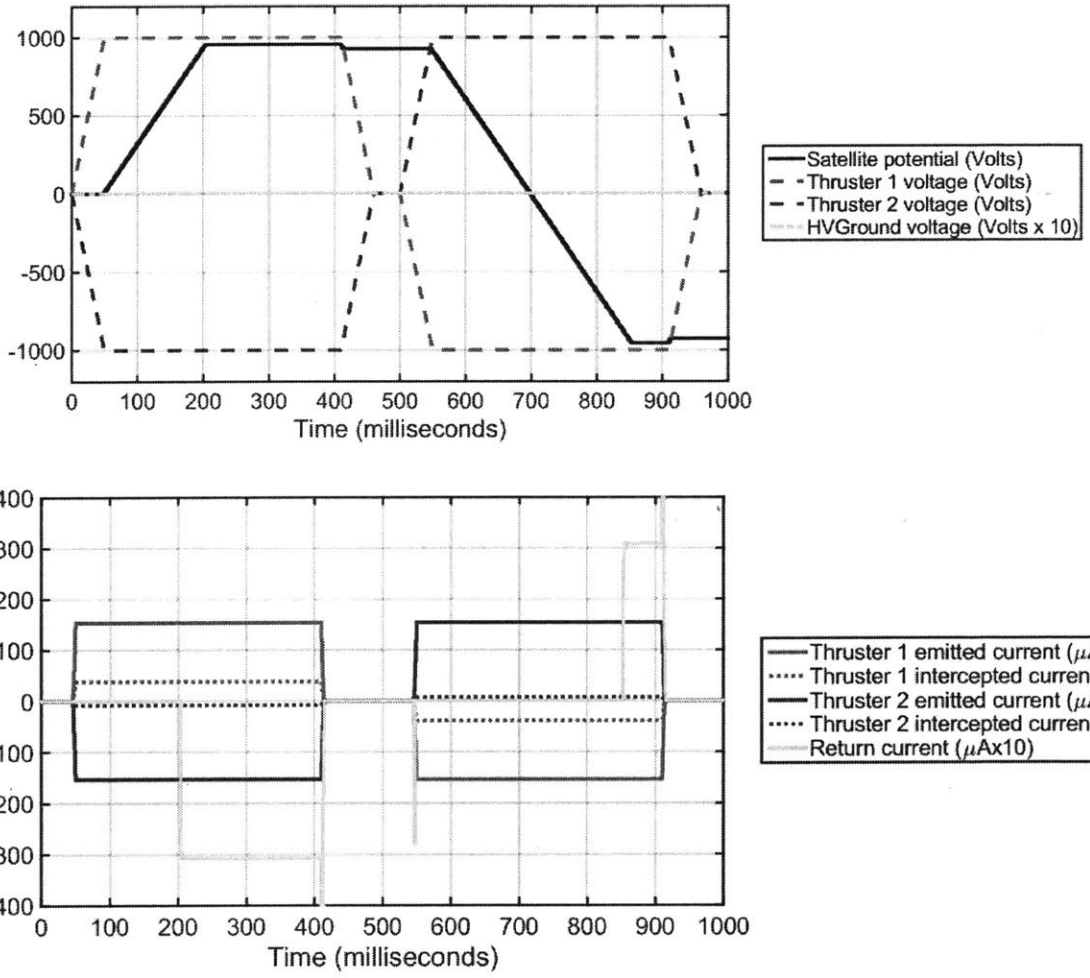

Fig. 4.13 Simulation of the return current effects for a monoenergetic beam.

At the beginning of the test the results look very similar to those on Fig. 4.10 except the satellite potential never exceeds the thruster potential. The spacecraft charging produced by the differential interception fraction of the thrusters is mitigated by the return current. At time 200 ms, the satellite potential stops increasing and suddenly the return current becomes non-zero. Note the different unit scale for the return current in the figure. At this point the satellite has charged up sufficiently positive to attract some of the negatively charged ions emitted by T_2. These ions return to the spacecraft, depositing their charge and neutralizing it. The amount of return current necessary to impede further spacecraft charging is the same as the difference in intercepted currents, around 30μA in this case.

4.3.5 Return current, thruster ion beam

A simulation using a representative ion energy distribution from an iEPS filled with EMI-BF4 is presented next. The energy profile is shown in Fig. 4.14 [11]. The smooth profile of the energy distribution indicates fragmentation in the acceleration region, which produces ions of all energies and not just in discrete steps. The simulation parameters are identical to the differential interception case, shown in Table 4.4. T_2 has a lower interception fraction than T_1.

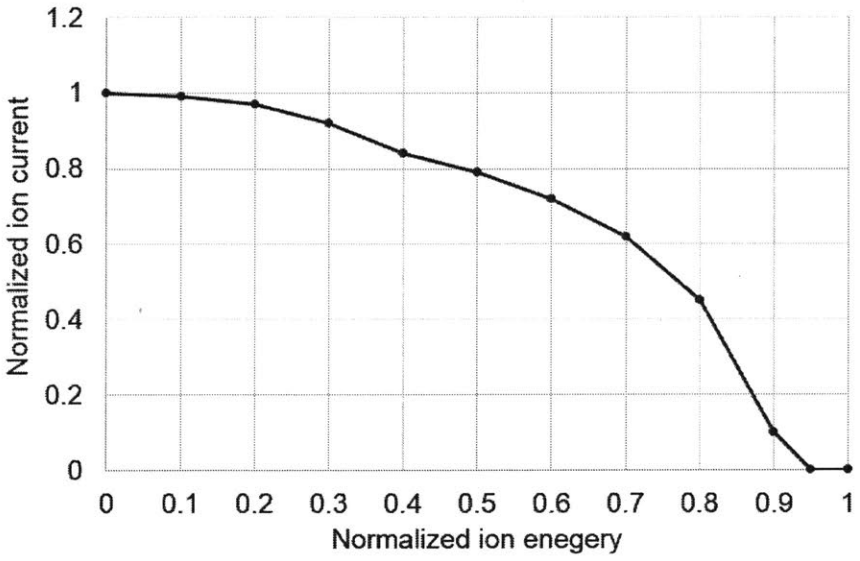

Fig. 4.14 Ion beam energy distribution of an iEPS filled with EMI-Bf4.

The higher fragmentation rate of the iEPS filled with EMI-BF4 reduces the final equilibrium satellite potential, ~500V, Fig. 4.15, compared to the mono-energetic case, ~970V. Ion beams with larger energy spreads will have low energy ions that return more readily to the spacecraft to provide neutralization. As in the previous example, the return current still neutralizes the

~30μA of differential intercepted current. In this case the potential that the satellite has to charge to attract this amount of return current is significantly lower than the mono-energetic case.

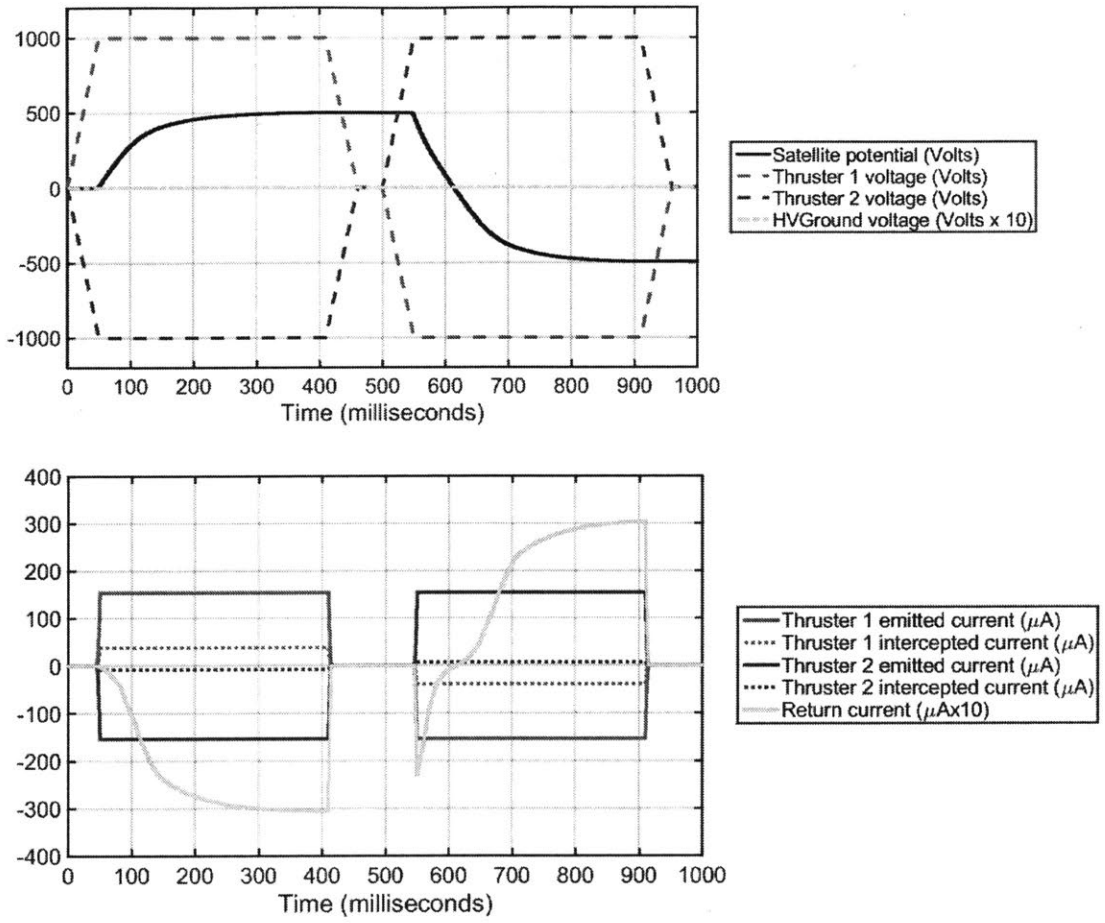

Fig. 4.15 Simulation of the return current effects for bipolar iEPS ion beams.

4.3.6 Return current, single emitter

Finally, an ion beam with a high dispersion energy profile is simulated. This type of energy profile is representative of single emitters fired at high voltages. The energy dispersion for a needle wetted with EMI-BF4, and with an emission voltage of 1600V is shown in Fig. 4.16. The simulation parameters are identical to the differential interception case, shown in Table 4.4. T_2 has a lower interception fraction than T_1. The discrete step at 35% of the normalized ion energy is product of dimers breaking into monomers after the acceleration region. The ions produced by these fragmentation events have low energies and will be effective neutralizers. The slope on the profile represents fragmentation in the acceleration region.

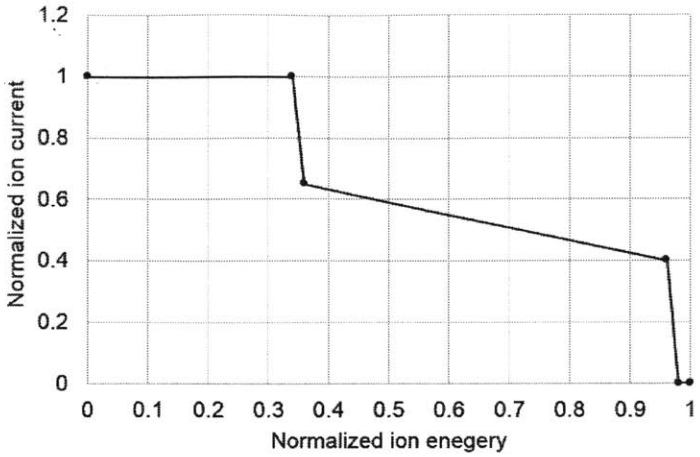

Fig. 4.16 Representative ion beam energy distribution of a single emitter wetted with EMI-Bf4 and fired at 1600V.

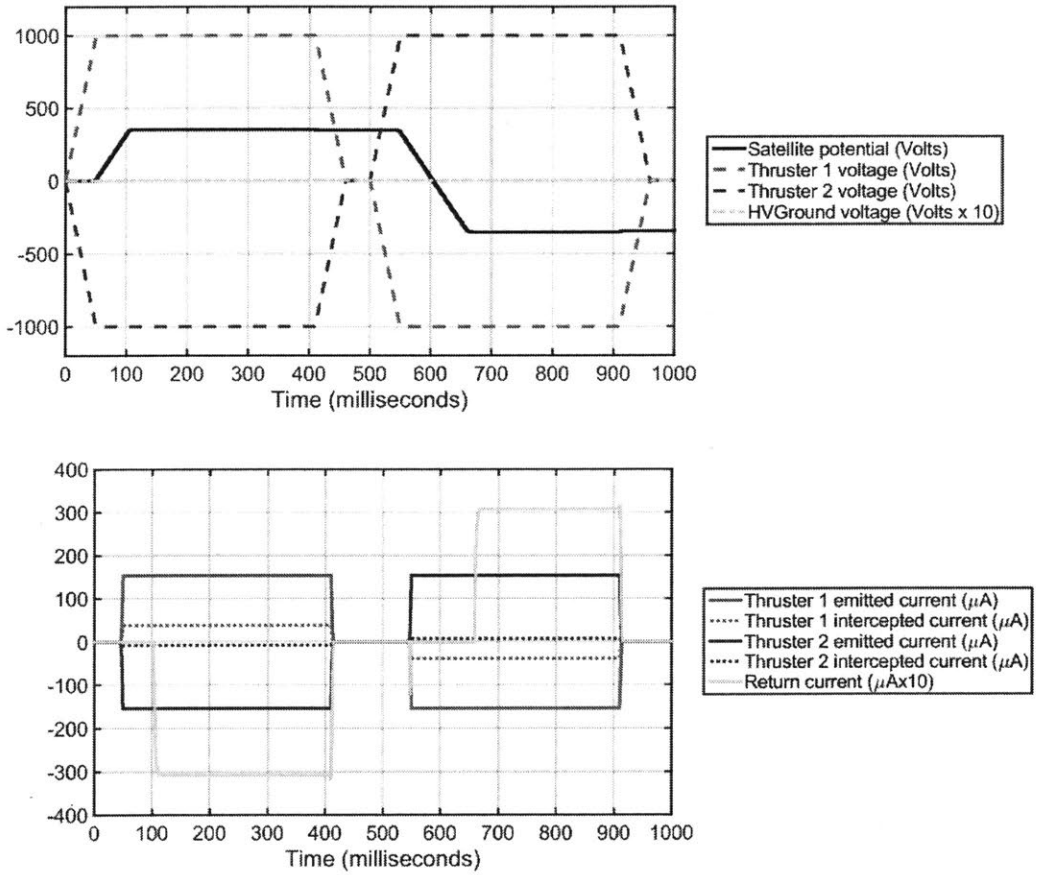

Fig. 4.17 Simulation of the return current effects for an ion beam with low fragmentation.

The simulation results are similar to the previous cases except that the satellite potential stabilizes at lower voltages, ~400V. This can be explained by the broader energy distribution of the ion beam with respect to the other cases. As soon as the satellite potential reaches ~35% of the thruster voltage, the ions born from a dimer to monomer fragmentation event return to the spacecraft to provide neutralization. There are enough of these ions to fully provide the 30μA of differential interception current driving the spacecraft charging.

4.3.7 Plasma effects, LEO

To simulate the neutralizing effects of the space plasma in LEO, the models described in 4.2.3 was used. The simulation assumes a representative LEO plasma (n_e=~10^6 cm^{-3}, T_e=0.4eV) and a 1U CubeSat with a surface area of 0.006m^2. The thruster emission parameters are identical to the differential interception case except for the self-capacitance of the satellite. The plasma is such an effective neutralizer that the pF self-capacitance of the satellite would have produced step-like changes in the satellite potential. The fictitious larger self-capacitance used in this simulation makes spacecraft charging effects evident in the timescales presented. The simulation parameters are shown in Table 4.6.

Table 4.6 Simulation parameters for the plasma in LEO scenario.

	Parameter	Value	Units
T_1	V_{str}	900	V
	R	65 x 10^6	Ω^2
	β	25	%
T_2	V_{str}	900	V
	R	65 x 10^6	Ω^2
	β	5	%
	C_{SC}	5	nF
	C_{HV}	0.1	μF

As expected, the electrons of the dense plasma in LEO are an effective neutralizer and limit the positive potential that the satellite could charge to close to zero volts. This can be seen in the first half of the simulation where the thrusters attempt to induce positive spacecraft charging. Notice how the electronic plasma current is able to provide the ~30μA necessary to counteract the differential interception current inducing spacecraft charging, magenta trace in Fig. 4.18. The ions on the other hand are not as effective neutralizers. Therefore, when the thrusters induce negative spacecraft charging, the ionic current cannot provide the ~30μA necessary for complete neutralization and saturates at ~3μA. The return current provides the

rest of the current necessary for neutralization, ~27μA. This can be seen in the second half of the simulation.

This result points to the possibility of firing electrospray thrusters in negative mode, to induce positive spacecraft charging, and relying solely on the dense LEO plasma for complete neutralization of the spacecraft. For a 1-U CubeSat with a surface area of 0.006 m^2 the saturation electronic current is around 900μA. As discussed in section 4.1.4, a more benign partial plasma neutralization scheme could be employed to reduce the amount of plasma current necessary for neutralization.

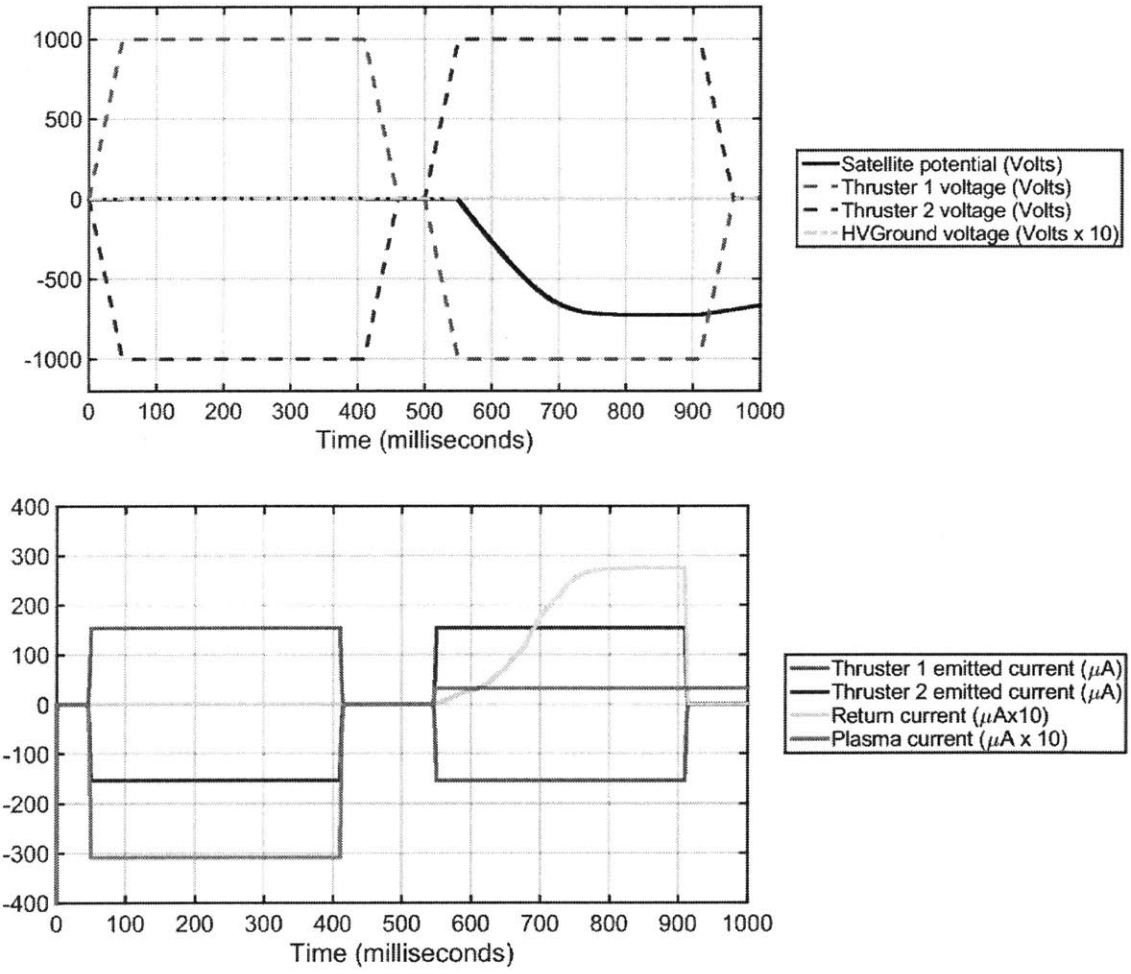

Fig. 4.18 Simulation of the plasma current effects in LEO environment.

4.3.8 Plasma effects, GEO

The neutralizing effects of the space plasma in GEO are presented next. The model described in section 4.2.3 was used to represent the plasma environment. The simulation assumes a representative GEO plasma (n_e=~10 cm^{-3}, T_e=10^3eV) and a 1U CubeSat with a surface area of 0.006m^2, as shown in Table 4.2. The thruster emission parameters are identical to the previous case, shown in Table 4.6.

As expected, the dilute plasma in GEO is not as effective neutralizing the spacecraft when compared to the dense LEO plasma. The GEO plasma cannot provide the necessary current to completely counteract the differential intercepted current, which drives spacecraft charging. The plasma currents saturate at around 100nA. Notice the difference in scale for the plasma trace in Fig. 4.19. As in the previous case, the return current provides the additional current necessary to neutralize the spacecraft.

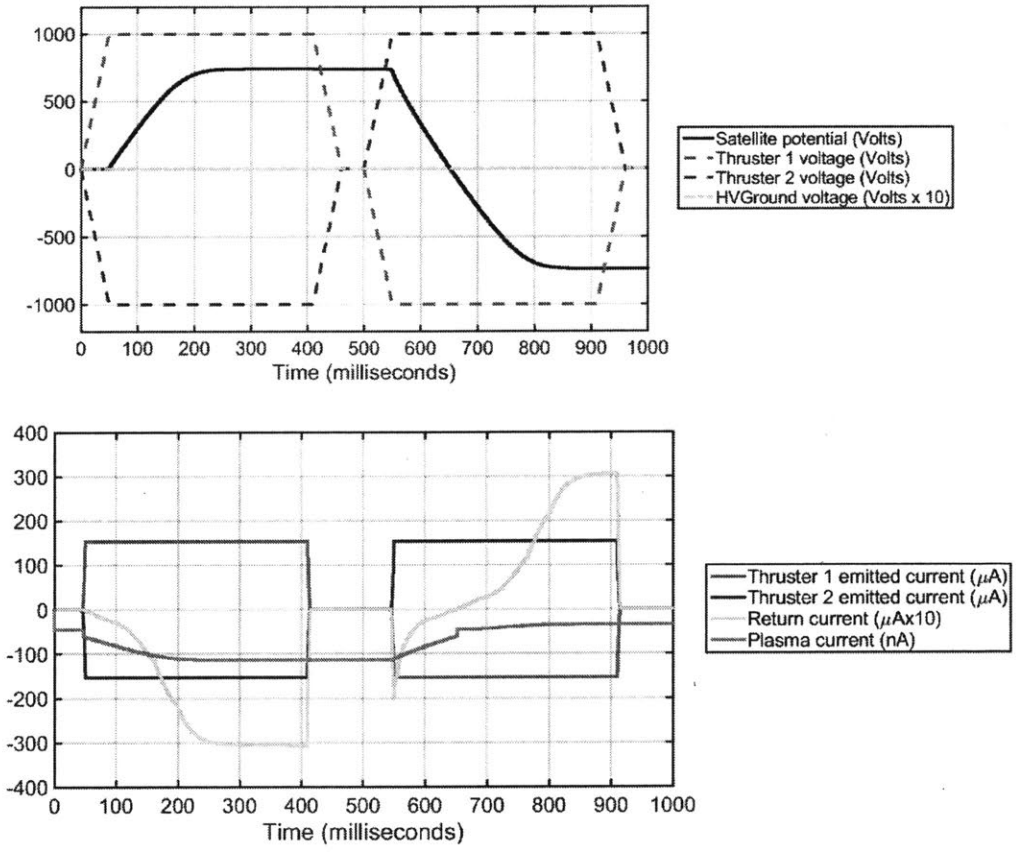

Fig. 4.19 Simulation of the plasma current effects in GEO environment.

4.4 Spacecraft charging effects on thrust

As seen in the previous examples, spacecraft charging is very likely to occur on a spacecraft operating electrospray thruster in the bipolar configuration. The main reason for this is the asymmetry in the thruster's emission profile. Generally speaking, the greater the magnitude of the emission profile differences the greater the magnitude or severity of the spacecraft charging induced. Since it is practically impossible, due to manufacturing tolerances, to produce two identical thrusters, spacecraft charging will always be present to some extent. For this reason, it is important to estimate the effects of spacecraft charging on thruster performance, mainly thrust.

Eq. 3.2 is the electrospray thrust equation. Several factors can be added to this equation in order to increase its accuracy. Courtney and Shea have shown that numerical factors can be applied to V_{Th} and (q/m) of Eq. 3.2 to account for different degrees of solvation in the emitted ions and energy dispersion in the beam [52, 53].

When electrospray thrusters fire in the bipolar configuration, a non-zero satellite potential will modify the nominal thrust by repelling one ion beam and attracting the opposite polarity ion beam. The thrust contribution of the polarity being attracted will be reduced while the one being repelled will be increased. The thrust that takes into account these charging effects, $\overline{F_*}$, is then calculated by introducing the potential of the satellite, V_{Sat}, into Eq. 3.2, resulting in:

$$\overline{F_*} = I_{thr}\sqrt{\frac{2(V_{Th} + V_{sat})}{(q/m)}} \qquad \textbf{Eq. 4.5}$$

An expression for the fractional change of the thrust with reference to its nominal value, $\overline{F}$, can then be obtained,

$$\frac{\overline{F_*}}{\overline{F}} = \sqrt{1 + \frac{V_{sat}}{V_{Th}}} \qquad \textbf{Eq. 4.6}$$

Applying this relation to the bipolar configuration where two thrusters are fired and normalizing by twice the nominal thrust, $\overline{F_b}$, results in the bipolar thrust fractional change, $\frac{\overline{F_{*b}}}{\overline{F_b}}$:

$$\frac{\overline{F_{*b}}}{2 \cdot \overline{F}} = \frac{\overline{F_{*b}}}{\overline{F_b}} = \frac{\sqrt{1 + \frac{V_{sat}}{V_{Th1}}} + \sqrt{1 + \frac{V_{sat}}{V_{Th2}}}}{2} \qquad \textbf{Eq. 4.7}$$

Assuming V_{Th1} is positive and V_{Th2} is identical in magnitude but negative, it is possible to graphically observe the effect of charge on thrust, Fig. 4.20.

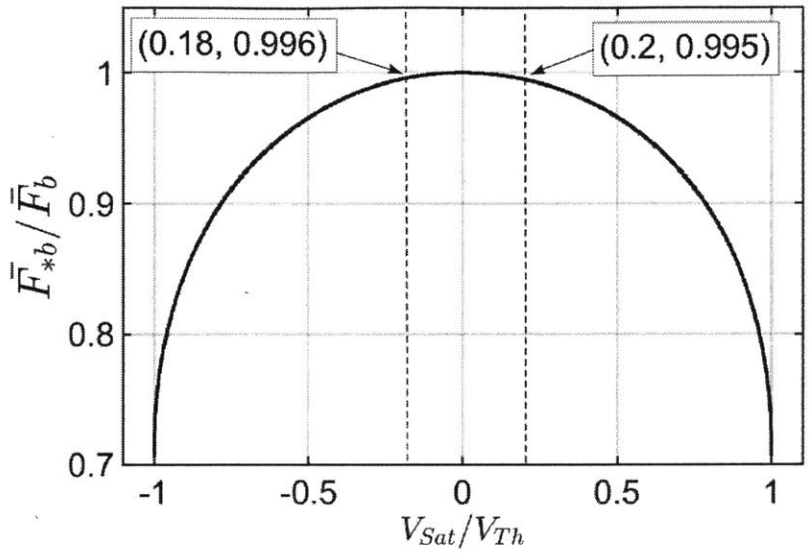

Fig. 4.20 Effects of satellite potential on thrust. The two coordinates represent the satellite potential boundary measured for the test described in Fig. 4.33.

As expected, when the satellite potential is zero, the pair of thrusters produce twice the nominal thrust of a single thruster. When the potential of the satellite deviates from zero the thrust is less than $\overline{F_b}$, with a square root dependence. In the worst case scenario, when the satellite fully charges to one of the thruster potentials, the total thrust would be 70% compared to the non-charged case. Even though the species of the different ion beams are being repelled and attracted by the same potential, the effect goes as the square root of the satellite potential. Therefore, the increase in thrust by the repelled ion beam is not sufficient to counteract the reduction in thrust by the attracted ion beam. The vertical dash lines in Fig. 4.20, show the charging envelope for the experimental test to be described in Fig. 4.33. As seen in the following sections, such envelope is representative of spacecraft charging experiments. Consequently, it is anticipated that charging will have an, albeit small, non-zero effect on thrust.

4.5 Experimental spacecraft charging results

4.5.1 Static, non-levitated experiments

In order to validate the results of the electrical model described previously a set of experiments were performed in the MagCube. The first of these experiments consisted in a

static test which allows more flexibility in the experimentation parameters and reduces complexity. By not levitating the satellite, one is able to artificially increase the capacitance of the satellite with respect to ground (self-capacitance) and to manually discharge the satellite when needed. The increase of self-capacitance allows otherwise instantaneous satellite potential changes to be recorded over longer period of times. The test consisted of placing the CubeSat which is equipped with batteries, computer, radio, PPU and a single electrospray thruster on Teflon insulators onto the MagCube. The Teflon insulators allow the satellite to charge with respect to the chamber ground. Teflon is an excellent electrical insulator but cannot compete with the electrical isolation provided by vacuum, which is enabled when the satellite is levitating. Therefore, some negligible leakage current was present in the experiments.

Electrical ground in this and all following experiments is considered to be the chamber metal wall which is electrically connected to the testbed frame. The pressures reached inside the vacuum chamber for all tests were lower than $5x10^{-6}$ Torr. The PPU in the satellite provides telemetry of emitted and intercepted currents, and thruster voltage. The telemetry is sampled at 10Hz. All telemetry is filtered by the PPU circuitry with an RC filter that reduces signal noise, improving PPU performance. The RC filters used have a cutoff frequency of 1.6 kHz. The emitted and intercepted current circuitry have a measured uncertainty of $\pm 3\mu A$. The voltage measurement circuitry have an estimated uncertainty of $\pm 5V$.

The thrusters used in this and all subsequent tests use EMI-BF4 as propellant. In order to fire a single thruster the capacitor, C_{HV} in the PPU was electrically shorted to satellite ground. This removed the floating power supply scheme and allowed the firing of a single thruster. Since only a single thruster is firing, with no neutralization source, spacecraft charging will be present. According to the model developed, spacecraft charging cannot continue indefinitely. When the satellite potential is similar to the thruster potential, the emitted and return currents become identical and the satellite stops charging.

The potential of the spacecraft was measured using a sensor similar to the one described in 2.2.6. The sensor was mounted outside of the vacuum chamber used. A high-voltage, low leakage capacitor was connected between the satellite and the chamber ground. This capacitor artificially increases the self-capacitance of the satellite making charging transients non-instantaneous. The capacitor had a capacitance of 147nF. A schematic of the static experiment is shown in Fig. 4.21.

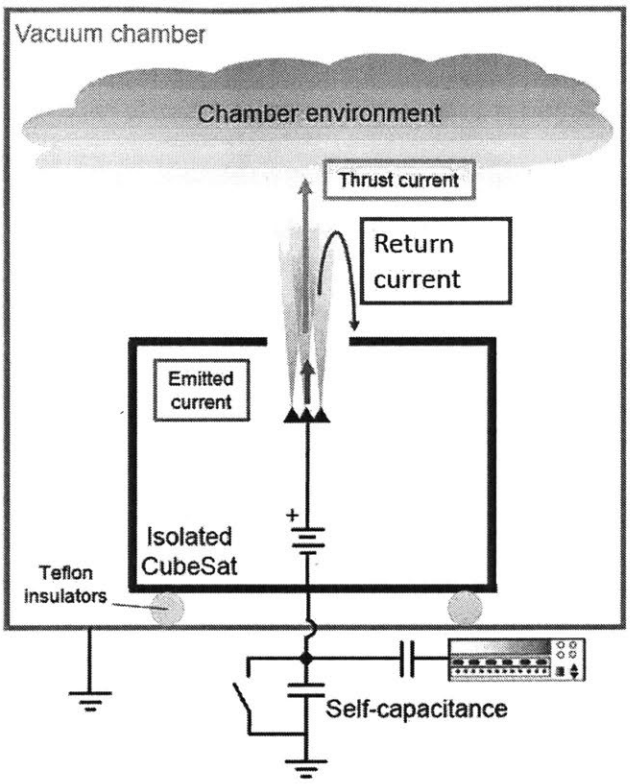

Fig. 4.21 Static test configuration.

When the thruster fires, the isolated CubeSat will charge up at a rate determined by the emitted current and the self-capacitance of the satellite and the capacitance of the charge sensor. The results of a representative test using this configuration is shown in Fig. 4.22.

Notice the emitted current is multiplied by 10, to help in the visualization. At the beginning of the test, the voltage is increased in steps to eventually achieve emission. Around time 42 s, the voltage is high enough to trigger emission. The emission at these voltages is so low, around 1 μA, that the emitted current measurement circuitry of the PPU is not able to measure it reliably.

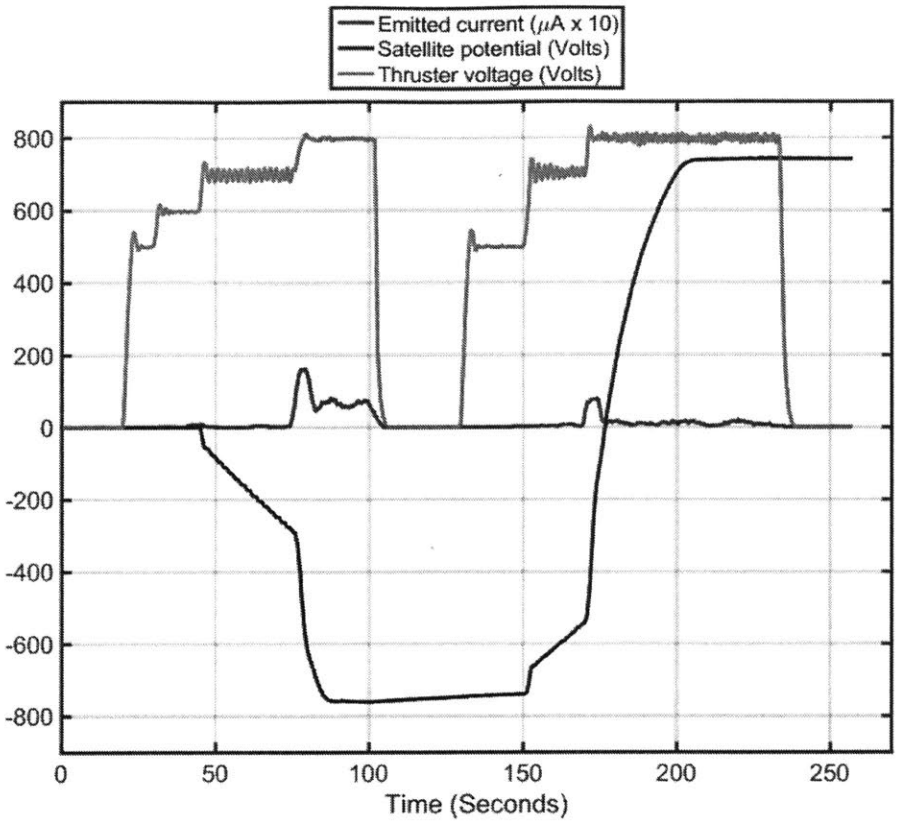

Fig. 4.22 Single electrospray thruster firing in static test

The effect of this relatively low emitted current can be seen on the satellite potential. Since the thruster is emitting positive ions, the spacecraft charges up to a negative potential. The dynamics of the charging can be seen thanks to the large capacitance artificially introduced in the system. Between times 42 to 75s, the ripple in the high voltage power supply creates a ripple in the emitted current which in turn creates a ripple on the potential on the satellite. This specific test was conducted with a preliminary voltage controller algorithm on the PPU, which resulted in significant voltage ripple. Later experiments used a more robust voltage controller that reduced ripple considerably. Once the satellite reaches a potential close to the thruster voltage, the satellite stops charging due to the return current providing neutralization. The return current was not measured in this test. At this point in the test, time 75s, it can be assumed that all the emitted current eventually makes it back to the satellite as return current. At time 102 s, the voltage is turned off and the thruster stops emitting. The potential on the spacecraft remains constant since there are no current sources acting on it. At time 150s, the voltage in the negative polarity is high enough to trigger emission. Since the thruster emits negative ions, the satellite

charges up positively limited by the return current. In a similar manner as before, when the voltage is turned off the charge on the satellite remains constant.

During some portions of this test, the voltages to the thruster were very close to the startup voltage, which made emission very sensitive to any voltage ripple and somewhat unstable. Notice how the emitted current transients follow the overshot and undershoot of the applied voltage. More importantly, notice how the satellite potential never exceeds the applied thruster potential. This effect can be attributed to the return current which now has been demonstrated both in simulations and experiments. **We can then conclude that the satellite potential will never be larger than any thruster potential due to the return current.**

As stated earlier, the thrust produced by an electrospray thruster is proportional to the emitted current. Therefore, it is important to study the potential effects of spacecraft charging on the emission parameters of the thruster. If one could change the potential at which the satellite charges during thruster emission, the effects of spacecraft charging and emitted current could be studied. Such an experiment was conceived using an identical setup as shown in Fig. 4.21. In this case, a switch is used to discharge the capacitor used to artificially increase the self-capacitance of the satellite. When the switch is engaged the satellite is grounded to the chamber. The test consisted of firing the thruster at a constant voltage and engaging this switch, Fig. 4.23.

Notice that the thruster voltage trace is inverted and the emitted current is multiplied by 10, to help in the visualization. At the beginning of the test, the voltage is increased until the thruster starts emitting. Since the thruster emits negative particles the satellite charges up positively. Once a stable current is reached, 48s, the voltage is left constant. The satellite potential also remains constant at this point. Between 70 and 100s, the switch that discharges the satellite is engaged (shown by the green regions in the plot), and the potential of the satellite is forced to zero. As soon as the switch is disengaged (shortly after being activated), the satellite is allowed to charge once more and the satellite potential climbs to a value slightly below the thruster potential. The return current does not allow the satellite potential to increase beyond the thruster potential. Notice how the abrupt changes in satellite potential caused by engaging and disengaging of the switch do not produce any noticeable difference in the emitted current. Since the CubeSat can be thought of as a closed system, its charge should not modify any internal

potential differences. **It can then be concluded that the satellite potential has no influence on the thruster's emission characteristics.**

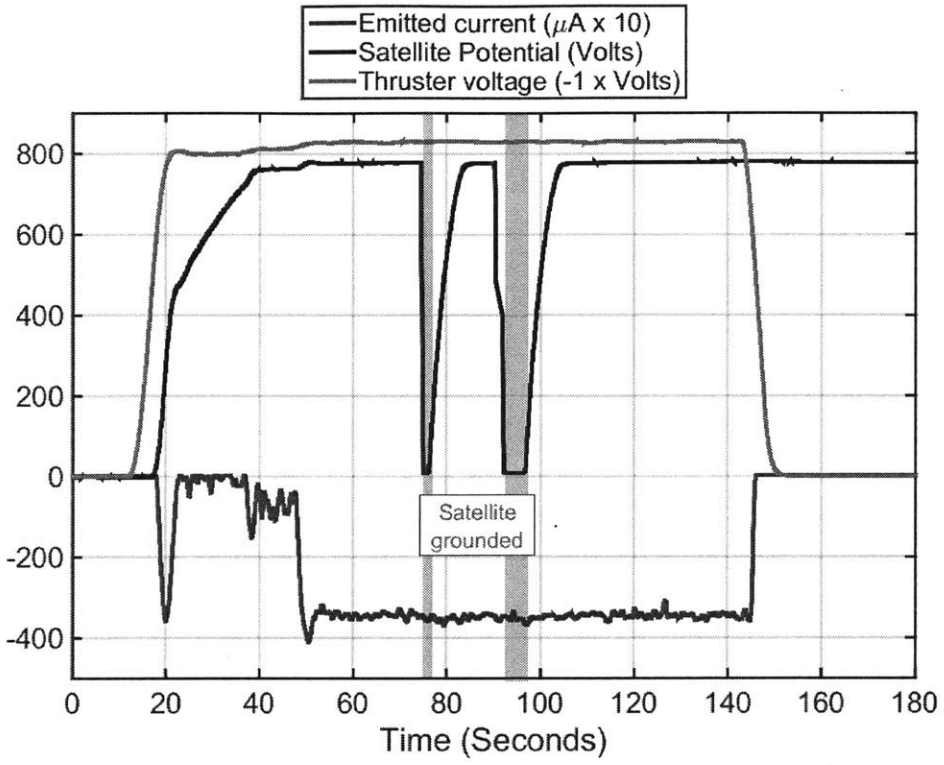

Fig. 4.23 Single thruster firing in static test while the satellite is manually discharged.

4.5.2 Charge sensor shield

The magnetic levitation in the MagCube provides an ideal electrically-isolated environment in which to perform spacecraft charging experiments. The very low self-capacitance of the CubeSat, tens of pF, translates into almost instantaneous changes in spacecraft potential for any non-zero current flowing into or out of the satellite. In a similar fashion, any external current that makes it to the charge sensor plate would be registered as a bogus satellite potential drift. Since the charge sensor is basically a capacitor, any external current source would raise the potential of this capacitor. Ions emitted by the thrusters, or secondary particles created from the collision of energetic ions with the chamber walls could, in some circumstances, reach the charge sensor and deposit their charge on the sensor's plate producing a bogus drift. Preliminary experiments on the MagCube showed evidence of bogus drift in the satellite potential signal. A set of additional experiments and modifications were carried out to reduce the effects of the

bogus satellite potential drift. This effect is not present in the static tests described previously since the charge sensor is physically outside the vacuum chamber.

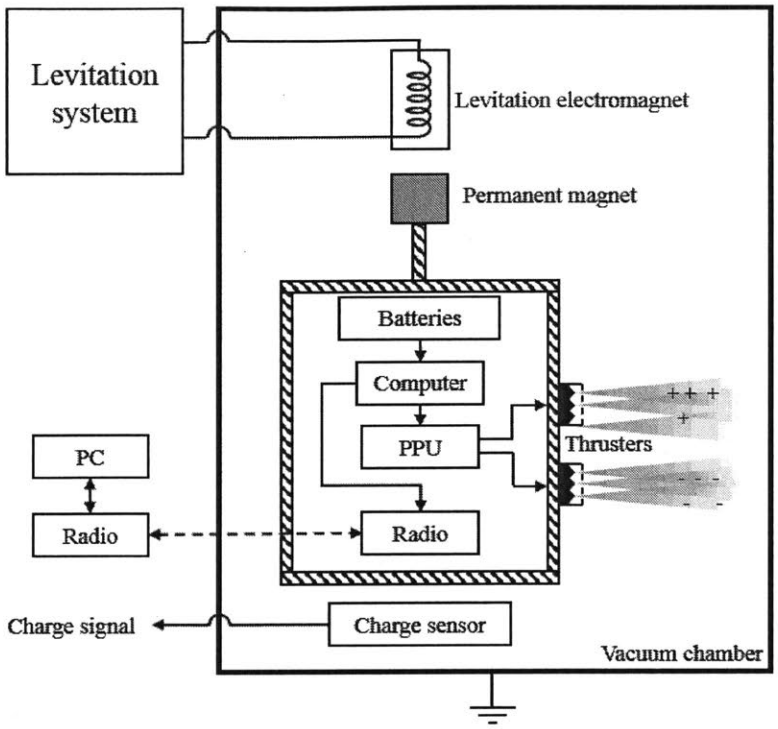

Fig. 4.24 MagCube tests with thrusters in the bipolar configuration.

A schematic of the preliminary tests is shown in Fig. 4.24. The tests consisted of firing a single thruster in two different polarities and recording the satellite potential signal produced by the charge sensor. The results for positive and negative emissions are shown in Fig. 4.25.

Notice that the thruster voltage trace is inverted, to help in the visualization. The top chart shows the charge drift due to negative emission and the one on the bottom due to positive emission. Notice that on both polarities the spacecraft rapidly reaches the thruster potential and then keeps increasing, something that would violate the conclusions reached previously. The satellite potential drift, volts per unit time, seems to be proportional to the emitted current. This leads to the hypothesis of some of the emitted ions or secondary particles created by them, make it into the charge sensor plate and disrupt the measurement. There seems to be an onset current in which satellite potential drift starts to occur, as can be seen on minute 0.7 on the positive emission plot. The drift for a given current is very different in each polarity. On the negative polarity, we can estimate a drift of 500 volts per hour while emitting

-100uA. In the positive polarity, for +100uA, the drift is estimated to be 30 kilovolts per hour, or around 500 volts per minute. Further research is needed in order to explain such differences in satellite potential drift for each polarity.

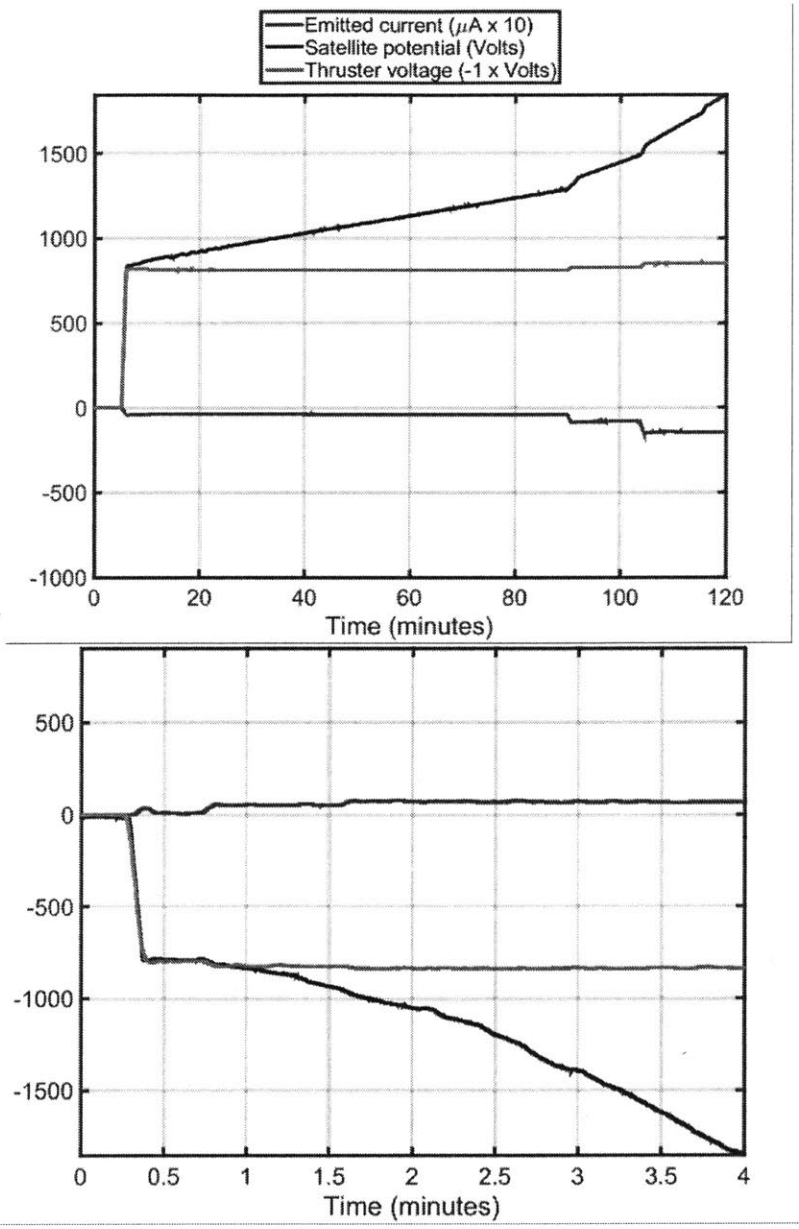

Fig. 4.25 Satellite potential drift. Top is negative emission, bottom is positive emission.

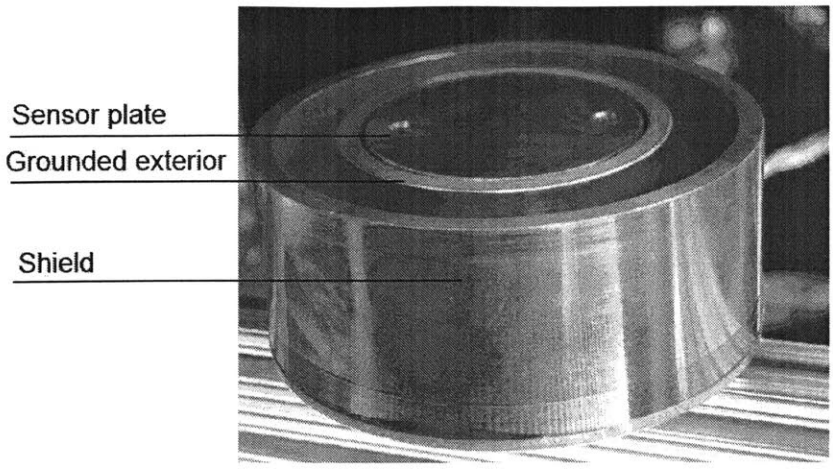

Fig. 4.26 Charge sensor equipped with shield.

To reduce the effects of the bogus satellite potential drift one must then reduce the amount of charged particles that are able to reach the charge sensor plate. A mechanical barrier, a shield, is used for this purpose. The charge sensor assembly, sensor plate and grounded exterior, are surrounded by a large tube that acts as a shield. The charge sensor assembly is flush with the upper surface of the tube, Fig. 4.26.

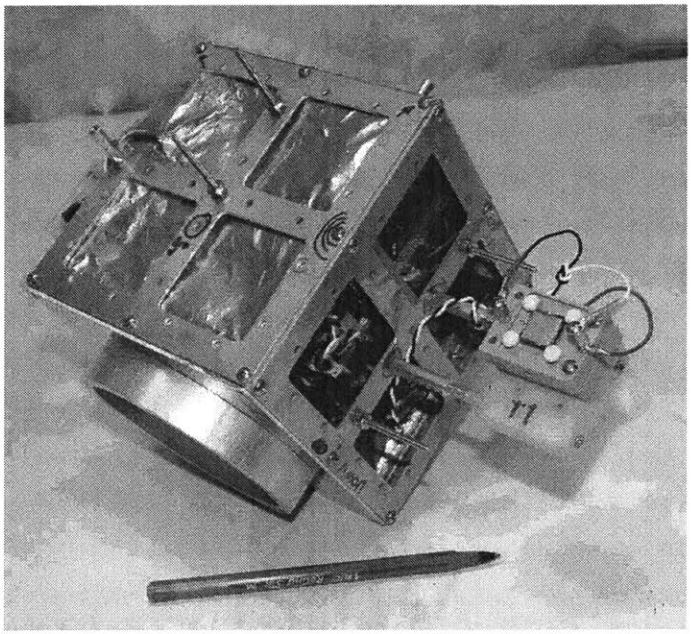

Fig. 4.27 Guard visible on the bottom side of the CubeSat.

The levitated CubeSat is equipped with a guard, a smaller diameter tube that is able to fit between the grounded exterior of the charge sensor and the shield tube when levitated. These mechanical barriers form a structure that resembles a maze that charged particles would have to cross in order to reach the charge sensor plate, Fig. 4.28.

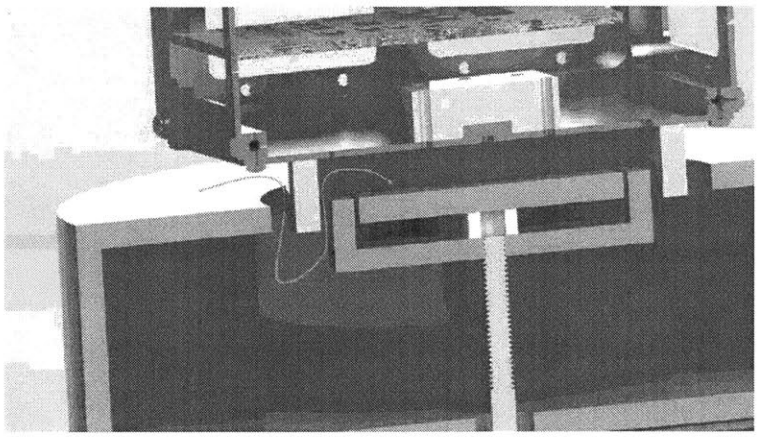

Fig. 4.28 Sliced view of charge sensor shield and CubeSat guard.

These mechanical barriers seemed sufficient to reduce the influx of charged particles to the charge sensor. With this modifications the charge sensor was able to provide reliable measurements on the satellite potential.

4.5.3 Single thruster experiments

Once the charge sensor was equipped with a shield, experiments in the MagCube proceeded. The first experiments recreated the static case described previously by also firing a single thruster. The results of such a test are shown in Fig. 4.29.

Notice that the thruster voltage trace is inverted and the emitted current is multiplied by 10, for visualization purposes. At the beginning of the test, a positive voltage is applied to the thruster, therefore positive current is emitted. The satellite is then left with excess negative charge, which translates to a negative satellite potential. Due to the extremely low self-capacitance of the satellite (estimated to be 10pF using a spherical geometry) this charging occurs within 2 ms or less with the 20-60 μA emitted current. The satellite potential magnitude follows the thruster voltage magnitude and does not exceed it. At time 50s the thruster voltage is +850V and the satellite potential is -843V. The emitted current spikes seen at the beginning of every voltage setpoint change can be attributed to a fast overshoot of the thruster potential induced by the non-ideal PPU voltage controller. The high voltage monitor circuitry of the PPU

is filtered using an RC filter, therefore some lag is expected between the actual voltage being applied to the thruster and the reported voltage. This explains the lag of the satellite potential with respect to the thruster potential, Fig. 4.29 (c). The maximum thruster voltage fall time was measured to be 5 seconds while the maximum rise time was 4 seconds.

When the thruster voltage is turned off, time 70s, the charge on the satellite is lost and the potential of the satellite reaches zero volts. Notice that in the absence of secondary current sources, the satellite should have retained its charge as it did on the test in Fig. 4.22. The charge loss behavior is only seen when emitting positive ions and at currents above 30 μA. It is hypothesized, that positively charged, secondary particle emissions generated by the ion beam colliding with the chamber wall could be the source of these external currents. Expelled secondary electrons generated by the collision of positive ions that return to the satellite could also account for this external current source. It should be noted that the test in Fig. 4.22 was performed in a smaller chamber and the charge sensor was placed outside the chamber. These experimental differences could account for the absence of the charge loss behavior.

At time 90s, the voltage is reversed to a negative polarity and the thruster starts emitting negative ions. The satellite charges rapidly to the positive emission potential and stabilizes. At time 110s, the thruster potential is -831V and the satellite potential is +828V. When the voltage is turned off (time 130s), due to the finite turn off time as can be seen in Fig. 4.29 (b), the satellite potential follows the voltage applied to the thruster until the thruster stops emitting completely. Notice that in this polarity the charge on the satellite is not completely lost and it remains with a +604V potential after firing. A sensor anomaly could also explain some of these behaviors.

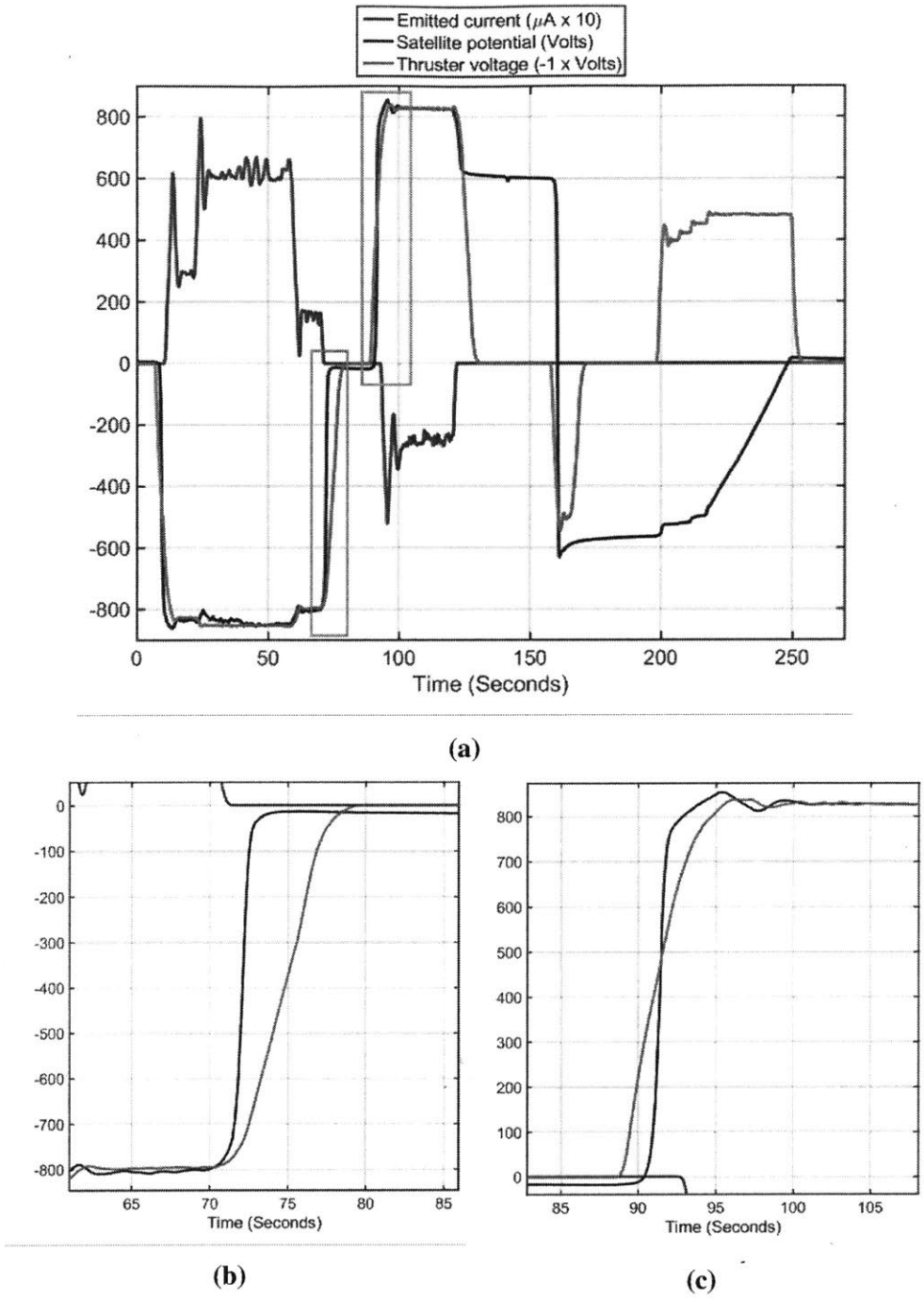

Fig. 4.29 Results of single electrospray thruster test in maglev testbed. (a) displays the complete test. (b) shows a detailed view of the turn-off transient shown in the leftmost box region of (a). (c) displays a detailed view of the turn-on transient shown in the rightmost box region of (a).

As previously explained, the pF self-capacitance of the satellite makes any thruster-induced charging practically instantaneous with respect to the acquisition systems sampling rate. Therefore, the satellite potential changes are seen as steps. Charging processes would take longer if very low currents were fired from the thrusters (exponential section of the I-V curve). This opens the possibility to explore some of the charging dynamics with the same experimental setup. Beginning at time 160s, in Fig. 4.29 (a), a positive voltage of 500V is applied to the thruster and the overshoot of the thruster voltage quickly charged the satellite negatively to -605V. The voltage is turned off and the satellite potential remains constant. Since the voltages are low, the emitted currents are also low, and the charge loss behavior described previously is not seen.

At time 200s, -400V are applied to the thruster and increased slowly until the satellite potential begins to change. At time 215s, while applying around -500V, the thruster is emitting such a small current that the charging behavior is slow enough to be clearly resolved by the instrumentation, a nearly linear ramp in this case. The current measurement circuitry in the PPU is not able to detect the small emitted current. However, given the estimated capacitive properties of the levitated satellite and assuming stable emission at these low voltages, it was calculated that the thruster was emitting 133 pA of current during this time. These low currents could also be attributed to electron field emission.

In order to validate the model explained in section 4.2, a test with a single thruster was simulated. The simulation, shown in Fig. 4.30, was performed using similar voltage profiles as the previously described experiment. The self-capacitance of the satellite was estimated to be 10 pF. The simulation parameters are shown in Table 4.7.

Table 4.7 Simulation parameters for single thruster test.

	Parameter	Value	Units
T_1	V_{str}	800	V
	A	1.075×10^{-24}	V^{-1}
	B	1.173	$V^{-1/2}$
	R	1.074×10^{8}	Ω^2
	β	1	%
T_2	V_{str}	850	V
	A	1.075×10^{-24}	V^{-1}
	B	1.173	$V^{-1/2}$
	R	1.074×10^{8}	Ω^2
	β	10	%
	C_{SC}	50	pF
	C_{HV}	100	nF

Notice the resemblance of the simulation results, Fig. 4.30, with that of the experimental test of Fig. 4.29. However, due to the absence of secondary current sources in the model, the simulation does not capture the charge loss anomaly described earlier.

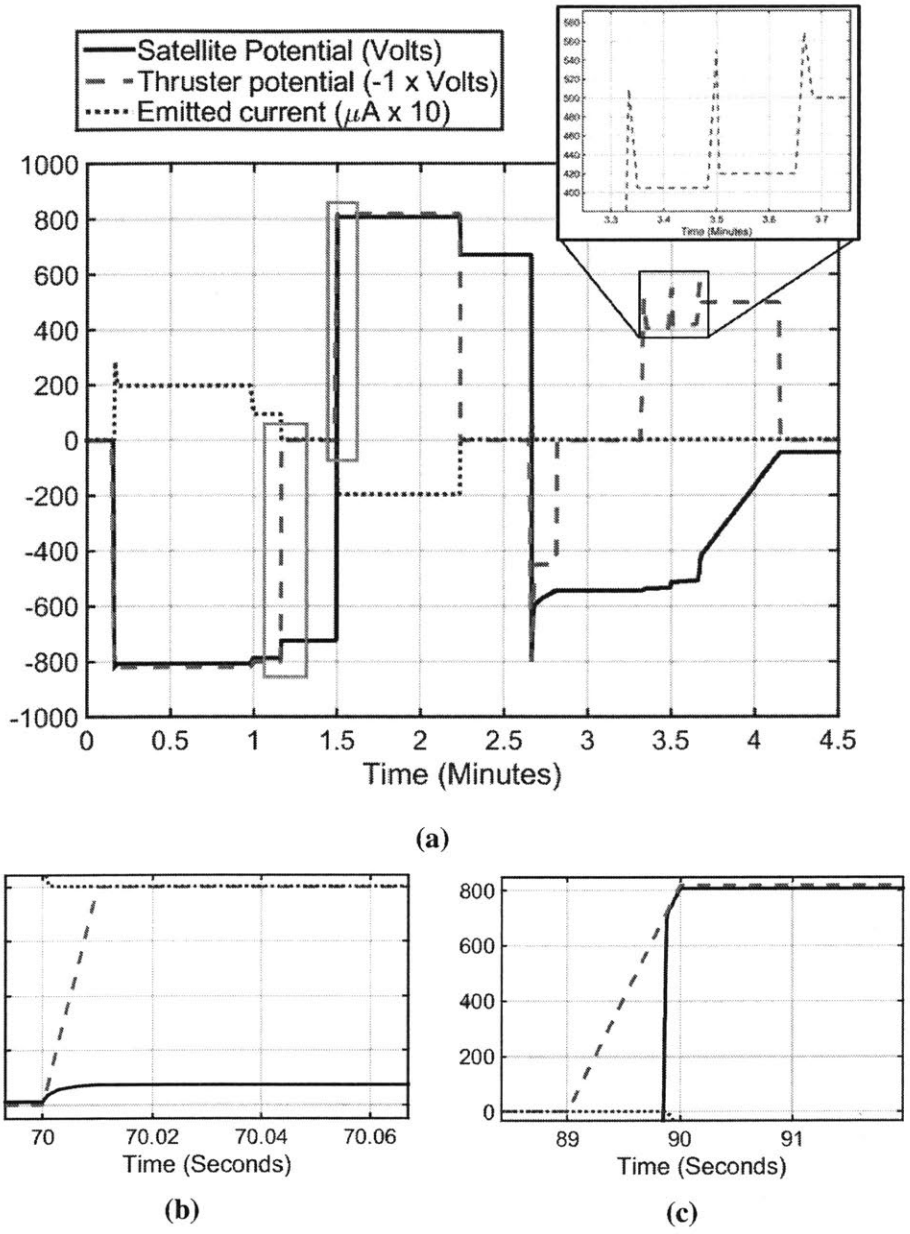

Fig. 4.30 Recreation of results of single thruster test in maglev testbed by simulation. (a) displays the entire simulation. (b) and (c) show the transient details of the leftmost and rightmost boxes of (a) respectively.

4.5.4 Experimental evidence of return current

The PPU electronics are able to monitor the current collected by the extractors, which is reported as intercepted current. When the satellite is levitating, it is able to charge and therefore return current will most likely be present. Firing a single thruster will ensure spacecraft charging and therefore return current. On their return journeys, the charged particles that make up the return current, impact the satellite in various locations, one of them the extractors. Therefore, some portion of the return current could be measured as intercepted current. If the satellite is not levitating and is in contact with the grounded testbed frame there is no spacecraft charging and the return current should be zero.

To quantify the difference in collected currents between these two situations, a single-thruster experiment was performed using the same setup as described previously. The results of the test are shown in Fig. 4.31. The thruster voltage trace is inverted to help visualization. At the beginning of the experiment the satellite is levitating, therefore electrically isolated. At minute 0.2 the thruster is fired with a negative polarity, which positively charged the satellite. The interception current is a fixed fraction of the emitted current, around 50%. When the voltage is turned off, at minute 1.1, the satellite potential follows the thruster potential until the startup threshold is reached. For this particular thruster, the startup voltage was around 780V. The thruster is then fired in the opposite polarity with similar results as before, from minute 1.3 to 2.5. Notice the charge loss after turning the thruster off, an effect discussed previously. At minute 2.7, marked with a vertical dashed line, the levitation controller is turned off and the satellite drops and contacts the grounded structure of the testbed. Once more, with the satellite grounded, a positive voltage is applied to the thruster. Positive current is then ejected (around 40 μA at 900V). When the satellite is grounded the interception current is less than 10%. The thruster is then fired in the negative polarity where the interception fraction is close to 1%.

When the satellite is levitating the return current limits the satellite potential to a value no higher than the thruster potential. When the ions return to the satellite, a significant portion of them hit the extractor, depositing their charge. The returning ions are then measured as an abnormally high interception current, up to 50% in the levitated case. At that point, the monitoring circuitry is reporting the interception current plus the return current. If the satellite is grounded there is no charging, therefore no return current, and the monitoring circuitry reports only the nominal interception current.

Returning ions, besides providing neutralization, modify the optical properties of surfaces they impact. In this test, a significant portion of the returning ions were colliding with the extractor. After hours of continuous firing in this configuration, the gold coating on the extractor was significantly discolored, see Fig. 4.32. Severe discolorations are not present on thrusters that are fired in a grounded scheme, even if they fire for hundreds of hours.

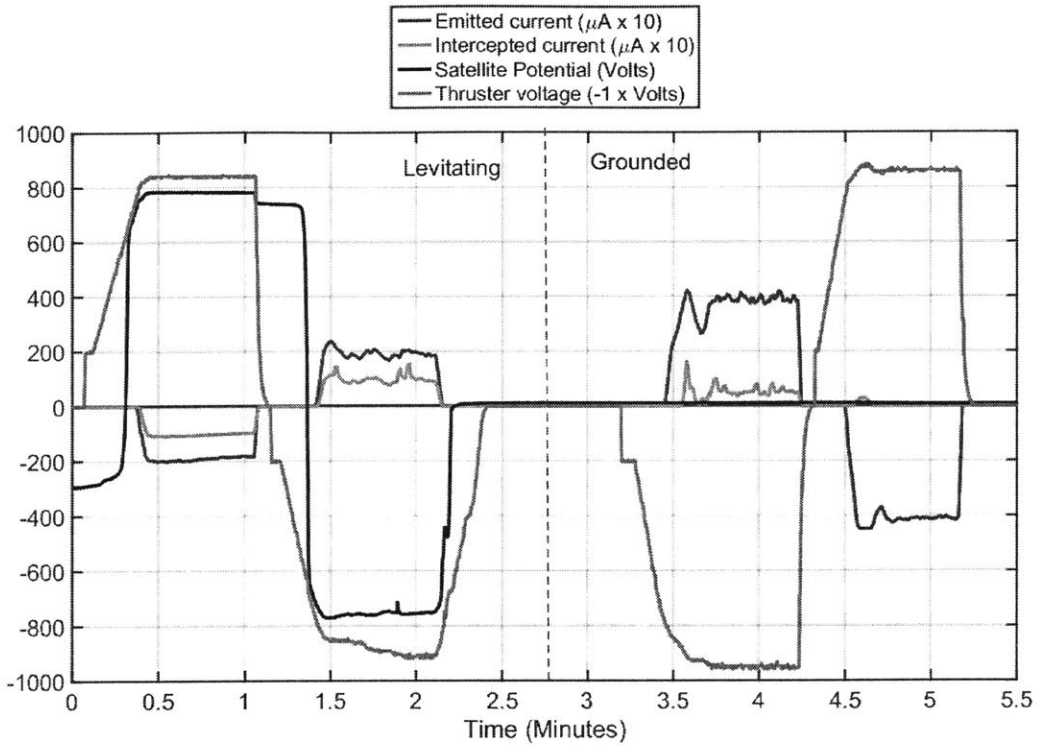

Fig. 4.31 Evidence of return current while firing an electrospray thruster in the maglev tested.

4.5.5 Bipolar operation experiments

The more realistic scenario of bipolar operation was explored in the MagCube. The schematic of the setup used in this experiment can be seen in Fig. 4.24. Charge balancing is achieved by the operation of two thrusters firing in opposite polarities. The thrusters were mounted on the satellite so as to fire in opposite directions to maximize torque. The results are summarized in Fig. 4.33. Notice that the emitted currents are multiplied by a factor of 10.

The thrusters were fired using a high voltage square wave profile that switched polarity every 30 seconds, similar to the waveform used on the simulation shown in section 4.3. The

satellite potential remained within a ±200V range during bipolar emission. Thanks to the self-regulating mechanism of the floating power supply, during emission, the emitted currents differ by less than 0.9μA as reported by the PPU telemetry. Assuming that both emitted currents are identical during stable emission, the only reason why the satellite charges during each alternation cycle is due to a difference in interception fractions. Any charging due to the transient in which C_{HV} charges is mitigated by the return current. Between times 27 and 55 seconds, T_1 is emitting positive ions while T_2 emits negative ions. The satellite potential at that time is positive, therefore the extractors must be collecting a net positive current. It can be inferred that T_1 has a higher interception fraction than T_2.

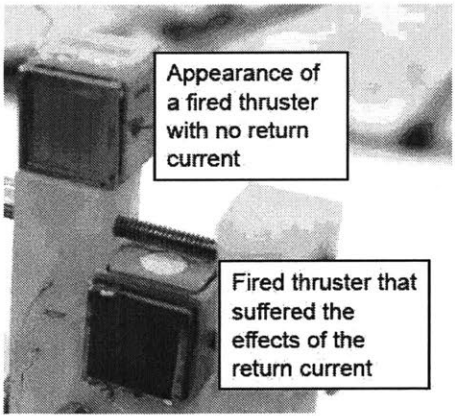

Fig. 4.32 Effects of the return current on the extractor.

Table 4.8. Parameters used for simulation.

	Parameter	Value	Units
T_1	V_{str}	915	V
	A	1.075×10^{-24}	V^{-1}
	B	1.173	$V^{-1/2}$
	R	430×10^{6}	Ω^2
	β	1.4	%
T_2	V_{str}	900	V
	A	1.075×10^{-24}	V^{-1}
	B	1.173	$V^{-1/2}$
	R	430×10^{6}	Ω^2
	β	1	%
	C_{SC}	10	pF
	C_{HV}	1	nF

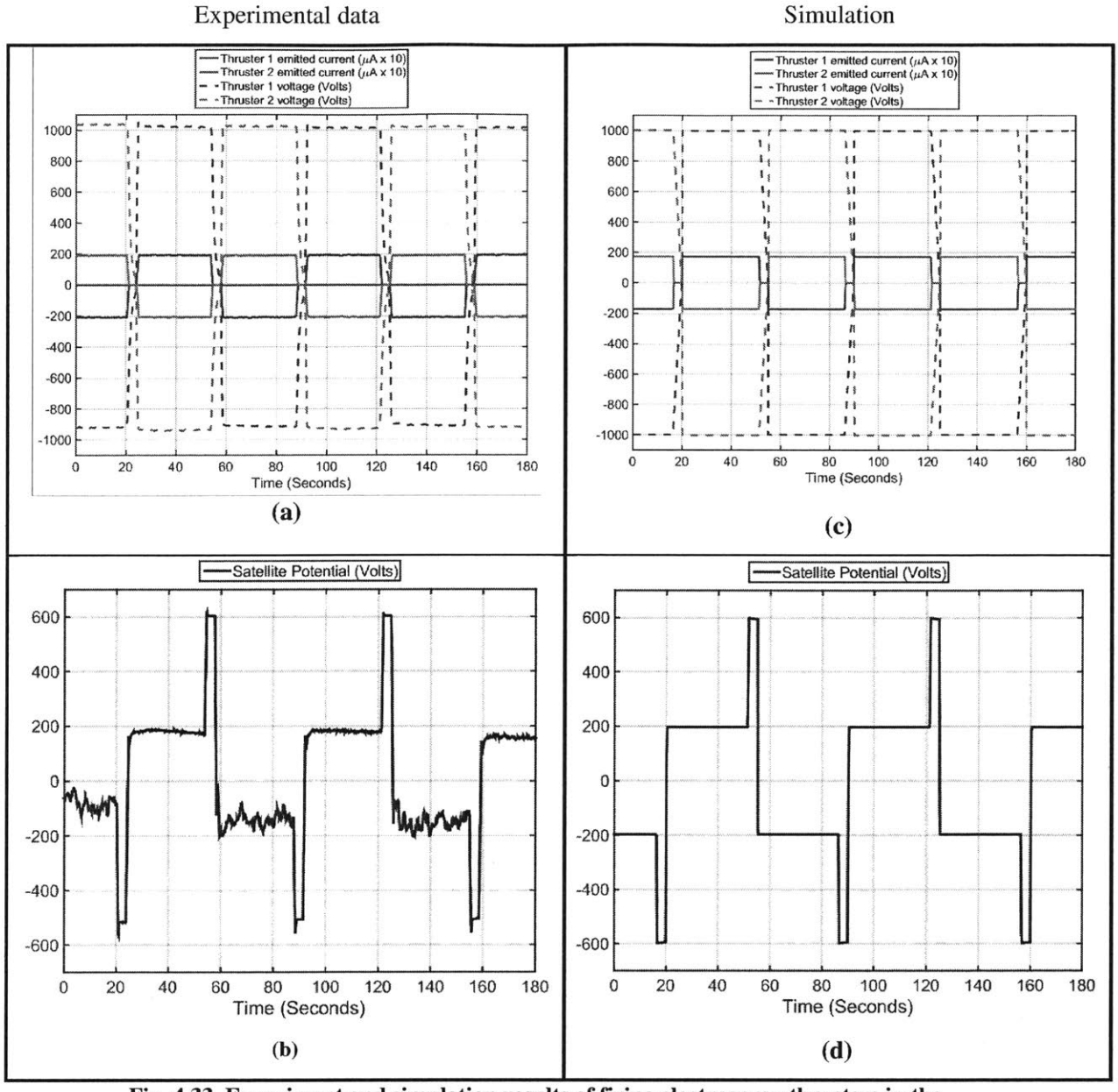

Fig. 4.33 Experiment and simulation results of firing electrospray thrusters in the bipolar configuration. (a) and (b) show measured thruster variables and measured satellite potential, respectively. (c) and (d) display the simulated thruster variables and simulated satellite potential, respectively.

The satellite potential during bipolar emission has a more dynamic behavior compared with the single thruster cases, especially when thruster T_1 emits negative current. Whenever the power supplies turn off, for example at time 20s, the satellite jumps to a higher potential and remains constant. This jump in potential can be attributed to the short, but finite, time it takes

the thruster potential to fall to zero and the differences of startup voltage between thrusters. The turn off transient of the power supply can be seen in Fig. 4.33(a). While the thruster voltages are falling, the startup voltage of T_1 is reached first and transitions to the low current exponential profile. At that instant, T_2 is still emitting a significant amount of positive ions which rapidly forces the satellite potential to -500V. Shortly after, the potential across T_2 reaches a point where it stops emitting completely. At this time, since there is no significant emission, the potential of the satellite remains constant until the thrusters are activated again. It can then be concluded that for this test T_2 had a slightly lower startup voltage than T_1. At time 90s, the thruster voltages are reduced, the polarity of the power supply is flipped and the satellite potential reaches a new equilibrium state with a negative polarity.

Experiments in the MagCube showed an interesting effect, for higher average emitted currents the satellite potential envelope was reduced. This effect can be appreciated in Fig. 4.34. In this test two thrusters in the bipolar configuration are fired at distinct current levels. The hypothesis is that with higher currents there is an increase in quantity and types of charged species within the ion beams. A larger number of particles of different energies facilitate neutralization and therefore the satellite does not need to charge as much to collect the necessary neutralizing particles from the return current. It could also be that at higher emitted currents the differences in the emission profiles of the thrusters becomes less pronounced and therefore a more equilibrated emission follows, which tends to reduce the charging potentials.

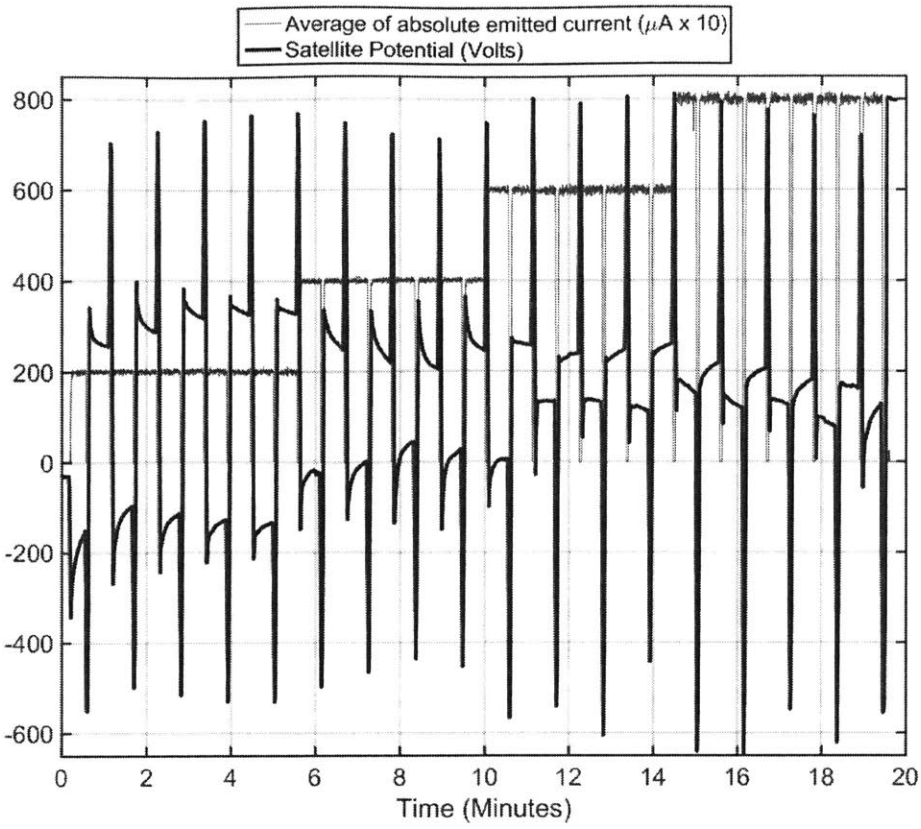

Fig. 4.34 Satellite potential for different emitted current levels.

Following the trend, the satellite potential profile while emitting low currents proved to be more sensitive to changes in the thruster voltages. This can be seen in Fig. 4.35. In this test the thruster voltages applied to both thrusters did not exceed 500V. Therefore the thrusters were in the exponential section of their I-V curve, emitting very small amounts of current, ~pA-nA. The PPU is not able to read such small currents. The thruster voltage was constant for couple of minutes, while alternating, and then it was raised slightly. The voltages at the top of Fig. 4.35 represent the absolute thruster voltages applied during each phase. The satellite started with a ~600V produced by previous tests. Notice the evolution of the satellite potential. It is challenging to interpret what is forcing such a strange satellite potential profile. It could be that at those low thruster voltages emission is not stable. Further investigation is needed to understand this behavior including the interaction of the emitted ions with the facility walls.

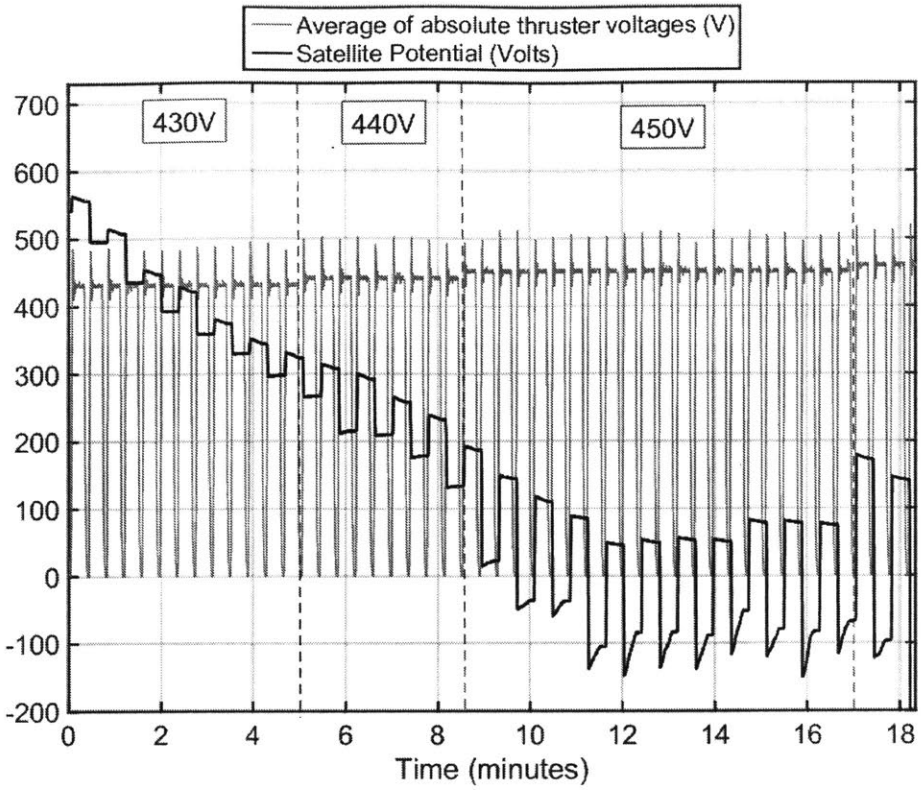

Fig. 4.35 Satellite potential evolution while emitting low currents.

4.5.6 Experiments with plasma

Simulations of the electrical model showed the significant neutralizing effects of space plasma on a spacecraft operating electrospray thrusters. To experimentally characterize these effects a hot-cathode was placed in proximity to the testbed to recreate the space plasma environment. The cathode construction and plasma characterization are described in sections 2.3 and 2.3.1 respectively. As explained on those sections, only the dense LEO-like plasma was successfully characterized using a Langmuir probe. Nevertheless, by using data gathered from experiments, the characterization of parameters of the higher altitude plasmas was possible.

Plasma leakage

Preliminary tests with plasma produced a strange behavior in the measured variables. Interpretation of the data led to the conclusion that the plasma was leaking into the CubeSat electronics and more importantly into the thruster emitters. As explained in section 1.2.3, any orifice that is larger than the plasma Debye length will allow the plasma to enter. Since initially the CubeSat had exposed electronics and thrusters the plasma flowed freely towards them, Fig. 4.36. The high voltage points in the electronics collected significant plasma currents corrupting the behavior of the PPU.

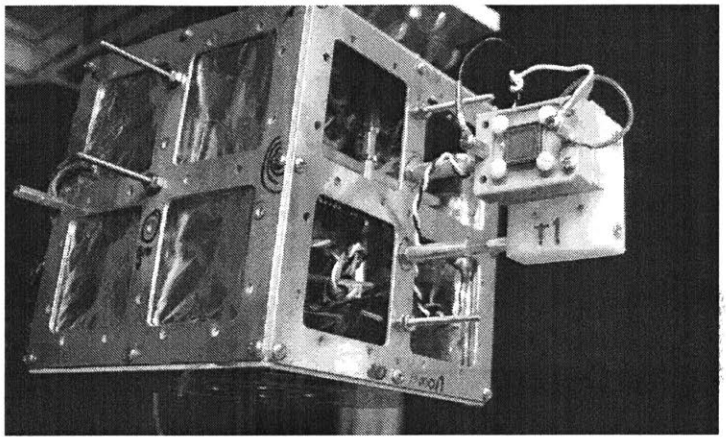

Fig. 4.36 Exposed electronics and thrusters in the levitated CubeSat.

The plasma leakage was especially significant when applying a high voltage to the thrusters. The way the thrusters were mounted on the CubeSat, meant that the large side openings of the thrusters were exposed to the plasma (red arrows in Fig. 4.37). When a positive high voltage was applied to the device, electrons in the plasma were collected by the thruster substrate and frame inducing a bogus emitted current.

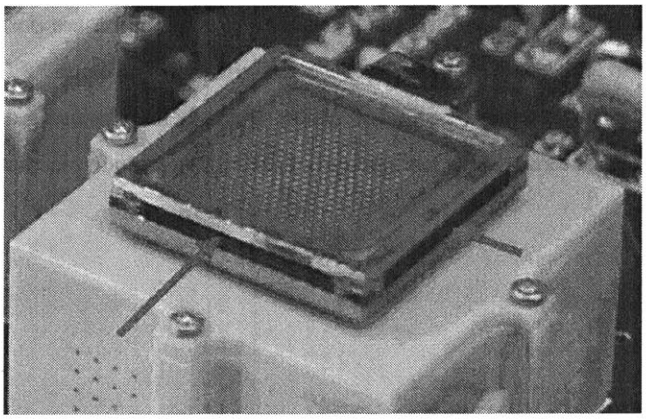

Fig. 4.37 Side openings in thrusters.

A test which shows the effects of plasma leaking into the thrusters is shown in Fig. 4.38.

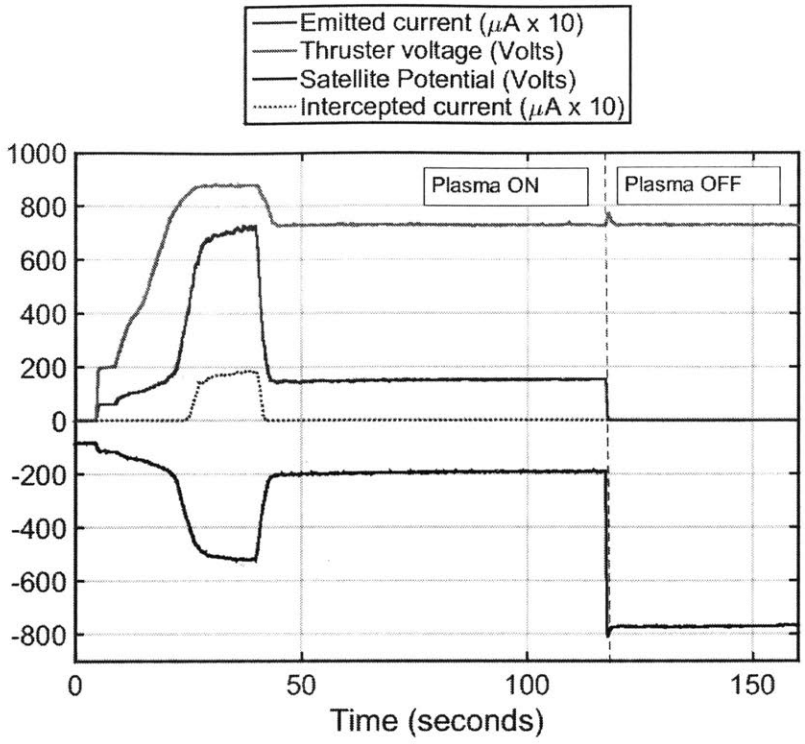

Fig. 4.38 Effects of plasma leaking into thruster substrate.

In this test, a single thruster was fired while the cathode was generating a plasma around the MagCube. Notice that the emitted current circuitry registers a significant current, ~15μA when the thruster voltages are below 600V. This voltage is significantly lower than the thruster startup voltage. The anomalous current can be attributed to the plasma leaking into the thruster. At voltages above 800V the thruster emits and the satellite charges accordingly. Notice that the satellite potential does not reach the thruster voltage. The reason for this is the neutralizing effects of the plasma. As the satellite charges negatively, ions in the plasma begin to be collected by the spacecraft reducing its potential. As always, the return current contributes the rest of the neutralizing current as can be seen by the anomalously high interception current measured. A similar effect was described in Fig. 4.31. At time 45, the thruster voltage is reduced to stop any significant emission. The satellite potential follows. Even though the thruster voltage is below the startup voltage, the thruster is still emitting small amounts of current as it is in its exponential part of the I-V curve. This small currents is responsible for the -200V satellite potential seen between time 40 and 118. Notice that the plasma current is affecting the emitted current measurement during this time. At time 118 seconds, the cathode is turned off. At this instant the plasma disappears and the satellite immediately charges to the thruster

voltage, since there is still some emission occurring. Notice the absence of anomalous emitted current when the cathode is off.

To counteract the plasma leakage a mount that shielded the thrusters and electronics from the environment was designed. The mount mimicked the way electrospray thrusters would be mounted on a real satellite, Fig. 4.39. In a real satellite, the thrusters would be positioned underneath a plate with precise cutouts, allowing only the extractors to be exposed to the environment. This reduces the areas where plasma can leak into.

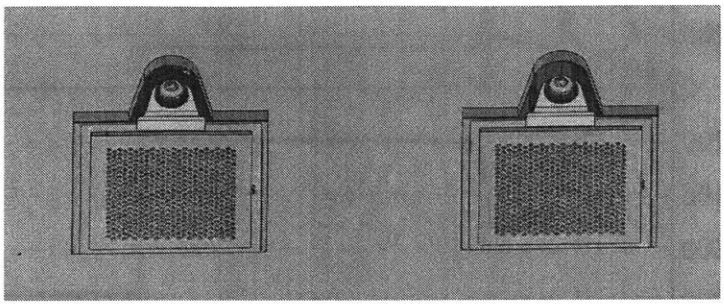

Fig. 4.39 Electrospray thrusters on the top face of a CubeSat.

The connections from the thruster mounts to the satellite electronics were made using shielded coaxial cable with shielded connectors. Shielded cables are necessary so the high voltage present in the conductors does not attract plasma, which would then be collected on the cable insulation. A grounded shield around the HV conductor eliminates the attracting electric field and no significant plasma current is deposited on the cable insulation. The thruster mount exposes only the extractors to the environment, Fig. 4.40. The metallic structure that makes the mount is electrically grounded. Furthermore, a negative bias is applied to the otherwise grounded extractors to repel any electrons that might leak through the extractor apertures. The satellite was also completely covered with grounded metallic plates or foils. This shielded the CubeSat electronics from the external plasma.

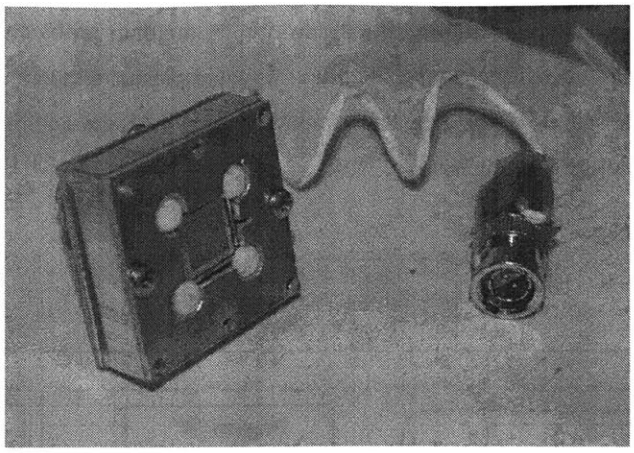

Fig. 4.40 Shielded thruster mount and shielded connector.

Dilute plasmas

Once the thrusters and satellite were shielded from the plasma, experiments could proceed. In the first round of experiments, to simplify the interpretation of the data and ensure spacecraft charging, a single thruster was fired at a constant current while the external plasma parameters were varied. The setup was identical to previous experiments and can be seen in Fig. 4.24. The results of such a test are shown in Fig. 4.41.

At the beginning of the test the thruster is emitting ~26μA of constant negative current, the cathode is off (no plasma), and therefore the CubeSat charges positively to almost the thruster potential ~ 1000V. At this point the spacecraft is being neutralized completely by the return current. At time 20, the cathode is activated by passing a 3.8A current through the tungsten filament and biasing it to -5V. A plasma is then generated by the cathode and fills the vacuum chamber. The plasma density at this point is not high enough to neutralize the spacecraft completely but reduces de satellite potential to 620V. Notice that the thruster voltage and the emitted current do not vary during this transition. The emitted current is not affected by the external plasma. At time 45, the current passing through the cathode's filament is increased to 4.0A. The plasma density increases accordingly and the satellite potential is reduced to ~380V. It is clear that higher density plasmas are more effective neutralizers.

From the cathode characterization efforts described in section 2.3.1, it was known that the plasma density generated at these filament currents was low enough to be considered thick-sheath regime. As explained previously, the Langmuir probe used in the plasma characterization was not able to correctly measure plasma properties with such low density.

Nevertheless, the plasma temperature estimate from the Langmuir probe analysis should still be valid for these low density plasmas. With an estimated plasma temperature, we can try to approximate a plasma density using the data available in Fig. 4.41, the satellite dimensions, and assuming certain thruster parameters.

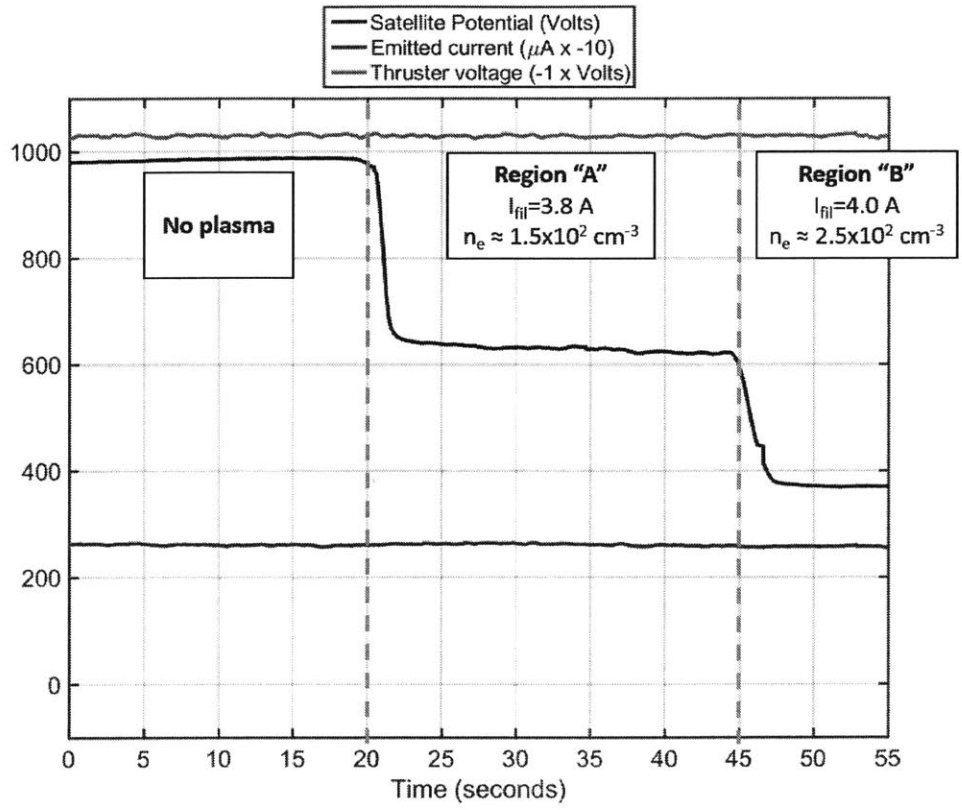

Fig. 4.41 Electrospray firing at constant current while the plasma parameters are varied.

When the satellite potential is constant, we know that the satellite's input and output currents are identical. In this test, the current flowing out of the spacecraft is only the thruster emitted current, ignoring the interception current since it has such a small magnitude. The currents being collected by the satellite are the return current and the plasma current. This gives us the following equilibrium condition:

$$I_{emitted} = I_{return} + I_{plasma} \qquad \textbf{Eq. 4.8}$$

The return current can be calculated by assuming a representative energy distribution profile of the emitted ion beam, and by knowing the potential at which the satellite floats to. For this

analysis, the energy distribution profile shown in Fig. 4.7 was used. Since the satellite potential is relatively large and positive, we can assume that the plasma current is equal to the electronic saturation current. We can then use the thick-sheath equation for the electronic current, Eq. 1.12, to calculate the plasma current being collected by the satellite. In this case the levitated structure geometry is closer to a cylinder than to a sphere so the cylindrical thick-sheath factor is used. Since the filament current was the only parameter varied during this test, the plasma temperature is assumed the same as when the cathode generates a LEO-like plasma, around 5eV.

Table 4.9 Estimated plasma parameters for the dilute plasma experiment.

	Parameter	Value	Units
	Area	0.17	m^2
	T_e	5	eV
Region "A"	I_{rtn1}	3.38	μA
	V_{sat1}	630	V
	$I_{plasma1}$	22.62	μA
	n_{e1}	**~$1.5x10^2$**	**cm^{-3}**
Region "B"	I_{rtn2}	7.8	μA
	V_{sat2}	370	V
	$I_{plasma2}$	22.62	μA
	n_{e2}	**~$2.5x10^2$**	**cm^{-3}**

With the assumptions and variables described previously, we can then estimate the plasma densities at the different time regions of the test shown in Fig. 4.41. These estimates are shown in Table 4.9. The estimated plasma densities are $1.5x10^2$ and $2.5x10^2$ cm^{-3} for region "A" and region "B" respectively. These plasma densities are representative of the plasma environment found in an orbit that is lower than GEO but higher than LEO, a MEO orbit. It should be noted that this analysis only provides a very crude approximation of the plasma parameters and should only be taken as a rough estimate.

The following test shows the different neutralization properties of the electrons and ions in the plasma. We can expect the more mobile electrons to be more effective neutralizers than the heavier ions. This behavior is shown in Fig. 4.42.

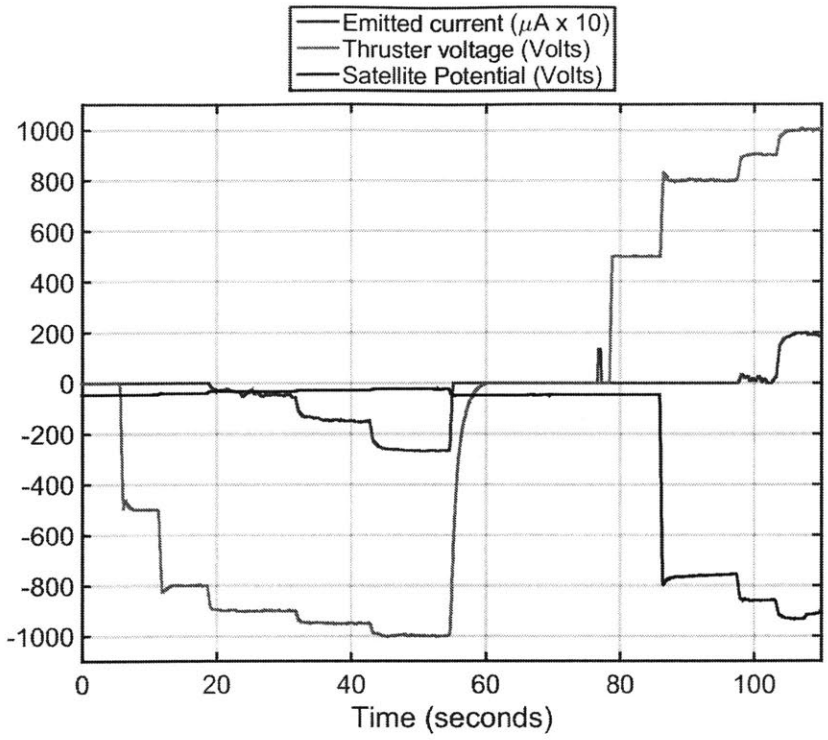

Fig. 4.42 Effects of a MEO-like plasma on a spacecraft firing a single electrospray thruster.

The cathode is operating with constant parameters throughout the test. The plasma generated by the cathode was chosen to be representative of a MEO orbit with a plasma density estimated to be between 10^3 to 10^4 cm^{-3} and a plasma temperature of around 5 eV. A single thruster is fired in this environment, first in the negative polarity, time 5 to 60s in Fig. 4.42, followed by positive emission, time 75 to 120s. Note the slightly negative satellite potential at the beginning of the test. When the thruster are off, the plasma charges the satellite to a small negative potential to equilibrate electronic and ionic fluxes. When the thruster emits negative ions, the satellite attempts to charge to a positive potential but is neutralized by the mobile electrons in the plasma. Small steps in the satellite potential can be seen in during this part of the test. When the thruster fires in the positive polarity, the satellite charges to negative potentials, repelling electrons and attracting ions. The ions, due to their lower mobility, are not as effective neutralizers and the satellite potential closely tracks the thruster potential. The ionic current is not able to neutralize the spacecraft and neutralization is achieved by the return current. Notice the similar results of the simulation in Fig. 4.18.

For this reason, if given a choice, one would chose to charge up to positive potentials with respect to the plasma to rely on mobile electrons for neutralization. As discussed in 4.2.3, when firing pairs of thrusters, if the currents are not identical, a slightly larger negative emitted current is desirable for this reason.

Dense plasmas

Performing experiments in dense LEO-like plasmas, and therefore small Debye lengths, proved challenging due to plasma leakage. This was true even with the addition of charge sensor shield. With high densities, the plasma was able to leak into the charge sensor, depositing negative charge, and producing a constant but bogus drift in the satellite potential measurement, similar to the effect described in 4.5.2. The openings produced by the charge sensor shield were larger than the plasma Debye length. To counteract this, the charge sensor plate was biased to -8V to repel plasma electrons. This measure did not solve the problem completely but reduced its effects to a more manageable range. A test in which a pair of thrusters fire while the CubeSat is surrounded by a dense, LEO-like plasma environment, can be seen in Fig. 4.43.

The average of the absolute emitted current of both thrusters is plotted in blue. The thrusters were connected in the bipolar configuration. Every 10 seconds the PPU turns off the high voltage to switch polarity, as can be seen by the step like signals. The test begins with the cathode generating a LEO-like plasma and the thrusters off. Such dense plasma leaks through the charge sensor shield and into the negatively biased charge sensor plate producing a bogus drift in the satellite potential measurement, minute 0.1. The bogus satellite potential drift continues even when the thrusters are firing as seen between time 0 to time 3.5 minutes. The emitted current was manually increased through this portion of the test. Note that during this period there are no "steps" in the satellite potential that correspond to the polarity switching events as seen in tests with no plasma. This can be taken as evidence that the plasma is able to completely neutralize the spacecraft and only the bogus drift signal is present. The satellite potential during this part of the test was therefore, very close to zero.

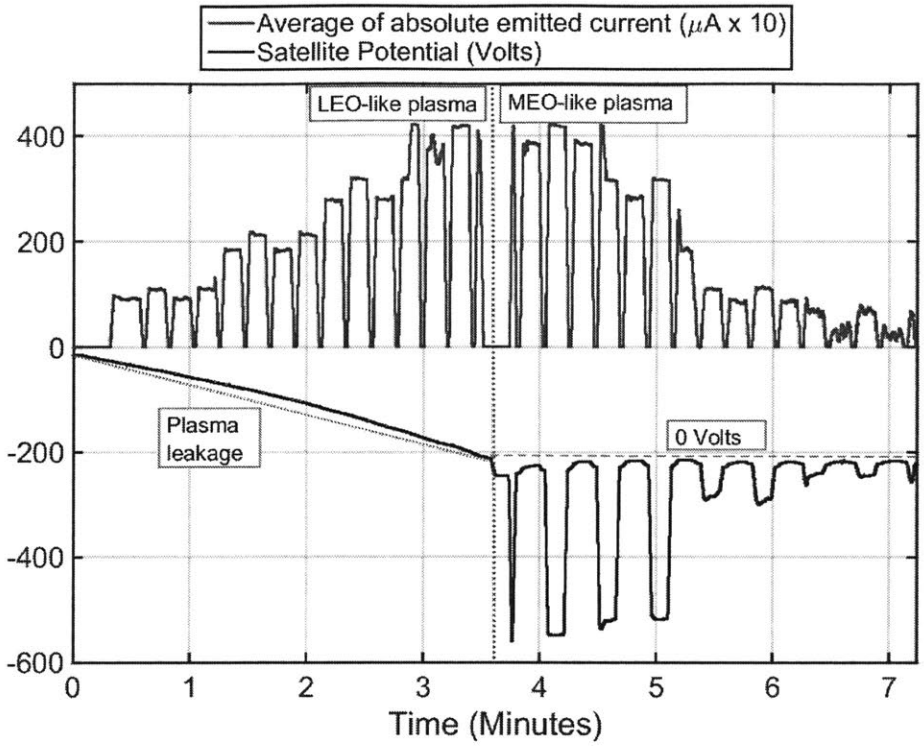

Fig. 4.43 Pair of thrusters in the bipolar configuration firing in a dense plasma environment.

At time 3.5 minutes, the density of the plasma is reduced to a MEO-like environment by reducing the filament current. In this phase of the test, the plasma is not dense enough to completely neutralize the spacecraft or to leak into the charge sensor, therefore the bogus drift stops. The -200V boundary on the satellite potential should really be 0V. The -200V offset is caused by the plasma leakage during the first portion of the test. Notice that the spacecraft never charges above the offset -200V mark, or in reality, zero volts. This is because the electrons of the MEO-like plasma are abundant enough to completely neutralize the spacecraft when it attempts to charge in the positive mode. Therefore, only negative spacecraft charging occurs. The emitted current was manually reduced during this portion of the test. Notice that a significant change in the satellite potential behavior occurs at time 5.3 minutes. This can be attributed to the lower current being commanded, the thruster then shifts to a different operation regime in which charging is less severe.

Finally, a test in which a pair of thrusters in the bipolar configuration were fired with a constant current while varying the surrounding plasma parameters was performed, Fig. 4.44.

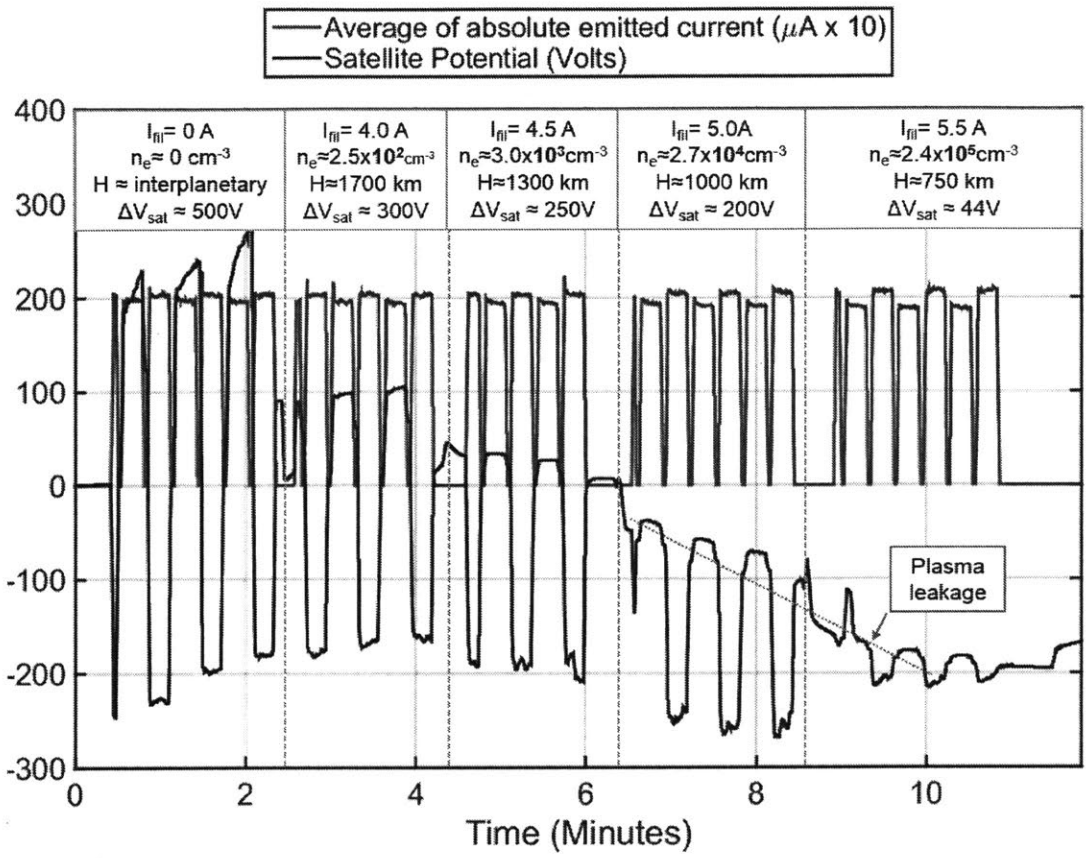

Fig. 4.44 Thrusters firing in the bipolar configuration while plasma parameters were varied.

In a similar fashion as the test previously described, the average of the absolute emitted currents is plotted. Two thrusters continuously fired ~20μA, while every ~10s the PPU turned off the voltages to switch polarity. The cathode was disabled at the beginning of the test, turning on at time 2.5 minutes. The density of the plasma generated by the cathode was increased in discrete steps for the rest of the test as seen by the labels in the top of Fig. 4.44. I_{fil} represents the filament current of the cathode, n_e is the estimated plasma density, H is the approximate orbital height of such a plasma, and ΔV_{sat} represents the envelope of the spacecraft charging. The plasma densities generated by the cathode were estimated based on the filament current by using an exponential fit produced with 3 data points. The data points where the LEO-like density measured with the Langmuir probe as described in 2.3.1, and the two densities estimated

in the test shown in Fig. 4.41. The estimated plasma densities should only be taken as rough approximations.

As in the previous test, with higher plasma densities plasma leakage is increased and the bogus satellite potential drift appears which corrupts the satellite potential measurement. Disregarding this bogus drift and focusing only on the satellite potential envelope, it can be seen that charging is less severe with higher plasma densities as seen by the reduction of ΔV_{sat} throughout the test. This result is to be expected, a higher density plasma is able to deliver larger currents, both positive and negative, to neutralize the satellite. If the plasma density is high enough, charging is almost negligible, as seen in the last portion of the test, time 10 minutes.

This test shows the importance of orbital altitude on spacecraft charging. At LEO-like orbits spacecraft charging is relatively low, therefore, any thruster emission asymmetries would not be as significant. At higher altitudes, above 1000km, spacecraft charging becomes more relevant and more care should be taken to pair thrusters with similar emission characteristics. This would be especially true for GEO or interplanetary trajectories as the main neutralization source would be the return current which could have detrimental effects on the spacecraft.

5 Attitude control and electrosprays

Employing electrospray devices as reaction thrusters opens the possibility of omitting traditional attitude control actuators such as reaction wheels and magnetorquers. This is especially beneficial for a mission that requires propulsion and is employing electrospray thrusters anyways. The differences between an electrospray propulsion system with only propulsive capabilities and one with propulsive and attitude actuation capabilities are not very large. The major change is the orientation of the thrusters. The volume and mass savings obtained by omitting traditional attitude actuators would allow satellites to carry more payload mass, increasing performance. To study the performance of electrospray thrusters as attitude control actuators we begin by comparing them to the more traditional chemical thrusters when used for the same purpose.

5.1 Chemical thrusters as reaction thrusters

Chemical thrusters have been the predominant type of reaction thruster due to their wide range of thrust values and long space heritage. When chemical thrusters are used as reaction thrusters they can produce large torques that give a large control authority over the satellite, this means that changes in attitude can proceed rapidly. Chemical thrusters are usually operated as ON-OFF devices as they are usually not throttleable. Electromechanical valves are the main reason of this operation mode, they are usually designed to be either fully open or fully closed. The ON-OFF behavior of chemical reaction thrusters mandates some sort of modulation in order for them to form part of a control loop. The modulation is usually achieved with some variation of the Pulse Width Modulation (PWM) technique. The thruster is fired for short periods of time when low impulse is needed and for larger periods of time when large amounts of impulse are required.

The modulation achieved by the PWM technique is limited by the nature of chemical thrusters. There is a minimum time the chemical thruster can be producing thrust. This minimum time is particular for each thruster design and heavily depends on the valve used. Combining the minimum thrust time, t_{bit}, and the thrust during that time, F_{bit}, we can calculate the minimum amount of impulse the thruster can deliver, this is often called the minimum impulse bit, I_{bit}.

$$I_{bit} = F_{bit}\, t_{bit} \qquad \textbf{Eq. 5.1}$$

The minimum impulse bit is usually determined by the reaction thruster chosen and cannot be decreased at will. It also has very important implications for the performance of the control system. Since the minimum impulse is larger than zero, the torques that can be applied to the spacecraft are also always larger than zero. The discretization of torques implies that the satellite orientation will oscillate around the commanded setpoint. In an attitude control system employing On-Off thrusters, everything else being equal, a lower I_{bit} yields higher attitude pointing precision [60, 61]. This holds as long as the ACDS is not sensor-limited.

Fig. 5.1 shows a generic attitude controller system using an ON-OFF actuator. This example ignores any external perturbations. When a change in angular setpoint is commanded, the controller reacts and fires the thruster that rotate the spacecraft towards the new setpoint. At some point, when the satellite has gained sufficient rotational velocity and is close to the setpoint, the opposite thruster is fired to slow down the rotation and avoid a large overshoot. The satellite now enters the deadband state where it continually "bounces" between a high and low angle usually centered on the setpoint. Since the minimum torque that the thrusters can apply is always larger than zero, and there are no friction sources, the satellite will never settle on the setpoint exactly. Notice that once the satellite is in the deadband region, the thrusters are only activated briefly to change the direction of movement.

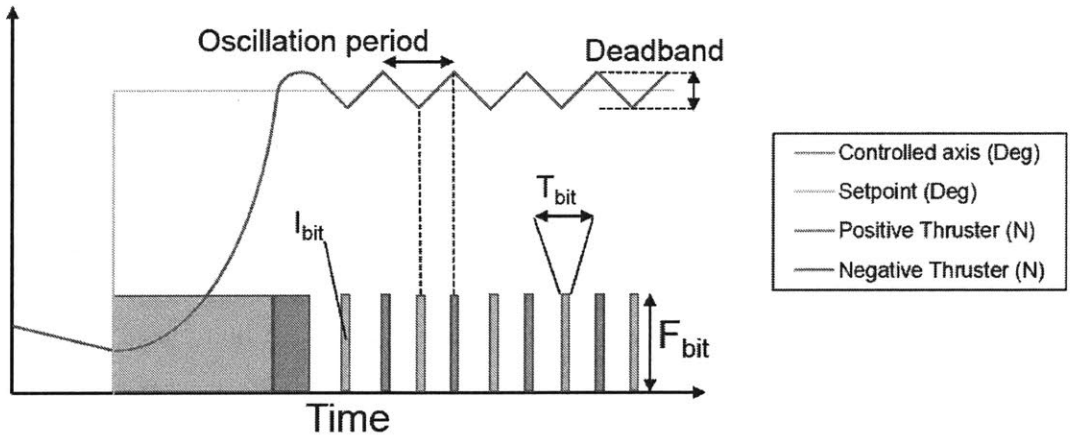

Fig. 5.1 Representative action of an attitude controller employing ON-OFF thrusters.

The amplitude of the steady state oscillations is usually called the deadband and can be thought of as the precision of the attitude controller. The shorter the firing intervals in which such thrusters are activated translates into a higher attitude control precision. On the other hand,

longer firing intervals consume less propellant, increasing mission lifetime. Therefore, a tradeoff between attitude control performance and propellant lifetime must be made.

5.2 On-Off thrusters

An analysis of propellant consumption for On-Off thrusters acting as attitude control actuators for one-axis follows. This analysis assumes impulsive maneuvers are performed to maintain the attitude of the satellite within a certain angular deadband, 2θ. As soon as the satellite reaches the deadband two thrusters are activated producing an asymmetric impulse equal to $2I_{bit}$, shown as red arrows at the graph in Fig. 5.2. This implies that each thruster fires at its lowest possible thrust, F_{bit}, and for the shortest amount of time, t_{bit}. Between firings, the satellite coasts with constant angular velocity for a time t_{coast}. For this analysis, it is assumed that the satellite provides perfect attitude knowledge and it is not under external disturbances.

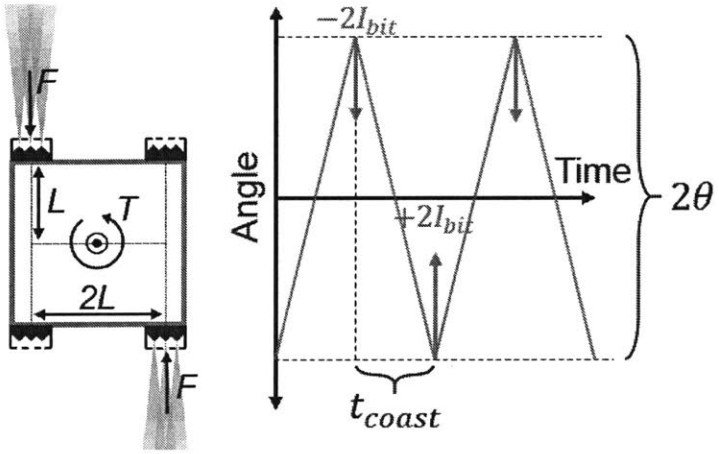

Fig. 5.2 ACDS test case arrangement and behavior.

Four identical thrusters are placed in a configuration as shown in Fig. 5.2. The minimum change in angular velocity ($\Delta\omega_{bit}$) induced when a pair of thrusters performs a minimum impulse firing is:

$$\Delta\omega_{bit} = 2\frac{L\,F_{bit}\,t_{bit}}{I} = 2\frac{L\,I_{bit}}{I} \qquad \textbf{Eq. 5.2}$$

Where I is the moment of inertia of the satellite and L is the thruster lever arm. The propellant mass consumed per minimum impulse firing per thruster, m_{bit}, is:

$$m_{bit} = \frac{I_{bit}}{g\,I_{sp}} \qquad \textbf{Eq. 5.3}$$

The time the satellite coasts from $+\theta$ to $-\theta$ if only minimum impulse firings are produced is:

$$t_{coast} = \frac{2\theta}{\Delta\omega_{bit}/2} = \frac{4\theta}{\Delta\omega_{bit}} \qquad \textbf{Eq. 5.4}$$

It is clear that a shorter t_{coast} produces a smaller deadband. The lifetime of the reaction thruster system, t_{life}, based on propellant consumption, is then:

$$t_{life} = \frac{m(2\,t_{coast})}{m_{bit}} = \frac{4\,g\,(I_{sp}mI\theta)}{L\,I_{bit}^{\,2}} \qquad \textbf{Eq. 5.5}$$

Where m is the propellant mass carried for each thruster. Notice that a specific pair of thrusters fires every $2 \cdot t_{coast}$. A quadratic dependence of lifetime on I_{bit} is expected because with lower I_{bit} less propellant is consumed on each firing and less firings per unit time are required to hold certain deadband.

Combining Eq. 5.3 and Eq. 5.5 we can calculate the achievable deadband as a function of I_{bit}:

$$\theta = \frac{t_{coast} I_{bit} L}{2I} \qquad \textbf{Eq. 5.6}$$

Fig. 5.3 shows the expected propellant lifetime of the ACDS, with respect to I_{bit} for different deadbands. Table 5.1 lists the parameters used for the calculation.

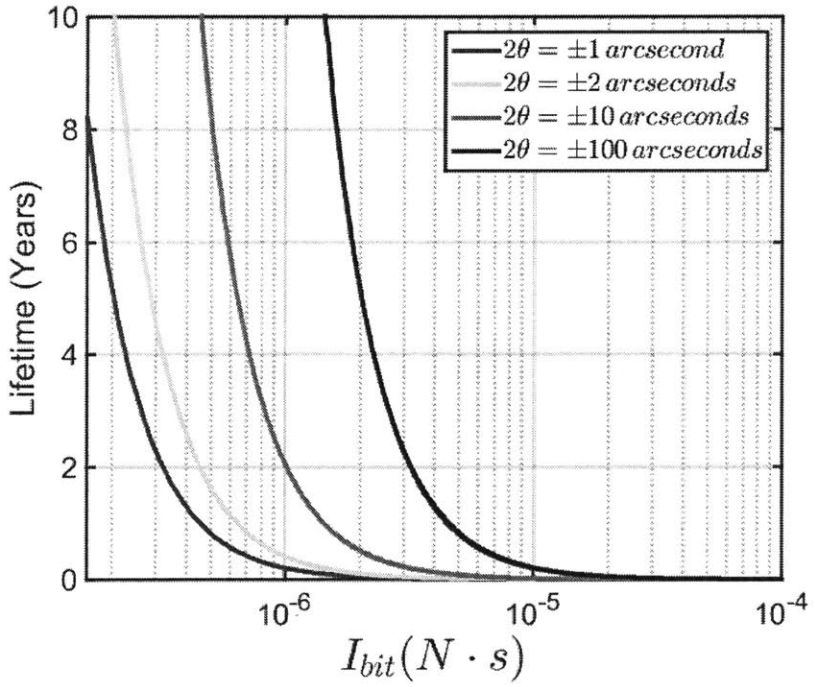

Fig. 5.3 Propellant lifetime with respect to I_{bit} for different deadbands.

Currently, chemical thrusters small enough to fit on a CubeSat have an I_{bit} of around 10^{-4} N·s and carry around 300 grams of hydrazine [5]. The I_{sp} of hydrazine thrusters is less than 300s [5, 6]. The large I_{bit} combined with the low I_{sp} allows only hours of continuous attitude hold for a 100 arcsecond deadband. Because of this, chemical thrusters are not good candidates for precision attitude control actuators in small satellites.

Table 5.1 1-U CubeSat test Case parameters

Parameter	Value	Units
I	0.0017	kg m^2
I_{sp}	1000	seconds
m	1	gram
L	5	cm

Using Eq. 5.6 and the parameters in Table 5.1 we can plot the required I_{bit} for a certain deadband, for several t_{coast}, Fig. 5.4.

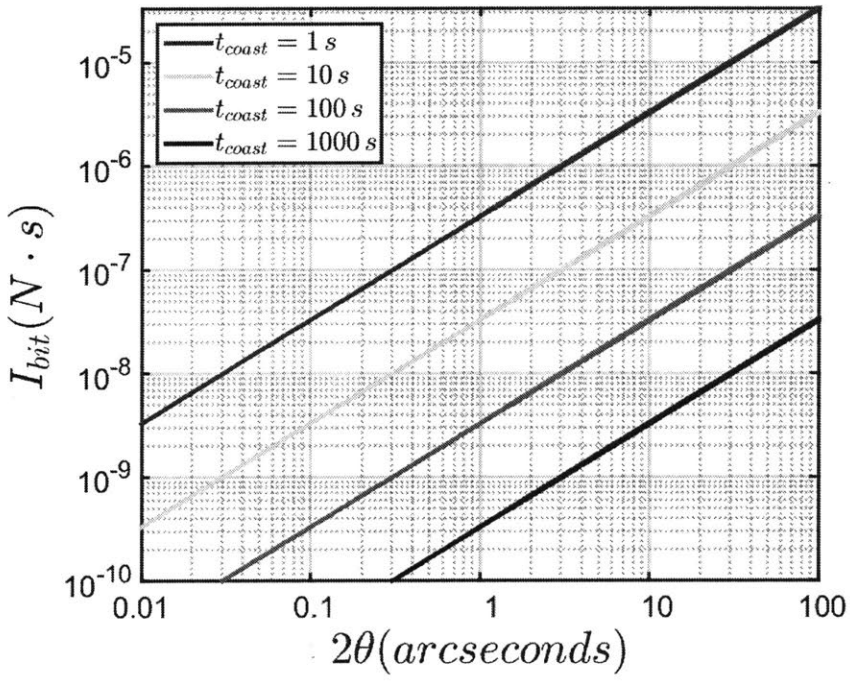

Fig. 5.4 I_{bit} required for a certain deadband for different t_{coast}.

It should be noted that these results do not take into account external torque perturbations. To counteract external perturbations when holding attitude, a thruster pair must fire continuously with a thrust level proportional to the disturbance magnitude. Table 5.2 shows the different sources and magnitudes of torque perturbations for a 1-U CubeSat in a 700km orbit. A residual magnetic dipole of $5x10^{-4}$ A·m^2 in the spacecraft structure is assumed. This was the measured residual magnetic dipole of the PACE [62].

Table 5.2 Torque sources and magnitudes for a 1-U CubeSat at 700km [63].

Torque perturbation source	Torque (N·m)
Aerodynamic	8.7×10^{-10}
Gravity gradient	6.8×10^{-10}
Solar pressure	3.7×10^{-9}
Residual magnetic moment	2.2×10^{-8}

Using the satellite and thruster parameters of Table 5.1, we can calculate the lifetime of 1 gram of propellant when the thrusters fire continuously to counteract each of the external disturbances sources, neglecting the propellant consumed for attitude control. For the solar pressure torque disturbance of 3.7×10^{-9} N·m the propellant lifetime would be ~8 years. For the larger residual magnetic moment disturbance, the lifetime would be reduced significantly to ~257days. Therefore, for this specific test case, it would be beneficial to reduce the remnant magnetic dipole of the spacecraft as much as possible to increase propellant lifetime or use counteracting techniques such as the ones described in [64].

5.2.1 Electrosprays as attitude control thrusters

Electrosprays are a promising reaction thruster technology for missions that require precise attitude control, especially small satellites. One of the attractive characteristics of electrosprays as reaction thrusters is their low thrust in the μN range or lower, and corresponding low I_{bit}. Since there are no moving parts, they do not produce any jitter. Furthermore, electrosprays thrusters are fully throttleable, which is advantageous over On-Off thrusters. The thrust produced by these devices is a function of the voltage applied to their terminals. They are throttleable from a minimum startup current, which depends on the specific design of the iEPS thruster, repeatable and known, to a maximum current. Forcing a comparison to On-Off thrusters, we can estimate an electrospray equivalent I_{bit*} using conservative values obtained from the experimental characterization of iEPS.

The electrospray emission process takes several to tens of milliseconds to stabilize, therefore, the minimum firing time should be of the same order [65, 66]. However in practice, the minimum firing time is dictated more by the PPU than the thrusters themselves. A conservative minimum firing time for the PPU used in experiments to be described in later sections is around 1 second. The minimum thrust is also somewhat limited by the PPU since there is a minimum amount of emitted current the PPU can measure and therefore control. In the experiments reported here, 10 μA was the minimum emitted current this specific PPU could measure and control reliably.

This minimum current translates into ~0.8 μN of thrust [11, 43]. An estimate of the I_{bit} based on the minimum firing time and minimum thrust would then be ~8×10^{-7} N·s. Assuming a conservative coasting time of 10 seconds and a satellite configuration identical to the one in Table 1, the achievable deadband would then be ~12 arcseconds. In this same example, if only impulsive maneuvers are performed while holding attitude, the mass of the propellant per thruster (1 gram) would last for ~3 years. This lifetime is on the order of a successful CubeSat mission.

It is possible that this performance can be improved. Notice that the minimum current scales with the number of emitter tips in each thruster, in this case 480. By reducing the number of tips in each thruster, the minimum stable current could be reduced, decreasing the I_{bit} even further. In the limit, a single emitter tip could be used, thus reducing the I_{bit} by a factor of ~480 and resulting in an I_{bit} of ~1.67×10^{-9} N·s. This neglects further reductions, by a factor of 10 to 100, when using a PPU capable of faster pulses. In such high-accuracy configurations, separate denser thrusters could be used to expedite slew maneuvering while single emitters provide the required fine control.

5.3 Attitude controller and power processing unit

The MagCube was used to study the performance of electrospray thrusters as attitude control actuators. The zero-friction rotational DoF the magnetic levitation provides is an ideal environment to test precise attitude control maneuvers, usually measured in arcseconds. Although control systems can be complex, the tests conducted at the MagCube were aimed to

be a proof of concept and not optimized procedures. There is significant room for improvement on the attitude controller performance presented in the following sections.

As explained in section 2.2.7, the angular movement of the levitated CubeSat is measured with a high precision non-contact angular encoder. By using an external attitude sensor, we can decouple thruster attitude performance from sensor performance and simplifies the implementation of the system.

The external attitude determination sensor allows off-board computation of the control algorithm, easing implementation. A PC is used to read the angular encoder and compute the controller algorithm. The PC then sends the manipulation outputs, via radio, to the satellite PPU. A block diagram of the attitude control experiments is shown in Fig. 5.5.

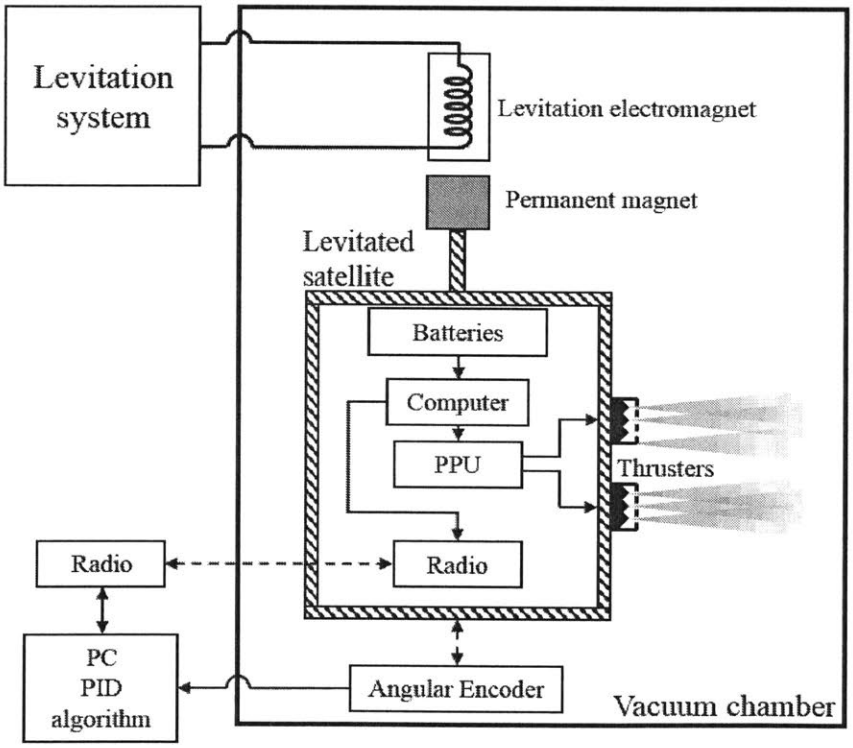

Fig. 5.5 MagCube schematic for attitude control experiments.

A standard PID controller was used as the attitude control algorithm. There was no optimization of either maneuver time or fuel consumption. The PID algorithm on the PC runs

at 50 Hz. The derivative output of the algorithm is smoothed with a 20-sample real time averaging filter, to avoid thruster manipulation jitter. A block diagram of the controller algorithm is shown in Fig. 5.6.

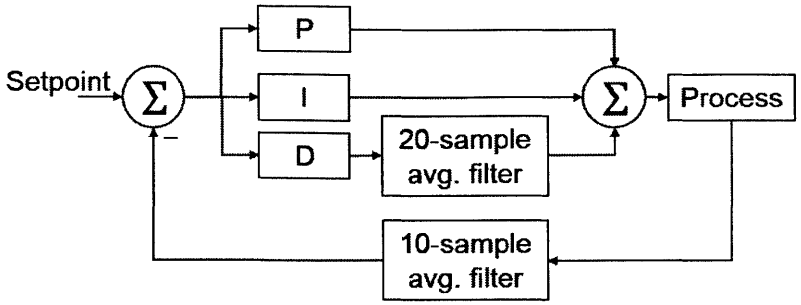

Fig. 5.6 Attitude control PID Diagram.

The PPU inside the CubeSat is described in section 2.5. The electronics are able to fire two thruster pairs with different throttle levels simultaneously. The PPU includes a microcontroller, high voltage converters, and housekeeping circuitry. The PPU receives a -100% to +100% manipulation signal from the PC, which is then translated into firing the respective thruster pair. The two thruster pairs onboard the satellite are never fired simultaneously when performing attitude control experiments. The maximum thrust produced by the thrusters, which corresponds to a manipulation signal of 100%, is mapped to a maximum emitted current setting in the PPU. Thrust produced by electrospray thrusters is proportional to emitted current as shown by Eq. 3.2.

5.4 Experimental results

5.4.1 Counteracting perturbations

Tests on the MagCube started with the attitude controller being off, therefore only the perturbing restoring torque mentioned in section 2.1.2 is acting on the levitated satellite. The attitude controller was then turned on. A representative attitude control test is shown in Fig. 5.7.

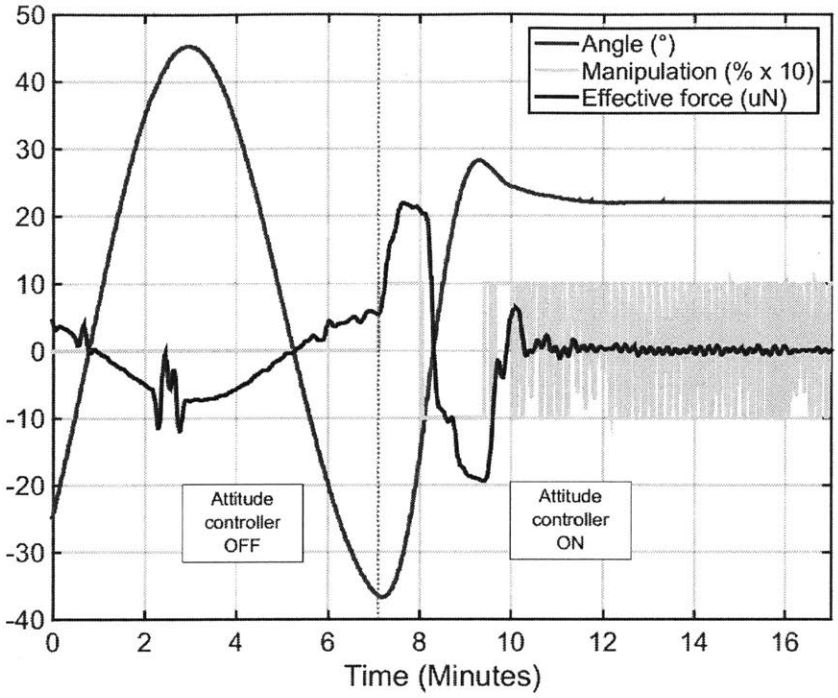

Fig. 5.7 Activating the attitude controller.

The vertical dashed line indicates the moment when the attitude controller is activated. The setpoint was held constant at 22° for this specific test. The satellite parameters for this and following tests are shown in Table 5.3. The angle has been filtered as discussed in section 2.2.7. The manipulation signal is the output of the control algorithm and has bounds in the range 1 to -1. A manipulation of 1, or 100%, means the thrusters that produce a positive torque are fired with their maximum thrust F_{max}, which is then set by a maximum emitted current parameter, I_{max}, on the PPU.

Table 5.3 Levitated satellite parameters

Parameter	Value	Units
I	0.0065	kg m^2
I_{max}	10 - 90	μA
F_{max}	0.8 – 7.2	μN
L	9.8	cm

The effective force trace, is the instantaneous torque acting on the satellite at any given moment transformed into an equivalent force applied at the thruster location. For example, at

the time the attitude controller is activated, the effective force is around 5μN. Each thruster, in the thruster pair that produces negative torque, would then have to produce 2.5μN of continuous thrust in order to counteract the perturbing torque when the satellite is at that specific angle. Since the effective force is calculated by differentiating twice the angle signal, any error in the angle signal is greatly amplified. The noisy portion at time 2.5 minutes is an artifact of this differentiation, the angular data was particularly noisy at that instant. Significant smoothing of the angular data using an averaging filter is required in order to differentiate twice and get results beyond noise. This smoothing also introduces a time delay on the effective force signal.

Once the attitude controller is activated the effective force tracks the thrust being produced by the thrusters in addition to any other external forces. When the attitude controller is suddenly activated the difference in the setpoint and angle make the controller dictate a 100% throttle in the positive direction. For this test, the upper current range of 80 μA for I_{max} was used. At this time, the thrusters produce around 14.4 μN. The satellite starts to rotate towards the setpoint. At minute ~8, the velocity on the satellite is large enough for the D term on the PID controller to activate the opposite pair of thrusters, effectively slowing down the rotation to reduce overshoot. At minute 13 the satellite has stabilized at the setpoint. Notice the On-Off behavior seen on the manipulation signal, bouncing from 100% to -100%. This was due to the constants of the controller being tuned too aggressively in this particular test.

5.4.2 Small step response

The performance of setpoint step tracking was also explored. Fig. 5.8 shows the ability of the thrusters to rotate the satellite in 1° decrements with precision. For this test I_{max} was set to 30 μA or an F_{max} of 2.4 μN. The dashed box on the left plot indicates the portion of the plot that is taken into account to calculate the attitude error shown on the right plot. The attitude error, for this and subsequent charts, is calculated based on the filtered angle signal, as explained in section 2.2.7.

During the time represented by the dashed box, the satellite holds its setpoint within 15 arcseconds 3σ of error. The time it takes the satellite to make the 1° step change, in this case ~3 minutes, is dictated by the maximum thrust allowed, in this case ~2.4μN. Such a low value was selected to reduce the amount of overshoot. In reality the thrusters are able to generate up to 15μN of thrust. A more sophisticated controller algorithm, possibly employing gain

scheduling or phase space techniques could allow to decrease the slew maneuver time and still hold attitude precisely.

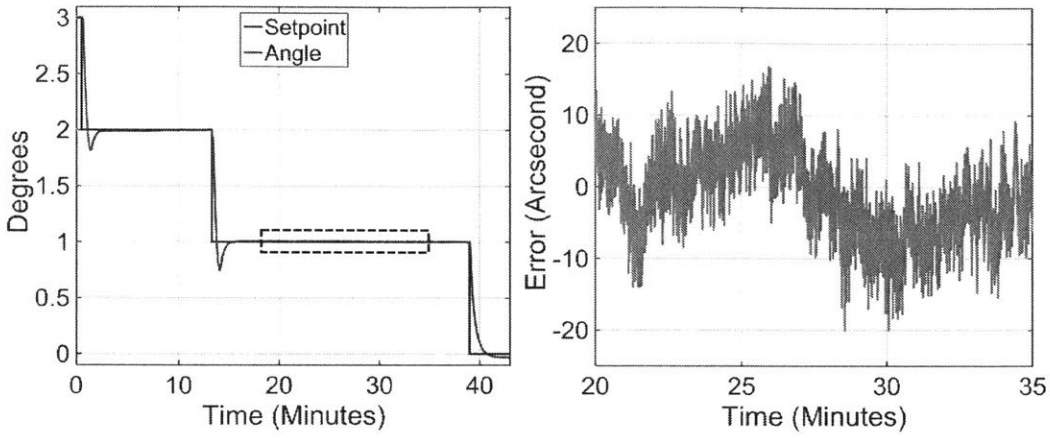

Fig. 5.8 One degree step changes.

5.4.3 Large step response

Larger setpoint change maneuvers were also explored with the same I_{max} as before . In Fig. 5.9, a 23° setpoint change was commanded. The satellite rotates to its new setpoint in about 13 minutes, holding its attitude within 15 arcsecond 3σ. The non-uniform angular evolution visible around the 10 minutes mark, is caused by the non-uniformity of the perturbing torque as discussed in section 2.1.2.

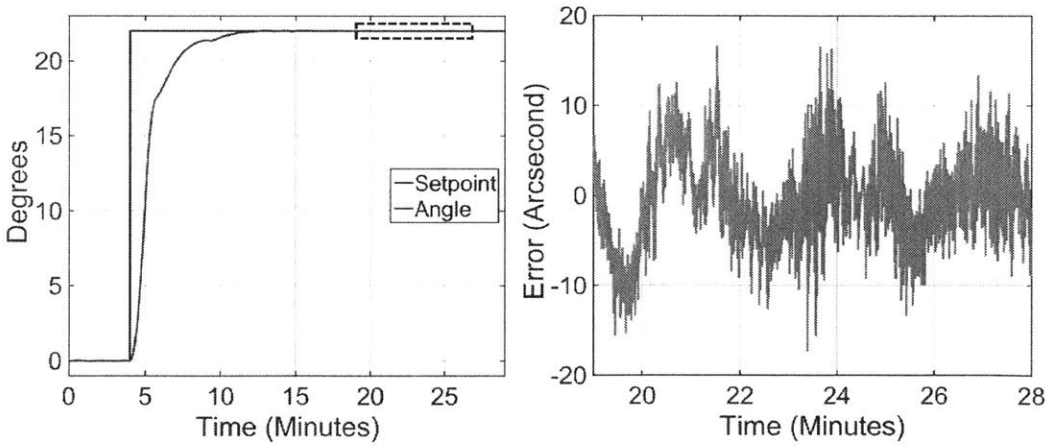

Fig. 5.9 Twenty three degree setpoint change

5.4.4 Long duration

Holding attitude for long periods of time is paramount for space missions, especially those requiring long exposures for observation. In Fig. 5.10, a constant setpoint of zero degrees was continuously held during 10 hours, limited by the battery life of the satellite. Over this timeframe, the satellite was able to hold its attitude within 22 arcseconds 3σ of error (shown as horizontal dashed lines in the figure) with respect to the filtered angular signal for ~10 hours.

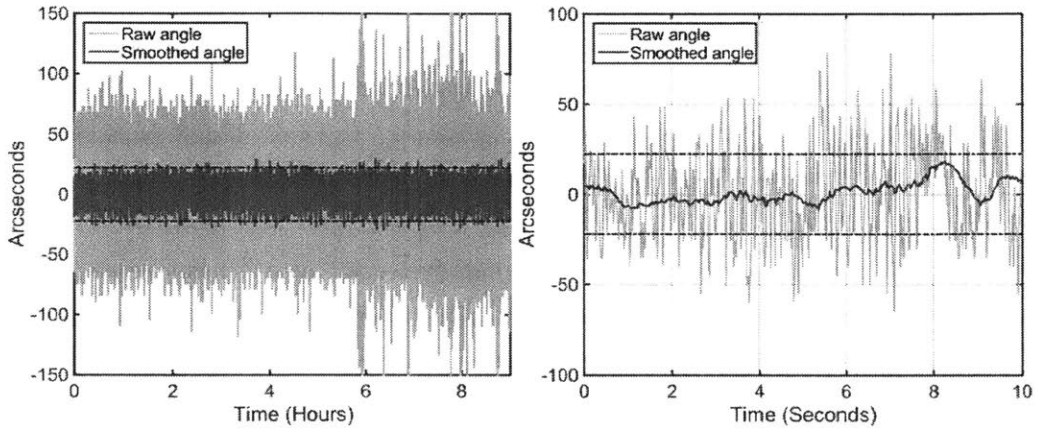

Fig. 5.10 Satellite holding attitude for ten hours. Dashed lines indicate 3σ boundary.

The manipulation in this long duration test remained within 40% and -20% envelope, with an average value of 7.8% during the test (marked with a horizontal dashed line in Fig. 5.11). Since the angular position of the satellite only varied tens or several arcseconds during the test, the perturbing torque, which only depends on the satellite angle, can be regarded constant. The maximum current parameter for that specific test was set to 10μA meaning the 7.8% average manipulation represents 0.78μA of average emitted current per thruster.

This average emitted current corresponds to ~0.06 μN of perturbing thrust per thruster assuming satellite parameters depicted in Table 5.3. By transforming perturbing thrust into a torque we then get a perturbing torque of 1.22×10^{-8} N·m. This implies that during the 10 hours that the test lasted, the thrusters were continuously counteracting this torque perturbation. We can compare this perturbation torque to representative torque perturbation sources in orbit, see Table 5.2 [63]. The 1.22×10^{-8} N·m perturbing torque in the test is higher than perturbations induced by solar pressure but lower than perturbations induced by residual magnetic moment, for a 1-U CubeSat at 700km.

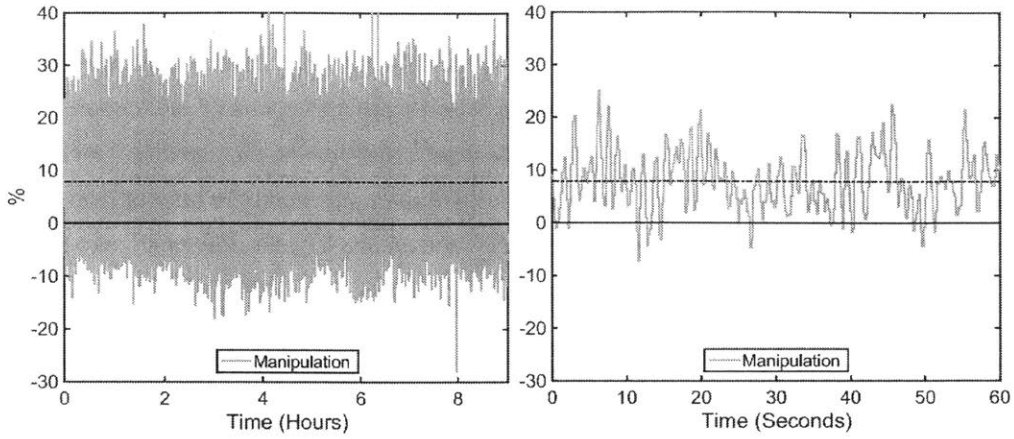

Fig. 5.11 Manipulation for a constant setpoint during a 10 hour period. Dashed line indicates average manipulation over the entire test.

At this rate of continuous firing and assuming the test case of Table 5.3, 1 gram of propellant in the thrusters would theoretically last for ~5 years. The larger lever arm, 9.8cm helps increase the lifetime of the propellant as the thrusters produce larger torques when firing.

6 Conclusions and recommendations

Electrospray thrusters are becoming a game-changing technology able to provide small satellites with efficient propulsion. Their low size, high efficiency and high specific impulse makes them ideal to propel these small spacecraft to more daring missions. The main motivation for the research presented in this work is to characterize parameters and properties of these thrusters that have eluded investigation thus far. Some of the concerns that worried first electrospray researchers have been quenched. The results obtained through this study confirm that electrospray thrusters can operate in space conditions for prolonged periods of time without critical issues. Electrospray thrusters are now a mature technology ready to be deployed into space.

6.1 MagCube

The bulk of the experiments of this research took place in the MagCube. This new type of testbed combines the thrust-measuring capabilities of traditional torsional balances with the rotational allowance of air bearings. The testbed magnetically levitates a mock-up satellite in a vacuum environment, producing a zero friction rotational degree of freedom. Besides electrospray thrusters, the levitated satellite is equipped with all relevant electronics like batteries, radio, computer and thruster electronics. Once under vacuum, the thrusters are able to actuate the satellite with μN forces. The complete mechanical and electrical isolation of the levitated satellite opens up the study of thruster aspects that would otherwise had to be performed in separate testbeds. Besides thrust, the testbed can be used to study spacecraft charging and attitude control performance of any type of relatively small thruster that can be mounted on the mock-up satellite.

Thrust measurements techniques are described and thrust estimates for an electrospray thruster presented. The magnetic levitation scheme presented perturbation torques that reduced the final thrust measuring capabilities of the testbed. A mitigation technique that reduces the perturbation torques is described in 3.1.1. The final thrust measurement uncertainty is estimated to be around ±0.35 μN (3σ). This uncertainty is in the range of some torsional balances. This figure could be reduced by improving the angular acceleration measurement of the levitated satellite or perhaps by using contact force probes like the ones described in 2.1.1. If a sufficiently good continuous angular acceleration measurement could be made, then continuous thrust could be obtained.

The thrust measurements of iEPS produced by this instrument confirm the linear relationship between thrust and emitted current, around 0.8μN/μA for this specific version of thruster. The thrust measurements were validated by comparing them to external thrust measurement produced by a torsional balance. The thrusters were fired using a custom PPU that went through several design iterations. The final PPU architecture offers substantial amounts of housekeeping information and is expandable to larger number of thruster channels.

The nature of the MagCube makes it a thrust-integrator instrument. Therefore, it is an ideal platform to test pulsed thrusters which are usually more challenging to characterize using torsional balances. The isolation of the levitated satellite removes any bogus thrust (produced by large currents or thermal effects) that might be picked up by torsional balances. Besides thrust, the MagCube could be used to characterize the propellant consumption rate to estimate specific impulse. This could be done by carefully measuring the current going through the levitation electromagnet. This current is sensitive to the weight of the levitated structure. The challenges of this approach are the sophisticated instrumentation required to measure the changes of this current and the dynamic effects of the testbed. Finally, the testbed could be fitted with additional components that could be used to measure performance of other satellite subsystems. A bright lamp can be used as a sun simulator. The performance of solar panels, and power distribution systems along with sun-pointing algorithms can be studied. By adding small white LEDs around the chamber, stars can be simulated, useful for a small satellite relying on star trackers for precise attitude determination. A hot surface on the otherwise ambient temperature vacuum chamber can be used as an Earth infrared signature simulator which can add Earth sensor data. The combination of the sun, Earth and stars simulators can help determine the performance of an attitude determination system. When the CubeSat is equipped with not only attitude sensors but actuators, the whole ADCS performance can be analyzed in a relevant vacuum, and zero-friction environment.

6.2 Spacecraft charging

The electrical isolation environment provided by the MagCube is used to thoroughly characterize the spacecraft charging effects induced on a spacecraft operating electrospray thrusters. The main conclusions reached through experimentation and simulation of a satellite firing a pair of electrospray thrusters in the bipolar configuration with a floating power supply, Fig. 4.2, are listed and explained in more detail below.

- **Under normal circumstances, the satellite potential will never exceed the thruster potential.**
- **The satellite potential does not affect the emission current of the thrusters.**
- **The floating power supply scheme ensures identical emitted currents from both thrusters.**
- **Differential intercepted current is the main driver of spacecraft charging and has to be counteracted by either return current or plasma current.**
- **The neutralizing effects of the return current depend heavily on the energy distribution of the emitted ion beams.**
- **Under normal circumstances, a denser plasma is a more effective neutralizer than a dilute one.**
- **Satellite potential affects total thrust with a square root dependence.**

The results obtained in simulations and experiments demonstrate that charge balancing with heavy ion species is indeed possible. There are two key passive mechanisms that allow this: the floating power supply and the return current. Allowing the thruster high voltage power supply to float with respect to the satellite ground, ensures that the emitted currents from two thrusters firing in the bipolar configuration become symmetric. The timescale to reach this equilibrium depends proportionally on the capacitance of C_{HV}. This effect can be seen in the results from Fig. 4.11. The MagCube tests presented in Fig. 4.29 and Fig. 4.31, make the presence of the return current evident. From these tests it can be concluded that the satellite potential will never exceed the thruster potential.

Another property of electrospray thrusters can be extracted from Fig. 4.23. Any charge on the satellite would not modify the potential difference between the thruster emitter tips and its extractor. In other words, the amount of emitted current from an electrospray thruster does not depend on the satellite potential. Although the emitted current might not be affected by the satellite potential, the net thrust produced certainly is, as shown in section 4.4. It is then beneficial to operate within a small satellite potential range to maximize thrust in the bipolar configuration. Finally, results from Fig. 4.29 show that the charge in the satellite does not increase indefinitely. This is due to the return current counteracting the difference in intercepted currents. In consequence the satellite potential at which an equilibrium is reached depends on the difference of intercepted currents and the energy distribution of the ion beams. This allows

the electrical model to precisely predict the steady state charging levels of a satellite from the emission and interception properties of specific thruster devices.

It is important to notice the detrimental effects of the return current, as shown in Fig. 4.32. The ions that make it back to the spacecraft will deposit themselves on the surfaces they collide in, in general interacting with them. If they have sufficient energies, they could erode the surfaces. Very low energies could lead to deposition. **In either case, deposition or erosion, return current will result in surface contamination or deterioration.** Satellite manufacturers and operators are strongly concerned about the effects that any propulsion system might have on the satellite surfaces, especially on solar panels and instrumentation optics. Therefore, any contamination produced by propulsion systems should be minimized. Since in electrospray thrusters, the main source of contamination is the return current, one must then minimize the differential interception current which drives the return current. The interception properties of a thruster is given mainly by its mechanical parameters. The separation of the extractor to the tips, the size of the extractor apertures, and the shape of the emitter tips are all variables that would have to be very well matched from thruster to thruster to ensure the smallest difference in interception currents between them. Better manufacturing techniques, with smaller tolerances, would then reduce the return current and therefore the possibility of contaminating spacecraft surfaces.

It should be noted that the trajectories of the charged particles that constitute the return current determines which satellite surfaces they will interact with. For example, if the trajectories are local to the thruster, meaning that most particles that return interact with the extractor grid, then the contamination effects would mainly be constrained to the thruster surfaces. If on the other hand, the returning particles are able to travel significant distances and therefore impact other parts of the spacecraft the effects could be more severe. In all likelihood the interactions would remain local to the thruster but further modeling and experimentation are needed.

There are several behaviors on these tests that need further explanation. In Fig. 4.29, the sudden loss of charge at time 1.1 minutes is abnormal. Positively-charged, secondary particles generated in the vacuum chamber due to ion collisions with the wall, secondary electrons generated when the return current collides with the satellite, and sensor anomalies seem like plausible explanations. However these hypotheses require further work before confirmation.

The dynamic response of the satellite potential shown in Fig. 4.33, Fig. 4.34 and Fig. 4.35 could be explained by changes in the operational modes of the thrusters. The capacitances involved C_{SC} and C_{HV} are small but they do not allow instantaneous changes in potential. The time delay induced by these capacitors could lead to fast oscillations on the emitted currents and therefore on the satellite potential. Further experimentation is needed to verify this hypothesis.

Plasmas simulations and experiments produced relevant results with significant consequences for spacecraft operating electrospray thrusters. The mobile electrons in the plasma readily collect in a positively charged spacecraft. Ions on the other hand are not as effective neutralizers. Therefore, if given a choice, one would prefer the satellite to charge up positively in order to attract electrons for neutralization. A dense LEO-like plasma is an effective neutralizer, especially at the <1mA currents electrospray thruster currently operate in. The satellite potential will be limited by the plasma current, with more dramatic neutralizing effects for denser plasmas.

Taken to its logical extreme, a single thruster could be fired in negative mode (emitting negative ions) to charge the satellite positive. The plasma electrons could then provide neutralization. As discussed in section 4.1.4, this scheme wastes half of the propellant. A more benign scheme would be to fire two thrusters in opposite polarities but ensuring the one emitting negative current emits slightly more than the one emitting positive ions. This ensures the satellite charges up positively allowing the plasma to effectively neutralize it. As explained in sections 4.1.2 and 4.1.4, this scheme would not require a floating power supply. **A PPU with no floating power supply is significantly less complex and could fit in smaller volumes.** The operation of thrusters in this scheme would also be significantly less complex compared to operation in the floating power supply mode. Using the plasma as a neutralizer would only work in sufficiently dense plasmas which are able to deliver the differential emitted currents to the satellite. For interplanetary missions, where there is practically no plasma, the floating power supply scheme would have to be used. In this scenario photoelectric currents, which could be as large as 0.3μA for a 1-U CubeSat, could play a neutralizing role.

6.3 Attitude control

The results obtained in the experiments performed in the MagCube demonstrate that precise attitude control with electrospray thrusters is indeed possible. This is enabled mainly by their intrinsically low I_{bit} and throtability. The high specific impulse of these devices ensures that

relatively small amounts of propellant (grams) will last for a significant amount of time (years) for even single digit arcsecond deadbands if only used for this purpose. Even though the experiments were only performed in a single axis, extension to 3-axis control should be possible. This is especially true as in most tests, the satellite is holding setpoint with arcsecond precision, practically immobile, meaning axis coupling is minimal. The experimental results could be improved by using space attitude determination sensors. State of the art star trackers compatible with small satellites report an accuracy below 10 arcseconds [67]. The slow datarate (5 Hz) of these star trackers is partially compensated by using faster but lower accuracy sensors such as gyros or sun sensors and performing sensor fusion algorithms.

In these experiments, the levitated satellite is always acted by a small, but not negligible, perturbing torque. The tests, demonstrate that the thrusters are able to compensate for external perturbations comparable to perturbations in orbit. Further experiments could introduce stronger and variable perturbing torques, via the Helmholtz coils, to simulate stronger attitude perturbations in space. The fact that the average thrust of the devices can be used to precisely calculate the external perturbation opens the door to map the perturbation environment in orbit as seen by the test in Fig. 5.10.

The maximum thrust allowed during these tests (>0.8μN) was always set relatively low with respect to the actual maximum thrust of the devices (~15μN). The limit in thrust was imposed to reduce overshoot and allow the simple controller to perform relatively well. A gain scheduling or phase-space control algorithm might allow a lower maneuvering time and more precise attitude control. Furthermore, a more sophisticated controller could optimize for either propellant consumption or attitude performance. The high performance of electrospray thrusters as attitude control actuators opens the possibility of omitting reaction wheels for small satellite missions that require precise attitude control. This would be especially important for missions where thrusters are required to desaturate reaction wheels anyways, such as interplanetary or high altitude orbits.

7 References

[1] Chin, A., Coelho, R., Nugent, R., Munakata, R., and Puig-Suari, J. "CubeSat: The Pico-Satellite Standard for Research and Education," *AIAA SPACE 2008 Conference & Exposition*, 2008.
doi: 10.2514/6.2008-7734

[2] Larson, W. J., Wertz, J. R., and D'Souza, B. *SMAD III : Space mission analysis and design, 3rd edition : workbook*: El Segundo, CA. : Microcosm Press, c2005., 2005.

[3] Blue Canyon Technologies. "XACT Datasheet." 2016

[4] Whitlock, C. "Application of Ion Electrospray Propulsion to Lunar and Interplanetary Missions," *Department of Aeronautics and Astronautics*. Vol. Masters, Massachusetts Institute of Technology, Cambridge, MA, 2014.

[5] Masse, R. K., Carpenter, C., Schmuland, D., Overly, J., and Allen, M. Y. "CubeSat High-impulse Adaptable Modular Propulsion System (CHAMPS) Product Line Development Status and Mission Applications," *49th AIAA/ASME/SAE/ASEE Joint Propulsion Conference*, 2013.
doi: 10.2514/6.2013-3760

[6] Schmuland, D., Carpenter, C., and Masse, R. "Mission Applications of the MRS-142 CubeSat High-Impulse Adaptable Monopropellant Propulsion System (CHAMPS)," *48th AIAA/ASME/SAE/ASEE Joint Propulsion Conference & Exhibit*, 2012.
doi: 10.2514/6.2012-4269

[7] Gamero-Castaño, M., and Fernández de la Mora, J. "Mechanisms of electrospray ionization of singly and multiply charged salt clusters," *Analytica Chimica Acta* Vol. 406, No. 1, 2000, pp. 67-91.
doi: 10.1016/S0003-2670(99)00596-6

[8] Fernández de la Mora, J. "The Fluid Dynamics of Taylor Cones," *Annual Review of Fluid Mechanics* Vol. 39, No. 1, 2007, pp. 217-243.
doi: 10.1146/annurev.fluid.39.050905.110159

[9] Legge, R., and Lozano, P. "Electrospray Propulsion Based on Emitters Microfabricated in Porous Metals," *Journal of Propulsion and Power* Vol. 27, No. 2, 2011, pp. 485-495.
doi: 10.2514/1.50037

[10] Dandavino, S., Ataman, C., Chakraborty, S., Shea, H., Ryan, C., and Stark, J. "Design and fabrication of the thruster heads for the MicroThrust MEMS electrospray propulsion system," *33rd International Electric Propulstion Conference*, 2013.
doi: IEPC-2013-127

[11] Krejci, D., Mier-Hicks, F. T., Robert , and Haag, T. "Emission characteristics of passively fed electrospray microthrusters with propellant reservoirs," *Journal of Spacecraft and Rockets (AIAA)* Vol. Submitted for publication, 2016.

[12] Deng, W., Klemic, J. F., Li, X., Reed, M. A., and Gomez, A. "Increase of electrospray throughput using multiplexed microfabricated sources for the scalable generation of monodisperse droplets," *Journal of Aerosol Science* Vol. 37, No. 6, 2006, pp. 696-714.
doi: 10.1016/j.jaerosci.2005.05.011

[13] Alexander, M. S., Stark, J., Smith, K. L., Stevens, B., and Kent, B. "Electrospray Performance of Microfabricated Colloid Thruster Arrays," *Journal of Propulsion and Power* Vol. 22, No. 3, 2006, pp. 620-627.
doi: 10.2514/1.15190

[14] Courtney, D. G. "Ionic liquid ion source emitter arrays fabricated on bulk porous substrates for spacecraft propulsion," *Aeronautics and Astronautics*. Vol. PhD, MIT, Cambridge, MA, 2011.

[15] Lai, S. T. *Fundamentals of Spacecraft Charging: Spacecraft Interactions with Space Plasmas*: Princeton University Press.

[16] NASA. "Low earth orbit spacecraft charging design handbook," 2007. NASA Handbook: NASA-HDBK-4006.

[17] Hastings, D., and Garrett, H. *Spacecraft-Environment Interactions*. Cambridge, UK: Cambridge University Press, 1996.
doi: 10.1017/CBO9780511525032

[18] Sawyer, S. T. "Experimental Studies of Spacecraft Plasma Interactions: Facility Characterization and Initial Measurements," *Aerospace Engineering*. Vol. Masters Thesis., Virginia Polytechnic Institute and State University, Blackburg, Virginia, 2009.

[19] Mandell, M., Katz, I., and Cooke, D. "Potentials on large spacecraft in LEO," *IEEE Trans. on Nuclear Science* Vol. NS-29, No. 6, 1982, pp. 1584-1588.

[20] Chu, E., and Goebel, D. M. "High-Current Lanthanum Hexaboride Hollow Cathode for 10-to-50-kW Hall Thrusters," *IEEE Transactions on Plasma Science* Vol. 40, No. 9, 2012, pp. 2133-2144.
doi: 10.1109/TPS.2012.2206832

[21] Goebel, D. M., Watkins, R. M., and Jameson, K. K. "LaB6 Hollow Cathodes for Ion and Hall Thrusters," *Journal of Propulsion and Power* Vol. 23, No. 3, 2007, pp. 552-558.
doi: 10.2514/1.25475

[22] Goebel , D. M., and Katz, I. *Fundamentals of Electric Propulsion: Ion and Hall Thrusters*. Pasadena Ca: JPL Space Science and Technology Series, 2008.

[23] Ziemer, J. K., and Merkowitz, S. M. "Microthrust Propulsion for the LISA Mission," *40th AIAA/ASME/SAE/ASEE Joint Propulsion Conference and Exhibit*, 2004.
doi: 10.2514/6.2004-3439

[24] NASA Mission Design Division. "Small Spacecraft Technology State of the Art," 2015.
doi: NASA/TP–2015–216648/REV1

[25] Janson, S., and Welle, R. "The NASA Optical Communication and Sensor Demonstration Program," *27th Annual AIAA/USU Conference on Small Satellites*, 2013. AIAA Paper SSC13-II-1.

[26] Kingsbury, R., Riesing, K., and Cahoy, K. "Design of a Free-Space Optical Communication Module for Small Satellites," *27th Annual AIAA/USU Conference on Small Satellites*, 2014. AIAA Paper SSC14-IX-6.

[27] Nguyen, T., Riesing, K., Kingsbury, R., and Cahoy, K. "Development of a pointing, acquisition, and tracking system for a CubeSat optical communication module," *SPIE 9354, Free-Space Laser Communication and Atmospheric Propagation XXVII*. Vol. 93540O, 2015, pp. 93540O-93540O-9.

[28] Muri, P., and McNair, J. "A Survey of Communication Sub-systems for Intersatellite Linked Systems and CubeSat Missions," *Journal of Communications* Vol. 7, No. 4, 2012.
doi: 10.4304/jcm.7.4.290-308

[29] Committee on Achieving Science Goals with CubeSats Space Studies Board. Division on Engineering and Physical Sciences. National Academies of Sciences. *Achieving Science with CubeSats: Thinking Inside the Box*: The national acamies press, 2016. doi: 10.17226/23503

[30] Pong, C. M., Lim, S., Smith, M. W., Miller, D. W., Villaseñor, J. S., and Seager, S. "Achieving high-precision pointing on ExoplanetSat: initial feasibility analysis," *MIT Open Access Articles* Vol. 7731, 2010, pp. 77311V-77311V-16.

[31] Maryland Aerospace Inc. "MAI-400 Datasheet." 2016

[32] Gamero-Castaño, M. "A torsional balance for the characterization of microNewton thrusters," *Review of Scientific Instruments* Vol. 74, No. 10, 2003, pp. 4509-4514. doi: doi:http://dx.doi.org/10.1063/1.1611614

[33] Selden, N. P., and Ketsdever, A. D. "Comparison of force balance calibration techniques for the nano-Newton range," *Review of Scientific Instruments* Vol. 74, No. 12, 2003, pp. 5249-5254. doi: doi:http://dx.doi.org/10.1063/1.1623628

[34] Soni, J., and Roy, S. "Design and characterization of a nano-Newton resolution thrust stand," *Review of Scientific Instruments* Vol. 84, No. 9, 2013, p. 095103. doi: 10.1063/1.4819252

[35] Polk, J. E., Pancotti, A., Haag, T., King, S., Walker, M., Blakely, J., and Ziemer, J. K. "Recommended Practices in Thrust Measurements," *33rd International Electric Propulsion Conference*, 2013. Paper Number: IEPC-2013-440.

[36] Kuninaka, H., and Molina-Morales, P. "Spacecraft charging due to lack of neutralization on ion thrusters," *Acta Astronautica* Vol. 55, No. 1, 2004, pp. 27-38. doi: 10.1016/j.actaastro.2003.12.017

[37] Schwartz, J. L., Peck, M. A., and Hall, C. D. "Historical Review of Air-Bearing Spacecraft Simulators," *Journal of Guidance, Control, and Dynamics* Vol. 26, No. 4, 2003, pp. 513-522. doi: 10.2514/2.5085

[38] Hyunwook, W., Octavio, R., Simone, C., and Marcello, R. "CubeSat Three Axis Simulator(CubeTAS)," *AIAA Modeling and Simulation Technologies Conference*. American Institute of Aeronautics and Astronautics, 2011.

[39] Fickova, Z., Hort, T., Houstecky, L., Martin Hromcik, P., Jakubov, O., and Janosek, M. "The CzechTechSat – A Space-friendly CubeSat-class Picosatellite," *10th Annual CubeSat Developers Workshop*, 2013.

[40] Van de Winkel, D., and Craeynest, M. "Inertial Platform for CubeSat." Vol. Masters, Electronics-ICT, 2009.

[41] Blumber, E. J. "Testing of a Magnetically Levitated Rocket Thrust Measurement System Demonstrator for NASA," *Mechanical Engineering*. Vol. Masters, Virginia Polytechnic Institute and State University, Blacksburg, VA, 2002.

[42] Mier-Hicks, F. "Characterization on a magnetically levitated testbed for electrospray propulsion systems," *Aeronautics and Astronautics*. Vol. Masters, Massachusetts Institute of Technology, Cambridge, 2014.

[43] Mier-Hicks, F., Perna, L., Coffman, C., and Lozano, P. "Characterization of a CubeSat Compatible Magnetically Levitated Thrust Balance for Electrospray Propulsion Systems," *49th AIAA/ASME/SAE/ASEE Joint Propulsion Conference*, July 2013. doi: 10.2514/6.2013-3879

[44] Perna, L., Mier-Hicks, F., Coffman, C., Li, H., and Lozano, P. "Progress Toward Demonstration of Remote, Autonomous Attitude Control of a CubeSat Using Ion

Electrospray Propulsion Systems," *48th AIAA/ASME/SAE/ASEE Joint Propulsion Conference & Exhibit*. American Institute of Aeronautics and Astronautics, 2012.

[45] Femto Tools. "FT-S100 Datasheet,"

[46] Mier-Hicks, F. L., Paulo. "Thrust Measurements of Ion Electrospray Thrusters using a CubeSat Compatible Magnetically Levitated Thrust Balance " *Joint Conference of 30th International Symposium on Space Technology and Science and 34th International Electric Propulsion Conference and 6th Nano-satellite Symposium*, July 2015. IEPC-2015-148.

[47] Perez, A. T., and Garcia-Sanchez, P. "Permanent magnetic levitation of Levitron using periodic magnetic forcing," *XLII International Summer School–Conference APM* 2014.

[48] Earnshaw, S. "On the nature of the molecular forces which regulate the constitution of the luminferous ether," *Trans. Camb. Phil. Soc*, 1839, pp. 97-112.

[49] Zoellner, A., Hultgren, E., and Sun, K.-X. "Integrated Differential Optical Shadow Sensor for Modular Gravitational Reference Sensor," *8th International LISA Symposium*, 2013.

[50] MicroE. "Micro-E Mercury 3500V Datasheet,"

[51] Lozano, P., and Martínez-Sánchez, M. "Ionic liquid ion sources: suppression of electrochemical reactions using voltage alternation," *Journal of Colloid and Interface Science* Vol. 280, No. 1, 2004, pp. 149-154.
doi: 10.1016/j.jcis.2004.07.037

[52] Courtney, D. G., Dandavino, S., and Shea, H. "Comparing Direct and Indirect Thrust Measurements from Passively Fed Ionic Electrospray Thrusters," *Journal of Propulsion and Power* Vol. 32, No. 2, 2015, pp. 392-407.
doi: 10.2514/1.B35836

[53] Courtney, D. G., and Shea, H. "Fragmentation in Time-of-Flight Spectrometry-Based Calculations of Ionic Electrospray Thruster Performance," *Journal of Propulsion and Power* Vol. 31, No. 5, 2015, pp. 1500-1504.
doi: 10.2514/1.B35837

[54] Druge, J., Jean, C., Laurent, O., Méasson, M. A., and Favero, I. "Damping and non-linearity of a levitating magnet in rotation above a superconductor," *New Journal of Physics* Vol. 16, No. 7, 2014, p. 075011.

[55] Lozano, P., and Martínez-Sánchez, M. "Ionic liquid ion sources: characterization of externally wetted emitters," *Journal of Colloid and Interface Science* Vol. 282, No. 2, 2005, pp. 415-421.
doi: 10.1016/j.jcis.2004.08.132

[56] Lozano, P., Glassand, B., and Martinez-Sanchez, M. "Performance Characteristics of a Linear Ionic Liquid Electrospray Thruster," *29th International Electric Propulsion Conference*, October 2005. Paper: IEPC-2005-192.

[57] Lozano, P., and Martinez-Sanchez, M. "Efficiency Estimation of EMI-BF4 Ionic Liquid Electrospray Thrusters," *41st AIAA/ASME/SAE/ASEE Joint Propulsion Conference & Exhibit*, July 2005.
doi: 10.2514/6.2005-4388

[58] Iribarne, J. V., and Thomson, B. A. "On the evaporation of small ions from charged droplets," *The Journal of Chemical Physics* Vol. 64, No. 6, 1976, pp. 2287-2294. doi: 10.1063/1.432536

[59] Guerra-Garcia, C., Krejci, D., and Lozano, P. "Spatial uniformity of the current emitted by an array of passively fed electrospray porous emitters," *Journal of Physics D: Applied Physics* Vol. 49, No. 11, 2016, p. 115503.

[60] Sidi, M. J. *Spacecraft dynamics and control : a practical engineering approach*: Cambridge ; New York : Cambridge University Press, 1997., 1997.

[61] Micci, M. M., and Ketsdever, A. D. *Micropropulsion for small spacecraft*: Reston, Va. : American Institute of Aeronautics and Astronautics, c2000., 2000.

[62] Springmann, J., Cutler, J., and Bahcivan, H. "Magnetic Sensor Calibration and Residual Dipole Characterization for Application to Nanosatellites," *AIAA/AAS Astrodynamics Specialist Conference*. American Institute of Aeronautics and Astronautics, 2010.

[63] Rawashdeh, S. A. "Passive Attitude Stabilization for Small Satellites.." University of Kentucky, 2010.

[64] Inamori, T., Sako, N., and Nakasuka, S. "Magnetic dipole moment estimation and compensation for an accurate attitude control in nano-satellite missions," *Acta Astronautica* Vol. 68, No. 11–12, 2011, pp. 2038-2046. doi: http://dx.doi.org/10.1016/j.actaastro.2010.10.022

[65] Gassend, B. L. P. "A Fully Microfabricated Two-Dimensional Electrospray Array with Applications to Space Propulsion," *Department of Aeronatuics and Astronautics*. Vol. Phd., Massachusetts Institute of Technology, 2007.

[66] Martel, F., Perna, L., and Lozano, P. "Miniature Ion Electropsray Thrusters and Performance Tests on CubeSats," *26th Annual AIAA/USU Conference on Small Satellites*, 2012. AIAA Paper SSC12-VI-5.

[67] Blue Canyon Technologies. "Nano Star Tracker Datasheet." 2016